ENVIRONMENTAL RESPONSE OF COMPOSITE PAVEMENTS

by

Matthew Addison Geary

Bachelor of Science in Civil Engineering, University of Pittsburgh, 2009

Submitted to the Graduate Faculty of

The Swanson School of Engineering in partial fulfillment

of the requirements for the degree of

Master of Science

University of Pittsburgh

2014

UNIVERSITY OF PITTSBURGH

SWANSON SCHOOL OF ENGINEERING

This thesis was presented

by

Matthew Addison Geary

It was defended on

November 11, 2013

and approved by

Luis E. Vallejo, PhD, Professor, Department of Civil and Environmental Engineering

Donald J. Janssen, PhD, Associate Professor, Department of Civil and Environmental Engineering

Thesis Advisor: Julie M. Vandenbossche, PhD, Assistant Professor, Department of Civil and Environmental Engineering

ENVIRONMENTAL RESPONSE OF COMPOSITE PAVEMENTS

Matthew Addison Geary, M.S.

University of Pittsburgh, 2014

A composite pavement is a pavement structure with at least two dissimilar layers. These pavements are typically constructed using hot-mix asphalt (HMA), Portland cement concrete, or both. Typically, composite pavements are created when a new pavement layer is placed atop an older pavement layer. This research however focuses on the relatively less common composite pavements built as new construction and includes new concrete pavements with an HMA overlay and composite concrete pavements placed "wet on wet."

While these types of composite pavements have been constructed in Europe for years, the American experience has been limited. Significant barriers to the common adoption of new construction composite pavement exist. These barriers include the lack of a formal design procedure, construction experience, and performance and cost data supporting the benefits of composite pavements constructed in this manner.

As a means to overcome these limitations, the Second Strategic Highway Research Program (SHRP2) undertook project R21 entitled "Composite Pavement Systems" to investigate the implementation of composite pavements as new construction in the United States. Part of R21 involved the construction of three heavily instrumented composite pavements sections at the MnROAD National Research and Technology Center (MnROAD).

Two major assessments were performed in this thesis as part of meeting some of the goals of the R21 project. One assessment consisted of evaluating the environmental data obtained from the instrumented composite pavement slabs at MnROAD. The second assessment consisted of a stress sensitivity analysis performed using the pavement finite element software ISLAB. Together the results of these analyses were used to comment on the factors influencing the environmental conditions and stresses that develop in composite pavements. Suggestions were then made for the design and construction of long lived composite pavements.

TABLE OF CONTENTS

LIST OF TABLES

LIST OF FIGURES

PREFACE

I would first like to thank the SHRP 2 administrators for providing funding for the composite pavement project at MnROAD. Secondly, I would like to thank MnDOT and its personnel Jack Herndon, Tim Clyne, and Leonard Palek for their work in the instrumentation and data collection aspects of this project and for introducing me to the "Minnesota Nice". I would also like to thank Dr. Lev Khazonovich, Derek Thompkins, Mary Vancura, and Luke Johanneck from the University of Minnesota for their help in the instrumentation portion of this project.

From the University of Pittsburgh, I would like to thank my colleagues Luis Ramirez, Somayeh Nassiri, Manik Barman, Kerri Cutright, and Tom Adams for their support in all aspects of this work and express my enjoyment at the opportunity to have worked beside them. A special acknowledgement is due to Feng Mu. I am extremely grateful to my friend and colleague for the investment of his energies into the technical and emotional aspects of a thesis.

My mom and dad, Karen and Don, have always selflessly supported me in my academic career. Their role in my acceptance at the University of Pittsburgh was 18 years in the making and for that contribution I am eternally grateful. Throughout this process, and especially during the most difficult times, the blessing of my wife Katie and our relationship was my greatest joy and most valuable source of encouragement.

The final acknowledgement is due to Dr. Julie Vandenbossche. As the source of both the means and the inspiration to attend graduate school, her role in this work cannot be understated. I am grateful to have been her student, employee, and friend.

1.0 INTRODUCTION

1.1 BACKGROUND

A composite pavement refers to a pavement structure consisting of at least two different surface layers placed independently. Typically, composite pavements in the United States, consist of a newer surface layer being placed over existing structures that have already been in-service. The most common composite pavement in the United States is a hot-mix asphalt (HMA) overlay of an existing concrete pavement. In this vein, the newer upper layer of the pavement is used as a rehabilitation measure to extend the life of the existing underlying pavement. For decades however, some European nations, such as Austria and Germany, have been constructing composite pavements as part of the initial construction of roadways.

The most common types of composite pavements used in new construction have been concrete pavements overlaid with relatively thinner HMA layer and composite concrete pavements. These composite concrete pavements are constructed using two different concrete mixtures placed "wet on wet." In this construction, both the upper and lower concrete mixes are still in a plastic state when the final pavement thickness is realized. Although the initial construction of a composite pavement in this manner is more labor intensive, experience has shown significant life cycle benefits for these pavements.

From a performance perspective, the appeal of the aforementioned construction procedure is the ability to optimize the pavement structure in regards to economics and sustainability. Additionally, in Europe, these composite structures have been found to have equivalent or improved performance relative to a conventional Portland cement concrete (PCC) pavement. Composite concrete pavements can be optimized with respect to economics through the use of a lower layer comprised of locally available or less expensive aggregates. In a conventional PCC pavement, these same aggregates may result in concrete of an adequate structural capacity but may have less desirable wearing characteristics for a surface layer. By using the lower wear resistance aggregate in the lower layer and comprising the upper layer of durable aggregate, a more efficient and economical section is obtained. In addition to being able to use an aggregate with poor or moderate wearing characteristics, a recycled aggregate could also be used in the lower PCC layer. This is another means of economic optimization and also improves the sustainability of the pavement. In the European experience, the coarse aggregate of the upper PCC layer does consist of a more durable aggregate. The concrete is finished as exposed aggregate concrete (EAC) providing a safe, quiet, and durable riding surface [1].

For HMA pavements constructed over un-trafficked PCC pavements, the same economic and sustainability advantages can be achieved through the incorporation of recycled/ non-wear resistant aggregates in the lower pavement layer. In this type of composite pavement construction, the HMA layer provides a wear resistant and smooth riding surface. The HMA surface is also a surface that can be rapidly renewed through patching, milling, or overlaying. Open graded stone matrix asphalt (SMA) has also been constructed over the lower PCC layer with the benefit of reduced vehicle spray.

Although these pavements have been constructed in Europe, the construction of composite pavements in the United States has been limited. As part of the Second Strategic Highway Research Program (SHRP2) enacted by the United States Congress in 2006, project R21 entitled "Composite Pavement Systems," was undertaken. This project is aimed at furthering the renewal goal of the program. Specifically, the objective is to produce long-lived facilities to renew the highway infrastructure.

As part of the R21 project of SHRP 2, three composite pavements sections were constructed on the westbound mainline section of Interstate 94 at the Minnesota Road Research Facility (MnROAD) near Albertville, MN. The design for the composite pavement sections consist of three 9-in pavements. Each pavement has a 6-in lower layer and 3-in upper layer. The three composite structures consist of a HMA layer over a recycled concrete layer, an EAC layer over a recycled concrete layer, and an EAC layer over a concrete layer with high fly-ash content. The relatively high fly-ash content concrete results in a lower cost relative to typical MnDOT paving concrete mixes. This high fly-ash concrete will be referred to as the low-cost concrete throughout this work.

As part of constructing these composite pavements, two slabs within each pavement type were instrumented with a variety of sensor types. These types include thermocouples, relative humidity sensors, and static strain gauges. The sensors were installed throughout the pavements both spatially and throughout the depth. Data collection was performed every 15 minutes. In addition to sensors embedded within the pavement, a weather station is also located at MnROAD. The weather station captures ambient temperature, solar radiation magnitude, wind speed magnitude and direction, and precipitation duration and quantity.

1.2 RESEARCH OBJECTIVES AND APPROACH

Although composite pavements have been constructed in various European countries for decades, no published research with respect to the analysis of measured environmental pavement data from composite pavements is currently available. This thesis will therefore focus on presenting the findings from the first ten months of data obtained from the instrumented cells at MnROAD characterizing the environmental response of these composite pavements.

Conclusions regarding composite pavement performance will be made based on direct analysis of the strain, temperature, and moisture measurements for the pavement sections at MnROAD. Additionally, these measurements will be further interpreted through the use of the pavement finite element program ISLAB. ISLAB will also be used to perform a systematic assessment (sensitivity analysis) to determine influential parameters on the stresses that are generated by environmental and vehicle loading conditions.

Using both the results of the pavement sensor data analysis and ISLAB sensitivity analysis, conclusions will be made regarding the pavement structural properties that control both the location and magnitude of the critical stresses generated in composite pavements. These conclusions will then be extrapolated into recommendations for the design of future composite pavements in the United States and abroad.

1.3 THESIS STRUCTURE

The structure of this thesis is broken down into seven chapters. The second chapter consists of a literature review regarding the importance of determining the stresses in pavements for mechanistic design procedures as well as influential factors for the stresses in composite pavements. The third chapter consists of a description of the instrumented pavement sections at MnROAD. The fourth chapter is an analysis of the measured data from the composite pavements at MnROAD. The focus of the fifth chapter is to relate the measured differences in the response of the composite pavements to the environment to stresses within the pavement using ISLAB. The sixth chapter discusses the setup and results of the sensitivity analysis performed using ISLAB on composite concrete pavements. Chapter seven includes conclusions regarding inferences made from the sensor data regarding the three composite pavements constructed at MnROAD as well as conclusions regarding composite concrete pavements obtained from the sensitivity analysis.

2.0 LITERATURE REVIEW

2.1 COMPOSITE PAVEMENTS

2.1.1 Composite Pavements in the United States and Europe

Composite pavements consist of at least two different materials acting together to provide the structural capacity to sustain a given amount of traffic. In this sense of the definition, there are many composite pavements in the United States. One common and widespread example of a composite pavement is an HMA overlay of an existing rigid pavement. Another example is whitetopping, in which concrete is placed over an existing HMA pavement. Still other examples include bonded and unbonded concrete overlays of pre-existing concrete pavements.

In Europe, other kinds of composite pavements are also constructed and have shown good performance. These composite pavements are the focus of this research and include an HMA layer constructed over an un-trafficked concrete layer and composite concrete layers constructed during initial construction in a method known as "wet on wet." While these pavements utilize similar materials to traditional pavements, the difference in the European application is the sequencing of the construction. In the United States, a composite pavement is typically constructed when a new layer is constructed over an existing layer that is somewhat structurally or functionally deficient.

From a cost standpoint, the initial construction cost of European composite pavements is higher because of the additional construction equipment and personnel required for constructing two layers. While the construction costs may be higher, the impetus behind the construction of composite pavements in Europe is a combination of a sense of environmental responsibility, cost concerns, availability issues associated with adequate aggregates, and a history of exemplary performance for composite pavements.

Composite pavements constructed in Europe are also optimized with respect to functional and structural performance with each composite pavement type having its own unique advantages. For composite concrete pavements constructed "wet on wet," a stiffer, more abrasion resistant aggregate is used as the coarse aggregate fraction for the upper concrete layer. An aggregate with substandard wearing characteristics or recycled aggregate can be used for the lower layer. This utilization saves money without compromising the overall pavement wearing resistance. New concrete pavements with an HMA surface layer take advantage of the fact that that the HMA layer is a rapidly replaceable layer. Because the HMA can be replaced rapidly, the required length of traffic interruptions for functional rehabilitations is significantly decreased. While regular HMA has been used for the HMA layer, stone matrix asphalt (SMA) has also been used and provides enhanced safety by reducing vehicle spray on highways.

The total thickness of the composite pavement is dictated by a pavement structural design procedure and the relative thickness of each layer is pre-determined and based on experience. In Europe, whether the composite pavement is HMA/PCC or PCC/PCC constructed wet on wet, the thickness of the upper layer has been found to range from approximately 2- to 4-in. The remainder of the total required thickness is made up of the base composite pavement concrete.

2.1.2 Composite Pavement Materials

The previous section pointed out that based on the European experience, composite pavements provide both a functional and economical advantage. The functional advantages are in the form of rapidly renewable or highly durable, quiet riding surfaces for HMA/PCC and PCC/PCC pavements respectively. The economic advantages come in the form of the ability to use recycled or somewhat substandard aggregates in the concrete mix design. These modifications, while beneficial, also influence the engineering properties of the materials relative to a homogeneous pavement. While this section will point out the differences in the materials used between composite and homogeneous pavement construction, the specific implications of these differences are the focus of the remainder of this work.

In the construction of composite pavements, specifically wet-on-wet composite concrete pavements, two factors that are unique to this type of construction have a significant influence on the layers' engineering properties. One factor is the use of recycled concrete aggregate in the mix design. The second is the inherent differences in the mix design for each of the two layers.

Using recycled concrete aggregate in new pavement construction has been shown to influence two important material properties, the coefficient of thermal expansion (CTE) and elastic modulus. The coefficient of thermal expansion (α) represents the strain experienced by a material per unit change in temperature and the elastic modulus can be defined as the strain experienced by a material per unit change in load. The primary way that using recycled concrete aggregate influences the CTE is through the higher paste content in the concrete mix. The higher paste content is due to the residual mortar on the recycled aggregate fraction. The residual mortar clinging to the recycled aggregate is in turn a function of the crushing process used to create the recycled aggregate. It has also been found that the influence of using recycled concrete aggregate

in a new mix with respect to elastic modulus is that the elastic modulus is lowered. Elastic moduli values of concrete containing recycled concrete aggregate compared to a control using virgin aggregates have been found to be between 1 and 50 percent lower than a mix containing virgin aggregates [2].

With respect to the mixture designs for the different composite pavement concrete layers, European composite pavements typically have an upper layer with a higher cementitious content and a lower aggregate top size relative to the lower layer. Both factors contribute to a common situation where the strength and elastic modulus of the upper EAC layer is high than that of the underlying layer.

When an HMA pavement is constructed over a new PCC pavement, the materials used are the same as for a typical paving operation. As mentioned previously, the primary difference between the composite AC/PCC pavements constructed in Europe are the phasing and the use of recycled concrete aggregate in the underlying PCC layer.

2.2 DESIGN OF PAVEMENT STRUCTURES

The significance of the differences between composite and homogeneous pavements highlighted in the previous section can only be appreciated within the correct analysis framework. The state of the practice in pavement design is currently in a transitional period moving from an empirical design procedure to a mechanistic-empirical procedure. In the United States, the history of a rational pavement structural design method for jointed plain concrete pavements (JPCP) begins with the first Guide for Design of Pavement Structures published in 1972 by the American

Association of State Highway and Transportation Officials (AASHTO). This guide, and all subsequent versions were completely empirical in nature.

In the empirical framework, performance data of observed distresses would be subjected to regression analysis and a relationship would be established to provide designers with guidance on specifying layer thicknesses and material types, among other things.

Recognizing the limitations of the purely empirical version of the Guide for Design of Pavement Structures, the AASHTO Joint Task Force on Pavements, which is responsible for pavement design technologies, started the effort required to develop a new design guide based on mechanistic principles rather than relying solely on empirical evidence [3]. In the mechanistic-empirical approach, there are generally more variables that are considered. Another important aspect of the mechanistic-empirical approach is that stresses are determined that are dependent on the enhanced variable consideration. The stresses are then used in a fatigue analysis. Once sufficient fatigue is accumulated in a pavement, it is assumed that a given distress will occur and subsequently impact the functional or structural performance of the pavement. In this way, factors controlling a specific distress type can be examined and modified in the design procedure to mitigate pre-mature deterioration of the pavement ride quality.

The result of the effort undertaken by the AASHTO Joint Task Force on Pavements was the Guide for the Mechanistic-Empirical Design of New and Rehabilitated Pavement Structures referred to herein as the MEPDG. The MEPDG allows pavement designers to consider variables in the areas of climate, traffic, materials, and structure. The MEPDG makes considerations for these variables and projects the rate of occurrence of various failure mechanisms such as cracking and faulting as well as their effect on road roughness.

While the MEPDG is an improvement in terms of the variables that are considered, there is still an empirical aspect of the guide. The empirical aspect of the guide is incorporated in some instances with material characterization, while it is incorporated in other ways with through the relationship between the computation of stress or strain with an actual distress in the field [3]. The main limitation in applying the current version of the MEPDG to composite pavements lies in the bridge between mechanistic analysis and an empirical relationship between predicted stress and performance in terms of observed distresses.

The MEPDG also relies heavily on the use of neural networks in its computations. Within the MEPDG, neural networks are used to find the stresses and deflections that develop for a given analysis condition. Neural networks are much more efficient at obtaining these values of interest as they avoid executing and processing many finite element models each time a design scenario is assessed. In order for the neural networks to be successful however, the network must be populated with the results of many finite element model calculations. In the instance of the composite pavements focused on in this work, these finite element model runs have not been executed and populated into the neural network database.

In addition to the lack of available finite element model runs, there are currently only a few test sections of the kind that are the focus of this research. The instrumented pavements constructed at MnROAD provide both an additional performance dataset and a detailed accounting of material properties and applied traffic and environmental loads.

2.3 FACTORS INFLUENCING STRESSES IN JPCPS

With composite pavements, as with traditional homogeneous pavements, deriving mechanistic performance relationships involves accurately predicting a calculated stress and the influence of various parameters on its value. The factors that influence the stress that is generated in a JPCP are the geometrics of the pavement structure itself, the environment, traffic loadings, and material behavior of the concrete such as creep and drying shrinkage. While these factors are influential on their own, there are also interaction effects that play a role in the magnitude and location of the stresses that are generated. This section elaborates upon these factors and highlights some of the differences in the way traffic and the environment affect resulting stresses in both homogeneous and composite pavements.

Loads from traffic and the environment contribute to the development of distress. The next section will briefly discuss the stresses induced by traffic. Subsequent sections will focus on environmental stresses in JPCPs.

2.3.1 Traffic Induced Stresses in JPCPs

In the MEPDG, traffic induced stresses are determined for each loading scenario over the life of the pavement. This is accomplished using neural networks developed from an assemblage of results using the finite element computer program ISLAB. A fundamental understanding of the stresses caused by traffic in a jointed plain concrete pavement however, can be obtained by examining the closed form solutions proposed by Westergaard in 1926 and modified by Ioannides in 1985[4].

The closed form solution for the critical tensile stress at the bottom of the slab under three unique loading conditions is shown in Equation 2 through Equation 4. These equations are applicable for a circular single wheel load of magnitude P and with radius a, applied to a pavement slab with a radius of relative stiffness, ℓ (Equation 1) and subgrade foundation modeled as a bed of independent springs with uniform stiffness k. The unique loading conditions considered in Equation 2 through Equation 4 are for a corner loading, interior loading, and edge loading respectively[4]. In these equations, E is the elastic modulus of the concrete, h is the slab thickness, k is the modulus of subgrade reaction, and ν is the Poisson's ratio of the concrete.

$$l = \sqrt[4]{\frac{E \cdot h^3}{12 \cdot \left(1 - \upsilon^2\right) \cdot k}} \qquad \text{Equation 1}$$

$$\sigma_c = \frac{3P}{h^2} \cdot \left[1 - \left(\frac{1.722a}{l}\right)^{.72}\right] \qquad \text{Equation 2}$$

$$\sigma_i = \frac{3 \cdot (1 + \upsilon) \cdot P}{2 \cdot \pi \cdot h^2} \cdot \left(\ln\left(\frac{l}{b}\right) + .6159\right) \qquad \text{Equation 3}$$

$$\sigma_e = \frac{3 \cdot (1 + \upsilon) \cdot P}{\pi \cdot (3 + \upsilon) \cdot h^2} \cdot \left[\ln\left(\frac{Eh^3}{100 \cdot k \cdot a}\right) + 1.84 - \frac{4 \cdot \upsilon}{3} + \frac{1 - \upsilon}{2} + \frac{1.18(1 + 2\upsilon) \cdot a}{l}\right] \qquad \text{Equation 4}$$

In these three closed form solutions, the critical stress is always generated when the load is at the longitudinal edge of the slab. These equations, which were used for years as the primary analysis tool for the stresses generated in concrete pavements, consider the slab to be flat and fully supported. As a result of these assumptions, the location of the critical tensile stress based on Equation 4 is always at the bottom of the slab along the outside edge at midslab.

As can also be seen from Equation 1 through Equation 4, the structural parameters that influence the stresses in the pavement are the modulus of elasticity of the concrete, the thickness

of the pavement, and the Poisson's ratio. Although not implicated in these equations other structural factors have also been shown to influence the stresses generated in concrete pavements. These features include dowel bars, tie bars, and the type of base layer. Dowel bars serve to transfer load across joints and reduce the corner stresses and deflections [4]. The base layer induces tensile stresses in the concrete by restraining the movement of the slab as it expands and contracts during temperature changes.

2.3.2 Environmental Stresses in JPCPs

Two primary environmental factors that change throughout the life of a pavement and that can influence the stress in a JPCP are the temperature and moisture distribution within the slab. Not only are these gradients are a function of the physical environment in which the pavement is placed, but they are a function of the materials used to construct the pavement as well.

In response to temperature and moisture changes, there are two primary responses of a pavement. One is that the slab will exhibit a uniform expansion or contraction. The other is that the slab curls upwards or downward. Restraint to both curvature in the slab, as well as uniform expansion or contraction is a significant source of stress in the slab. The following sections will discuss the relationship between typical temperature and moisture conditions in the slab and the stresses they induce. Inherent in the discussion is how environmental stresses are considered in the analysis and design of concrete pavements and how material properties influence the temperature and moisture conditions throughout the slab.

2.3.2.1 Temperature effects on stresses in composite pavements

At relatively low stresses, of the kind experienced by a typical pavement, the stress/strain behavior of concrete can be characterized as linear elastic. For linear elastic materials, Hooke's law, expressed in Equation 6, is applicable and the magnitude of the stress generated by a restrained movement can be related to the stiffness, E, and strain, ε, induced in the material. For stresses associated with changes in temperature, the strain is linearly related to the CTE. As stated previously, the CTE represents the strain undergone by a material during a unit change in temperature. The strain induced in a material due a temperature change therefore is given by Equation 6.

$$\sigma = E\varepsilon \qquad \text{Equation 5}$$

$$\varepsilon_{thermal} = \alpha \Delta T \qquad \text{Equation 6}$$

Although a material may experience strain due to a change in temperature, there is no external stress applied to the material so long as the thermal strain is not restrained. The next section discusses the sources of restraint in concrete pavements.

Tensile stress generated between the slab and base layer While concrete slabs are nearly constantly changing temperature conditions, there is a reference condition in which there is no restrained strain or stress in the slab. For concrete pavements, the reference point is established at the time of construction. This reference point is defined as the climatic conditions present at the time the concrete has gained sufficient stiffness and that restrained expansion or contraction will generate a stress in the concrete. This reference condition is referred to as the zero stress time and is accompanied by a corresponding zero stress temperature of the pavement.

Once the zero stress time is reached, one source of slab restraint is the base layer. The base layer restrains thermal movement of the slab because the slab and base do not have corresponding thermal expansion and contraction tendencies. The stress generated in the slab by restraint of thermal expansion or contraction provided by the base is expressed by Equation 7. In Equation 7, γ is the unit weight of the concrete, L is the length of the slab, f_a is the coefficient of friction between the base and the bottom of the slab, and σ is the maximum tensile stress generated in the concrete at the center of the slab. When the slab contracts due to a drop in the pavement temperature the stress induced in the slab by the base is tensile in nature.

$$\sigma_c = \frac{\gamma_c \cdot L \cdot f_a}{2} \qquad \text{Equation 7}$$

If the stress induced by the base is greater than the concrete strength, then cracks can form in the pavement. In the design of JPCPs, the joint spacing is reduced so that the tensile stress generated from this restrained movement does not exceed the strength of the concrete. The optimal joint spacing to both reduce the number of joints and limit stresses is 15-ft. This spacing is in consideration of both slab curling and uniform contraction concerns.

Stresses generated due to slab curvature Curvature is induced in concrete pavements during the presence of a temperature gradient. In a homogeneous concrete pavement, when the top of the slab is warmer than the bottom of the slab, the slab is curled downward because the top of the slab wants to expand more than the bottom of the slab. Accordingly, when the bottom is warmer than the top of the slab, the slab is curled upward. An illustration is provided in Figure 2.1.

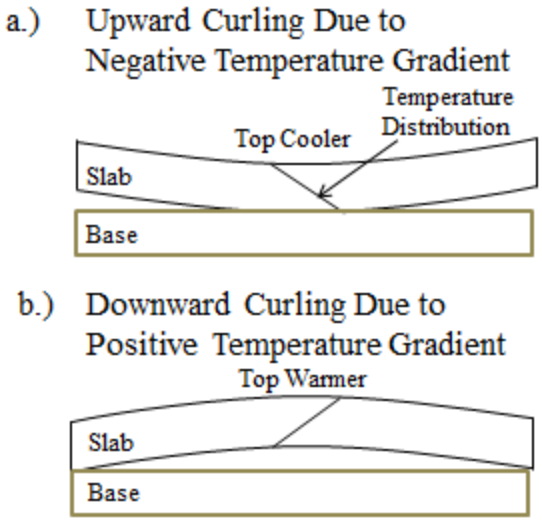

Figure 2.1: Effect of Temperature Gradient on Curling

The curvature of the slab is constantly changing and is influenced by a variety of both internal and external factors. Some of these factors include the ambient temperature, solar radiation, and precipitation [5]. Because of the typical daily patterns in solar radiation and ambient temperature, there is also a correlation with time of day and season. A negative temperature gradient, as defined in Figure 2.3(a) generally occurs at night. At night, the ambient temperature drops while the temperature at the bottom of the slab is still relatively warm from the latent heat of the day. During the night, the latent heat at the bottom of the slab is eventually lost to the environment and the temperature distribution throughout the slab becomes more uniform. When the sun comes back up in the morning however, the concrete at the top of the slab becomes warmer than the bottom. A positive temperature gradient occurs and results in upward curling of the slab as shown in Figure 2.3(b).

Slab curvature generates stress because when the slab curls, it becomes unsupported at some point along its length. The self-weight of the slab in the unsupported regions restrains this

curvature, which results in stress. More curvature increases the amount of the unsupported area, which induces high stresses in the pavement. When a negative temperature gradient is present in the slab and causes the slab to assume the shape illustrated in Figure 2.3(a), the outside edges of the slab are unsupported. The weight of these regions cause the upper half of the slab at mid-slab to go into tension and cause the lower half of the slab at mid-slab to go into compression. Conversely, when a positive gradient, such as illustrated in Figure 2.3(b), is present in the slab, the central portion of the slab is unsupported at mid-slab. The weight of the unsupported middle causes the bottom half of the slab to go into tension and the top half of the slab to go into compression.

A quantitative analysis of the stresses induced by a linear temperature gradient was first performed by Westergaard in 1929. His analysis was performed assuming a fully supported infinite plate resting on a bed of springs, also known as a Winkler foundation. This formulation was modified by Bradbury in 1938. In Bradbury's formulae, the slab, represented by an elastic plate, was finite in dimensions and with a free edge boundary condition. Bradbury presented the formulae for calculating the stress due to a linear temperature gradient at the edge and middle of this fully supported slab. These formulae are presented in Equation 8 through Equation 10. In these formulae, α is the coefficient of thermal expansion, E is the slab elastic modulus, ν is Poisson's ratio, and ΔT represents the temperature difference between the top and the bottom of the slab. C_x and C_y are parameters that are a function of the slabs structural properties as well as the slab's geometry.

$$\sigma_{x\_or\_y} = \frac{E\alpha\Delta T}{2} \cdot C_{x\_or\_y} \qquad \text{Equation 8}$$

$$\sigma_{interior\_x} = \frac{E\alpha\Delta T}{2\cdot\left(1-\mu^2\right)}\cdot\left(C_x + \mu C_y\right) \qquad \text{Equation 9}$$

$$\sigma_{interior\_y} = \frac{E\alpha\Delta T}{2\cdot\left(1-\mu^2\right)}\cdot\left(C_y + \mu C_x\right) \qquad \text{Equation 10}$$

More specifically, Equation 8 represents the critical stress due to curling at the outside edge of the slab at the mid-point between the slab corners. Equation 9 and Equation 10 represent the critical stress at the middle of the slab in two orthogonal directions. The location of the critical stress on either the bottom of the top of the slab is dependent on whether or not the temperature difference is either positive or negative, respectively.

Characterizing temperature gradients Within a given day, hour, or even minute, there are an infinite number of unique temperature distributions that can be present in the slab that cause curvature. The curvature in the slab influences both the stresses and ultimately the performance of the slab. For these reasons, it is important to characterize the curvature induced in a pavement by a unique temperature distribution so that it can be incorporated into a mechanistic design process.

In order to account for the variability in potential temperature distributions, the distributions are typically characterized into a relatively finite number of temperature gradients. In Figure 2.1, the curvature depicted in the slab was due to a linear temperature gradient. The temperature at each depth can be defined knowing only the temperatures at the top and bottom of the slab. In reality however, the temperature variation with depth within the slab exhibits at least some non-linearity as shown in Figure 2.2. Furthermore, the curvature in the slab is influenced by both the shape of the temperature distribution and magnitude of temperatures in the slab.

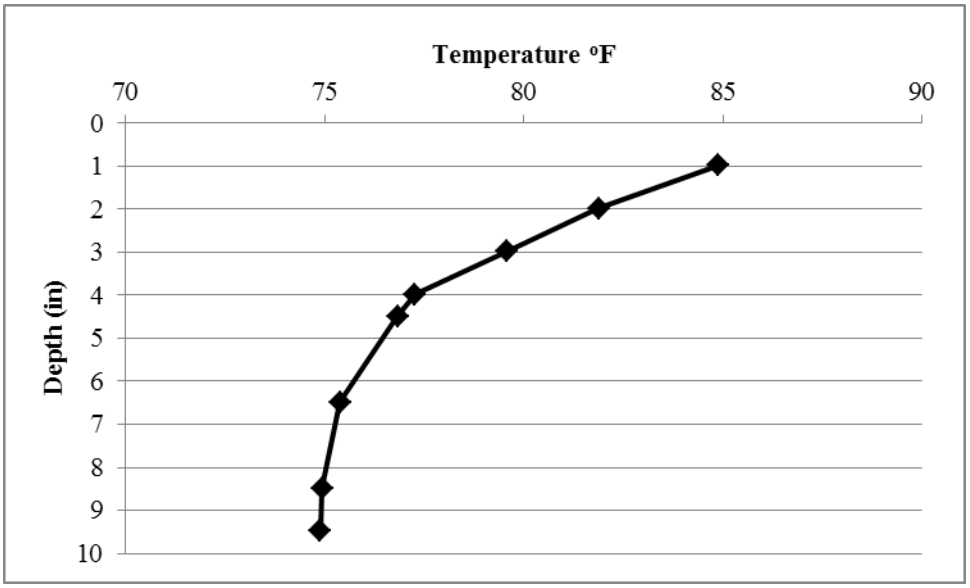

Figure 2.2: Temperature Profile with Depth for a Concrete Pavement

In order to assess the slab curvature induced by an arbitrary temperature distribution and to solve some of the aforementioned issues, Tomlinson, who was studying plate theory in the 1940s, proposed separating a temperature distribution of a slab into three components [6]. The three components are derived considering that the total temperature related strain at any given depth in the concrete pavement is given by Equation 11. Equation 12 through Equation 14 show the mathematical expression for the three constituent components of the total temperature strain at a given depth within the slab. As in Equation 5 and Equation 6, E and α represent the modulus of elasticity and the CTE, respectively, and can be expressed as a functions of depth (z). The depth (z) is defined as the distance below the slab's neutral bending axis. T(z) is the temperature at given depth and at an arbitrary point in time while T_o represents the layer's reference temperature determined at the zero stress time.

$$T_{total} = \alpha(z)\cdot\left(T(z) - T_0(z)\right) \qquad \text{Equation 11}$$

$$T_c(z) = T_o + \frac{\int_0^h \alpha(z)\cdot E(z)\cdot\left(T(z) - T_0\right) dz}{\alpha(z)\cdot\int_0^h E(z)\, dz} \qquad \text{Equation 12}$$

$$T_L(z) = T_o + \frac{z}{\alpha(z)}\cdot\frac{\int_0^h \alpha(z)\cdot E(z)\cdot z\cdot\left(T(z) - T_0\right) dz}{\int_0^h E(z)\cdot z^2\, dz} \qquad \text{Equation 13}$$

$$T_N(z) = T_{total}(z) - T_c(z) - T_L(z) + 2\cdot T_0 \qquad \text{Equation 14}$$

$$\sigma_{Nxxoryy}(z) = \frac{-E(z)}{1-\mu}\cdot\alpha(z)\cdot\left(T_N(z) - T_o\right) \qquad \text{Equation 15}$$

Equation 12 represents the portion of the temperature distribution that results in a uniform strain throughout the depth of the pavement. For a pavement that can expand and contract freely, no stress is generated within the pavement. The remaining two components of the temperature distribution as expressed in Equation 13 and Equation 14 are illustrated in Figure 2.3.

In Figure 2.3, the linear portion of the temperature distribution, as expressed in Equation 13, is indicated by the diagonal line. The non-linear portion, as expressed in Equation 14, is indicated by the arrows. The non-linear portion is simply the remainder of the temperature distribution after the uniform and linear strain components are subtracted out.

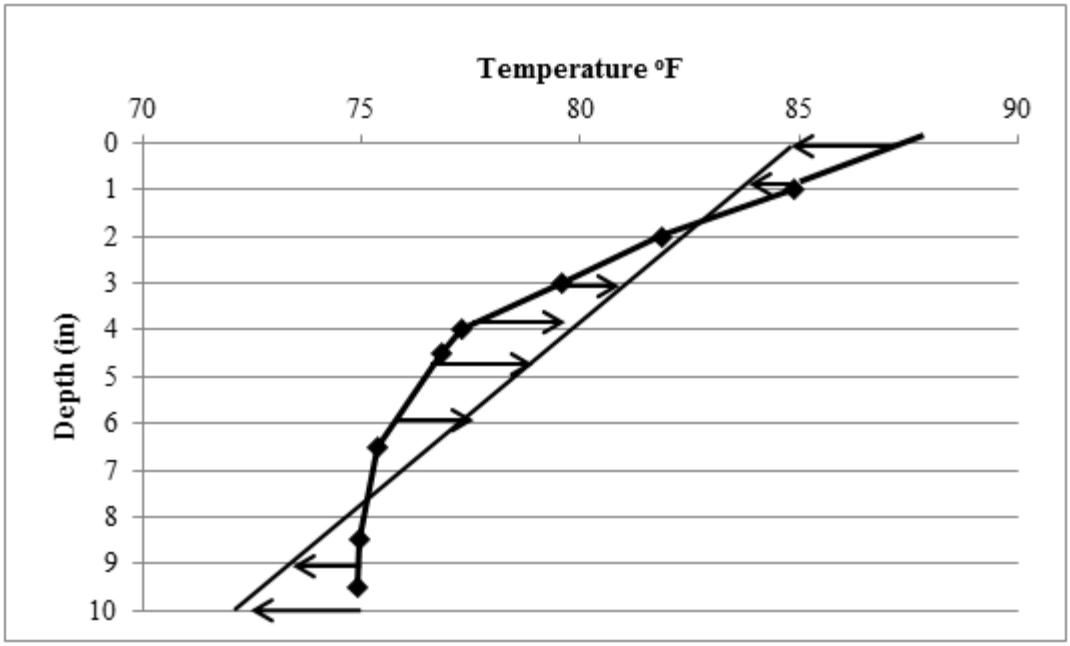

Figure 2.3: Linear and Non-Linear Components of an Arbitrary Temperature Distribution in a Homogenous Concrete Pavement

The linear strain component represented by Equation 13 is the component that results in curvature of the slab similar to that shown in Figure 2.1. Because of the weight of the slab, this portion of the temperature results in the development of stress in the slab. Additionally, when the pavement is subjected to a wheel load, the curvature in the slab influences the location and magnitude of the critical stress imposed by that load.

Equation 14, represents the remaining portion of the temperature distribution and is the self-equilibrating strain. Since one of the assumptions in the derivation of equations Equation 12 through Equation 15 is that normal vectors to the neutral plane remain normal after bending, the entirety of the non-linear strain component of the temperature distribution is restrained and results in residual stress within the slab [7]. The stresses that result from the non-linear portion of the temperature distribution can be estimated using Equation 15. Once the stresses from the

linear component of the temperature distribution are obtained, these stresses can be superimposed to obtain the total stress distribution in the slab due to temperature effects.

An alternative representation of the stress and deformation due to the temperature distribution is the equivalent linear temperature gradient. The equivalent linear temperature gradient (ELTG) concept was first forwarded by Timoshenko and Lessells, 1925, Bradbury, 1938 and Boresi 1965. Additionally, Mohamed and Hansen forwarded a formulation in 1997 that will be presented here [8].

This calculation of the equivalent linear temperature gradient is performed by obtaining the first moment of the strain distribution over the depth of the slab about the bottom of the slab. For a homogeneous slab, the first moment created by a given temperature strain distribution is equivalent to Equation 16. For a plate with rigidity given by Equation 17, the curvature is equivalent to Equation 18. Equating the moment induced by the temperature strain and a bending moment, a relationship between the temperature distribution and the slab curvature can be obtained. This relationship is presented in Equation 19.

$$M = \int_{\frac{-h}{2}}^{\frac{h}{2}} \varepsilon(z) \cdot z \, dz \qquad \text{Equation 16}$$

$$D = \frac{E \cdot h^3}{12 \cdot \left(1 - \nu^2\right)} \qquad \text{Equation 17}$$

$$\kappa = \frac{12 \cdot M}{h^3} \qquad \text{Equation 18}$$

$$\Delta T_{eq} = \frac{-12 M_{temp}}{\alpha \cdot h^2} \qquad \text{Equation 19}$$

With the equivalent linear temperature gradient calculated in Equation 19, the stresses associated with an arbitrary temperature distribution can be evaluated. This can be done using simple closed form solutions, such as those proposed by Westergaard and Bradbury. These solutions relate curvature to stresses such as those imposed by slab self-weight and subgrade reaction [8]. This concept is also valuable for its ability to characterize an infinite number of arbitrary temperature distributions with a relatively finite number of possible ELTGs.

Stresses due to curling can then be superimposed with stresses due to wheel loads to obtain the total stress. The total stress is an essential parameter in a mechanistic failure analysis that calculates damage.

Characterizing temperature gradients in composite pavements In the previous section, it was stated that the component of the temperature distribution causing uniform expansion and contraction of the slab does not generally result in residual stress in the pavement. This is because the stress is alleviated when the frictional restrain is exceeded and the slab expands. In a homogeneous pavement, this eliminates the significance of the reference temperature. For a composite pavement, however, the reference temperature is important. It can have a significant influence on the resulting temperature induced curvature in the slab. When two or more layers with different CTEs are bonded together, a change in temperature from the value of the reference temperature will result in a different thermal strain in each layer. A different elastic modulus for each layer will also result in the slabs neutral bending axis being at a depth other than mid-depth.

The formula for the ELTG in a composite pavement with bonded layers is shown in Equation 20.

$$\Delta T_{eff} = \frac{12}{h_{eff}^{2}} \cdot \left[\int_{-x}^{h_{Top}-x} \left(T(z) - T_o\right) \cdot z \, dz + \frac{\alpha_{Bot} \cdot E_{Bot}}{\alpha_{Top} \cdot E_{Top}} \cdot \int_{h_{Bot}-x}^{h_{Top}+h_{Bot}-x} \left(T(z) - T_o\right) \cdot z \, dz \right] \qquad \text{Equation 20}$$

In Equation 20, x is the distance from the slab neutral bending axis measured as positive below the neutral axis. The depth of the neutral axis is shown in Equation 21. The effective height of the pavement, h_{eff}, is given by Equation 22.

$$x = \frac{\frac{h_{Top}^{2}}{2} + \frac{E_{Bot}}{E_{Top}} \cdot h_{Bot} \cdot \left(h_{Top} + \frac{h_{Bot}}{2} \right)}{h_{Bot} + \frac{E_{Bot}}{E_{Top}} \cdot h_{Bot}} \qquad \text{Equation 21}$$

$$h_{eff} = \sqrt[3]{h_{Bot}^{3} + \frac{E_{Bot}}{E_{Top}} \cdot h_{Bot}^{3} + 12 \cdot \left[h_{Top} \cdot \left(x - \frac{h_{Top}}{2} \right)^{2} + \frac{E_{Bot}}{E_{Top}} \cdot \left(h_{Top} + \frac{h_{Bot}}{2} - x \right)^{2} \cdot h_{Bot} \right]} \qquad \text{Equation 22}$$

Material parameters influencing the temperature distribution in concrete pavements The previous sections discussed the relationship between the temperature distribution in the pavement and the subsequent curvature and stresses that are generated. The factors influencing the temperature distribution that develop in the pavement will be addressed in this section. These influences can generally be broken down into two categories, environmental influences and material property influences.

The climatic influences that are important in the determination of the temperature distribution in a pavement are the air temperature, percent sunshine, and wind speed [3]. The ambient temperature dictates the direction and rate of the heat flux through the pavement, and the long wave radiation emitted by the air [3]. The percent sunshine dictates the amount of short

wave solar radiation that reaches the pavement. The absorption of both short wave and long wave radiation warms the pavement and contributes to the diffusion of heat into and out of the pavement. Finally, the wind speed is related to the heat flux through the pavement as higher wind speeds exacerbate the removal of heat from the pavement surface.

The material properties that influence the temperature distribution in the pavement are the surface shortwave absorptivity and emissivity, thermal conductivity, and specific heat. The surface shortwave absorptivity represents the percentage of incident solar radiation absorbed by the pavement while the emissivity represents the ability of the pavement to emit radiation into the environment. The thermal conductivity represents the amount of heat flowing between two sides of a material subjected to a temperature gradient. The specific heat represents the amount of heat energy required to raise the temperature of a unit of material by one degree. Together, the thermal conductivity, specific heat, and material density can be combined to give the thermal diffusivity. This parameters is important because it controls the rate of temperature change in the pavement [9].

The surface shortwave absorptivity and emissivity are primarily influenced by the color of the paving material with lighter colors both reflecting more incident solar shortwave radiation and emitting less long wave radiation. For concrete, the thermal conductivity is primarily influenced by the aggregate volume fraction and the moisture content of the specimen [10]. Aggregates generally have a higher thermal conductivity than cement paste. Increasing the aggregate content increases the thermal conductivity of the concrete. In addition, thermal conductivity is also a function of the aggregate type [11]. The dependence of thermal conductivity on the moisture content can be explained because water has a higher thermal conductivity than air. As more of the pores in the concrete are filled with water, the thermal

conductivity of the concrete increases [10]. Thermal conductivity of concrete, like all materials, is also a function of density and generally increases with increasing density [9].

Unlike the thermal conductivity, the specific heat of concrete is not affected by the aggregate type [11]. Specific heat, is however, a function of the relative volume of aggregate in the concrete [11]. For a given volumetric aggregate content, the specific heat of concrete still varies due to the response of the paste fraction of the concrete. The specific heat of the paste is influenced primarily by the water content, porosity, and temperature [9]. While water content and temperature are influenced by the environment, porosity is primarily influenced by the concrete water to cementitious materials ratio.

For HMA, thermal properties have been found to be a function of degree of compaction, degree of saturation, and the temperature [12]. The specific heat, is primarily a function of the volumetric proportion of aggregate and, as with concrete, is independent of aggregate type. For this reason, the specific heat of concrete and HMA are similar in as much as the mixes in question have the same aggregate proportioning. Since HMA typically has a higher aggregate content than concrete, the specific heat of asphalt is generally higher than the specific heat of concrete. As with cement paste, there is a temperature dependence of the specific heat of the asphalt binder. The specific heat increases with increasing temperature[13]. While observations to the contrary have been made [14], in the MEPDG, the default value for thermal conductivity of HMA is lower than the thermal conductivity value for concrete. This can be attributed to differences in mix proportioning between HMA and concrete and differences in the thermal conductivity of asphalt cement and cement paste.

Together, the density of the paving material, thermal conductivity, and specific heat can be combined to form a parameter called the thermal diffusivity. The thermal diffusivity is the

rate that temperature change takes place in the material [9]. Subjected to a given temperature difference between the environment and the pavement, the thermal diffusivity relates how long it will take for the temperature in the environment and pavement to equilibrate. For a given depth in the pavement, the temperature difference must be maintained long enough between the pavement surface and the environment so that all of the pavement above a certain depth of interest can also reach the temperature of the ambient environment.

Considering the discussion on the difference between the HMA and concrete thermal material properties and the assumption of HMA possessing a lower thermal conductivity than concrete, it can be concluded that HMA has a lower thermal diffusivity than concrete. Because of this effect, the diffusion of heat through an HMA layer takes longer than it does through a concrete layer.

The primary practical influence of the thermal properties of HMA and concrete for composite pavements are that for composite pavements of HMA over concrete, the HMA layer acts as an insulating layer. The effect of this behavior is that the temperature gradients that develop in the underlying concrete are reduced. In addition to reducing the magnitude of the temperature gradients in the underlying concrete, the reduced stiffness of the HMA layer relative to the concrete layer decreases curvature. Curvature is decreased because the lower stiffness in the HMA serves to diminish the effect widely varying temperatures at the pavement surface have on curvature.

In HMA over concrete composite pavements, the primary factor inducing curvature of the overall slab is the temperature gradient in the concrete layer. Since the temperature gradients are not as severe, the corresponding stresses due to curvature are reduced for an HMA over a concrete composite pavement relative to a composite concrete pavement. The idea of the HMA

layer reducing the curling stress in a concrete pavement overlaid with HMA was proposed by Nishizawa et al (2007) [15].

This research indicated the reduction in temperature gradients that developed in the underlying concrete layer was found to increase with HMA thickness but that with HMA surfaces less than 4-cm thick the temperature gradient in the concrete slab might actually increase [15].

2.3.2.2 Moisture effects on stresses in composite pavements

Warping is the term used to define curvature in the slab induced by the differential drying shrinkage that occurs between the top and the bottom of the slab. Drying shrinkage is a relatively complicated mechanism commonly related to the relative humidity level within the concrete. The following sections will discuss the mechanisms of drying shrinkage followed by the influence of drying shrinkage on concrete pavements. Ways to account for drying shrinkage in a concrete pavement stress analysis will also be presented.

Mechanisms of drying shrinkage Drying shrinkage in concrete occurs because of negative pore pressures that develop within the pores of the concrete. Since these pore pressures cannot be directly measured, relative humidity measurements are used as a proxy. The relative humidity in a closed system can be defined as the partial vapor pressure relative to the saturation vapor pressure. Relative humidity within the cement paste can be influenced by a relative humidity gradient between the concrete and the ambient environment, by the degree of hydration of the cement paste, by the internal temperature of the concrete, and by the pore fluid salt concentration [16].

The negative pore pressures that induce drying shrinkage start when the concrete becomes unsaturated. When saturation is lost, a meniscus forms at the air-water interface within the pores of the cement paste. The meniscus is due to the adhesion between the water molecules and the pore surface. In this condition, water molecules in the pore want to escape to raise the relative humidity to its equilibrium condition (100 percent). This tendency is resisted by the hydrostatic tensile force in the fluid and a capillary stress is developed that acts on the concrete. The Laplace Equation, Equation 23, provides the relationship between the pore fluid pressure and the meniscus curvature while Equation 24 provides the relationship between the capillary stress in the fluid and relative humidity [9, 17] .

$$p_{gas} - p_{liq} = \frac{2\gamma}{r} \qquad \text{Equation 23}$$

$$\ln(RH) = K \cdot \left(\frac{2 \cdot \gamma}{r} \right) \qquad \text{Equation 24}$$

In Equation 23, P_{gas} is the pressure in the gaseous phase, P_{liq} is the pore fluid pressure, γ is the surface tension of the water, and r is the radius of the meniscus. In Equation 23, the gas pressure is minimal compared to the pore fluid pressure and can therefore be neglected. The constant, K, in Equation 24 is a product of the ideal gas constant and the molar volume of the fluid. Neglecting the gas pressure as discussed for Equation 23 and comparing Equation 23 and Equation 24 it can be seen that the pore fluid pressure is a function of the relative humidity in the pore.

The pore fluid pressure in a given capillary pore acts on both the fluid itself and the capillary pore walls. Stress on the pore walls is compressive in nature and works to compress the cement paste through inter particle rearrangement [9]. Capillary stresses are only important down to relative humidity levels of 45 percent because at this relative humidity level menisci become

unstable [9]. In addition to capillary stresses, disjoining pressure is also responsible for drying shrinkage. Disjoining pressure is the result of water molecules being adsorbed on the surface of the cement hydration product calcium silicate hydrate (C-S-H). The water absorbed between adjacent C-S-H molecules provides a disjoining pressure by limiting the attraction between adjacent C-S-H molecules. As relative humidity drops, and water evaporates out from in between adjacent C-S-H molecules, the van der Waals forces between the C-S-H molecules increases and results in bulk compression of the paste structure [9]. Like the capillary stresses, stresses associated with disjoining pressure show a similar relationship to relative humidity. Disjoining pressure stresses are also only significant down to relative humidity levels of about 45 percent [9]. While there are other shrinkage mechanisms that are effective at relative humidity levels below 45 percent they are not relevant for concrete pavements.

Drying shrinkage in concrete pavements consists of both a reversible and irreversible portion. The reversible portion is recovered upon rewetting after an initial drop in relative humidity. Drying shrinkage that is irreversible primarily occurs on the first drying of the concrete. The magnitude of the irreversible portion increases with porosity, a function primarily controlled by the w/c ratio of concrete [9]. Irreversible drying shrinkage is also influenced by the temperatures during curing. Lower temperatures increase the portion of the drying shrinkage that is irreversible. Irreversible drying shrinkage is important for concrete pavements because it results in a built-in permanent curvature of the slab.

Influence of drying shrinkage on concrete pavements Based on computer modeling, lab samples, and field samples, Janssen found that surface drying of concrete does not extend below a depth of approximately 2 in. This observation was explained to be due to the low porosity of

the concrete limiting the diffusion of moisture out of the concrete and in to the ambient environment. Since drying shrinkage causes a shortening of the length of an unrestrained concrete specimen, the top of the pavement, which experiences a significantly lower relative humidity, will shrink more than the bottom of the pavement. This strain pattern creates an upwards curl in the slab.

Characterizing moisture gradients in concrete pavements The characterization of warping in concrete pavements throughout their life is generally accounted for by considering two components, a permanent and a seasonal one. In the MEPDG for example, permanent warping is considered through a parameter called the permanent curl/warp effective temperature difference. Although the permanent curl/warp effective temperature difference considers the effects of differential drying shrinkage, its magnitude also accounts for other phenomena such as the built-in temperature gradient and the effects of creep. In the interest of facilitating stress prediction, these phenomena are considered by prescribing an effective linear temperature gradient. This effective linear temperature gradient, when applied to the pavement over its life, accounts for the effects of permanent warping, the built- in temperature gradient and the effects of creep. In the case of the MEPDG, its magnitude is established such that agreement is obtained between the damage accumulation algorithm and the observed field cracking in pavement sections used in the calibration of the MEPDG.

Like the method used to consider the permanent aspect of warping, the seasonal component of warping is also considered through prescribing an equivalent linear temperature gradient. The equivalent linear temperature gradient to account for monthly variations in relative humidity is shown in Equation 25.

$$ETG_{Shi} = \frac{3\cdot(\varphi\cdot\varepsilon_{su})\cdot(S_{hi} - S_{h.ave})\cdot h_s\cdot\left(\frac{h}{2} - \frac{h_s}{3}\right)}{\alpha\cdot h^2\cdot 100} \qquad \text{Equation 25}$$

In Equation 25, ETG_{Shi} represents the effective linear temperature difference between the top and bottom of the slab. This difference accounts for the effect of the relative humidity deviating from the annual average in a given month. The constant, φ, represents the reversible shrinkage fraction of the total shrinkage. The ultimate shrinkage is represented by the symbol, ε_{su} while, $S_{hi,}$ represents the relative humidity factor for a given month dependent upon the monthly average ambient relative humidity [3]. An annual average relative humidity factor, $S_{h\ ave}$ is also utilized. Finally, h_s represents the depth of the shrinkage zone, h, is the PCC slab thickness and α is the PCC coefficient of thermal expansion. Additional modifications can also be made to the calculation of the temperature difference to account for seasonal moisture effects. This is primarily done during the early life of the pavement prior to the ultimate shrinkage of the concrete being realized.

Material parameters influencing moisture gradients in concrete pavements Like heat transfer through a pavement, the transfer of moisture between the pavement and its environment is modeled as a diffusion problem. The primary material parameter relevant to diffusion of moisture through concrete is the porosity of the paste. The porosity of the cement is primarily influenced by the age of the concrete and the w/c ratio. Age and w/c ratio control both the size and distribution of the capillary pores. A higher permeability is present in the pore system at earlier ages and when higher w/c ratios are present [9].

Influence of moisture on thermal strains In examining the effects of moisture on stresses generated in concrete pavements, it is also important to discuss that the CTE responsible for temperature strains in concrete is not a constant value and instead depends on the moisture content. On a fundamental level, the apparent coefficient of thermal expansion of concrete is the bulk response of the individual constituents in concrete, which consist primarily of aggregate and cement paste. While the CTE of the aggregates is independent of moisture content, the CTE of the paste exhibits a higher CTE at intermediate relative humidity levels than it does at saturated or low relative humidity levels. According to Mindess (2003), this can be explained by considering the rearrangement of water in the concrete between capillary and gel pores [9].

2.3.3 Bonding Condition between Layers of a Composite Pavement

A unique concern for composite pavements is that of shear stresses generated between the two layers. When the bonding of concrete layers is proposed as a structural modification to any concrete structure, the ability of the composite structure to most effectively carry any additional loads relies on its ability to act monolithically. The benefit of the monolithic behavior is that when bonded together, the two layers have a higher bending rigidity relative to the layers acting separately. Increased bending rigidity reduces the deflection and bending stress induced in each layer by a given applied moment. Monolithic behavior, however, can only occur if the two layers are completely bonded together. The bond between the two layers, and the potential stresses that act to destroy it, are therefore imperative to characterize.

For composite concrete JPCPs, the sources of stress generated at the layer interface are associated with the differences in the layers' coefficients of thermal expansion, different zero stress temperatures and/or gradients, different tendencies to deform under an applied load, and

differential drying shrinkage. At least two of these influences, differential thermal strain properties and differential drying shrinkage have been referenced in the literature as potential causes of layer debonding between concrete overlays.

The source of interface shear stress associated with the composite layers acting monolithically is due to the strain continuity requirement at the interface. When bonded, the strain continuity requirement results in both layers being strained at a different magnitude from what they would experience if they were allowed to deform freely. The difference in the strain experienced and the strain that would be experienced if the layers were independent results in a residual shear stress. An illustration of the strains and stresses in two pavement layers that are bonded and unbonded is provided in Figure 2.4. The stresses resulting from bending and the restraint of expansion and contraction can be super-imposed to obtain the total stress distribution in the pavement.

Although, theoretically, the stress at the interface shown in Figure 2.4 could exceed the strength of the bond at the interface, in practice, this has never been observed on European composite pavements constructed wet on wet. There are many composite pavements that have been constructed in Europe and that have been in service for many years [1]. Despite this observation, an investigation into the literature on the de-bonding of concrete overlays was still performed to provide insight into why de-bonding of concrete overlays constructed wet on wet does not seem to occur.

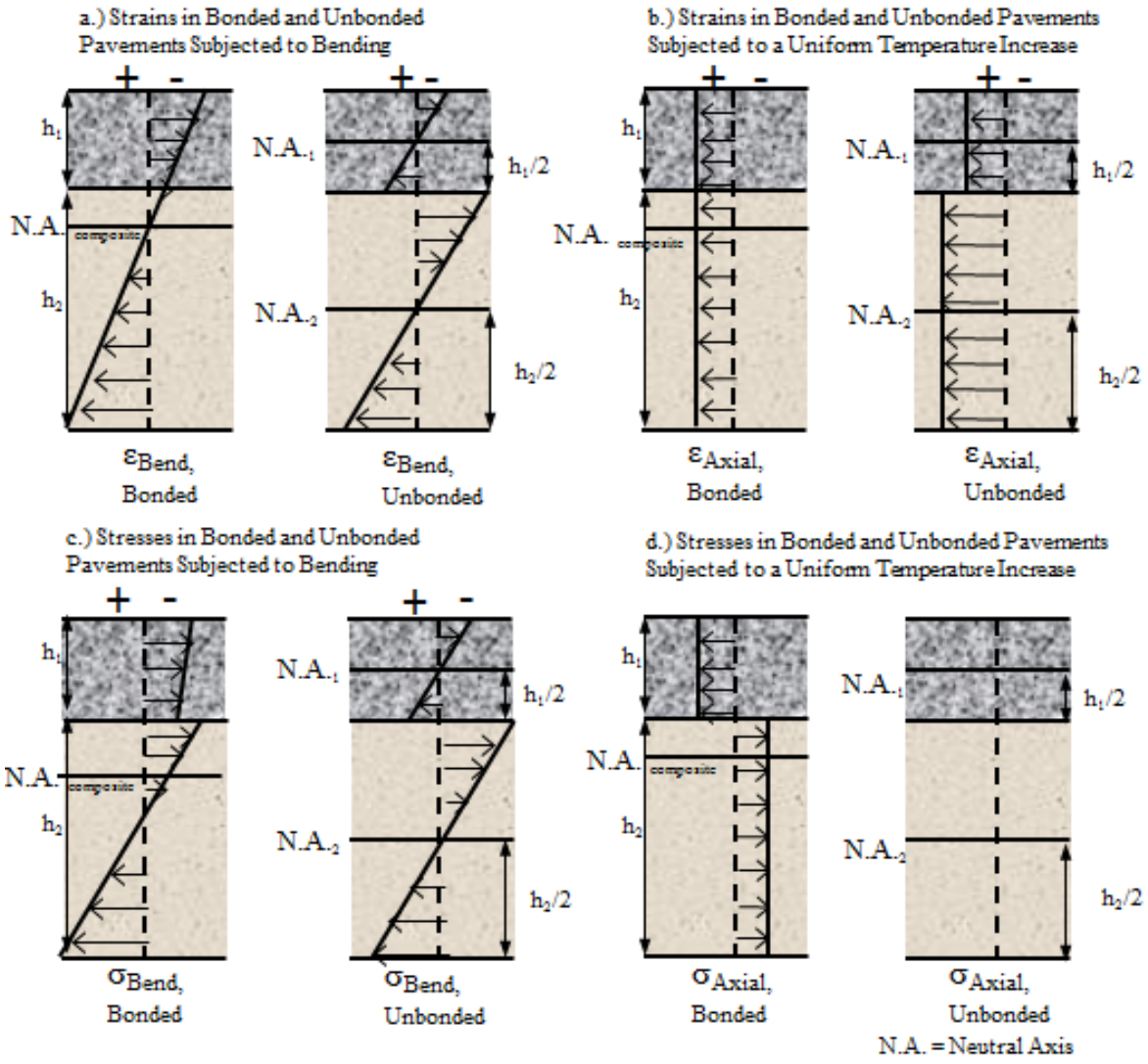

Figure 2.4: Theoretical Strain and Stress Distributions for Composite Pavements Subjected to Bending and Uniform Temperature Change

In 1984, Dhir, implicated temperature effects as the source of small unbonded areas along joints and corners of composite slabs. To study this, he cast a variety of overlays of fresh concrete on an existing concrete specimen. When casting these specimens he used two treatments as a means to reduce the development of temperature gradients. These included insulating blankets and casting in temperate conditions that would retard heat development in the

slab. His conclusion was that these methods would help reduce temperature variation throughout the depth of the slab (curling) and decrease the possibility for debonding at the slab edges where curling is most pronounced [18].

Other research into the de-bonding of concrete overlays has shown differential drying shrinkage to be responsible for the de-bonding of concrete overlays. Some researchers have characterized the de-bonding of concrete overlays due to differential drying shrinkage as the most influential factor causing the failure of the bond between concrete overlays [19]. This conclusion however is based on observations where one concrete member, having already undergone drying shrinkage associated with first drying, has an overlay cast on top of it. In this instance, drying shrinkage in the overlay is restrained by the substrate layer. After placement of the overlay, the substrate layer does not undergo further drying shrinkage on the same order of magnitude as the overlay. The restraint of the desired free shrinkage of the new overlay is most pronounced at the interface and can lead to a stress buildup that can initiate cracking in the overlay. Additional factors, such as substrate creep, can lead to a reduction in stress at the interface. This does not necessarily result in sufficient stress reduction to prevent fracture however [19].

Considering both temperature effects and drying shrinkage, it is clear that casting both the overlay and the substrate simultaneously reduces the influence of temperature effects and differential drying shrinkage. The subsequent stress is also then not generated. It is further believed that the restrained strain generated by differences in zero stress temperature or thermal coefficient of the two layers is significantly less than what could be caused by restrained drying shrinkage. The strain associated with drying shrinkage might be on the order of a couple hundred microstrain, while the amount due to a difference in CTE between the layers or a difference in

zero stress temperature is much smaller. Although the stress at the interface due to different bending rigidities between the layers would also contribute to the interface shear stress, its magnitude is unlikely to be sufficiently high to cause distress in a composite concrete pavement cast wet on wet.

For an HMA overlay of a concrete pavement, the combination of the use of a tack coat and surface texturing has been found to insure a good bond. This is to such an extent that de-bonding between the HMA and concrete layer is not typically observed in practice [1]. Additional credence is lent to the notion that debonding is insignificant relative to other distress types by the MEPDG. In the MEPDG, no direct consideration is made for the effect of de-bonding between the HMA and PCC. MEPDG documentation merely notes that de-bonding between these layers is often a bi-product of reflection cracking. When there is a crack in the lower PCC layer prior to HMA placement, the discontinuity created by the crack allows moisture and fines to infiltrate the crack. This degrades and leads to the eventual failure of the interface between the two layers [3].

2.4 FAILURE OF JPCPS

Up until this point, only the stresses in JPCPs have been discussed. Stress alone is not enough to relate the environmental conditions and traffic to structural failure of the pavement. Structural failure and the observation of different types of distresses are considered through fatigue analysis.

In the fatigue analysis of concrete pavements, the stress generated by the traffic loading are computed and compared to the strength of the material to calculate the stress ratio. For a

given stress ratio, there is a theoretical number of applications that will cause failure. The inverse of the number of cycles for a given stress ratio to cause failure is fatigue damage. According to Miner's hypothesis, failure of the specimen occurs whenever the fatigue damage of the specimen is equal to 1. In this way, the wide range of stresses generated by loads on concrete pavements can be summed together to obtain the fatigue damage due to all loads. Performing this calculation for each load over the life of the pavement can predict the given combination of traffic and environmental loadings that leads to failure of the concrete pavement.

2.5 MODELING OF JOINTED PLAIN CONCRETE PAVEMENTS

Although closed-form solutions exist for the stresses generated due to temperature gradients and applied wheel loadings in a concrete slab, the ability to consider the stresses at a variety of locations and due to a wide variety of loading, curvature, and restraint conditions is only accomplished using the finite element method. In using the finite element method as an assessment tool, it is also important to understand the governing principles. This allows for the assessment of variations in measured and predicted results between instrumented pavements and finite element programs.

Available Finite Element Programs

Many finite element programs exist that are capable of modeling pavement systems. These programs can generally be grouped into general purpose finite element programs and pavement specific programs. Some common general purpose finite element programs include

ABAQUS and ANSYS, which are 3D programs. These programs afford the user a wide variety of element types and loading procedures. Finite element programs developed specifically for pavements include ISLAB, EVERFE, JSLAB, KENSLAB and FEACONS-IV. These programs have fixed element types and loading procedures. Of these programs, only EVERFE is a 3D finite element program. In a comparison of available finite element programs, ISLAB was the program selected for use as the analysis tool to predict stresses for the calibration of the fatigue models in the MEPDG [20].

In part, ISLAB was selected for stress calculations performed for the MEPDG due to the high computational time required when using the general purpose finite element software ABAQUS. This was significant because of the large number of runs required when calculating stress for each load applied to the pavement throughout its design life. A comparison of the accuracy between ISLAB and ABAQUS found that ISLAB and ABAQUS both accurately predicted the maximum bending stress due to an interior loading. There were differences in stress prediction of up to 10 percent and differences in critical stress location when considering edge loads however.

Because ISLAB is not a 3D program, it does not calculate all of the stresses that may be of particular interest when analyzing composite pavements. Figure 2.5 presents a representation of a finite element in ISLAB. Perhaps the most notable stresses that are not calculated by ISLAB are the shear stresses in the z-x and z-y directions. These stresses are such that if their magnitude were high enough, the bond between adjacent elements on that plane could fail and delamination would occur.

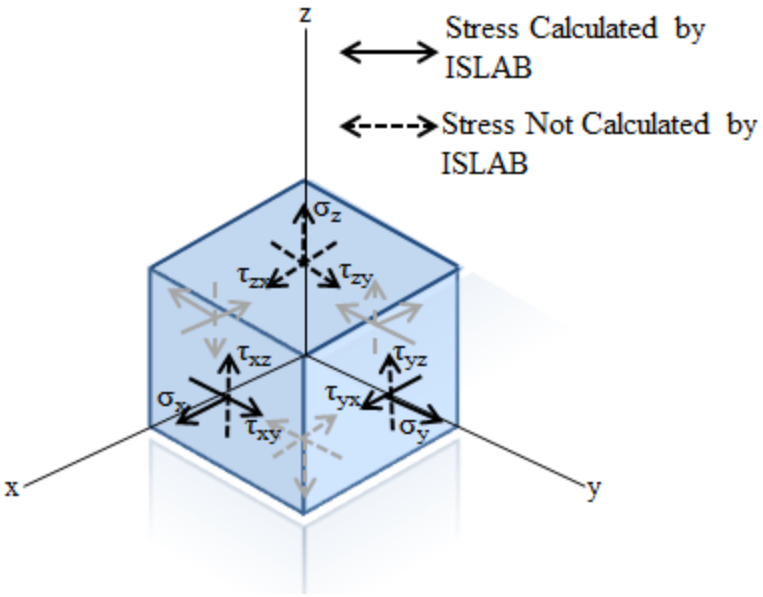

Figure 2.5: Element Stresses Calculated by ISLAB

With respect to the consideration of environmental loads, both general purpose finite element programs and some pavement specific programs have the ability to consider stresses induced by environmental loads. This is done be assigning nodal temperatures in the finite element model. Of the pavement specific finite element programs, ISLAB provides the most options regarding the consideration of environmental loads.

Ultimately, despite some of the aforementioned limitations, ISLAB was selected as the finite element analysis program for this work. ISLAB is a widely accepted finite element program for determining stresses in pavement slabs, has been used in the calibration on the MEPDG, can consider environmental loads defined in different ways, and is relatively easy to use.

Model Theory

Typically, rigid pavements are modeled according to medium thick elastic plate theory. The basic presupposition to this theory is that the material does not compress throughout its

thickness but instead only deflects due to bending. Ignoring the compressibility of concrete is reasonable considering its stiffness and relatively small magnitude of applied compressive loads. The compressibility of HMA however cannot be ignored. HMA compressibility is a critical consideration due to the importance of characterizing rutting.

Another important aspect that must be considered by a pavement finite element analysis is the relationship between the plate and its foundation. A general pavement section is modeled as a single plate resting on a continuous foundation. Typically, the pavement foundation is modeled as a dense liquid foundation. This model involves considering the foundation as a set of independent springs with stiffness k. Other models for pavement foundations include modeling the foundation as an elastic solid, and using a two parameter model such as the Kerr-Vlasov model. The dense liquid model assumes that the reaction force from the foundation is only a function of the deflection of the overlying slab and that the foundation has no shear interaction between adjacent points [21]. This means that the load from the weight of the slab and any vehicle is distributed to the foundation directly beneath the slab and does not distribute itself over a wider area with depth. Modeling the foundation as an elastic solid does consider shear transfer of load beyond the area just under the pavement slab. In reality however, the load of the pavement slab is not distributed over an area as wide as predicted by the ES model. The real behavior of the foundation soil is therefore in between the dense liquid and elastic solid model. The two parameter model addresses this issue by affording the ability to prescribe an interaction parameter between adjacent springs.

Conventional analysis consists of formulations of a single plate resting on a foundation. This is obviously a limitation for the analysis of a composite pavement since the material properties of the two layers differ. To circumvent this issue, the two bonded layers can be

transformed into an equivalent layer provided that these two layer have the same Poisson's ratio [21]. The method of transforming two bonded layers to a single layer assumes that the two bonded layers have the same deflections as an equivalent single layer with equivalent thickness and stress distribution as described by Ioannides et al (1992) [22].

3.0 INSTRUMENTATION AND CONSTRUCTION

As part of the Second Strategic Highway Research Program, the economic, sustainability, and expedient rehabilitation benefits seen in composite pavement systems constructed in Europe were investigated in a US setting. As one part of this investigation, three different composite pavement sections, or cells, were constructed and instrumented at the Minnesota Road Research Facility (MnROAD). This section describes the construction and instrumentation of these pavements as it relates to the data collected for this research.

MnROAD is the world's largest outdoor pavement laboratory. The facility consists of a three test sections including a low volume road, a farm loop, and a mainline section. The mainline section, which receives live traffic from Interstate 94, is northwest of Minneapolis, MN. The layout of the MnROAD facility can be seen in Figure 3.1.

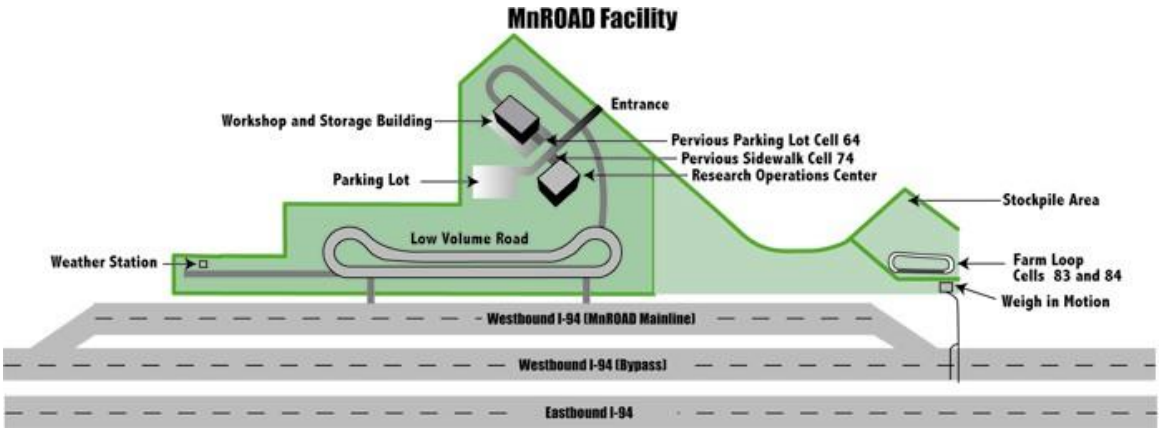

Figure 3.1: MnROAD Facility Layout [23]

MnROAD data obtained from a variety of sensors embedded in and around the various pavement sections at the facility have been used for many functions. MnROAD data has been used in the calibration of finite element structural models, validation of mechanistic-empirical design parameters and methods, the development of models to predict low-temperature cracking performance of HMA pavements, evaluations of drainage models for pavement systems, and in investigations of tire-induced stresses and surface-initiated cracks, [24]. As part of this research, thermocouples, vibrating wire static strain gauges, and relative humidity sensors were installed in the composite pavement layers. Additional weather data from a weather station constructed at MnROAD was also utilized

At MnROAD, different pavement types are designated by a cell number. The composite pavement cells were constructed at the location of cells 70, 71, and 72, as shown in Figure 3.2. These cells are part of the mainline section. This section receives actual traffic diverted from Interstate 94. The traffic is diverted off from the test sections and back onto Interstate 94 during data collection or construction on the experimental section.

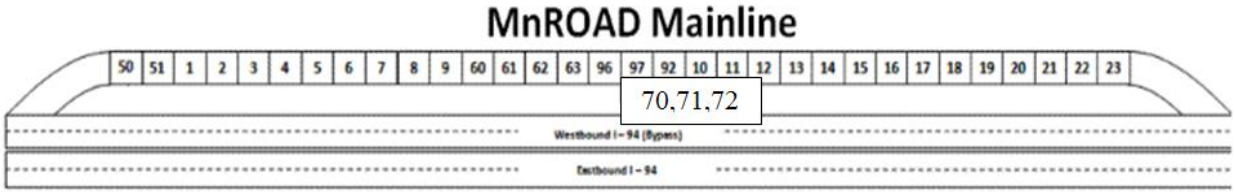

Figure 3.2: Location of Test Cells 70, 71, and 72 on WB Mainline [23]

3.1 COMPOSITE PAVEMENT SECTION DESIGN

3.1.1 Structural Design

For the cells constructed as part of this research, the three composite pavement structures that were chosen were an HMA placed over a recycled concrete layer (RCC), an exposed aggregate concrete (EAC) layer over a recycled concrete layer, and an exposed aggregate concrete layer placed over an economical or "cheap" mix (CHP). It is worth noting that the original intent of the economical mix was to use aggregates not typically allowed by MnROAD for concrete paving because of their relatively substandard characteristics. However, due to the unavailability of substandard aggregate, this objective was modified. Rather than using a substandard aggregate, the economical mix contained a relatively high amount of cement replaced with Class F fly ash.

The cross sections for the composite pavement structures constructed in each cell are shown in Figure 3.3. The base type for all three cells is a MnDOT Class 7 base as specified in Division III of the MnDOT Standard Specifications Book 2005. The base layer is 8-in in thickness. The subgrade is a clay subgrade.

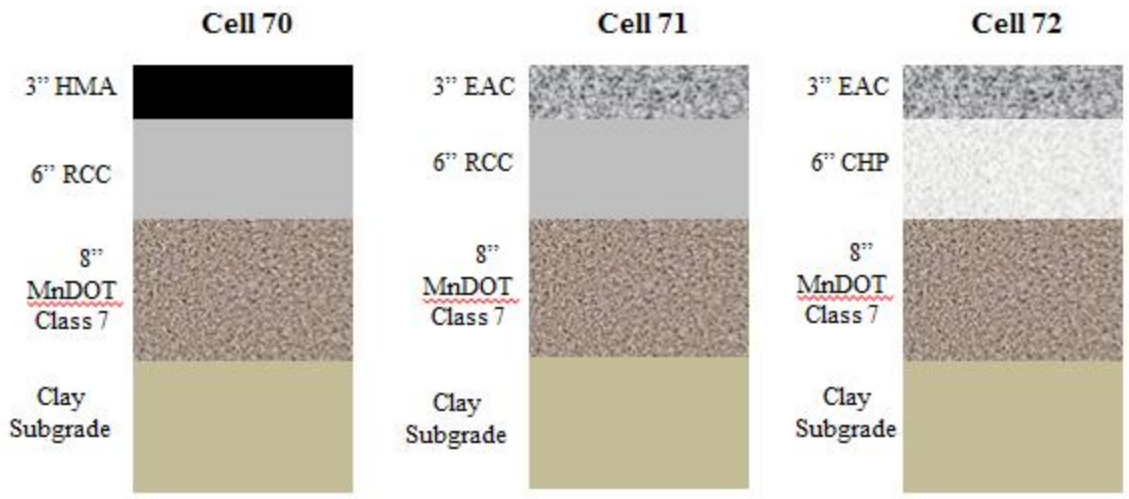

Figure 3.3: Composite Pavement Structures at MnROAD

The slabs in each cell include 15-ft long and 12-ft wide slabs. The slabs in which the various sensors were installed are in the driving lane of the westbound mainline of I-94. For Cell 70, 1.25-in dowel bars were installed between the joints in the driving lane and no dowels were installed in the passing lane. In Cells 71 and 72, 1.25-in dowels were installed in both the passing and driving lanes. Tie bars, 1-5/8-in in diameter and 30-in long were installed at 30-in on center between the driving and passing lane in each cell. After the original construction of the mainline sections, aggregate shoulders were installed and covered with a 3-in HMA wearing course layer. No subsurface drains were provided for the pavement in any of the cells.

3.1.2 Concrete Mixture Designs

Table 3.1 presents the concrete mix designs used for the construction of the MnROAD cells, while Figure 3.4 presents the aggregate gradations. With respect to proportioning and gradation, these mixes were selected to replicate the mixes used in the European experience with composite

pavements. European composite pavements have been constructed and have performed adequately for many years.

The recycled mix, which was used as the bottom layer for Cell 70 and Cell 71, incorporated approximately 25 percent recycled coarse aggregate by volume. Although recycled concrete aggregate has been used in the past for paving mixtures, it is currently not economically compatible with the design life used for concrete pavements in Minnesota [25]. Using both fly ash and recycled aggregate in the same mix is prohibited in current MnDOT paving concrete specifications.

The EAC mixture has a relatively high cement content. Additionally, granite was used for the coarse aggregate fraction to provide surface riding durability. The nominal maximum aggregate size of the granite coarse aggregate was 3/8-in. Overall, the EAC mix design was chosen to provide superior wear resistance and texture for the surface throughout the life of the pavement.

The economical mix is generally classified as such due to its low cement content and the high replacement percentage of cement with fly ash. In concrete mixtures not containing recycled aggregates, only 15 percent replacement by weight of fly-ash is currently allowed in MnDOT paving specifications. The replacement percentage in this mix is 60 percent.

Table 3.1: MnROAD R21 Concrete Layer Mix Designs

Material	Specific Gravity	Absorption	Batch Weight (per yd^3)		
			Low Cost (CHP)	Recycled (RCC)	EAC
Type I Cement (Holcim)	3.15	n/a	240 lbs	360 lbs	616 lbs
Fly Ash- Class F (Headwaters)	2.5	n/a	360 lbs	240 lbs	109 lbs
Fine Aggregate (Aggregate Industries, Elk River Concrete Sand)	2.63	1.24 %	1270 lbs	1200 lbs	843 lbs
Coarse Aggregate #1 (Aggregate Industries, Elk River #67 ¾" Gravel)	2.69	0.90 %	795 lbs	-	-
Coarse Aggregate #2 (Aggregate Industries, Elk River #4 1-1/2" Gravel)	2.7	0.90 %	1110 lbs	825 lbs	-
Coarse Aggregate #3 (Martin Marietta Aggregates, 3/8" Washed Granite Chips)	2.72	0.40%	-	-	843 lbs
Coarse Aggregate #4 (Martin Marietta Aggregates, 1/2" Washed Granite Chips)	2.72	0.40%	-	-	1133 lbs
Coarse Aggregate #5 (McCrossan #4 1-1/2" Recycled Concrete Aggregate)	2.49	2.93 %	-	920 lbs	-
Water Content	1	n/a	20.69 gals	27.99 gals	33.85 gals
Water Reducer (Sika 686)			1.0-3.0 oz	1.0-7.0 oz	14.5 oz
Accelerator (Sika Set NC)			180 oz	0.0-30.0 oz	-
Hydration Stabilizer (Set Retarder) (Delvo)			-	-	18.1 oz
Air Entrainment (Sika Multi-Air 25)			2.0-10.0 oz	2.0-15.0 oz	10.5 oz
w/cm Ratio			.29	.39	.39
Air Content			6.5 %	7.0 %	7.0 %
Slump			3" Max	3" Max	

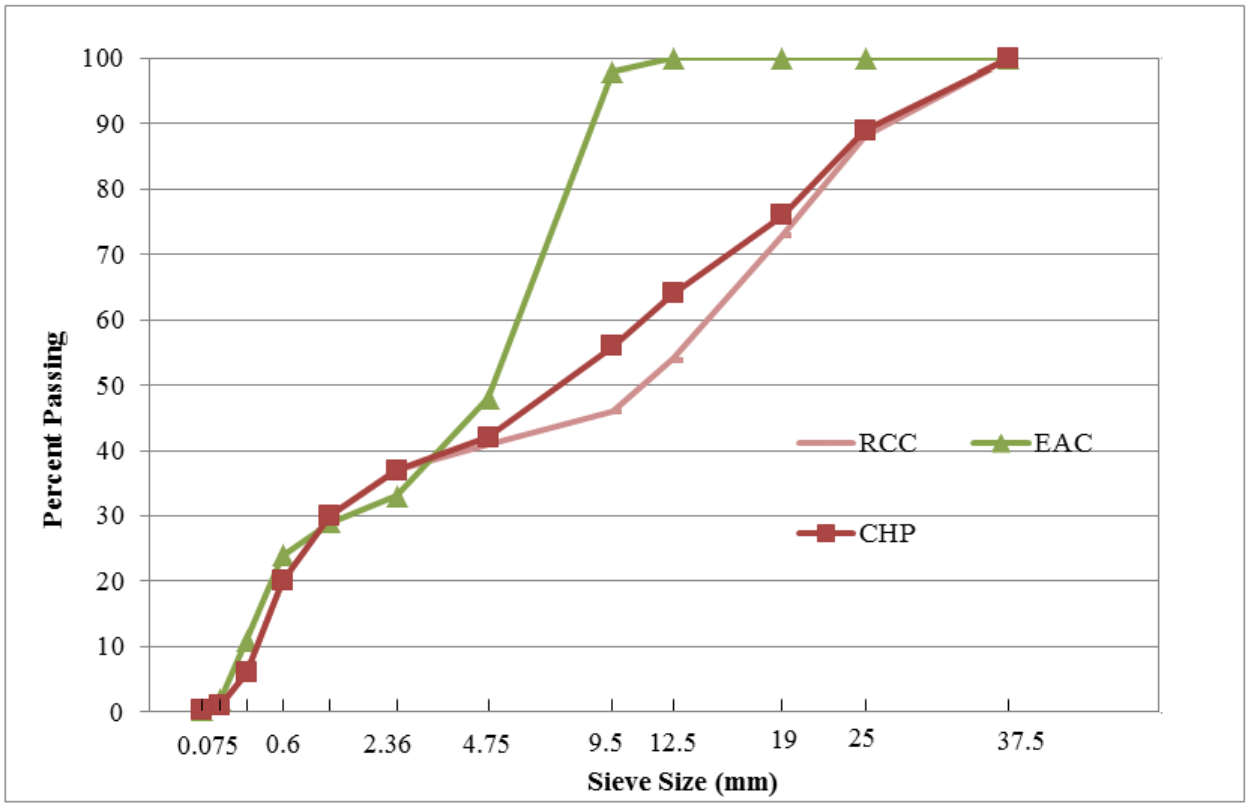

Figure 3.4: Aggregate Gradations for MnROAD Composite Pavement Concrete Mixes

3.1.3 Construction – Cell 70

Construction of the lower recycled concrete layer of Cell 70 began on May 5th 2010 at approximately 7:15 AM. The paver began passing the three instrumented pavement slabs at approximately 7:45 AM. During the construction of this pavement section, the concrete delivery trucks backed up to the paver on the grade and delivered the concrete directly in front of the paver. Before reaching the sensors, fresh concrete was hand placed in a mound around the sensors. It was then consolidated with an immersion type vibrator. The paving operation and concrete mounds around the sensor installations, can be seen in Figure 3.5.

Figure 3.5: Paving Operations and Concrete Covered Sensors - Cell 70

After the paver passed, concrete was removed from around the top three thermocouples. These thermocouples would eventually be installed in the HMA layer in Cell 70. Once the thermocouples were removed, concrete was placed in the resulting void and consolidated by hand. After the paver was finished with the relatively short section for Cell 70, longitudinal tining and a curing compound were applied to the lower concrete layer. On May 20th, at approximately 7:00 AM, HMA was placed on top of the recycled concrete layer of Cell 70. The thermocouples that were exposed during the paving of the lower layer were embedded in the HMA.

3.1.4 Construction – Cell 71 and Cell 72

Construction of Cell 71 began on the morning of May 6th 2010 at approximately 7:30 AM. The paver passed the sensors at approximately 8:00 AM. For Cell 72, construction occurred on May 10th at 8:00 AM with the paver passing the sensors at approximately 8:45 AM. The paving of both Cell 71 and Cell 72 utilized two pavers. One paver was used for each concrete layer. For the construction of the lower concrete layer, the concrete delivery trucks backed up to the paver on the grade and delivered the fresh concrete directly in front of the paver. The upper layer was placed utilizing a placer located along the haul road adjacent to the mainline. Except in the area of the sensors for Cell 71 and Cell 72, dowel bars and tie bars were installed in both the driving lane and passing lane as well as along the lane/shoulder joint as the paving progressed. For the dowels and tie bars that were part of the slabs containing the sensors, both dowel bars and tie bars were placed in baskets and secured to the grade before paving or instrumentation of the slabs began. As with Cell 70, before reaching the sensors, fresh concrete was mound by hand around the sensors and consolidated with an immersion type vibrator.

After passage of the first paver, concrete was removed from around the top of the sensor installation. Once the concrete was removed, specially manufactured couplings and extensions were attached to the sensor trees that were just protruding from the underlying concrete layer. These extensions allowed the sensors to be placed in the upper lift, as can be seen in Figure 3.6. Once the upper lift sensors were installed, additional concrete was placed around the lower layer sensors and consolidated by hand.

Figure 3.6: Installing Upper Layer Sensors after Passage of First Paver

For EAC layer placement, a placer stationed before the upper layer paver in the paving train was utilized. Placement of the upper layer of concrete can be seen in Figure 3.7. Approximately 45 minutes after the passage of the paver placing the lower layer, the paver responsible for paving the EAC layer passed the sensors.

Figure 3.7: Placement of Upper EAC Lift

After the passage of the second paver, the concrete was finished and a combination curing compound and set retarder was applied to the surface of the pavement. The setting of the concrete underneath the combination retarder/curing compound was monitored to determine the optimal brushing time. Monitoring consisted of test brushing an area of the pavement with a push broom and making visual observations regarding the amount of coarse aggregate and mortar removed with the brushing action. Once no coarse aggregate was removed with the brushing action, the finishing of the EAC was performed. This was performed using a tractor with a mounted wire brush attachment, as pictured in Figure 3.8. The tractor made multiple passes over the surface of the pavement to remove the mortar and expose the underlying granite aggregate underneath. The effectiveness of this technique was evaluated using a sand patch test, as shown in the left portion of Figure 3.9. A sample of the texturing after passage of the wire brush is also shown in this figure.

Figure 3.8: Tractor Mounted Brush Attachment for Providing EAC Finish

Figure 3.9: Sand Patch Test for Evaluating EAC Texture and EAC Texture Closeup

3.2 INSTRUMENTATION

This section discusses the sensors installed at MnROAD and the data collection scheme utilized. Although many different types of sensors have been installed at MnROAD, the primary sensors that were used as part of this research include thermocouples, vibrating wire strain gauges, and concrete relative humidity sensors. In addition to sensors installed within the pavement itself, data from a weather station at MnROAD was also utilized. A brief paragraph will discuss the theory of operation behind the embedded pavement sensors and will be followed by the data collection system and system setup used as part of this research.

3.2.1 Thermocouples

A thermocouple simply consists of a junction made between two dissimilar metal wires. The other ends of the metal wires attached to a device capable of reading electric potential. When two dissimilar metals come into contact, a measureable electric potential difference is created. This difference in electric potential is proportional to temperature. Therefore, if the relationship between potential difference and temperature is known for the two metals, then the temperature can be determined only knowing the potential difference. For the thermocouples installed as part of this research, Type T thermocouples were used. These types of thermocouples consist of copper and constantan wires and can measure temperatures between -200^{o}C and 350^{o}C. The limits of error in the measurements recorded by the thermocouples are 0.75 percent at temperatures above 0^{o}C and 1.5 percent below 0^{o}C

Figure 3.10 shows a typical thermocouple installation at MnROAD. The red and blue wires contain the copper and constantan wires. Plastic sheathing is used to prevent a junction

from being formed at a point not in the pavement. The wooden dowel tied to the gray pipe contains the sensors that were eventually placed in the upper pavement layer. These sensors were uncovered from the lower layer concrete after the paver that placed the lower layer passed. They were subsequently placed before the second paver with the EAC mix passed or before the concrete hardened in the case of Cell 70. The upper sensors for Cell 70 were left free in the air until covered later by the HMA layer.

Figure 3.10: Thermocouples Installed at MnROAD

3.2.2 Relative Humidity Sensors

The relative humidity sensors installed as part of the instrumentation of Cells 70, 71, and 72 are Sensiron SHT 75 relative humidity sensors as shown in Figure 3.11. Relative humidity is measured indirectly with the Sensiron SHT 75 sensor. For this sensor, the capacitance of a hydroscopic polymer is measured using the calibrated relationship between capacitance and relative humidity. Temperature effects are also considered with an onboard band gap temperature

sensor. These sensors are very sensitive to damage and must be encapsulated in such a way that they permit water vapor to reach the sensors but not fresh concrete.

Figure 3.11: Sensiron SHT75 Relative Humidity Sensor [26]

The potential sensor error within the working range of the relative humidity and temperature sensor associated with SHT 75 are shown in Figure 3.12 and Figure 3.13, respectively. It is important to emphasize the effects of sensor error and to mention that the error in the relative humidity is highest at values of relative humidity above 90 percent. When concrete is first cast, the relative humidity in the concrete pores is 100 percent. It can take considerable time for the relative humidity levels to drop below this value and into a range where more accurate relative humidity measurements could be expected.

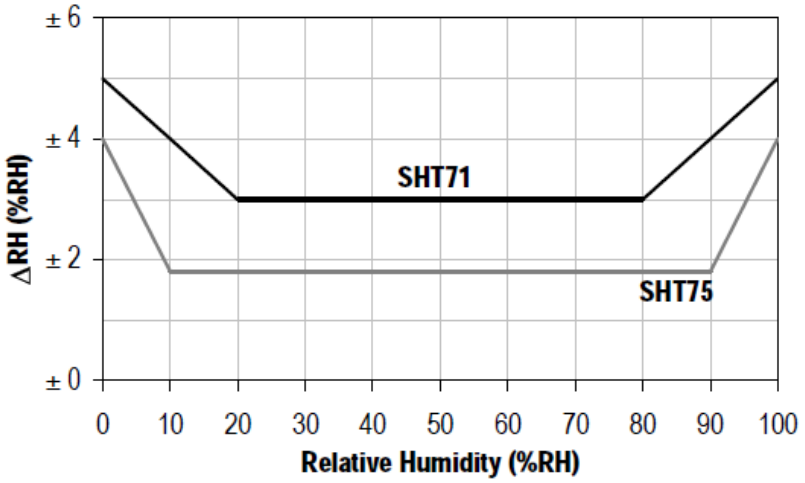

Figure 3.12: Relative Humidity Measurement Error [26]

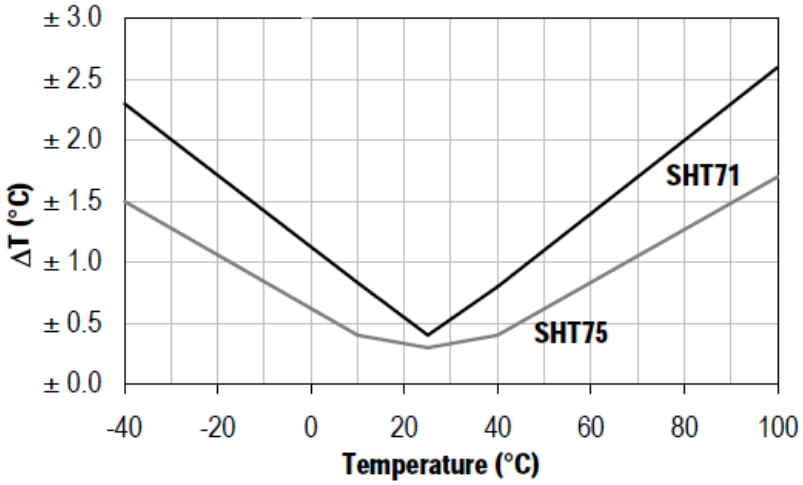

Figure 3.13: Temperature Measurement Error for Relative Humidity Sensors [26]

For installing the delicate relative humidity sensors into the pavement at MnROAD, the setup shown in Figure 3.14 was utilized. In this setup, the sensor itself is protected from the fresh concrete by the porous black cylinders. For Cell 70, only four relative humidity sensors were placed in the bottom recycled concrete layer to record humidity over time. The plastic sheeting shown in Figure 3.14 contains three additional sensors that were uncovered and installed in the

upper EAC layer of Cells 71 and 72. Cells 71 and 72 contained four relative humidity sensors installed in the lower layer and three relative humidity sensors in the upper layer at each location.

Figure 3.14: Relative Humidity Sensor Installation at MnROAD

3.2.3 Static Strain Gauges

Static strain gauges installed in pavements are capable of being influenced by many phenomena. This includes slab/base interaction due to uniform expansion and contraction of the slab, slab curvature, and drying shrinkage. Despite the complex phenomena that can be captured with static strain gauges, their theory of operation is relatively simple. The static strain gauges installed at the MnROAD facility operate using the vibrating wire principal.

When a wire in tension is electrically excited, it will vibrate with a certain frequency. This frequency can be related to the tension in the wire, which can subsequently be related to the strain in the wire. Since the concrete and strain gauge are bonded together, the tension in the wire

can also be related to the strain in the concrete. The static strain gauge that was installed at MnROAD is the Geokon 4200 shown in Figure 3.15. Since both changes in temperature and applied loads result in strain in the concrete, it is important to be able to separate these effects. This can be done with the embedded thermistor in the static strain gauge. The accuracy of the strain gauge is +/- 0.1 microstrain. The accuracy of the thermistor is +/- 0.5^{o}C.

Figure 3.15: Geokon 4200 Concrete Embedment Strain Gauge [27]

Figure 3.16 shows a typical installation for the vibrating wire gauges at MnROAD. Before paving the lower layer, the cylindrical plucker portion of the upper layer vibrating wire sensor was covered with plastic and tied to the lower wooden dowel rod. After the first paver passed, but before the second paver passed, the plucker was uncovered. Once uncovered, the extension shown on the right side of Figure 3.16 was installed and the plucker was attached to the vibrating wire gauge portion.

Figure 3.16: Vibrating Wire Installation - Cells 71 and 72

3.2.4 Weather Station

A weather station capable of measuring ambient temperature, ambient relative humidity, incident solar radiation, wind speed, wind direction, and precipitation, among other things, is installed at MnROAD. Data is collected from this weather station every 15 minutes and can be used to correlate responses of the pavement to change in the ambient environmental conditions.

3.3 DATA COLLECTION

Although the types of sensors installed at MnROAD have been discussed, the spatial distribution of sensors throughout the slab, the specific distribution of sensors with depth, and the data collection scheme has not been introduced. For the number and types of sensors used at MnROAD, various peripheral devices are also necessary to obtain data. These peripheral devices serve both functional and practical purposes. Controlling the timing of readings, sending excitation signals, storing temporary readings, and expanding the number of sensors that can be used for a given datalogger are all facilitated through peripheral devices. At MnROAD, the main peripherals that were used were Campbell Scientific CR-1000 dataloggers, AVW200 Vibrating Wire Interfaces, and AM-16/32 Multiplexors. These devices are shown from left to right in Figure 3.17.

Figure 3.17: Datalogger and Peripherals Needed for Collecting Data from MnROAD Sensors [28]

In the data collection scheme used at MnROAD, the CR-1000 multiplexors are the main component responsible for both coordinating sensor measurements and recording and reporting measurements to the MnROAD server. The CR-1000 takes its directions from a program that is uploaded to the CR-1000. A program can be written using the Shortcut software that accompanies the CR-1000 or a program can be coded in a text editor, such as MS notepad.

AM-16/32 multiplexors are connected to the CR-1000, or in the case of vibrating wires, to the AVW-200 to expand the number of measurements that can be controlled using one CR-1000 datalogger. For each pavement cell, two CR-1000 dataloggers were needed. One CR-1000 controlled the vibrating wire and thermocouple measurements while the other CR-1000 controlled the relative humidity sensor measurements. A schematic of the data collection system used for the MnROAD cells can be seen in Figure 3.18. In Figure 3.18, RH represents the relative humidity sensors, TC represents thermocouples, and VW represents vibrating wires.

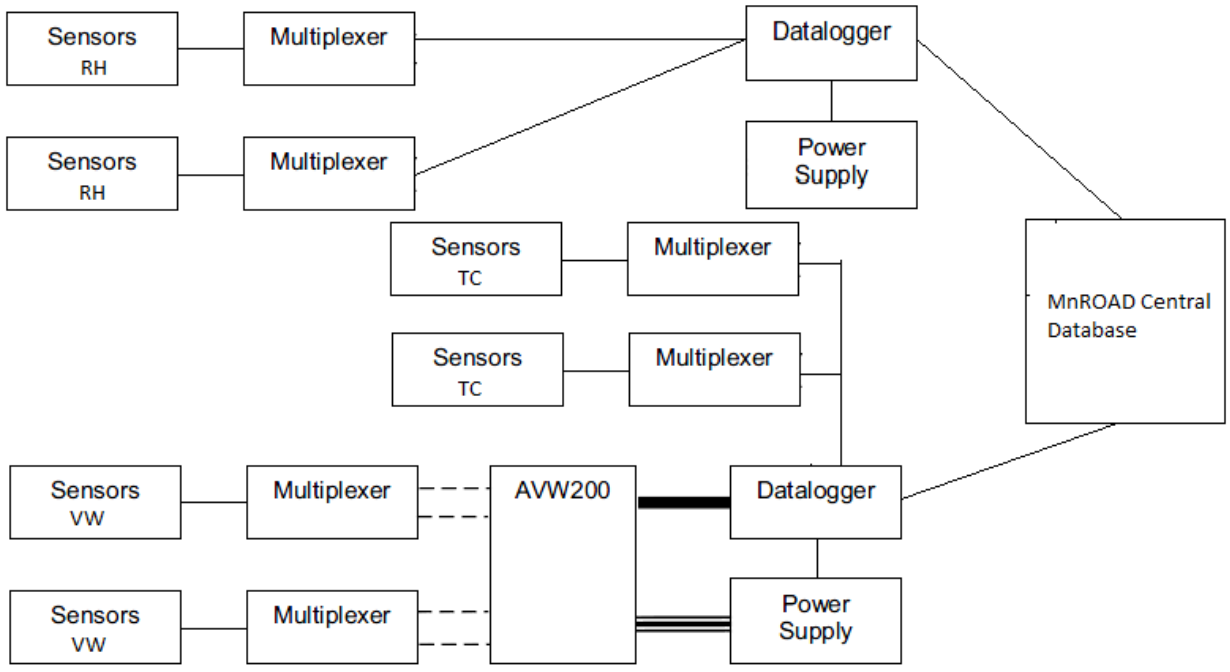

Figure 3.18: Typical Cell Data Collection Schematic

3.4 SENSOR LAYOUT

For Cell 70, 24 RH sensors, 72 TC sensors, and 20 VW sensors were installed throughout the pavement slabs or "panels." For Cells 71 and 72, 42 RH sensors, 72 TC sensors and 30 VW sensors were installed. The spatial distribution of these sensors throughout the panels for Cell 70 can be seen in Figure 3.19. Figure 3.20 shows the sensors locations for Cell 71 and Cell 72. The numbering system for the vibrating wires in Panel 2 was slightly different than Cell 71.

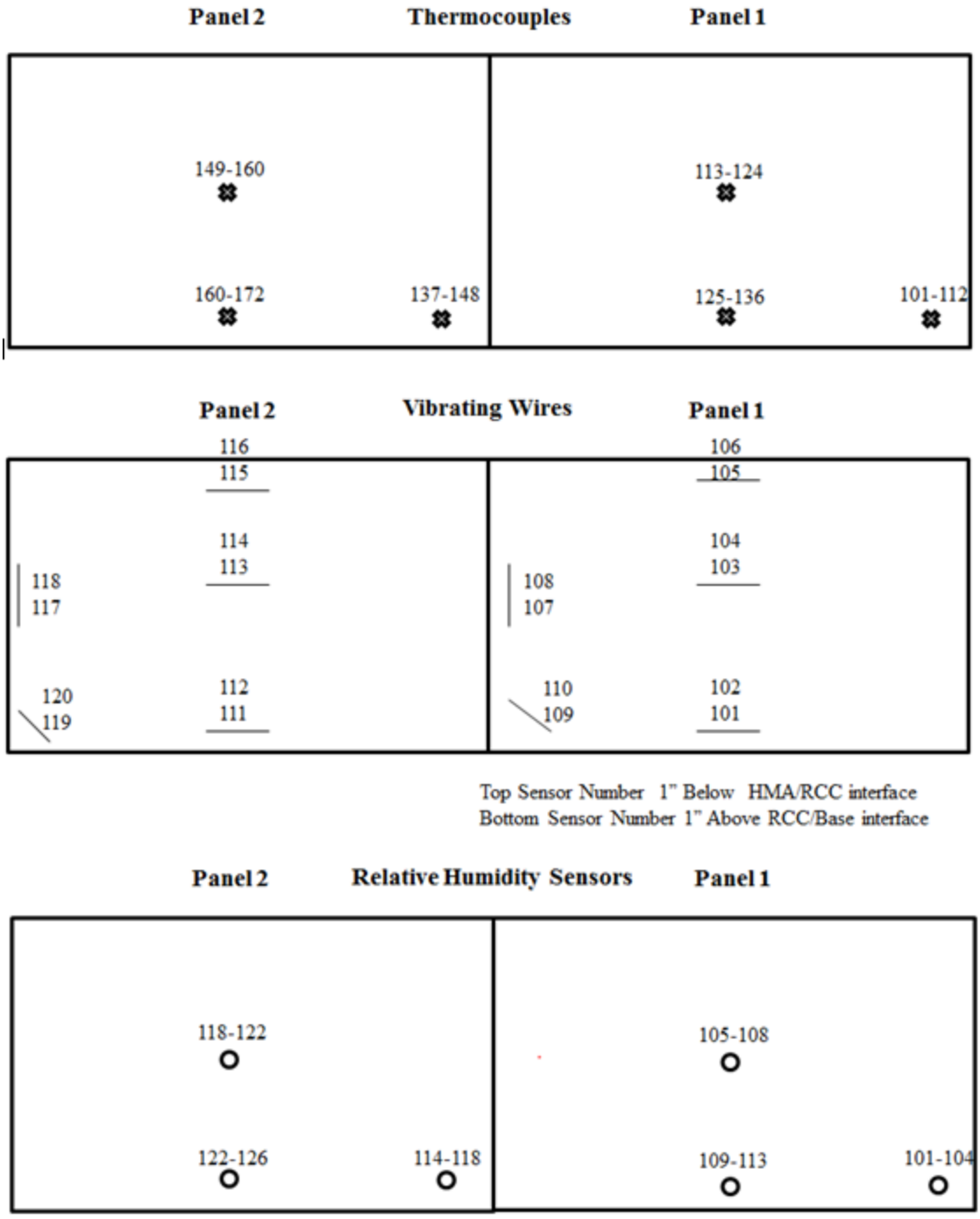

Figure 3.19: Cell 70 Sensor Layout

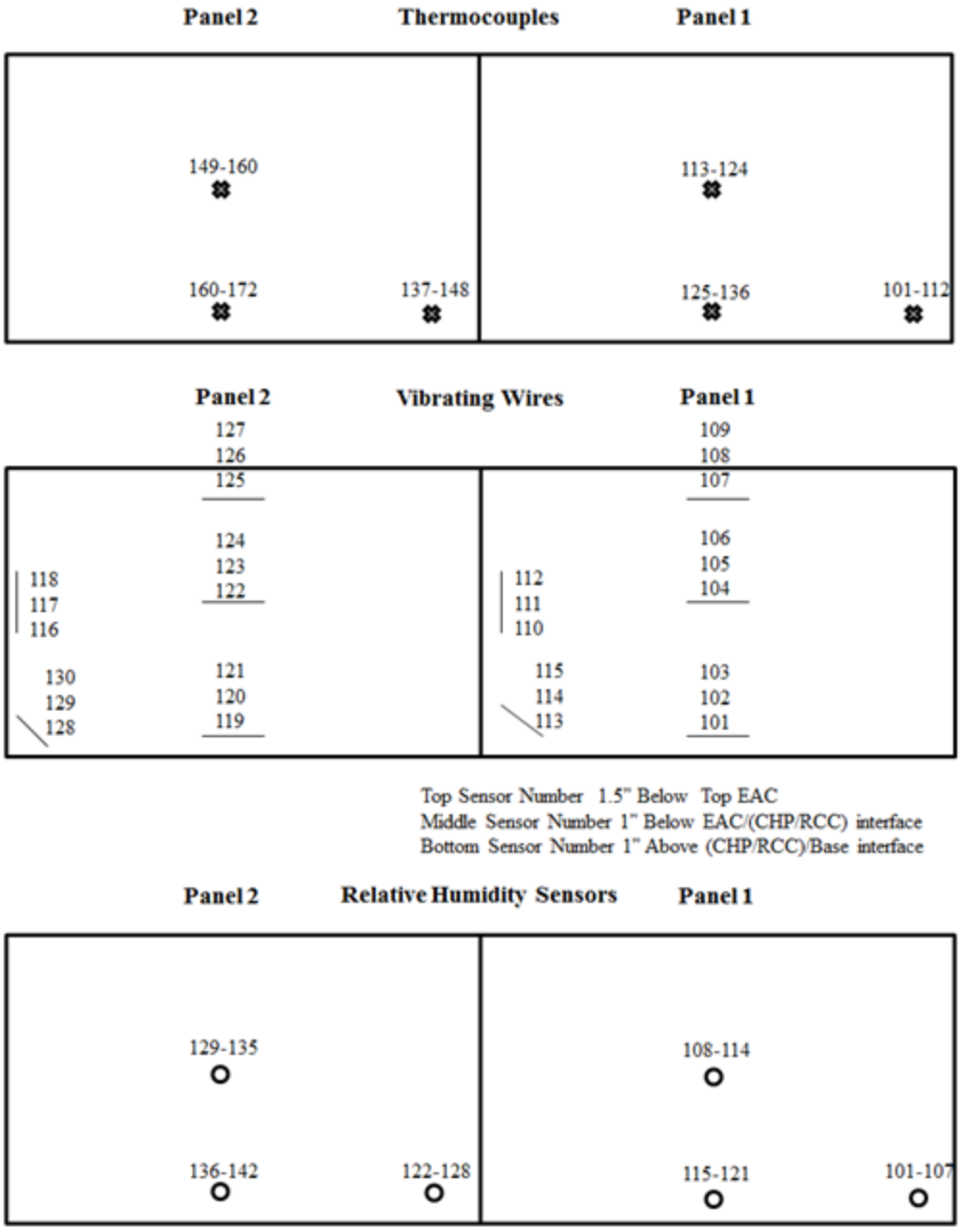

Figure 3.20: Cell 71 and Cell 72 Sensor Layout

The distribution of sensors with depth for Cells 70, 71, 72 can be seen in Figure 3.21. In Figure 3.21, only the thermocouples are present in the HMA layer for Cell 70. All three sensor types are present in the upper layer of Cells 71 and 72.

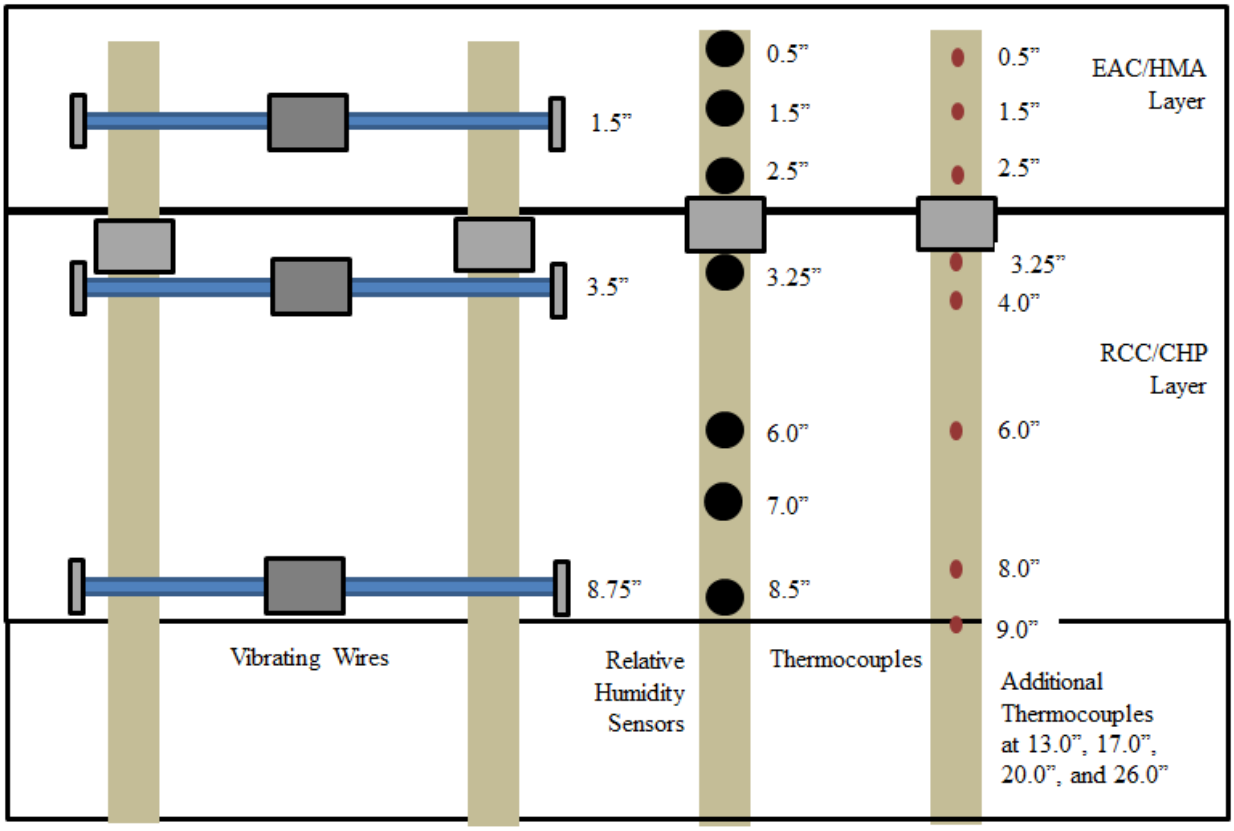

Figure 3.21: Distribution of Pavement Sensors with Depth

4.0 MEASURED RESPONSE OF COMPOSITE PAVEMENTS

In Section 2.0 the importance of assessing the contribution of the environment to stresses in concrete pavement, as well as some of the methodologies and tools to accomplish this goal, is established. In Section 3.0 the means through which the relevant environmental data was obtained for this study is presented. In this section, the first eleven months of data obtained from the pavements at MnROAD is assessed.

Each cell is assessed both individually, and against the response of the other two cells. The construction of these three cells at roughly the same time and the exposure of these cells to the same environmental and traffic conditions presents a unique opportunity for this comparative analysis. Because of the similarities between the cells, the variation in response can be attributed to the unique structure of each pavement.

This section, which covers pavement sensor data analysis, is broken down into five subsections. The first subsection focuses on establishing the initial environmental conditions of the three pavements, namely the zero stress temperature gradient and the reference temperature. The second subsection focuses on analyzing the temperature regimes and resulting temperature gradients that develop in the pavements. Thirdly, the relative humidity measurements that were obtained are presented and analyzed. After the relative humidity measurements are assessed, the curling of these pavements are assessed. This was determined through the strain measurements taken from the vibrating wire strain gauges. Finally, conclusions about the overall environmental response of these pavements are drawn.

4.1 DETERMINATION OF THE BUILT-IN CONSTRUCTION GRADIENT

4.1.1 Hydration of Portland Cement

Portland cement is the concrete constituent responsible for changing concrete from a thixotropic suspension to a hardened mass. This transformation is a governed by the hydration reaction of the constituents of the cement. While Portland cement itself is comprised of many constituents, tricalcium silicate, C_3S, is the constituent responsible for concrete hardening. When C_3S hydrates, calcium silicate hydrate, C-S-H, and calcium hydroxide, CH and others are formed in an exothermic reaction. Figure 4.1 outlines this reaction and illustrates the thermodynamic tendencies of the hydration of cement. In all, there are five distinct stages of cement hydration.

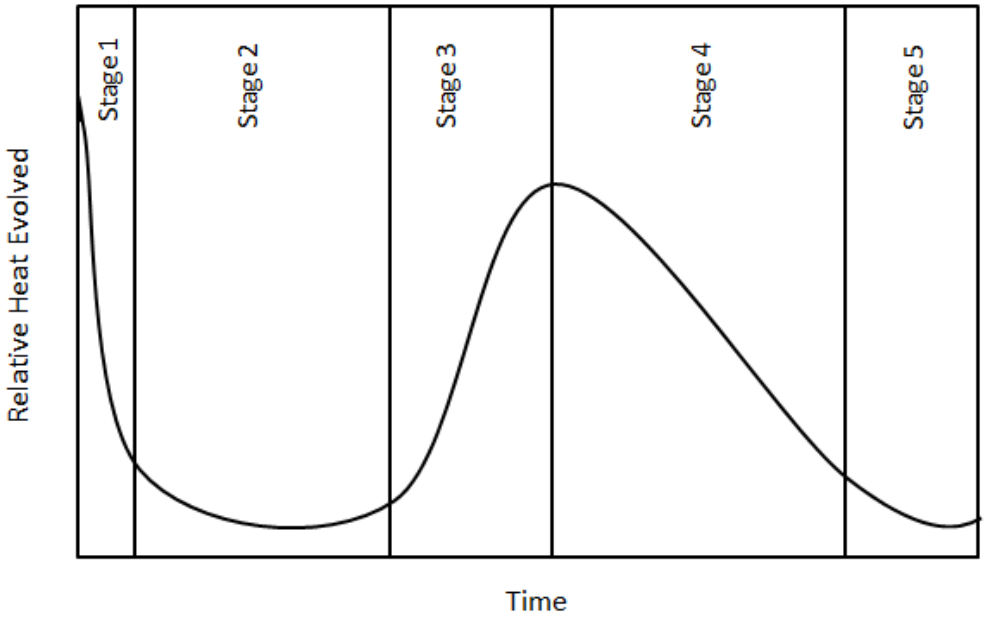

Figure 4.1: Hydration of Portland Cement

In stage one of Figure 4.1, the initial contact of cement with water causes a large evolution of heat. Stage 1 is also characterized by the release of calcium and hydroxide ions from the surface of the C_3S grains. This stage ceases after a short period of about 15 minutes. In stage 2 of Figure 4.1, known as the induction period, relatively little heat is evolved. During stage 2, the concentration of hydroxide and calcium ions continues to increase. This stage continues until a critical concentration is reached and the onset of stage 3, the acceleration stage, begins.

At the beginning of stage 3, the concentration of calcium and hydroxide ions is such that crystals of the hydration products C-S-H and CH start to rapidly form on the surface of the cement grains. It is approximately at the beginning of stage 3 that initial set occurs and the concrete beings to stiffen. Final set, which occurs at approximately the middle of stage 3, signals the beginning of hardening in the concrete. It is important to note that initial and final set are empirical definitions and do not signify a fundamental change in the hydration reaction occurring in concrete. Measureable strength gain begins a short time after final set.

As C-S-H and CH form on the surface of the cement grains, they begin to form a layer that becomes increasingly impermeable as it grows. Because of this decrease in permeability and a decrease in the ability of water to reach the unreacted portion of the cement grains, the hydration reaction rate slows. The slowing of the hydration reaction and reduction in the rate of heat evolution characterizes stage 4 which is known as the deceleration stage. Finally, in stage 5, the hydration of cement can be practically considered to be in a steady state. Hydration of cement continues to occur as long as there is available moisture and unreacted cement particles. This process continues to at least some degree for years after the hydration reaction begins.

4.1.2 Zero Stress Time

In early age concrete behavior, the ability of concrete to sustain an applied load is an attribute that the concrete establishes gradually. As mentioned in the previous section, measurable strength gain occurs after final set. For concrete hydrating in isothermal conditions, the concrete temperature rises after final set due to the continual heat evolution from the exothermic hydration reaction. Since the concrete has hardened and is restrained from deforming, however, a compressive stress develops within the concrete. The magnitude of this stress is proportional to the stiffness of the concrete. Stiffness of the concrete is in turn a function of the degree of hydration in the concrete.

As the rate of heat generation decreases in stage 4 of hydration, the temperature of the concrete also begins to drop. During this drop in temperature, some of the compressive stress generated by the restrained thermal expansion in stage 3 relaxes. At some temperature, which is usually higher than the temperature at final set, the stress in the concrete becomes zero. It is also at this point that the slab starts to curl in response to temperature gradients that develop in the slab. Together, the moment in time and temperature at that time are known as the zero stress time and zero stress temperature. These features are also illustrated in Figure 4.2.

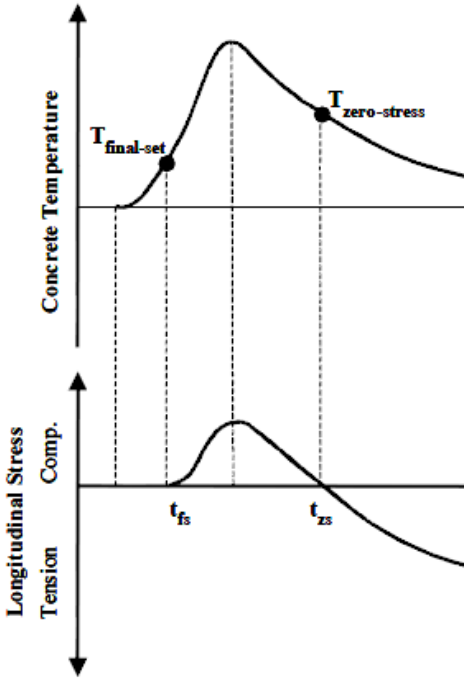

Figure 4.2: Illustration of the Zero Stress Temperature [29]

Once this transition in behavior occurs at the zero stress time, the temperature gradient in the slab becomes "locked in." This locked in temperature gradient is called the zero stress temperature gradient because it occurs when the slab is flat and there is no stress in the slab. After the zero stress time occurs and the zero stress temperature gradient is set, higher temperature gradients that develop in the slab will cause negative, downward, curvature. Temperature gradients lower than the zero stress temperature gradient will cause positive, upward, curvature in the slab.

For a given traffic or environmental load, determining the critical stress magnitude and location is dependent upon the curvature in the slab. Curvature is partly dictated by the temperature gradient in the slab. To know the curvature in the slab due to any arbitrary temperature distribution it is imperative to subtract out and account for the zero stress temperature gradient.

For composite pavements, the determination of the zero stress temperature is also important for establishing the initial weighted average temperature in each of the layers. The calculation of the weighted average temperature is given by Equation 26.

$$T_{wave} = \sum_{i=1}^{n-1} \left[0.5 \left[\left(T_i - T_{i.t.1} \right) \cdot \frac{\left(D_i - D_{i.t.1} \right)}{\left(D_i - D_n \right)} \right] \right] \qquad \text{Equation 26}$$

In Equation 26, n is the number of sensors and T_i and D_i are the temperature and depth of a given thermocouple at a particular moment in time.

4.1.3 Determination of the Zero Stress Time at MnROAD

The determination of the zero stress temperature at MnROAD was made using the strain and temperature data obtained from the vibrating wire strain gauges and their embedded thermistors. When these gauges are in hardened concrete, the response is such that the actual strain in the concrete can be determined using Equation 27. In Equation 27, R_1 and R_0 are strain readings. R_o is the strain at the time the gauges are zeroed and R_1 is the strain reading in the gauge at any time afterwards. T_o and T_1 in Equation 27 represent the thermistor temperatures and correspond with the zero time and time of interest respectively.

$$\varepsilon_{conc} = \left(R_1 - R_0 \right) \cdot B + CTE_{steel} \cdot \left(T_1 - T_0 \right) \qquad \text{Equation 27}$$

The relationship between strain and temperature posed in Equation 27 only holds for hardened concrete. This is important when looking at the early age readings from these gauges since the concrete gradually transitions from a thixotropic material capable of flow to a hardened material. Understanding the way the gauges function is integral to determining the point at which the gauge behavior becomes dictated by the concrete.

A vibrating wire strain gauge with labeled components is shown in Figure 4.3. The gauge is constructed such that tension is held in the wire by the aluminum shaft which prevents the two end blocks from coming closer together. The construction of the gauge is also such that the end blocks are relatively free to move in the aluminum shaft.

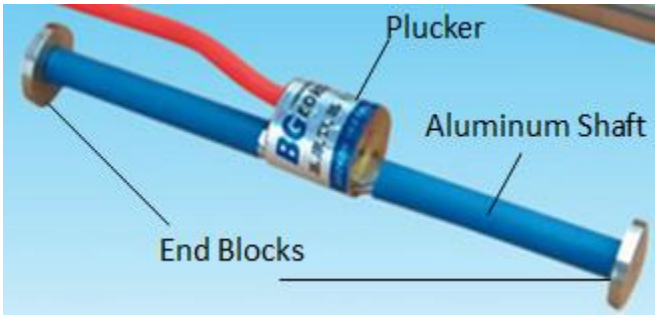

Figure 4.3: Vibrating Wire Strain Gauge and Components

Section 3.2.3 discussed that the strain in the gauge is calculated based on a relationship between tension in the wire and the measured resonant frequency of the wire subjected to electronic excitation. When the gauge is in air and subjected to a temperature increase, the overall expansion or contraction of the gauge is dictated by the thermal coefficients of the wire, and the aluminum shaft. The CTE of aluminum is approximately 13 $\mu\varepsilon/^{o}F$ while the CTE of the steel wire is 6.78 $\mu\varepsilon/^{o}F$. Because of this difference in CTEs and the temperature increase, the aluminum shaft wants to expand more than the steel wire and end blocks. This expansion is somewhat restrained by the steel wire and end blocks and generates an increased tensile stress in the vibrating wire. Increasing the tension in the vibrating wire subsequently increases the frequency of the excited wire. When cooled, the converse is true. The frequency of the vibrating wire decreases with a decrease in temperature.

The CTE of the concrete is such that it is usually lower than the CTE of steel. In hardened concrete, the movement of the end blocks, and hence the frequency in the wire, are completely dictated by the movement of the concrete. When the gauge in concrete is heated, the concrete expands but the wire wants to expand more than the concrete allows it to. The result of this arrangement is that the tension in the vibrating wire is relaxed and the frequency decreases. In concrete, an increase in temperature causes a decrease in frequency and a decrease in temperature causes an increase in frequency.

Figure 4.4 shows the early age response of vibrating wire frequency for a typical vibrating wire sensor embedded in fresh concrete. Figure 4.4 is a time series showing the history of the frequency in the vibrating wire strain gauge. The time series starts at a frequency of approximately 897.5 Hz. In general, it can be seen that the frequency follows four trends. These four trends include a period where the frequency increases at a constant temperature, a period of increasing frequency with increasing temperature, no change in frequency with increasing temperature, and finally a decrease in frequency with increasing temperature.

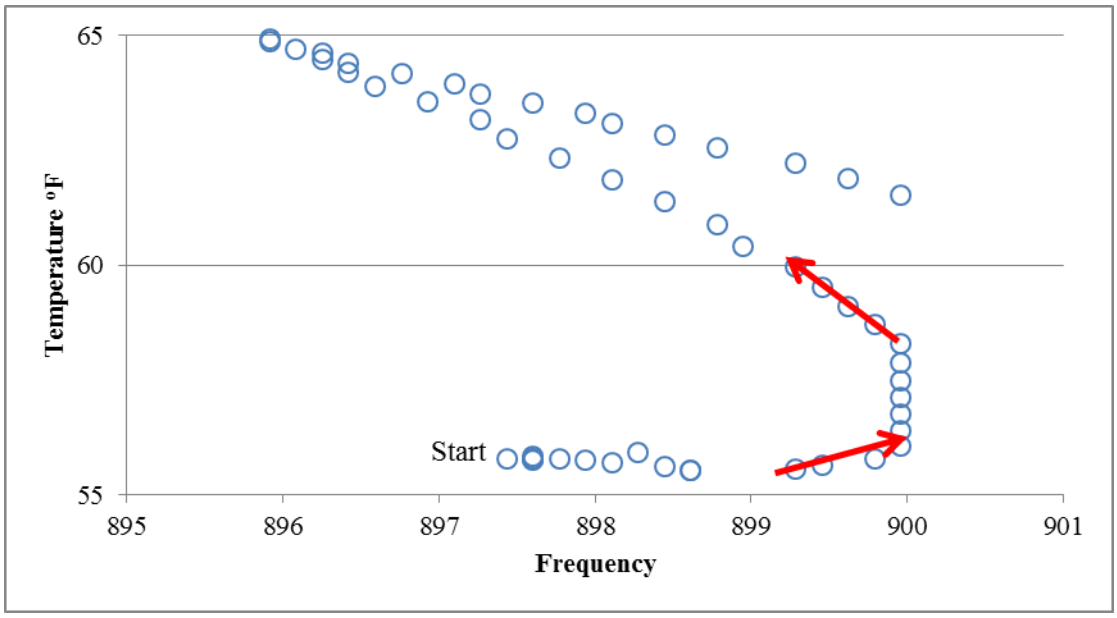

Figure 4.4: Early Age Response of Vibrating Wire Frequency

The initial period of increasing frequency with constant temperature is not understood, but is believed to be an adjustment period for the gauge as it responds to the fresh concrete. The second period is represented by the first arrow in Figure 4.4. This arrow represents the period during which the frequency in the gauge is dictated by the aluminum shaft. The second arrow indicates the start of the fourth period where the movement in the gauge is being dictated by the concrete. It is believed that within the transition region where no change in frequency is observed with a change in temperature that the concrete has set in the sense that it has reached sufficient stiffness to dictate the behavior of the gauge. This, therefore, is the appropriate point to initially zero the vibrating wire strain gauge.

A typical time series representing a period of 72 hours of vibrating wire strain and temperature readings from Cell 71 can be seen in Figure 4.5. This data is from the centerline location sensor oriented in the longitudinal direction and embedded in the bottom of the lower concrete layer. The three data points in Figure 4.5 that are not represented by open circles can be

used to highlight different aspects of the early age behavior of the concrete embedment strain gauges.

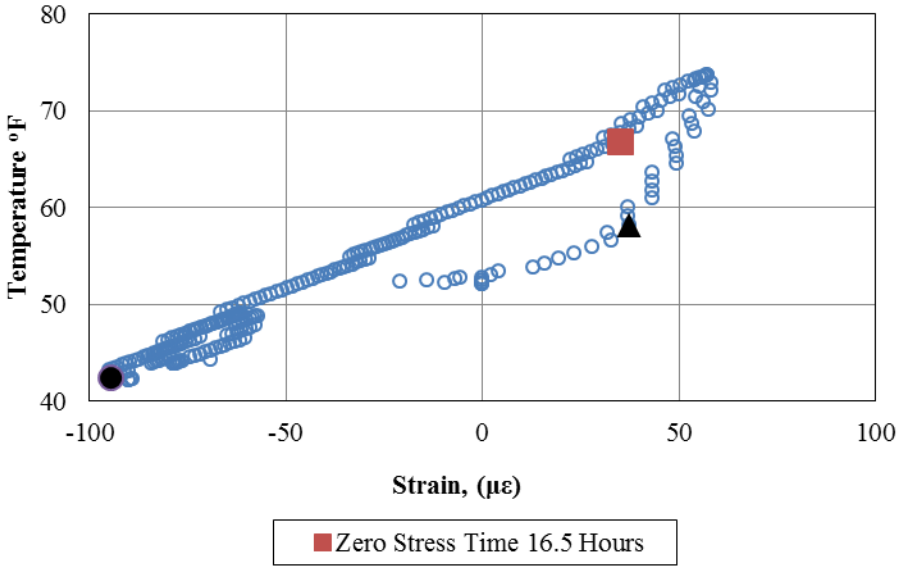

Figure 4.5: Strain and Temperature Relationship in Young Concrete used in Determining the Zero Stress Time

In Figure 4.5, the data series is first zeroed to the time that the concrete is placed around the sensors. Because the concrete has not hardened in the early readings of the time series, the early behavior in which the strain readings vary between approximately -25 and 25 are due to the background behavior of the gauge. The black triangle indicates the point at which the behavior of the gauge starts to become dictated by the concrete and was determined by looking at the frequency temperature relationship as discussed previously. Although it cannot be used to determine the precise value, a general correlation can be made between this transition and the final set time.

Between the black triangle and the zero stress time (red square), it can be noticed that the slope of the strain temperature relationship is different from the slope after the zero stress time. The relatively steeper slope means that less strain is occurring as a result of a change in temperature. Since less strain is being observed by the gauge in this region, it can be concluded that in this region there is more resistance to thermal expansion and contraction. This restraint is present because the slabs cannot freely deform yet. Attributing this observation to longitudinal restraint is bolstered by considering the strain temperature relationship for a sensor oriented in the transverse direction. The strain-temperature relationship for the sensor in the transverse direction can be seen in Figure 4.6. Once the gauge initially starts responding to the concrete, the point indicated by the black triangle, the slope of the strain and temperature plot is essentially constant. This is reasonable considering that in the transverse direction there is significantly less restraint.

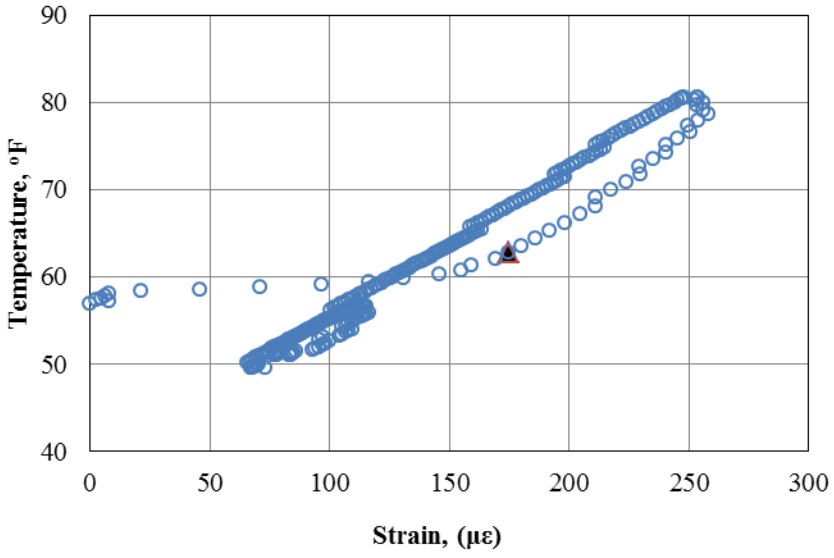

Figure 4.6: Early Age Strain-Temperature Relationship for Transverse Location Bottom Sensor

Additionally, Figure 4.5 shows that although the zero stress temperature and the behavioral transition indicated by the black triangle have similar strain values, the temperature is quite different. This difference in temperature at a given strain is believed to be the result of the relaxation of the concrete between the final set time and the zero stress time as discussed in the Section 4.1.2.

The other method used to define the zero stress condition is to look at the curvature in the slab. Although curvature alone could be analyzed, it is helpful to interpret the curvature with respect to temperature gradient as well. The calculation of curvature is made using Equation 28. In Equation 28, D is the distance between the vibrating wire sensors. The calculation of the linear temperature gradient is shown in Equation 29.

$$\rho = \frac{1}{R} = \frac{-\left(\varepsilon_{top} - \varepsilon_{bot}\right)}{D\cdot\left(1 + \frac{\varepsilon_{top}}{2} + \frac{\varepsilon_{bot}}{2}\right)} \qquad \text{Equation 28}$$

$$LTG = \frac{T_{top} - T_{bot}}{-\left(D_{top} - D_{bot}\right)} \qquad \text{Equation 29}$$

Figure 4.7 presents the curvature and temperature gradient in the slab after paving for a typical longitudinally oriented sensor in Cell 71. In the first 36 hours after paving, there is a range of temperature gradients present in the slab. The highest gradient occurs shortly after paving. The curvature series, which is zeroed to the time the gauges start responding to deformation in the concrete remains relatively constant until about 16 hours after paving. After this point, it can be seen that the slab starts to curl up due to the increasingly negative temperature gradient. Comparing the results of Figure 4.7 with the results of Figure 4.5 shows that either method provides a reasonable means for obtaining the time that the slab starts to curl. This time is the time at which the built-in temperature gradient and weighted average temperature can be assessed.

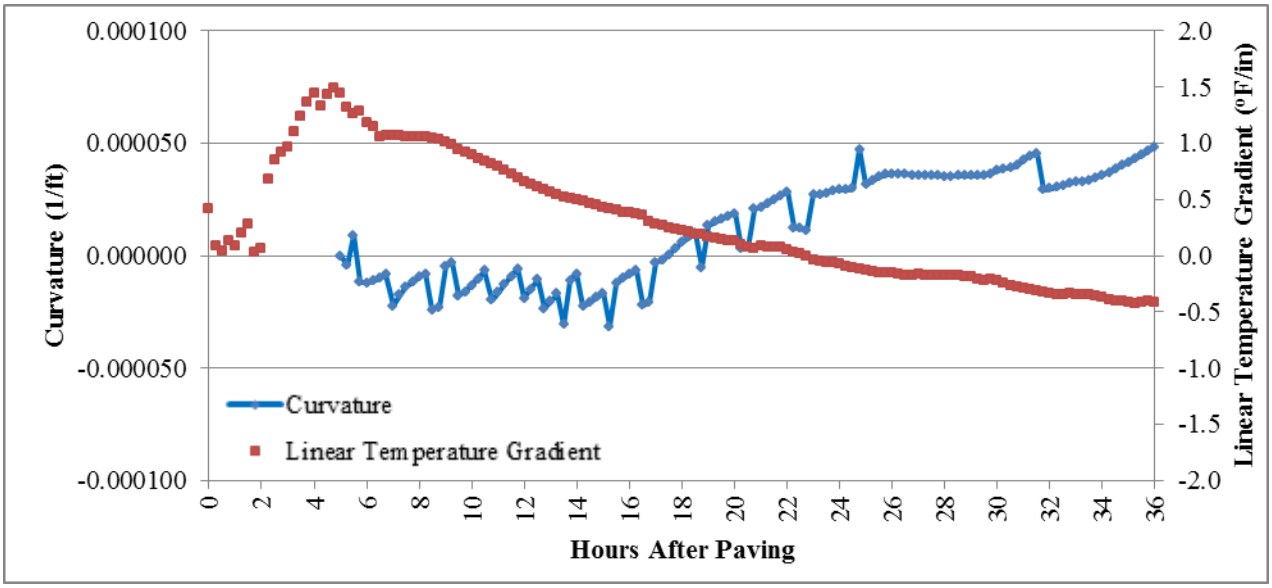

Figure 4.7: Curvature and Temperature Gradient in the Slab after Paving

A final check of the analysis method used to determine the zero stress time can be made by considering Figure 4.8. This figure shows the variation in the vibrating wire thermistor temperature and the ambient temperature over the first three days after paving. For the week of paving Cells 70, 71, and 72, the ambient temperature was relatively cool with overcast skies and a light breeze. During the day following construction of each cell, the ambient temperature was always below the concrete temperature and relatively constant. This somewhat mimics isothermal conditions and allows for a direct assessment of the degree of hydration from the concrete temperature measurements. The ambient temperature over the time of the data series used in Figure 4.5, as well as the highlighted data points from Figure 4.5 are shown in Figure 4.8. The point at which the gauge starts responding to the temperature changes in concrete and the point selected to zero the strain readings of the gauge agrees well with the qualitative descriptions of the final set time and zero stress time made in Section 4.1.2.

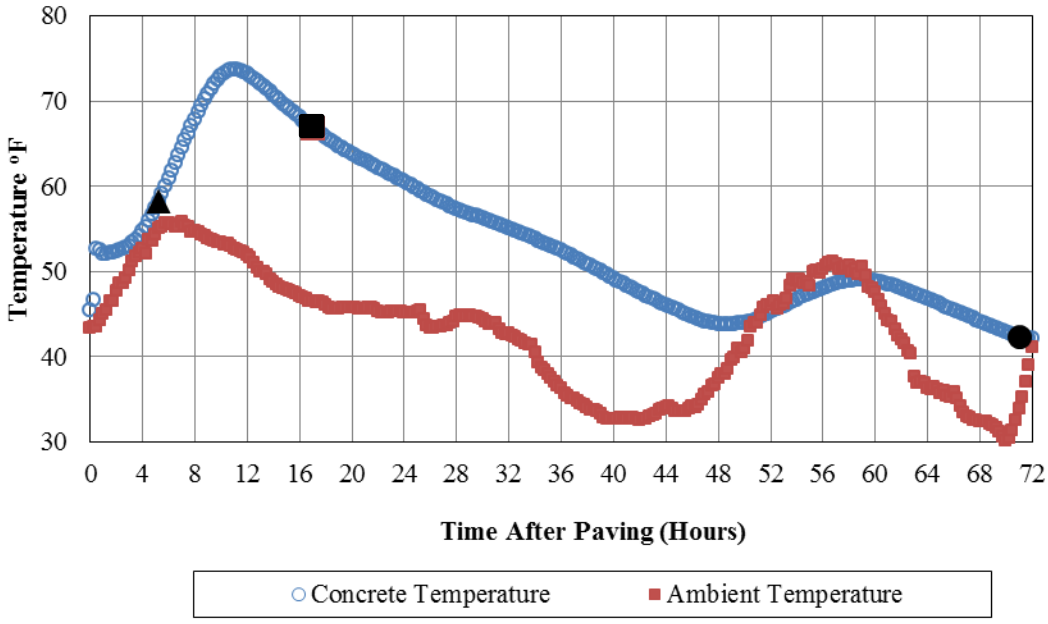

Figure 4.8: Comparison of Concrete and Ambient Temperature with Time After Paving

The following three sections present the utilization of the aforementioned methodologies in the determination of the specific zero stress time, zero stress temperature, and built-in construction temperature gradient for the three cells at MnROAD.

4.1.3.1 Cell 70

The bottom recycled concrete layer of Cell 70 was constructed on the morning of May 5th 2010 with the paver passing the instrumented cells at approximately 7:45 AM. A typical strain vs. temperature relationship for the vibrating wire strain gauges in Cell 70 can be seen in Figure 4.9. The first readings in Figure 4.9 are indicative of the time when the concrete was placed around the sensor and are indicated by the tail of the red arrow.

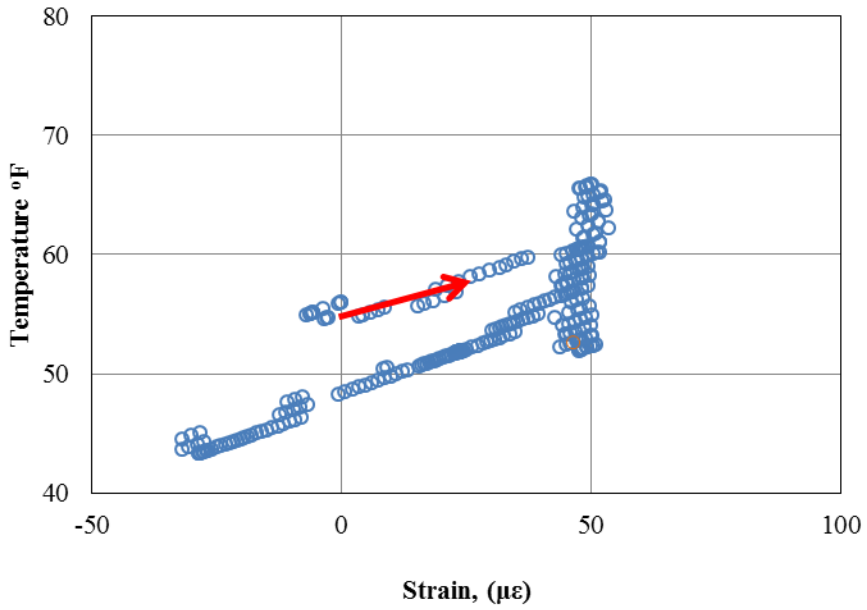

Figure 4.9: Typical Strain vs. Temperature Relationship for Cell 70

As can be seen in Figure 4.9, the general trend for the vibrating wire sensor readings in Cell 70 is that the strain readings oscillate around the zeroed strain and temperature value for approximately 10 hours, enter a period in which the strain does not change much with significant changes in temperature, and then suddenly starts to expand and contract with a relatively fixed relationship between strain and temperature. In this particular instance, it is difficult to use the relationship between strain and temperature to determine the zero stress temperature. Therefore, the curvature vs. time relationship was investigated.

Figure 4.10 through Figure 4.15 present the curvature and temperature gradients at the three longitudinally oriented locations for both of Cell 70's instrumented slabs. Each plot represents the first 36 hours after paving. The first moment in time at which the strain is calculated according to Equation 27 is when the frequency temperature relationship starts behaving as discussed in Section 4.1.2. From these plots, there appears to be no consistent set

time when comparing the sensors within a panel or when comparing the same location between panels.

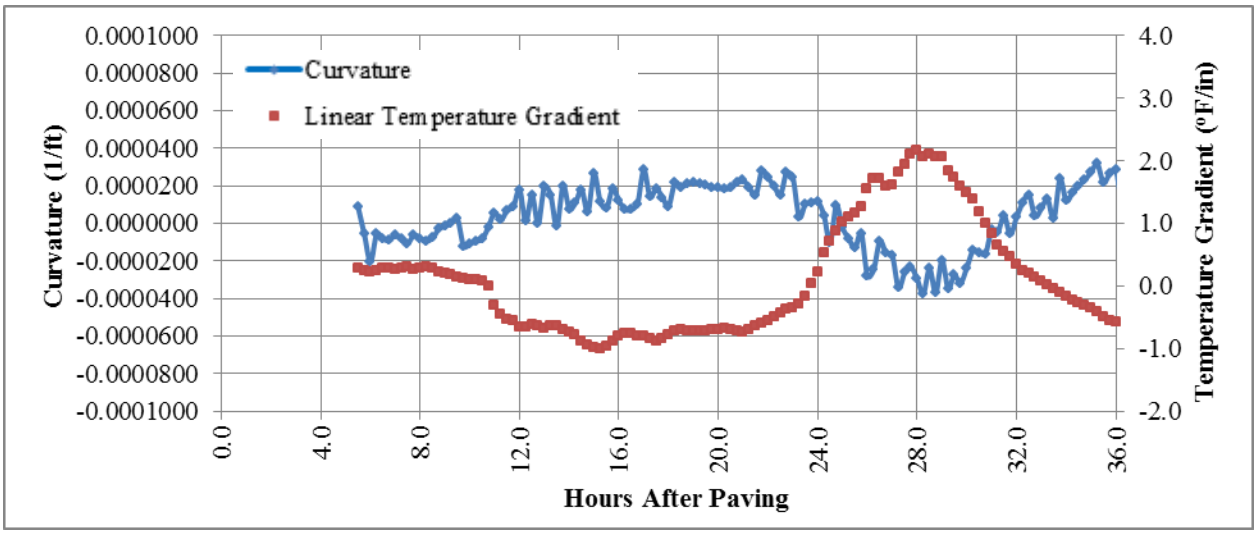

Figure 4.10: Curvature and Temperature Gradient in the Slab– Cell 70 Panel 1 Edge Location

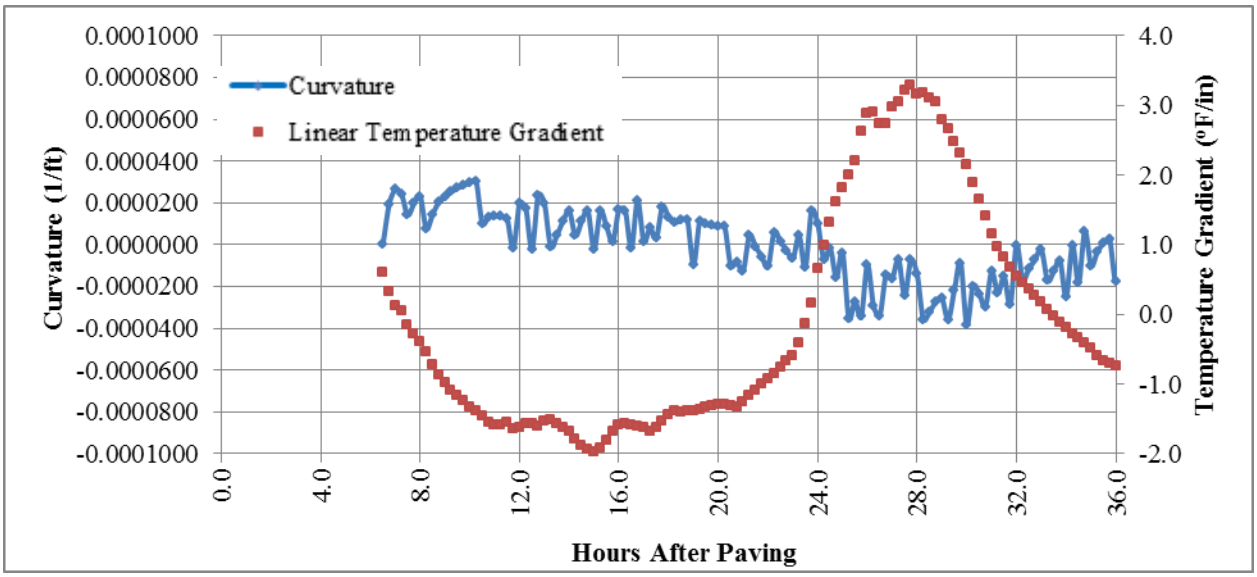

Figure 4.11: Curvature and Temperature Gradient in the Slab - Cell 70 Panel 2 Edge Location

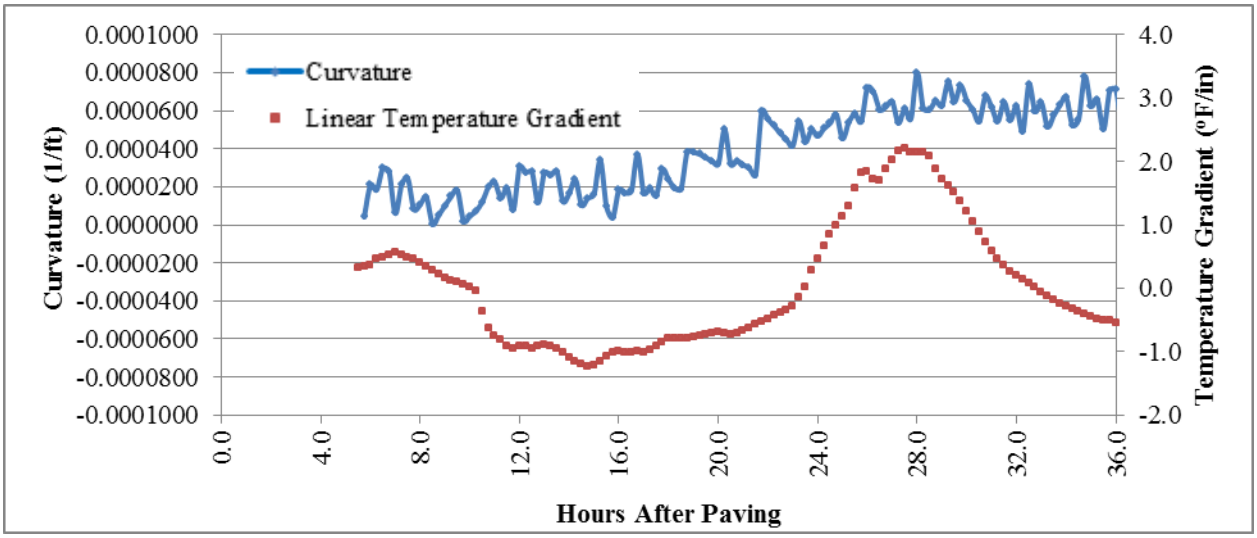

Figure 4.12: Curvature and Temperature Gradient in the Slab - Cell 70 Panel 1 Midslab Location

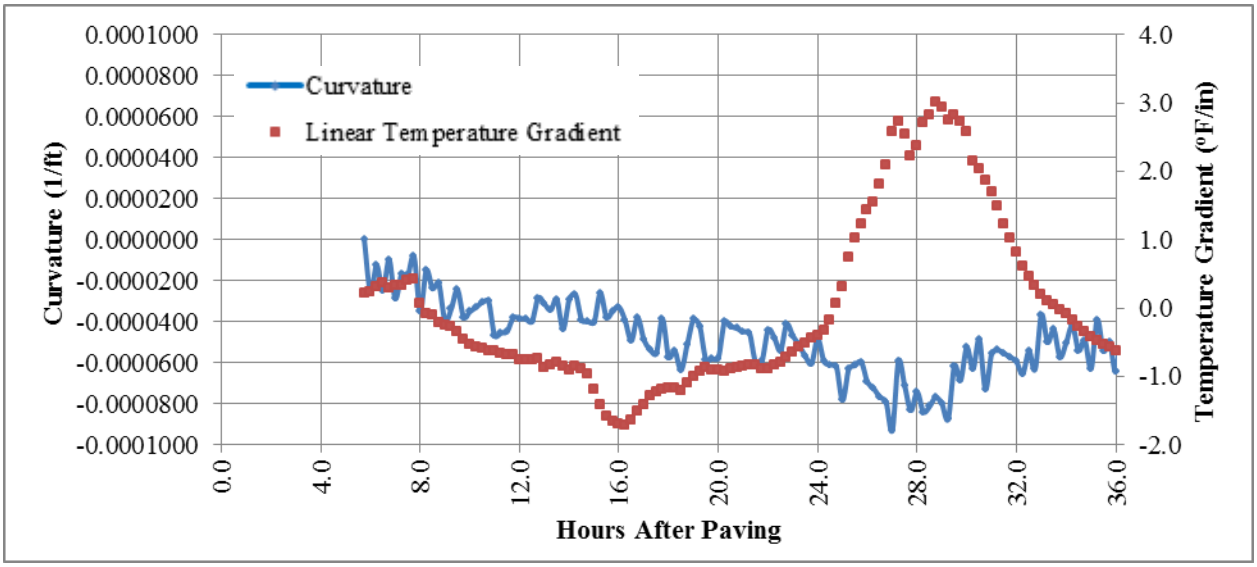

Figure 4.13: Curvature and Temperature Gradient in the Slab – Cell 70 Panel 2 Midslab Location

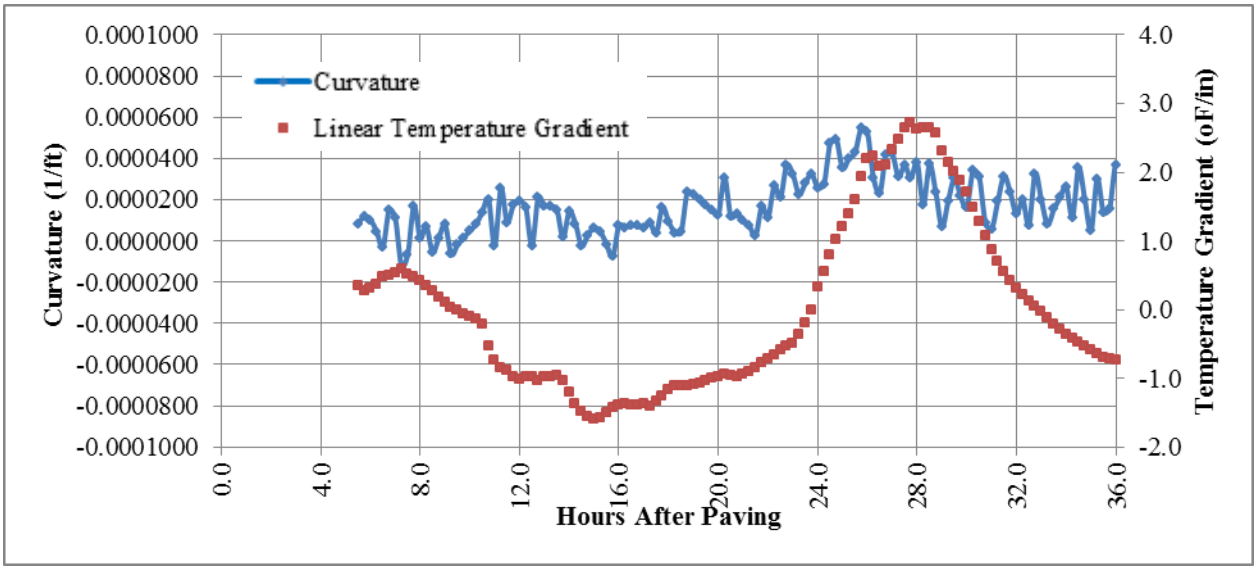

Figure 4.14: Curvature and Temperature Gradient in the Slab - Panel 1 Centerline Location

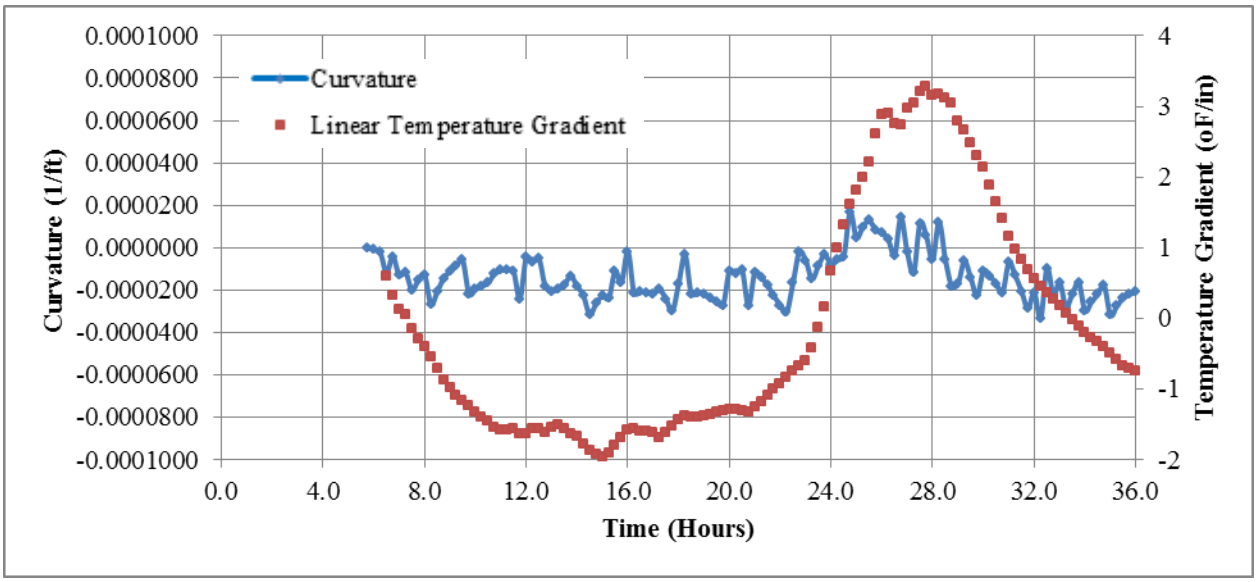

Figure 4.15: Curvature and Temperature Gradient in the Slab - Panel 2 Centerline Location

Despite the noted inconsistencies, Table 4.1 presents the estimated time of the initiation of curling for each of the preceding six figures. There is a significant difference between some

locations. Additional discussion regarding the zero stress time for Cell 70 is presented at the conclusion of this section when comparing the zero stress time for all three cells.

Table 4.1: Hours after Paving that Curling Initiates for Cell 70

Location	Panel 1	Panel 2
Edge	11	19
Midslab	18	9
Centerline	21	22

Using the zero stress times from Table 4.1, the corresponding built-in construction temperature gradient in the slab was determined at each location. Examination of Figure 4.10 through Figure 4.15 reveals that for most of the zero stress times chosen in Table 4.1, the temperature gradient does not vary considerably. It can also be seen when comparing the six figures that there is a difference in the temperature gradient in the slab at a given time. One potential source of this error is an error in the surveyed depth location of the sensors. The distance between the sensors is a significant input for both the calculation of curvature and the linear temperature gradient.

Since the temperature gradient calculated using the thermistor from the vibrating wire strain gauges varies between the locations and over the range of times presented in Table 4.1, the temperature gradient recorded by the thermocouples at the same point in time and at the same location was used to establish the built-in temperature gradient for Cell 70. The temperature gradients calculated for the range of times shown in Table 4.1 using thermocouple measurements are shown in Figure 4.16. Based on Figure 4.16, it can be approximated that the built-in temperature gradient for Cell 70 is -1.0^{o}F/in. This value was selected as it is the average value for times after about 12 hours after paving. As will be discussed in Section 4.1.3.4, which

compares the zero stress time of the three cells, the degree of hydration is relatively low in Cell 70 at any given time relative to Cell 71. The same concrete mix design was used to pave both cells. On the basis of the same mix design having similar degrees of hydration at the zero stress time, it is unlikely that the zero stress time occurred as early as is indicated by the nine hours and eleven hours shown in Table 4.1.

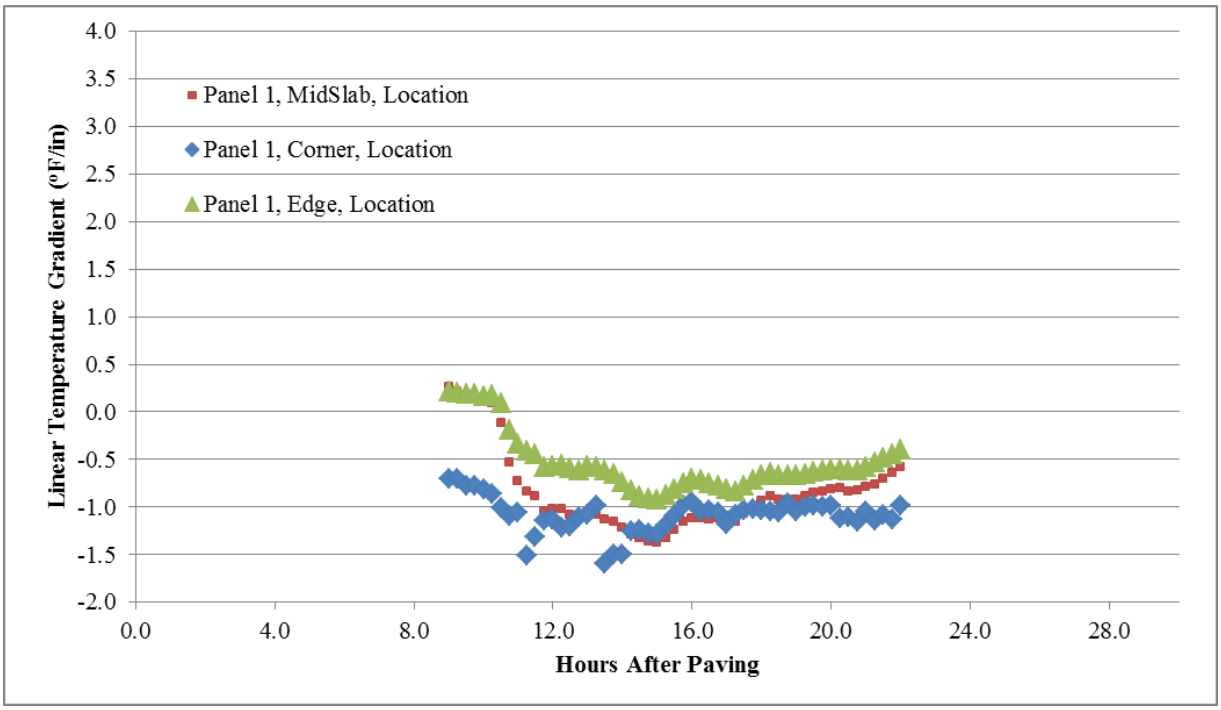

Figure 4.16: Early Age Temperature Gradients from Thermocouple Measurements in Cell 70

The weighted average temperature calculated using both thermocouple measurements and vibrating wire thermistor measurements over the range of potential zero stress times is shown in Figure 4.17. Figure 4.17 exhibits a location dependence for determining the weighted average temperature. This can most likely be attributed to the relatively insulated conditions at

midslab relative to the slab edges. For the midslab location, approximately 12 hours after paving, the weighted average temperatures is between 65.5°F and 57.5°F.

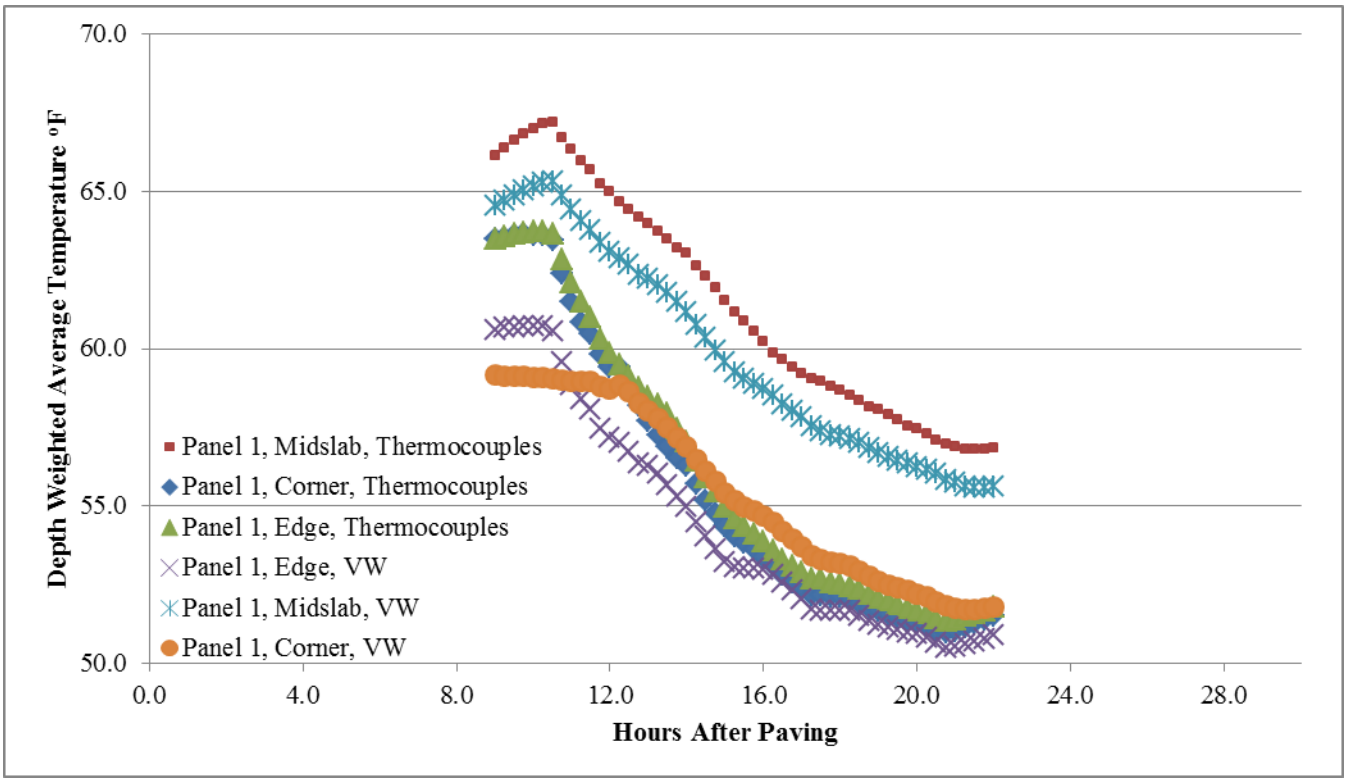

Figure 4.17: Weighted Average Temperature over Established Range of Zero Stress Times

4.1.3.2 Cell 71

Both the bottom recycled concrete layer and the upper EAC layer of Cell 71 were constructed on the morning of May 6th 2010. The paver passed the instrumented cells at approximately 7:15 AM. The mixture designs for both the bottom recycled concrete layer and the upper EAC layer of Cell 71 can be found in Table 3.1 in Section 3.1.2. A typical strain vs. temperature relationship for lower and upper layers in Cell 71 can be seen in Figure 4.18 and

Figure 4.19 respectively. Like with Cell 70, the zero strain and temperature readings in the figures were chosen to be the readings when the concrete was placed on the sensor.

The strain vs. temperature figures for Cell 71 were much easier to interpret than their counterparts from Cell 70. Typical relationships for both the lower and upper concrete layer are shown in Figure 4.18 and Figure 4.19, respectively. The difference in the shape of the strain vs. temperature relationship between the Cells 70 and 71 is believed to be due to the variation in the hydration history between the two cells. For Cell 71, the zero stress time determined from both the strain temperature relationship and the curvature time relationship generally showed good agreement. The zero stress time was ultimately selected based on the curvature vs. time relationship. This method was selected because there was somewhat more variation in the zero stress time determined based on the strain vs temperature relationship. Both methods however, will be compared in this section.

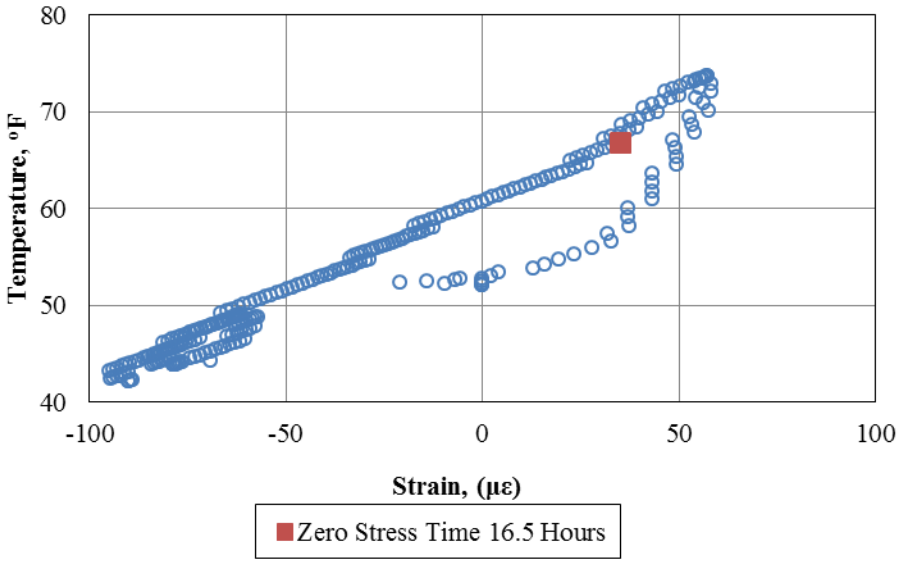

Figure 4.18: Typical Strain vs. Temperature Relationship for Lower Recycled Concrete Layer in Cell 71

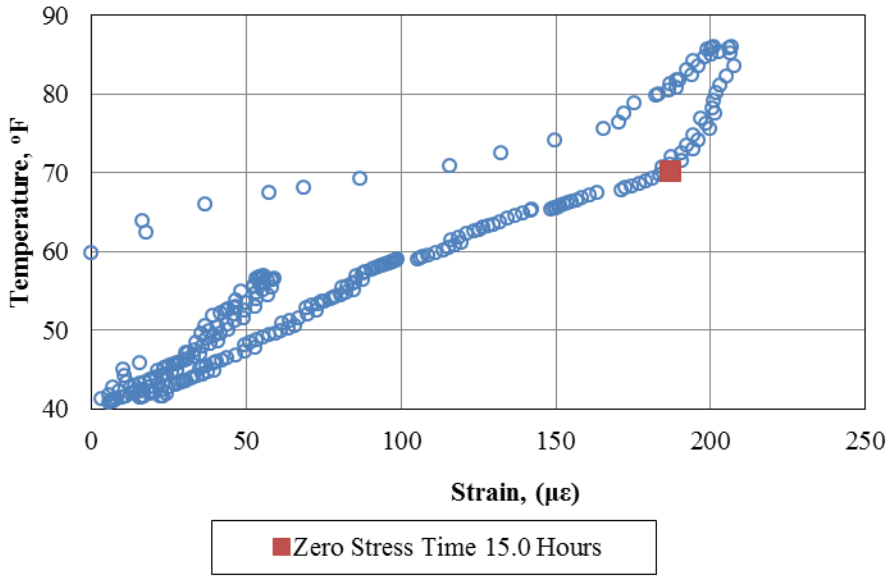

Figure 4.19: Typical Strain vs. Temperature Relationship for Upper EAC Concrete Layer in Cell 71

Table 4.2 presents a summary of the estimated time for the initiation of curling based on an assessment of curvature vs linear temperature gradient. The curvature vs time relationship for each location in Table 4.2 is presented in Figure 4.20 through Figure 4.23. Due to a datalogger programming error, early age curvature could only be calculated at four of the six locations at which longitudinal sensors were present. Figure 4.20 through Figure 4.23 show that while there is still some variation between the figures with respect to location, in general there seems to be a transition point with respect to curvature approximately 15 hours after paving.

Table 4.2: Hours after Paving that Curling Initiates for Cell 71

Location	Panel 1	Panel 2
Edge	15	14
Midslab	15	N/A
Centerline	15	N/A

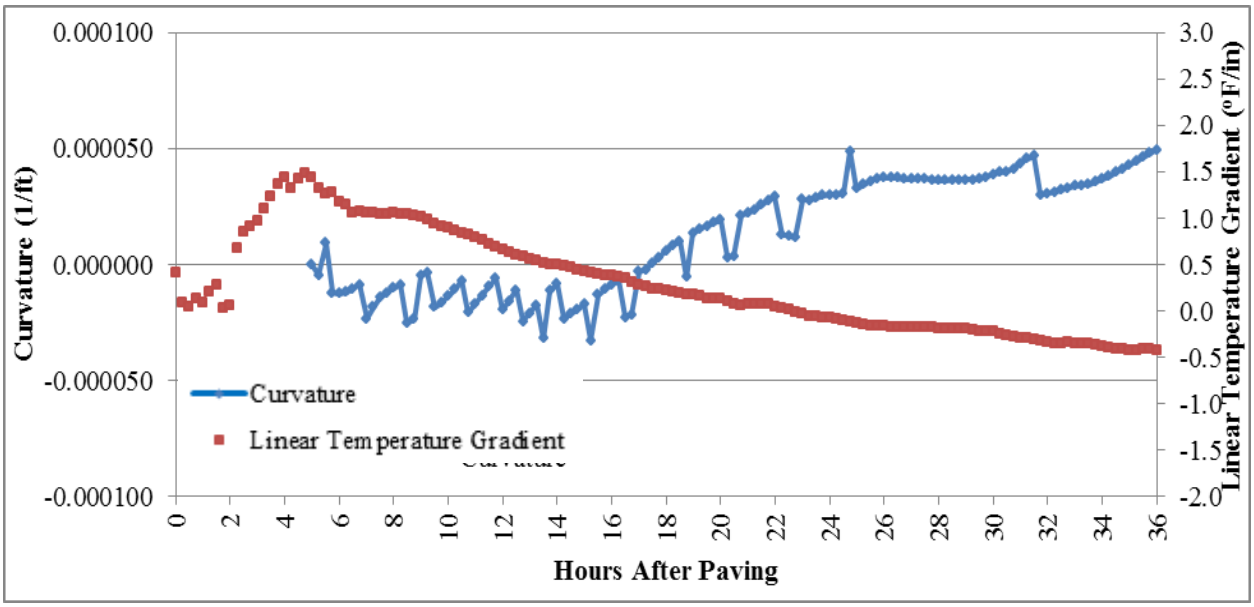

Figure 4.20: Curvature and Temperature Gradients in the Slab - Panel 1 Edge Location

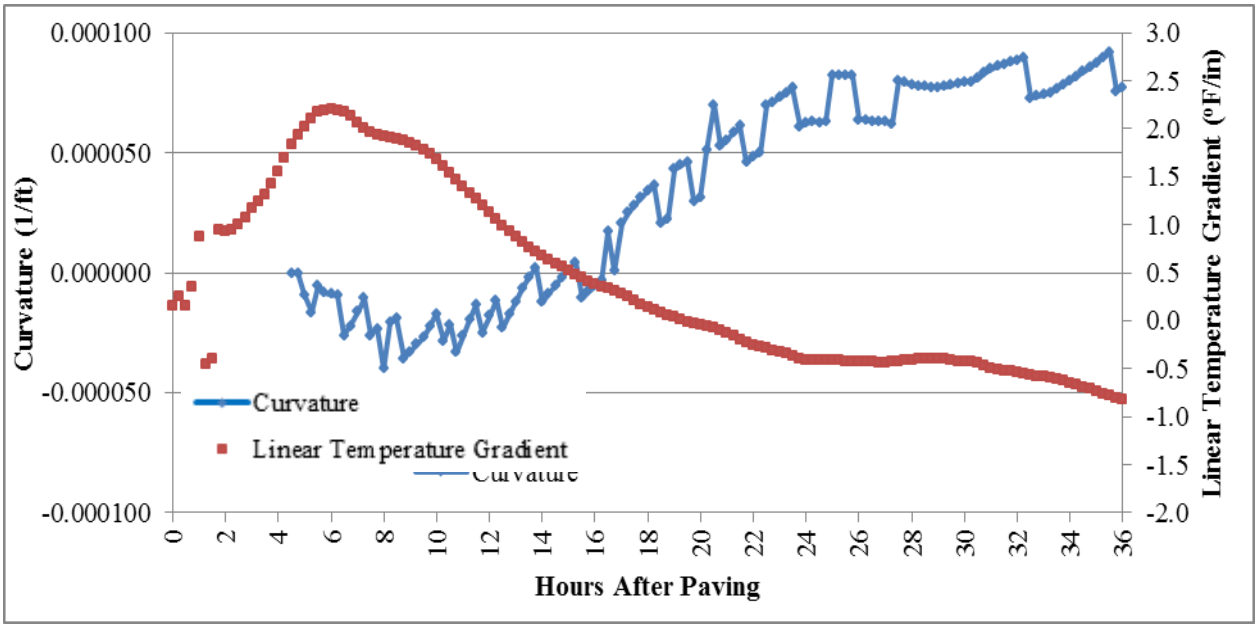

Figure 4.21: Curvature and Temperature Gradients in the Slab - Panel 2 Edge Location

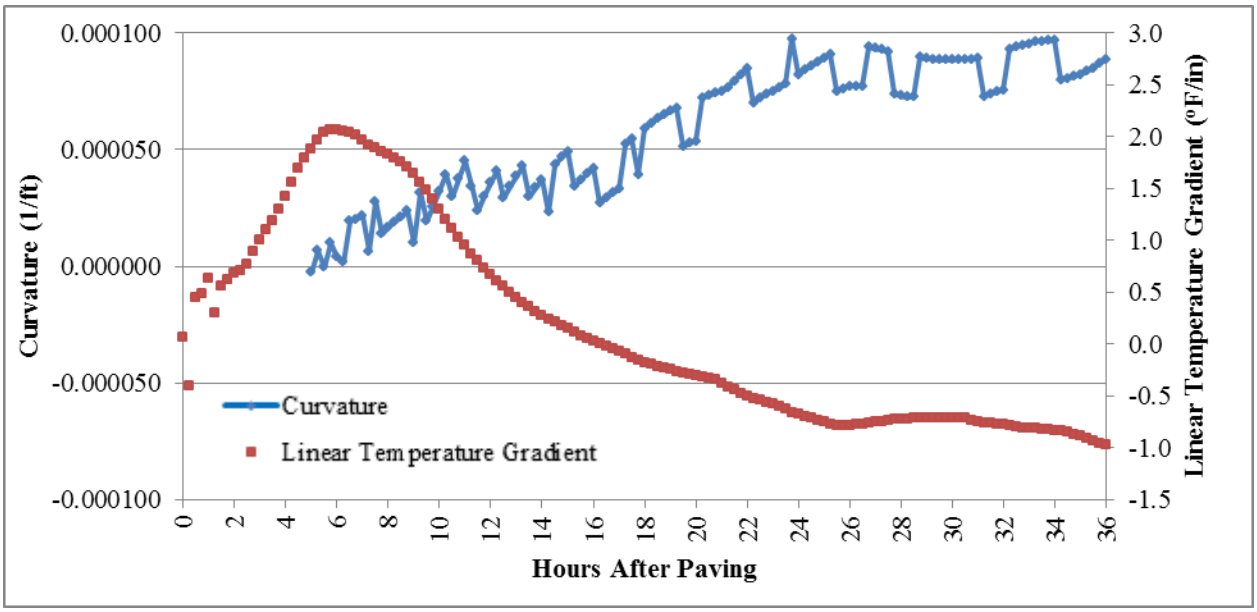

Figure 4.22: Curvature and Temperature Gradients in the Slab – Panel 1 Midslab Location

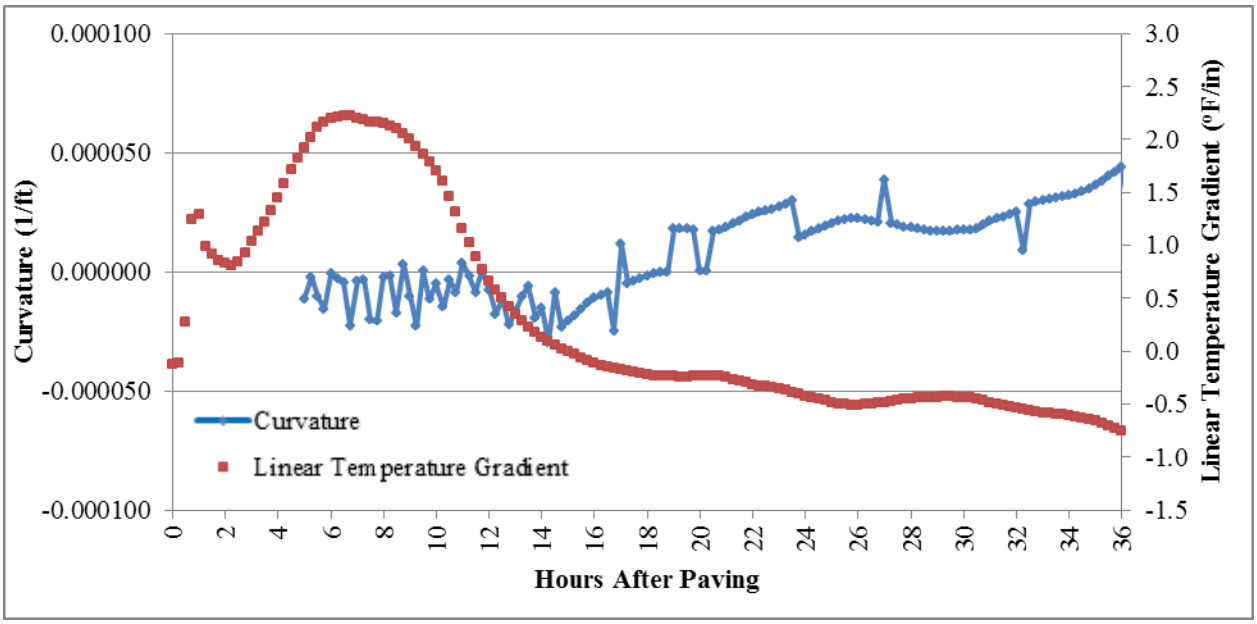

Figure 4.23: Curvature and Temperature Gradients in the Slab - Panel 1 Centerline Location

Figure 4.24 through Figure 4.26 show the strain vs. temperature relationship and the estimated zero stress time for the centerline location in Panel 1 of Cell 71. Similar figures from the other locations with longitudinally oriented sensors are presented in APPENDIX A. As with Cell 70, the temperature gradient at any given time calculated using the vibrating wire measurements varied and so the linear temperature gradients determined from thermocouple measurements were examined. The temperature gradients over the range of times shown in Table 4.2 are shown in Figure 4.27. Regardless of the exact time chosen to determine the zero stress temperature, the linear temperature gradient is approximately -0.5°F/in.

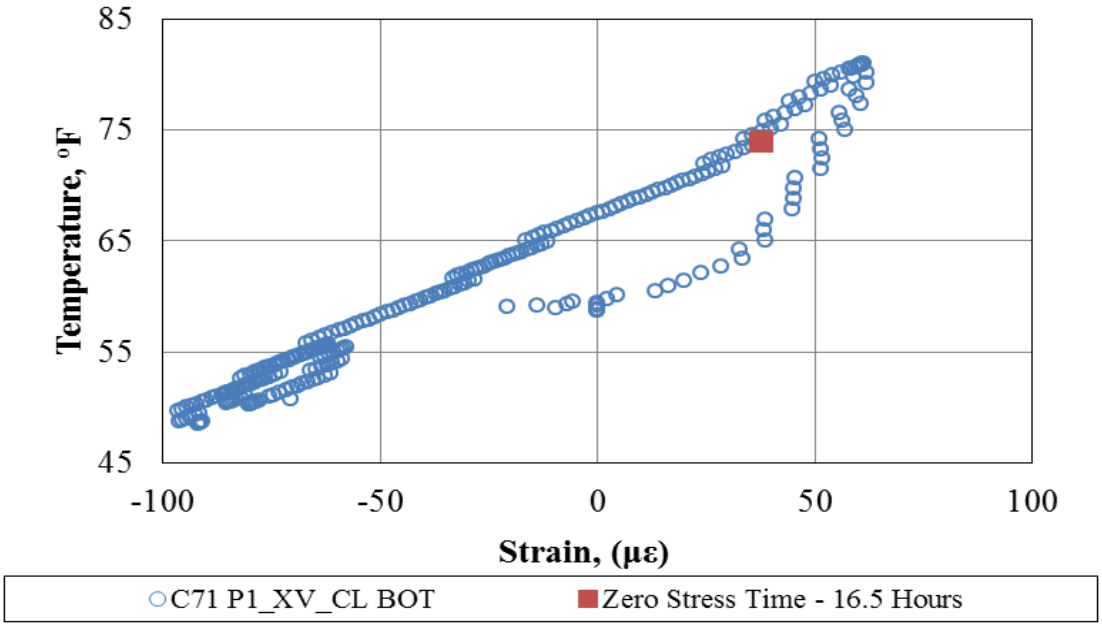

Figure 4.24: Zero Stress Time for Cell 71 Panel 1 Bottom Depth Centerline Location

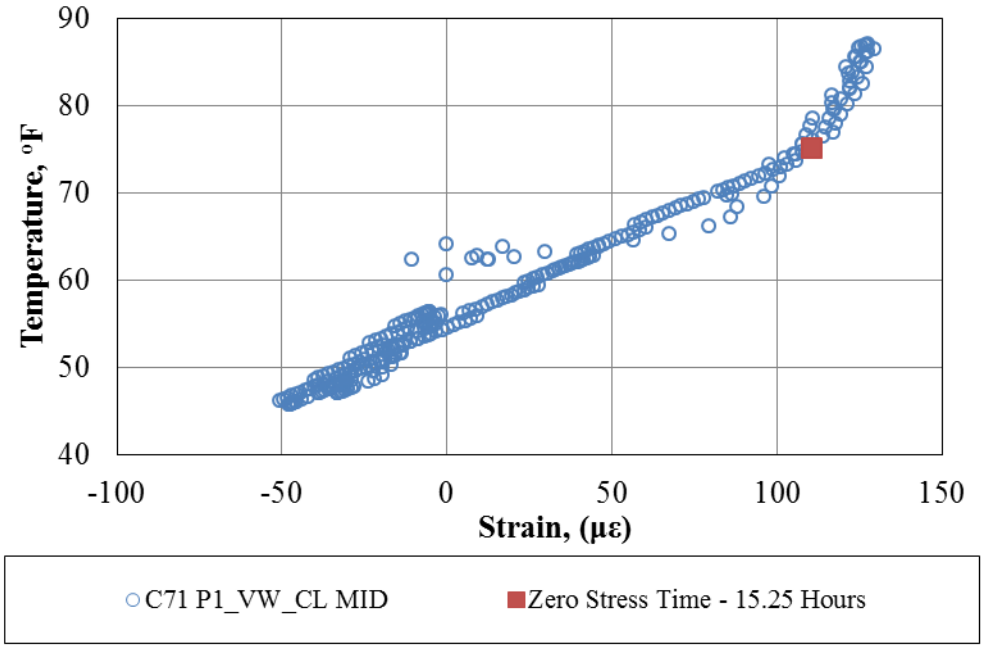

Figure 4.25: Zero Stress Time for Cell 71 Panel 1 Mid-Depth Centerline Location

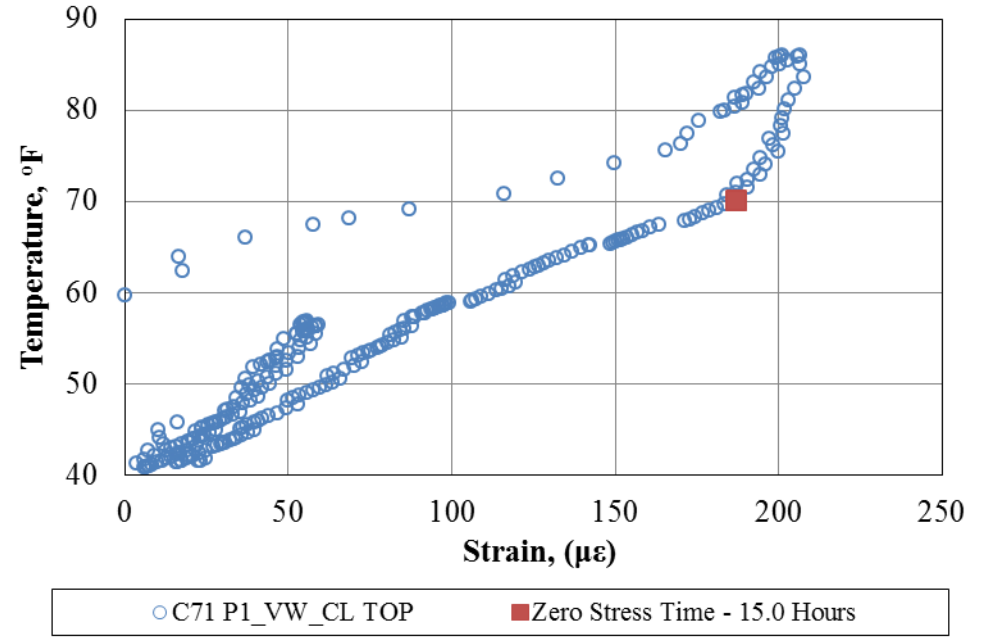

Figure 4.26: Zero Stress Time for Cell 71 Panel 1 Upper Centerline Location

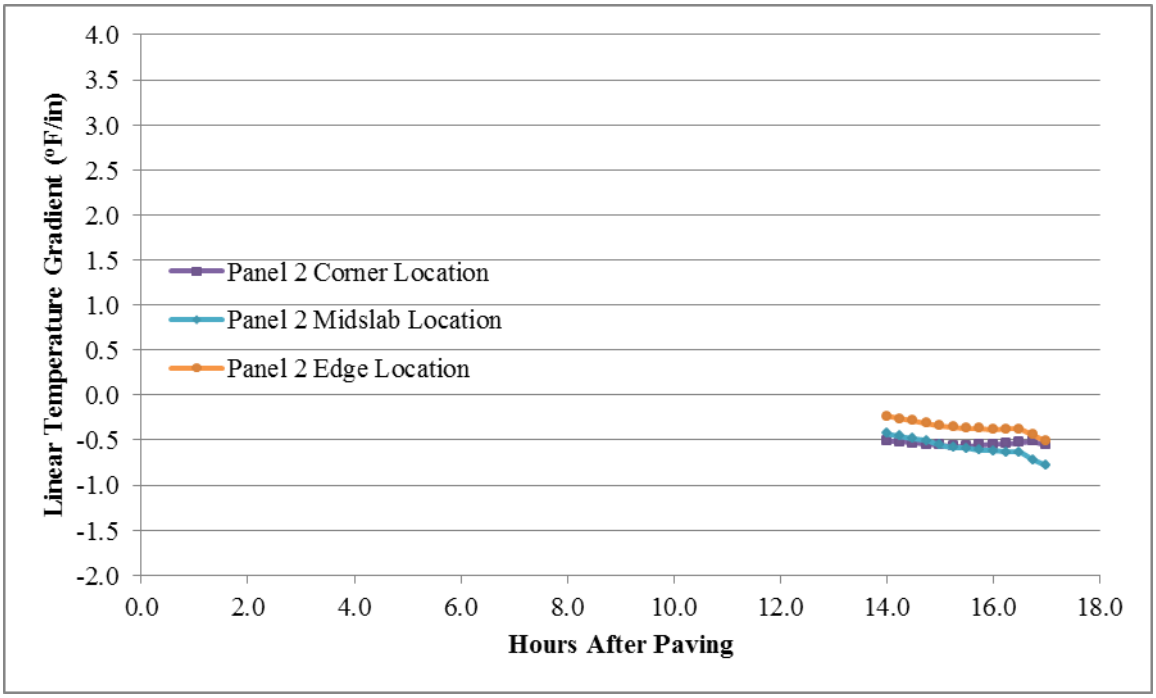

Figure 4.27: Thermocouple Temperature Gradient in Cell 71 after Paving

Figure 4.28 presents the weighted average temperature for the lower recycled concrete layer for Cell 71 throughout the times shown in Table 4.2. In Figure 4.28, it is remarkable that there is a significant difference in the weighted average temperature between locations. Figure 4.28 includes weighted average temperatures calculated using both thermocouple and vibrating wire thermistor data. Like with Cell 70, it was also found in Cell 71 that both the vibrating wire thermistors and thermocouples at the midslab location showed the highest value for the weighted average temperature. This is likely due to the relative insulation of this location compared to the edge and corner locations. Using the midslab location, the weighted average temperature in the lower recycled concrete layer over the range of potential zero stress times is approximately 81 to 77 ^{o}F.

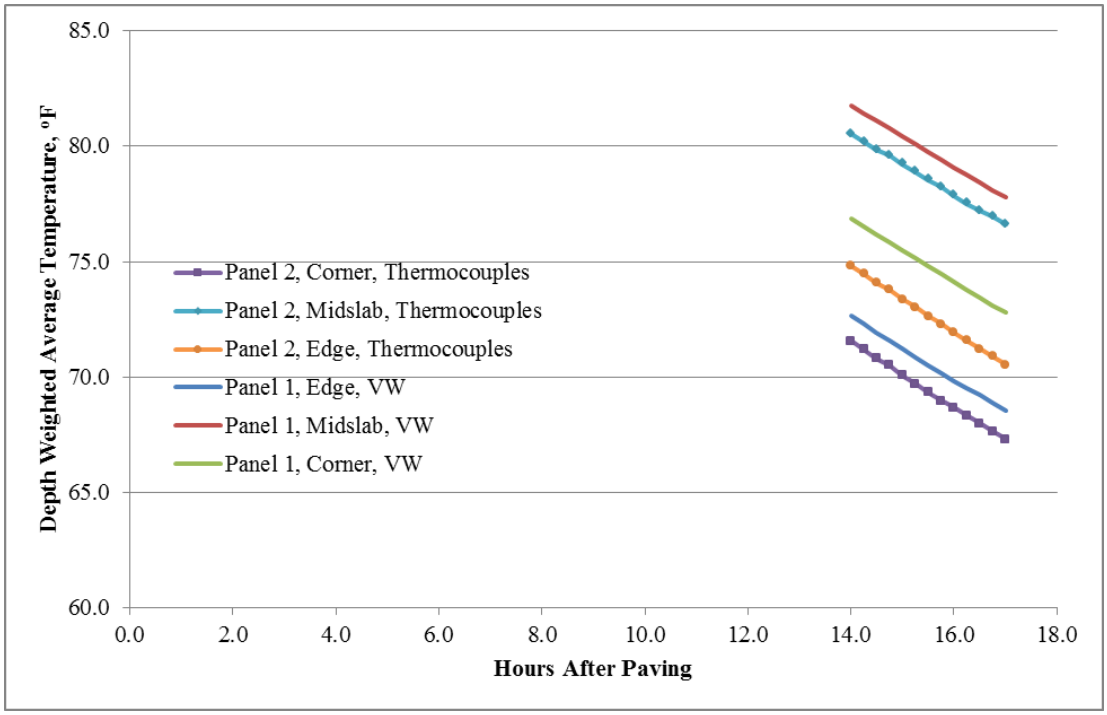

Figure 4.28: Weighted Average Temperature of Lower Recycled Concrete Layer after Paving

Figure 4.29 shows the range of the weighted average temperatures in the upper EAC layer of Cell 71 over the range of times established in Table 4.2. A similar location bias as was seen in the lower layer was observed. The range in the weighted average temperature over the time period of interest is less than that for the lower layer. The range of weighted average temperatures corresponding to the potential zero stress times are 77°F to 72°F.

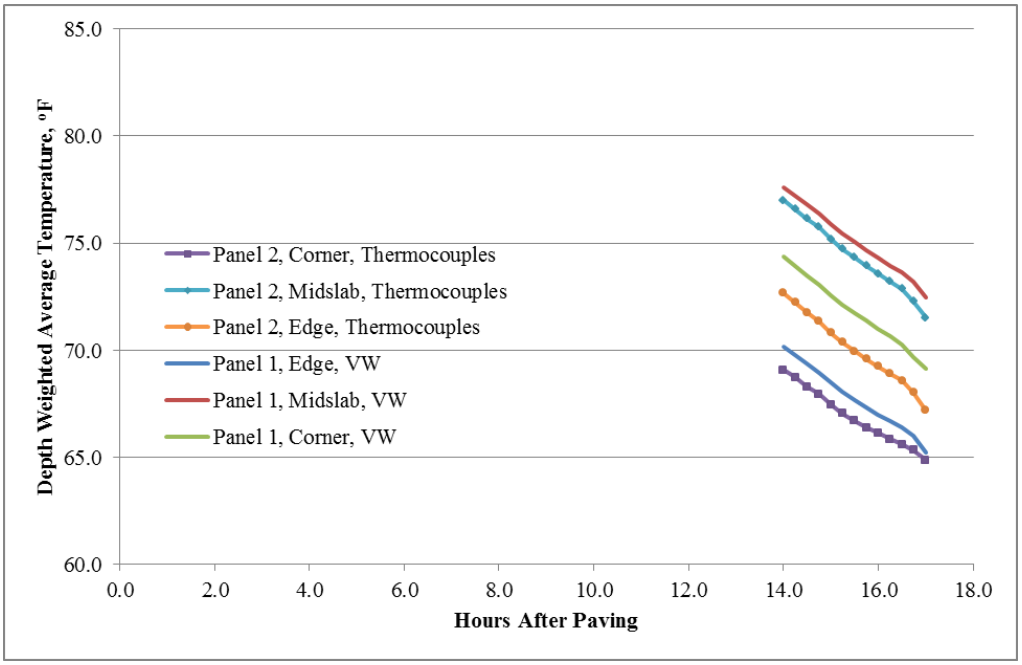

Figure 4.29: Weighted Average Temperature of Upper EAC Layer after Paving

4.1.3.3 Cell 72

Both the bottom economic mix concrete layer for Cell 72 and the upper EAC layer were constructed on the morning of May 10th 2010. The paver passed the instrumented cells at approximately 8:45 AM. Unfortunately, strain and thermistor data was not available to determine the zero stress time, built-in temperature gradient or the weighted average zero stress temperature.

Although this data was not available, some inferences can be made for Cell 72 using Figure 4.30. This figure shows the thermocouple temperatures for Cell 72 after paving and starting with the time that the concrete encompassed the sensors. The thermocouples from which the data was taken were located at the middle of each of their respective layers. From Figure 4.30, it can be seen that the temperature in both the upper EAC mix and lower economic mix rises in temperature despite a drop in ambient temperature. This temperature rise is due to the

hydration of the concrete. Since the zero stress temperature occurs after the peak hydration temperature, it can be estimated from Figure 4.30 that the zero stress times for Cell 72 lies somewhere between 16 and 20 hours after paving. The linear temperature gradient calculated based on the thermocouple readings over the time period of 16 to 20 hours after paving, shows that the potential variation in the linear temperature gradient is approximately between -0.5°F/in and -1.0°F/in. The average value is -0.6oF/in. The weighted average temperature over the same time period for both the lower economic mix layer and upper EAC layers are shown in Figure 4.29. These temperatures range from 66°F to 63°F for the lower economic mix layer and from 64°F to 58°F for the upper EAC layer.

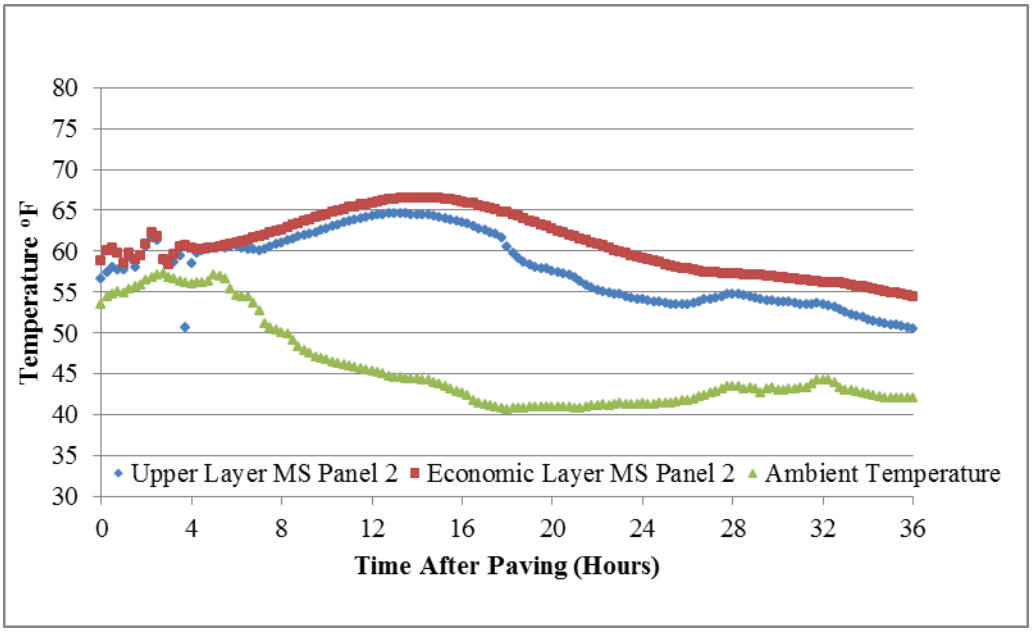

Figure 4.30: Thermocouple Readings for 72 Hours after Paving - Cell 72 Panel 2 Midslab

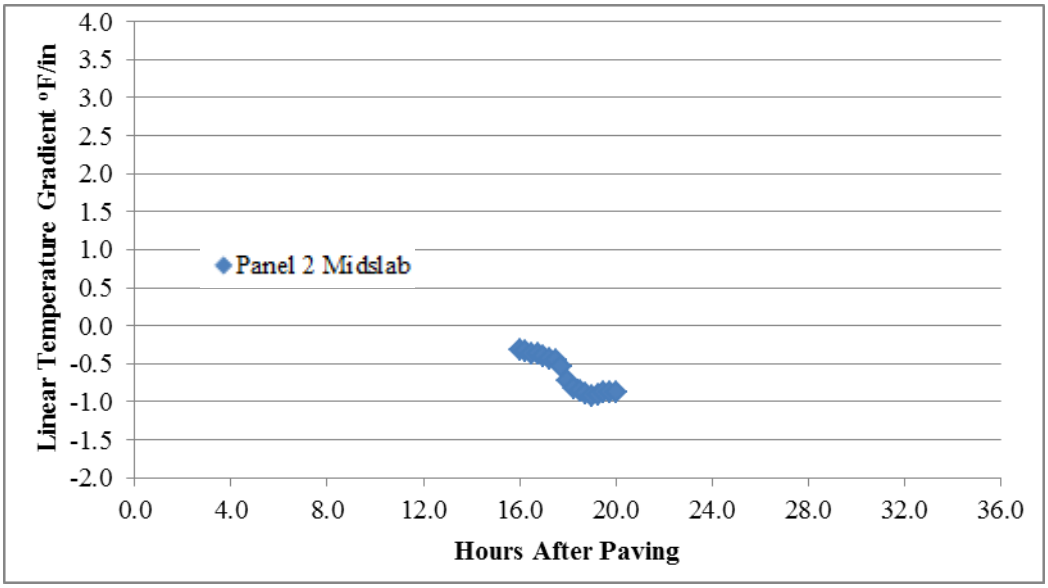

Figure 4.31: Linear Temperature Gradient over Hypothesized Time for Zero Stress Time

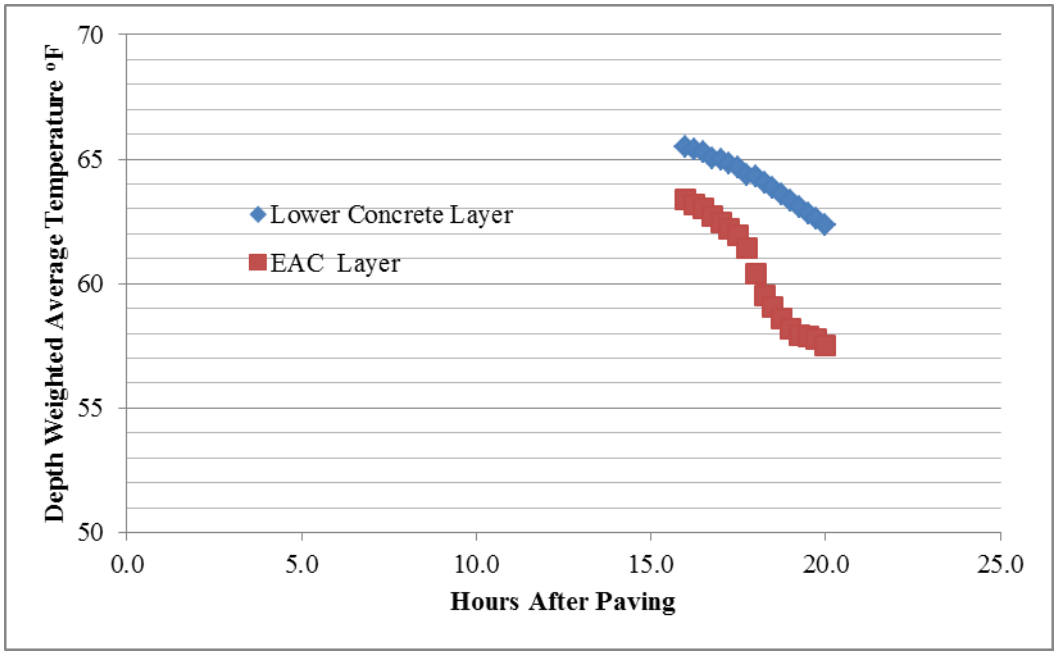

Figure 4.32: Weighted Average Temperature for Each Layer over Hypothesized Zero Stress Time

4.1.3.4 Comparison of zero stress condition between cells

Although this analysis was performed on a cell by cell basis, comparisons can also be made between cells to further assess the validity of these findings. For Cell 70 and Cell 71, the same lower layer was used, namely the recycled concrete layer. For Cell 71 and Cell 72, the same upper layer was used, namely the EAC layer.

Considering the uncertainty regarding the built-in conditions in Cell 72, perhaps the most remarkable difference between any of the cells was the difference in the strain temperature relationship and range of potential zero stress times between Cell 70 and Cell 71. For Cell 70, the strain vs. temperature relationship figures were not very helpful in establishing the zero stress time while the results obtained from the curvature vs. time figures showed significant variation. The difference between the cells necessitates an explanation considering that the mixes used in each instance were the same.

As mentioned in Section 4.1.3.1, part of the difference between Cells 70 and 71 was believed to be due to the hydration history of the two mixes. Figure 4.33 attempts to capture this difference. In Figure 4.33, the variation of thermistor temperature with time at the midslab, bottom location is shown for Cells 70 and 71. Also depicted in Figure 4.33 are the ambient temperature conditions following paving for both cells.

In Figure 4.33, the difference between the thermistor temperature and the ambient temperature can be used as a proxy for heat from hydration for each cell. In the first 72 hours after paving, the difference between the concrete temperature and ambient temperature for Cell 71 decreases over time. This is noticeably different than the behavior of Cell 70 where the difference between the concrete and ambient temperature remains relatively constant. In stages 3 and 4 of hydration, while significant heat is being generated by the concrete, a decrease in the

concrete temperature relative to the ambient temperature may be interpreted as an indicator that the hydration is slowing. A steady difference between the concrete and ambient temperature may indicate that hydration is still proceeding at a significant rate because the exothermic reaction is preventing the concrete temperature from trending towards the ambient temperature.

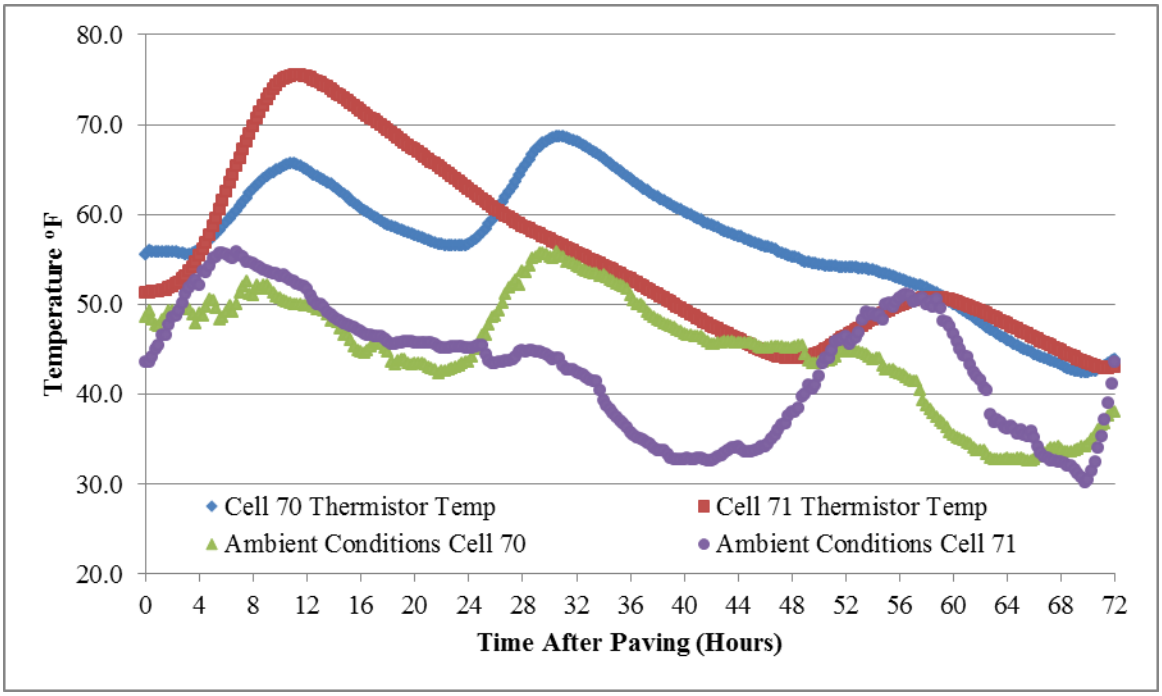

Figure 4.33: Recycled Layer Midslab Bottom Temperatures for 72 Hours after Paving

As can be observed in Figure 4.33, the difference in the concrete and ambient temperature early on is much more pronounced in Cell 71. This observation indicates that more hydration is going on in Cell 71 relative to Cell 70. The possibility of this observed difference to be attributable to mix related factors is unlikely. No significant difference in the mixes was observed based on analysis of the batch slips.

When paving Cell 70, as can be seen in Figure 4.33, the ambient temperature was relatively constant at around 50°F for the first 16 hours after paving. For Cell 71, however, the temperature started off cooler, around 45°F at the beginning of the day, and then increased in the middle of the day to around 55°F. The temperature then dropped down to approximately 50°F about 16 hours after paving.

In addition to temperature, other environmental influences on the hydration reaction of concrete, such as solar radiation and wind speed, were investigated. The solar radiation and wind speed for the day of paving for both Cell 70 and Cell 71 are shown in Figure 4.34 and Figure 4.35, respectively. From these figures, it is apparent that when Cell 70 was paved it was less sunny and also windier. Both factors would serve to slow the hydration reaction relative to Cell 71, which experienced more sunshine and less wind during the day of paving.

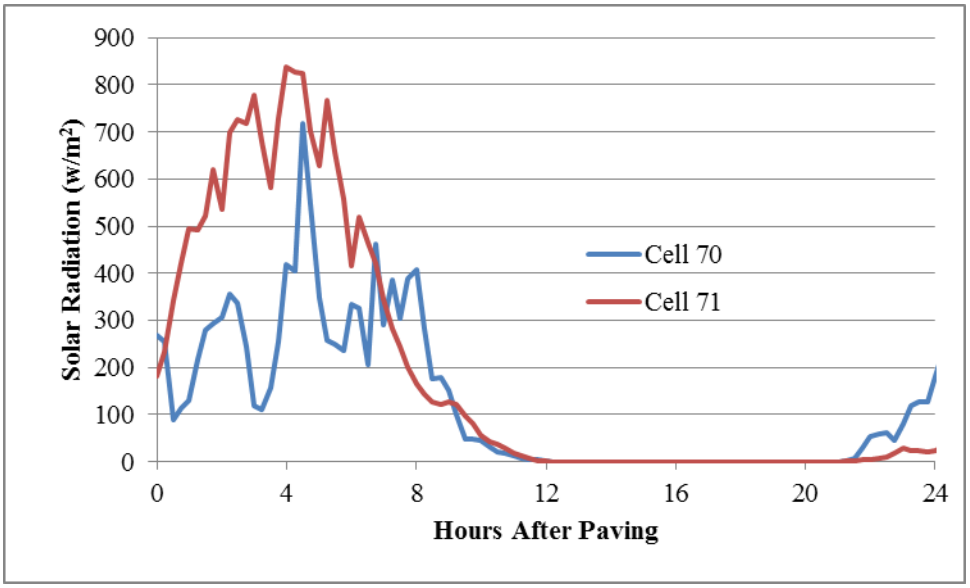

Figure 4.34: Solar Radiation after Paving for Cells 70 and 71

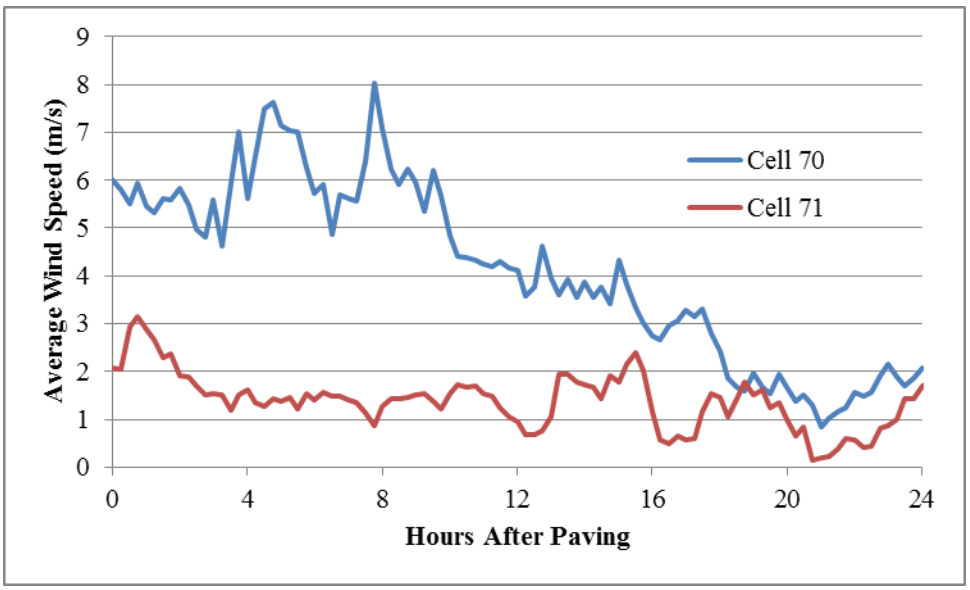

Figure 4.35: Wind Speed after Paving for Cells 70 and 71

One other important factor affecting the apparent hydration between Cell 70 and Cell 71 is that the temperature reading for Cell 71 is obtained at a location with approximately 8 in of concrete cover while the corresponding reading for Cell 70 only has 5 in of concrete cover. This is due to the fact that the 3 in AC layer was not placed on Cell 70 until May 20th. For Cell 71, the entire pavement thickness of 9 in was placed on May 6th.

Considering these differences, another way to relate the zero stress temperature between Cells 70 and 71 is by considering the degree of hydration at any given time. One indicator of degree of hydration is concrete maturity. Maturity of concrete is simply the integral of the time temperature curve above a given reference temperature. This reference temperature is commonly taken as 14^{o}F. Since there was more uncertainty regarding the zero stress time determined for Cell 70, the maturity of the concrete in Cell 71 at the zero stress time was used to comment on the potential for narrowing the range of zero stress times found in Section 4.1.3.1. Figure 4.36 shows the maturity of the concrete against the time after paving. From Figure 4.36, it is apparent

that the more appropriate value in the range of zero stress times determined for Cell 70 in Table 4.1 is towards the upper end of the range, around 18 to 20 hours. This further justifies the choice of -0.75°F/in for the built-in temperature gradient for Cell 70.

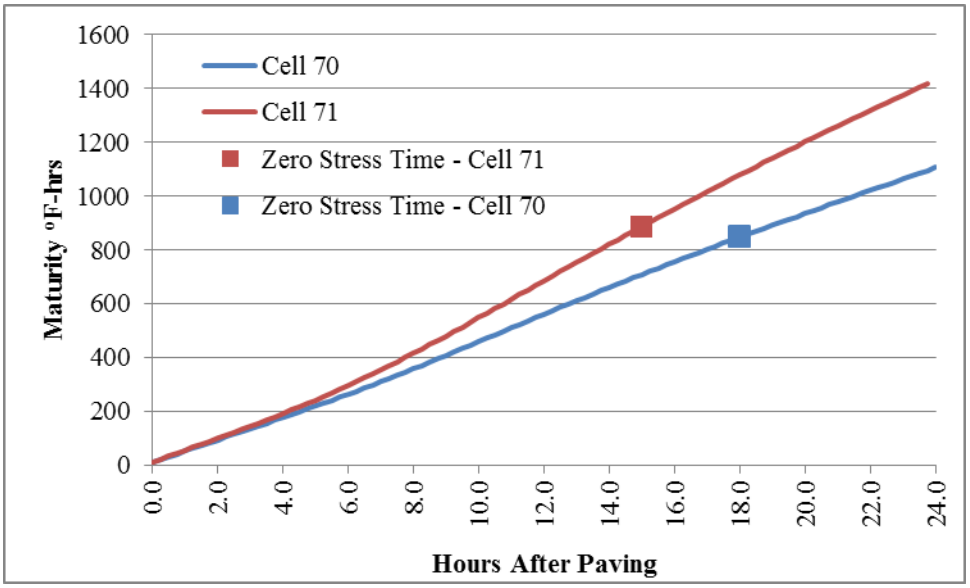

Figure 4.36: Comparison of Concrete Maturity at Zero Stress Time

4.1.3.5 Built-in warping

The effect of differential moisture conditions between the top and the bottom of the slab results in differential drying shrinkage. This drying shrinkage, which is more prevalent at the top of the slab, where there is often less moisture available, has the effect of causing the slab to deform differentially. Like the deformation caused by a temperature differential between the top and bottom of the slab, a moisture differential also results in the slab assuming a curved shape. Unlike a temperature differential between top and bottom, the differential deformation caused by moisture gradients works only to cause the slab ends to deform upward. This is because in the

case of a moisture gradient, it is always the top of the slab that contracts relative to the bottom of the slab. When slab curvature is caused by moisture effects, it is known as warping.

For fresh concrete, the moisture profile throughout the depth of the slab has been shown to be such that at the zero stress time, the moisture profile is completely saturated throughout the depth of the slab [7]. Since this is the case, there is no moisture gradient that must be considered when determining the built-in construction gradient. For the MnROAD cells, the moisture gradient present in the slab at the zero stress time can be observed in Figure 4.37, Figure 4.38, and Figure 4.39. The lack of a moisture gradient at the zero stress time is confirmed through these figures. Figure 4.37 through Figure 4.39 show all depths having relative humidity values higher than 95 percent at the zero stress time.

Although drying shrinkage can occur at any relative humidity below 100 percent, its does not generate significant stresses at relative humidity levels above 95 percent. In this range of relative humidity, water is only being removed from the capillary pores. The capillary stress generated is small because of the relatively large surface to volume ratio of capillary pores [9].

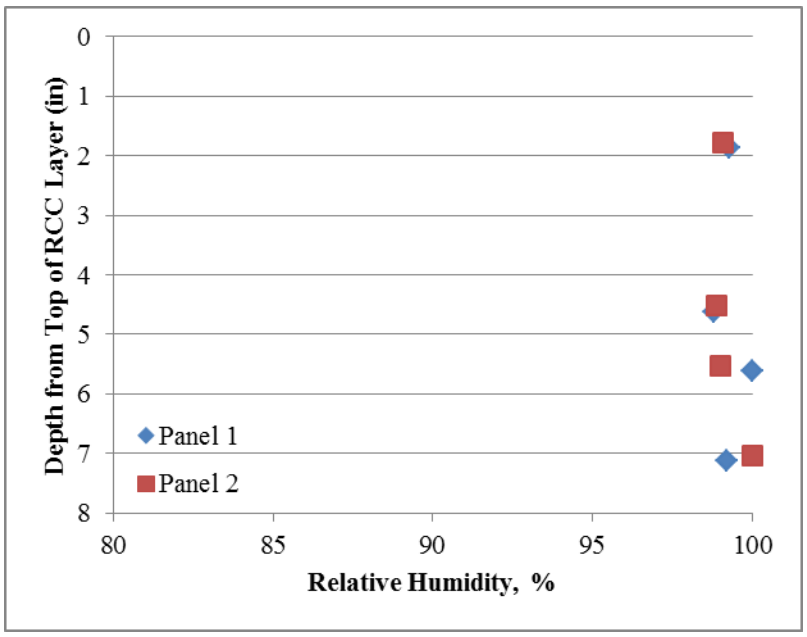

Figure 4.37: Moisture Gradients in Cell 70 at the Zero Stress Time

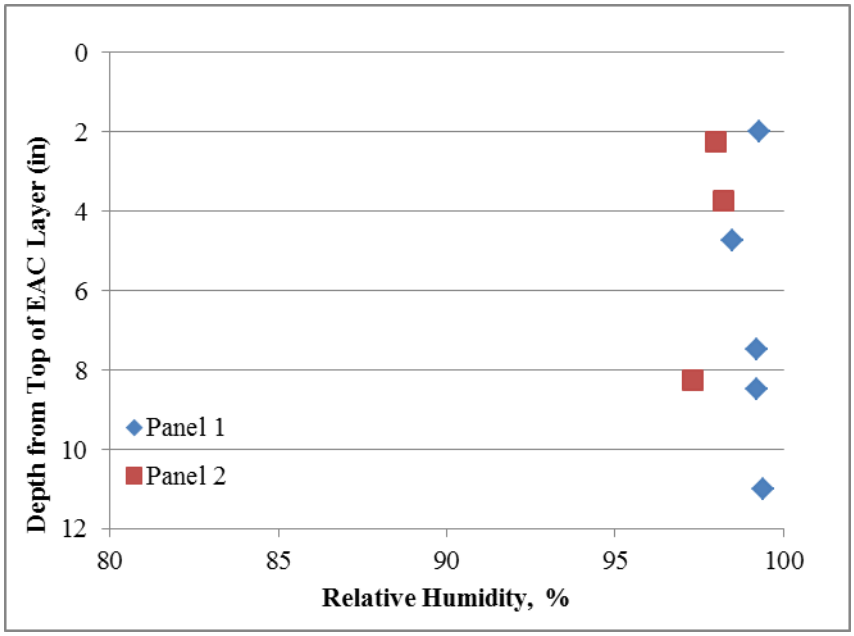

Figure 4.38: Moisture Gradients in Cell 71 at the Zero Stress Time

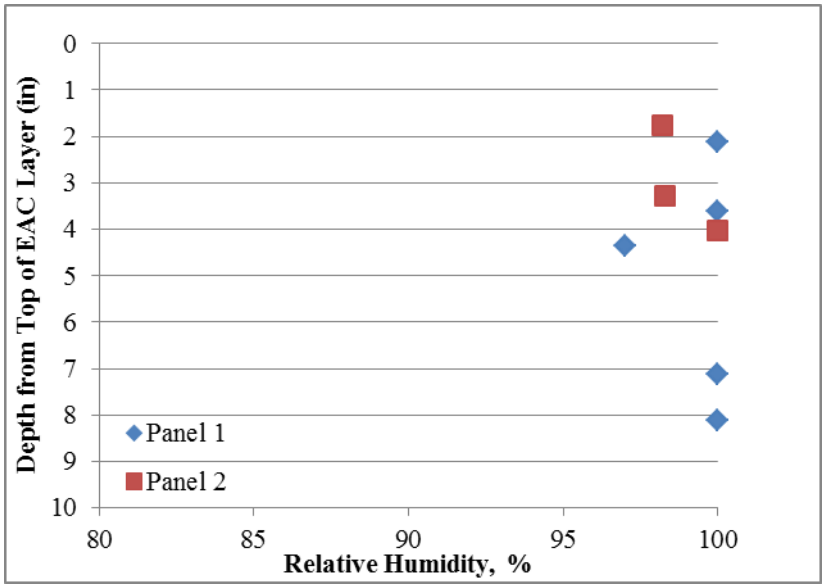

Figure 4.39: Moisture Gradients in Cell 72 at the Zero Stress Time

The built-in construction gradient in a PCC slab consists of the temperature and moisture gradient present in the slab at the zero stress time. Since the built-in moisture gradient is zero, the built-in construction gradient can be characterized by the temperature gradient in the slab at the zero stress time. The estimate of the built-in temperature gradient, as well as the weighted average temperature for each layer of each cell was made in the previous sections.

4.2 CHARACTERIZATION OF TEMPERATURE GRADIENTS

This section assesses the temperature regimes that developed throughout the three different composite pavements constructed at MnROAD. As was highlighted in Chapter 2, different temperature regimes will induce different stresses and causes different curvature in each structure. Two primary analyses are performed as part of this work. First, the measured

temperatures are assessed so as to comment on measurement irregularities, spatial variation of temperature throughout the slab, and to compare the fundamental differences in the temperature profiles that develop between the cells. Secondly, the effects of the pavement structure are incorporated. This is done through the calculation of the equivalent linear temperature gradient considering both the specific structures of Cells 70, 71, and 72 as well as other hypothetical structures.

4.2.1 Variation With Respect to Location

For each cell, temperature profiles were available throughout the depth of the slab at three replicated locations in two adjacent slabs. This makes it possible to assess differences between the temperature profiles that develop at each location. In Section 4.1.3, it was found that at the zero stress temperature, there was significant variation in the weighted average temperature as a function of location. The boundary conditions at that point in time are quite different than the boundary conditions that would be present throughout the life of the pavement however. Most notably, after construction, and before opening the road to traffic, shoulders were placed. This modification of the pavement structure, relative to the construction condition, provides more insulation to the sides of the pavement. Also, at the zero stress time there is still heat being released due to hydration. This heat will be retained at the interior of the slab more so than at the slab periphery. Throughout the service life of the pavement, the temperature distribution throughout the slab is completely dictated by the environment since the heat generated due to hydration has diminished.

Although the temperature gradient in the slab is generally the point of interest for stress analysis, the only way that the temperature gradient in the slab could differ between locations is

if the boundary conditions between locations were different. The difference in boundary conditions can therefore also be assessed using the weighted average temperature. The weighted average temperature is also a more inclusive parameter as compared to the linear temperature gradient since it includes measurements from all of the thermocouples in the slab rather than just those at the top and bottom.

To assess the spatial variation in the temperature in the slab after the zero stress time occurs, and the shoulders are placed, the weighted average temperature of the concrete layer for each of the three cells was calculated over a representative day, specifically July 19, 2010. On this day large temperature gradients developed. The weighted average temperature at all the available thermocouple locations for Cells 70, 71, and 72 are shown in Figure 4.40, Figure 4.41, and Figure 4.42 respectively.

For Cell 70, although there is a good match between all of the locations throughout the majority of the day, it seems that the weighted average temperature increases more in the late afternoon at the midslab location and remains warmer after the sun goes down in the evening. Interpretation of the available depth information as shown in Table 4.3 does not shed light on possible reasons for the discrepancy because the available information shows that the depths of the sensors are relatively the same for every location. Other than sensor depth, there is no other perceivable cause for this observation. Depth could still be an influencing factor however since the available depth information seems questionable.

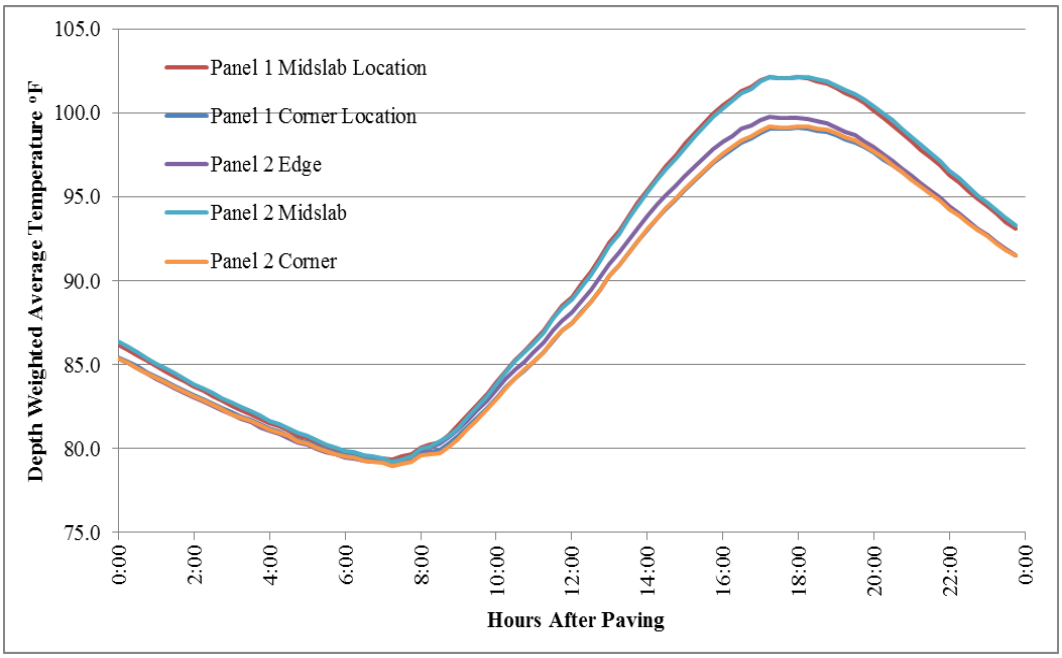

Figure 4.40: Weighted Average Temperature for RC Layer at Various Locations for Cell 70 on July 19, 2010

Table 4.3: Depth for Thermocouples in Cell 70

Cell 70 Thermocouple Depths, in					
Panel 1			Panel 2		
Corner	Midslab	Edge	Corner	Midslab	Edge
3.75	3.75	3.75	3.75	3.95	4.04
4.25	4.25	4.25	4.25	4.45	4.54
6.25	6.25	6.25	6.25	6.45	6.54
8.25	8.25	8.25	8.25	8.45	8.54
9.25	9.25	9.25	9.25	9.45	9.54

Unlike in Cell 70, the weighted average temperature calculated at different locations within Cell 71, and as shown in Figure 4.41, does not seem to show variation with respect to location. For Cell 72, there again seems to be variation with respect to location, except for Cell 72 the weighted average temperature of the midslab location seems somewhat lower than the other locations. Available depth information, shown in Table 4.4 does not provide helpful information for interpreting this observation.

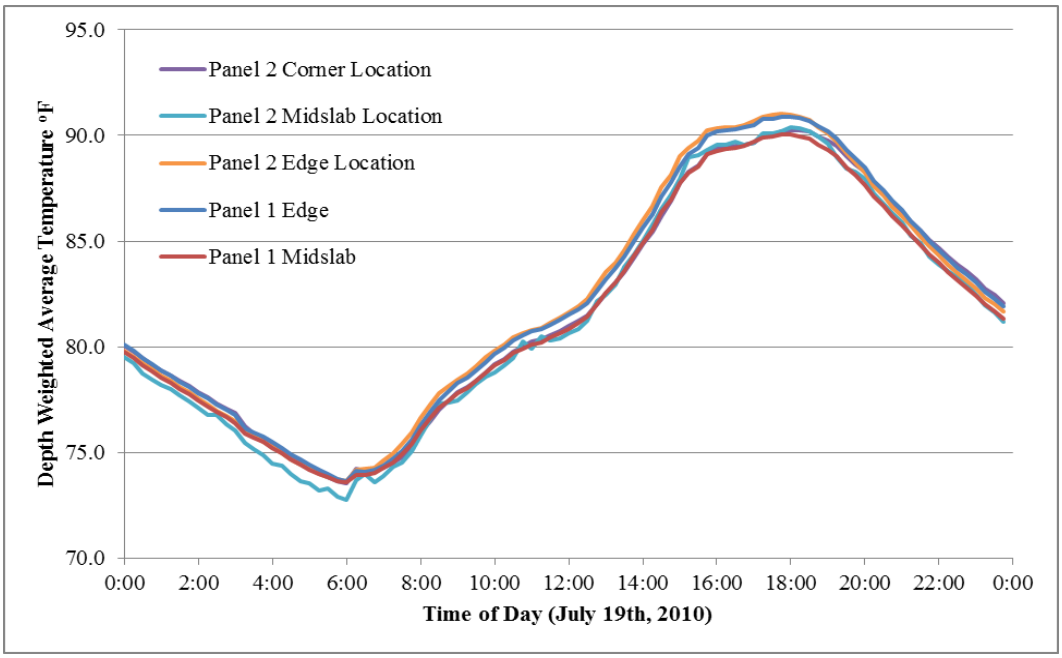

Figure 4.41: Weighted Average Temperature at Various Slab Locations for Cell 71 on July 19, 2010

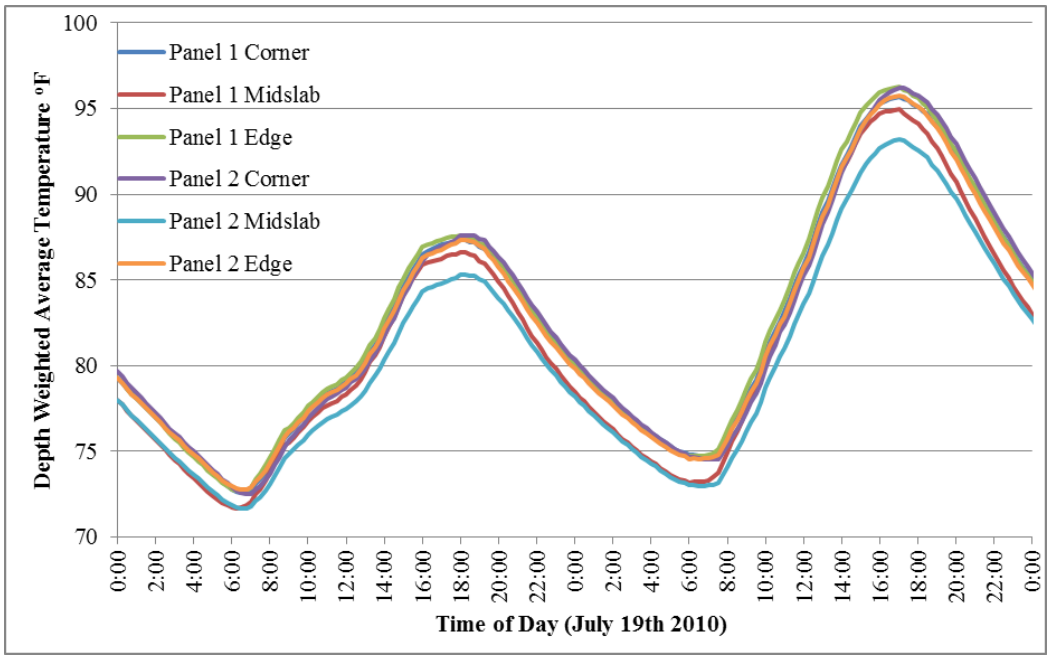

Figure 4.42: Weighted Average Temperature at Various Slab Locations for Cell 72 on July 19, 2010

Table 4.4: Depths for Thermocouples in Cell 71 and Cell 72

Cell 71 and Cell 72					
Panel 1			Panel 2		
Corner	Midslab	Edge	Corner	Midslab	Edge
0.75	0.75	0.75	0.75	0.75	0.75
1.75	1.75	1.75	1.75	1.75	1.75
2.75	2.75	2.75	2.75	2.75	2.75
3.75	3.75	3.75	3.75	3.75	3.75
4.25	4.25	4.25	4.25	4.25	4.25
6.25	6.25	6.25	6.25	6.25	6.25
8.25	8.25	8.25	8.25	8.25	8.25
9.25	9.25	9.25	9.25	9.25	9.25

Based on a comparative analysis of the variation of temperature with location, it was found that no consistent relationship existed between the cells with respect to spatial variation in the weighted average temperature. Because of the inconsistencies in the relationship between the weighted average temperatures of the three cells, in addition to the uncertain depth information, no definitive conclusions can be drawn on spatial variation of temperature throughout the slab. Despite this conclusion, it can be seen that in general, the location within the slab shows good agreement between adjacent panels. It also appears that there is no definitive location that should be used for interpreting the temperature gradients that develop between cells.

4.2.2 Magnitude of Linear Temperature Gradients

Because of the significance of the temperature gradients that develop in a pavement with respect to stress, the magnitude and frequency of the temperature gradients that developed in the cells at MnROAD were assessed. In order to facilitate both an assessment of each individual cell, and a comparison between cells, histograms of the weighted average temperature and the linear

temperature gradients were constructed. Material parameters influencing the temperature distribution in a concrete pavement were mentioned in Section 2.3.2. These include surface shortwave absorptivity, thermal conductivity, and specific heat. In addition, the depth within the slab of each of the sensors influences its value and variation.

The first assessment that was performed with respect to temperature gradient magnitude was a comparison between Cells 71 and 72. This assessment was made to examine potential differences with respect to the thermal gradients that developed. For Cell 72, errors in the data collection made data before 7/16/10 and data between 12/6/10 and 3/14/11 unusable. Only times with valid data were therefore assessed

Based on the available data range, the statistics in Table 4.5 were obtained for the weighted average temperature. It is evident that the statistics agree better between panels within a given cell than between cells. It can also be seen in Table 4.5 that there is a larger range and more variation in the weighted average temperature when comparing Cell 71 to Cell 72. This systematic variation, especially with respect to the standard deviation of the weighted average temperature, could be attributed to the depths of the sensors rather than any fundamental difference between the two cells. In terms of analyzing these results with respect to depth, the depths of these sensors would be required. Unfortunately, available data regarding the as-built depths of the sensors indicate that all of the sensors are at the same depth and is believed to be erroneous. Despite the missing depth information, the calculation of the weighted average temperature is not affected. The weighted average temperature is only a function of the relative distance between sensors. The as-built relative distance can reasonably be assumed to be correct since the thermocouple trees were constructed to ensure the proper distance between the thermocouples.

Considering the data presented in Table 4.5 it might be concluded that the upper layer was somewhat thicker in Cell 72 than Cell 71. This conclusion could potentially account for the decreased maximum temperature, increased minimum temperature, and smaller variation seen in Cell 72 relative to Cell 71.

Table 4.5: Weighted Average Temperature Statistics for Cell 71 and Cell 72

	Temperatures, ^{o}F			
	71 - Panel 1	**71 - Panel 2**	**72 - Panel 1**	**72 - Panel 2**
Average	62	62	60	60
Maximum	104	106	98	96
Minimum	16	15	15	16
Standard Deviation	21	21	19	19
Median	63	63	62	62

Figure 4.43 through Figure 4.46 and Table 4.6 summarize statistics from the histograms of the linear temperature gradient distribution in Cell 71 and Cell 72. From these figures and Table 4.6, it is apparent that, although there is variation between panels within the same cell, there is also a systematic variation between the two cells. The variation between the two cells is more apparent with respect to the standard deviation of the linear temperature gradients. A higher standard deviation with respect to linear temperature gradients indicates Cell 71 seems to experience more severe temperature gradients more frequently. This can also be attributed to the depth of the sensors and its effect on the weighted average temperature in each slab. If the top sensor in Cell 72 is deeper in the pavement structure than the corresponding sensor in Cell 71, the magnitude of the linear temperature difference that develops is bound to be reduced.

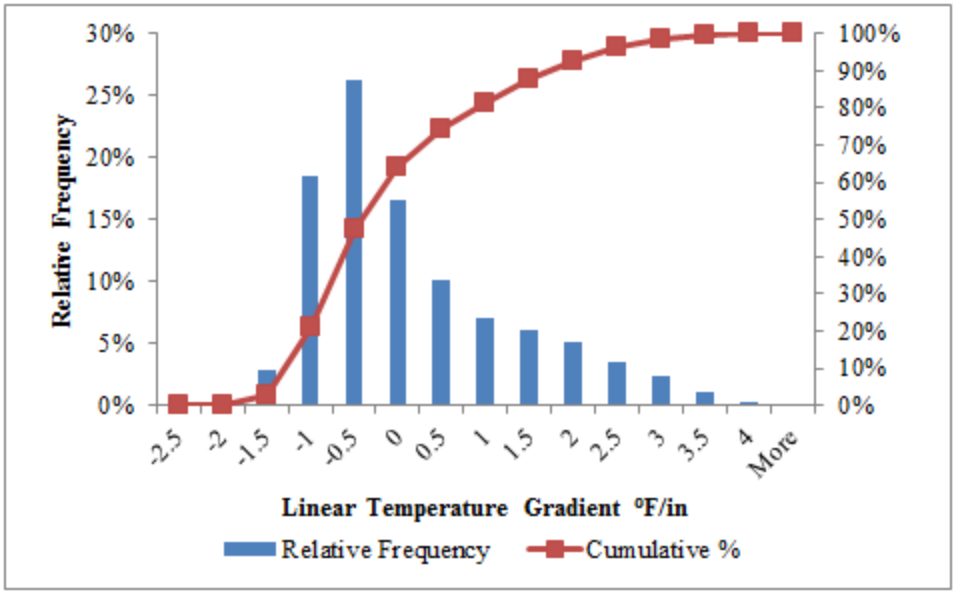

Figure 4.43: Linear Temperature Gradient Distribution - Cell 71 Panel 1

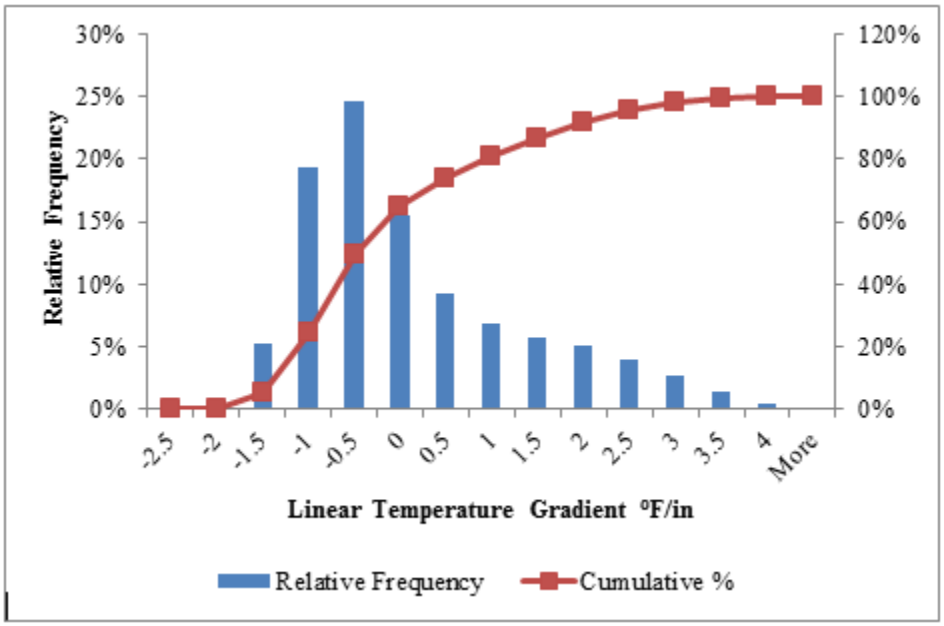

Figure 4.44: Linear Temperature Gradient Distribution - Cell 71 Panel 2

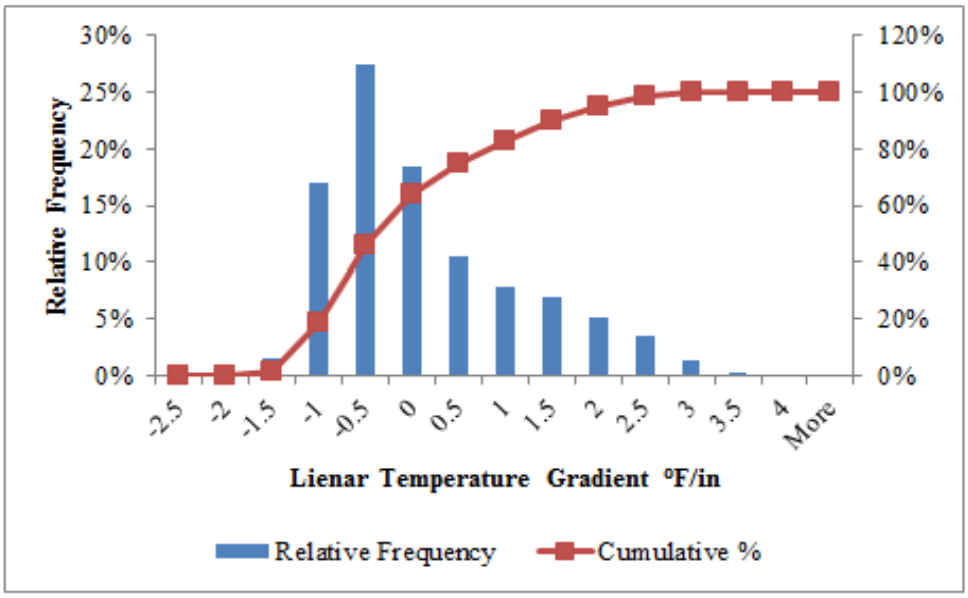

Figure 4.45: Linear Temperature Gradient Distribution - Cell 72 Panel 1

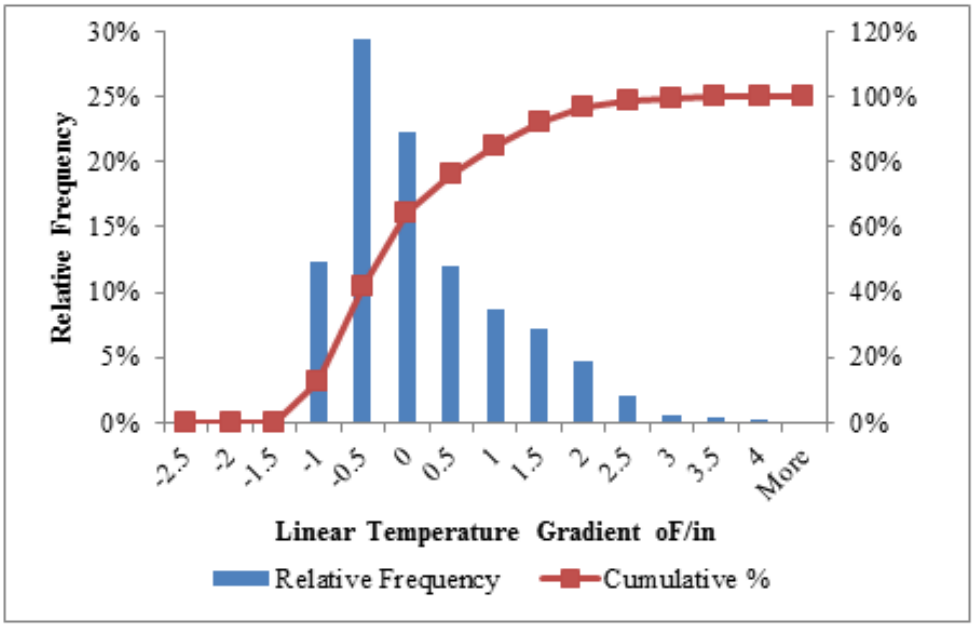

Figure 4.46: Linear Temperature Gradient Distribution - Cell 72 Panel 2

Table 4.6: Linear Temperature Gradient Statistics Comparing Cells 71 and 72

Linear Temperature Gradients ^{o}F/in	**71 Panel 1**	**71 Panel 2**	**72 Panel 1**	**72 Panel 2**
Average	-0.09	-0.10	-0.10	-0.09
Standard Deviation	1.14	1.22	1.04	0.93
	Cell 71		**Cell 72**	
Average	-0.09		-0.10	
Standard Deviation	1.18		0.99	

Comparing the histograms for the LTG in Cells 71 and 72, it can be seen that the range and relative frequency at which the temperature gradients develop are similar for Cell 71 and Cell 72. It can also be seen that there is a slight difference in the variation between these two cells in terms of the magnitude of LTGs that develop. The cause of this variation however may be just as likely to be due to variation in the pavement thickness, depth of the sensors, or both. For comparison between the temperature gradients that develop in the composite concrete pavements and Cell 70, the data from Cell 71 will be used in the analysis. Cell 71 is believed to be advantageous for comparison since it does not have the data gaps associated with Cell 72. Characterizing the frequency distribution of the temperature differences between Cell 71 and Cell 70, as well as assessing the degree of non-linearity, provides a useful background for interpreting results of the stress analysis presented in Chapter 5.

As mentioned in Section 2.3.2, the overall curling of a concrete slab overlaid with HMA is dictated by the temperature gradient in the underlying concrete slab. This is due to the relatively lower stiffness of the HMA. Characterizing the temperature gradient in the underlying concrete slab is therefore the primary focus in this section for Cell 70. In Cell 71, the curling

induced by a temperature gradient, is caused by the temperature distribution throughout the entire slab depth. In assessing the temperature induced curling between these two cells, the LTG across the appropriate depth will be compared. Figure 4.47 through Figure 4.50 show the distribution of the linear temperature gradients in the concrete layer of Cell 70 and the entire slab for Cell 71. Table 4.7 compares the statistics of the distributions of linear temperature gradients. From Table 4.7 and Figure 4.47 through Figure 4.50, the linear temperature gradients that develop are less severe for Cell 70 than Cell 71. Additionally, most of the temperature gradients in both cells are negative. This is most likely a function of the time interval over which the data was analyzed. This time interval consists of May 2010 through March 2011. The fact that more of the data came from times when the subgrade was relatively warmer than the air (winter), likely resulted in more negative gradients being predominant.

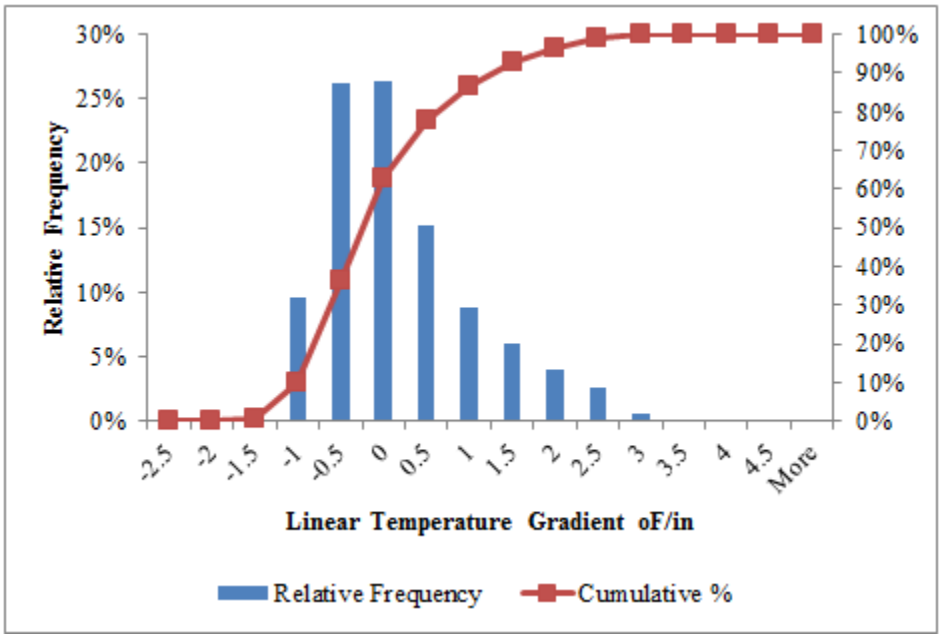

Figure 4.47: Linear Temperature Gradient Distribution - Cell 70 Panel 1

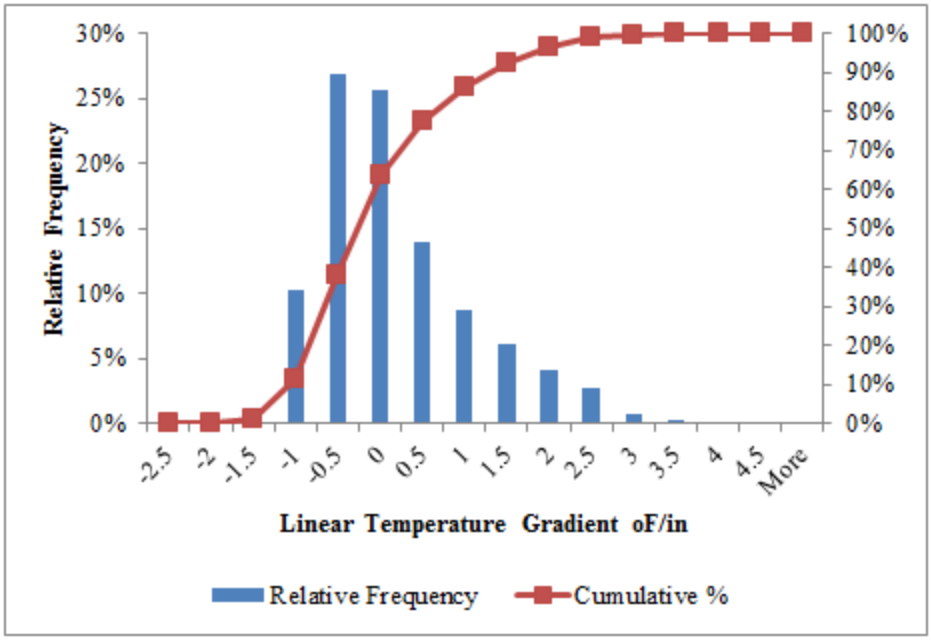

Figure 4.48: Linear Temperature Gradient Distribution - Cell 70 - Panel 2

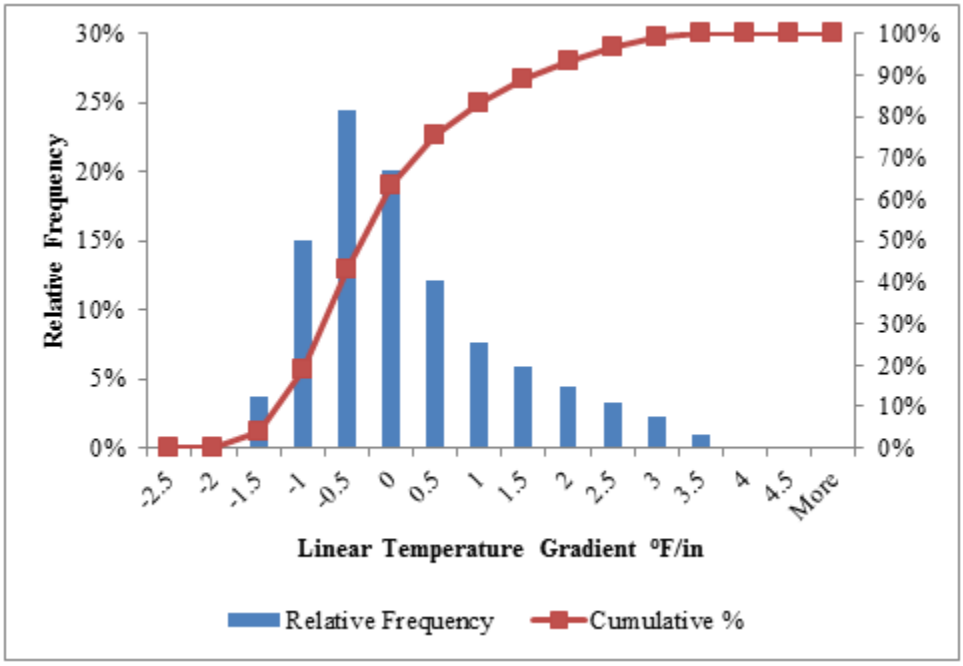

Figure 4.49: Linear Temperature Gradient Distribution - Cell 71 - Panel 1

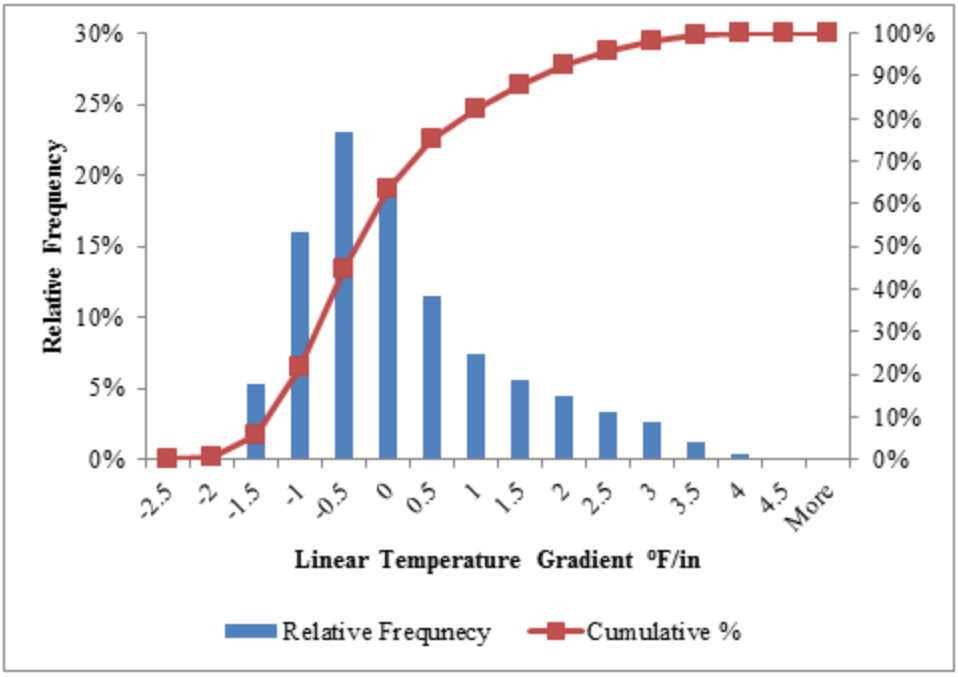

Figure 4.50: Linear Temperature Gradient Distribution - Cell 71 - Panel 2

Table 4.7: Linear Temperature Gradient Statistics Comparing Cells 70 and 71

	Temperature Gradients, °F/in			
	70 Panel 1	**70 Panel 2**	**71 Panel 1**	**71 Panel 2**
Average	-0.06	-0.08	-0.08	-0.09
Maximum	3.32	3.37	3.94	4.14
Minimum	-1.83	-1.97	-2.20	-2.26
Standard Deviation	0.88	0.90	1.10	1.17
Median	-0.27	-0.30	-0.36	-0.38

In addition to Table 4.7, Figure 4.51 provides a direct comparison between the frequency distribution of the two cells. The data representing each cell is an average of the two panels within each cell. For a single pavement subjected to the temperature gradients shown in Figure 4.51 and at the respective frequencies, there is a significant difference in the resulting stresses that would be generated due to the higher occurrence of relatively extreme temperature gradients

in Cell 71 as opposed to Cell 70. Specifically, Cell 71 has 203 percent more positive temperature gradients with a magnitude above 2°F/in and 191 percent more negative temperature gradients with a magnitude greater than 1°F/in relative to Cell 70.

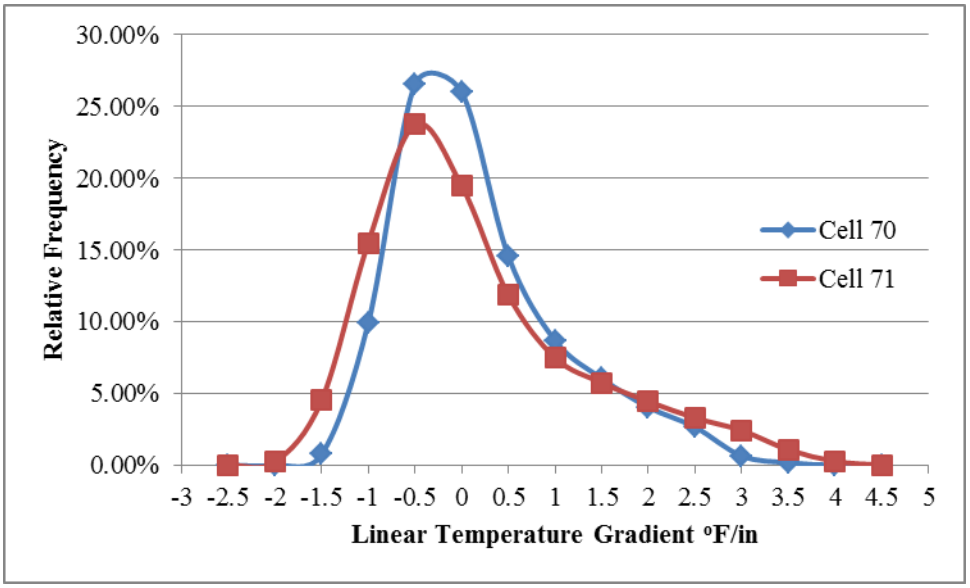

Figure 4.51: Comparison between Relative Frequencies for Temperature Gradients in Cells 70 and 71

4.2.3 Equivalent Linear Temperature Gradients

The previous section looked at the effect of the different composite pavement structures on the linear temperature gradients that developed in the pavements over almost eleven months. This analysis was done using only two temperature measurements, the temperatures at the top and bottom of the concrete layer. This was also performed irrespective of the pavements' structural properties. In Section 2.3.2.1, a formulation was presented for an equivalent linear temperature gradient in either a homogeneous or composite pavement. These equations, Equation 19 and

Equation 20, consider structural concrete properties, thermal concrete properties, and the variation of temperature with depth throughout the slab.

In this section, the first item to be addressed will be the relationship between pavement properties and the resulting non-linearity of the temperature profiles that develop in the composite pavements. Additionally, the role the pavement structures' engineering properties play on the ELTGs that develop will be assessed.

In pavements, the temperature distribution is the most non-linear in the upper portion of the slab. Since Cell 70 has HMA over the concrete, it is believed that the temperature distribution in the concrete slab will be more linear in Cell 70 relative to Cell 71 and 72. Figure 4.52 and Figure 4.53 illustrate the temperature gradients that developed over the same summer day in Cell 70 and Cell 71, respectively. It is clear from these figures that the deviation in the temperature profiles from a linear gradient is more pronounced in Cell 71.

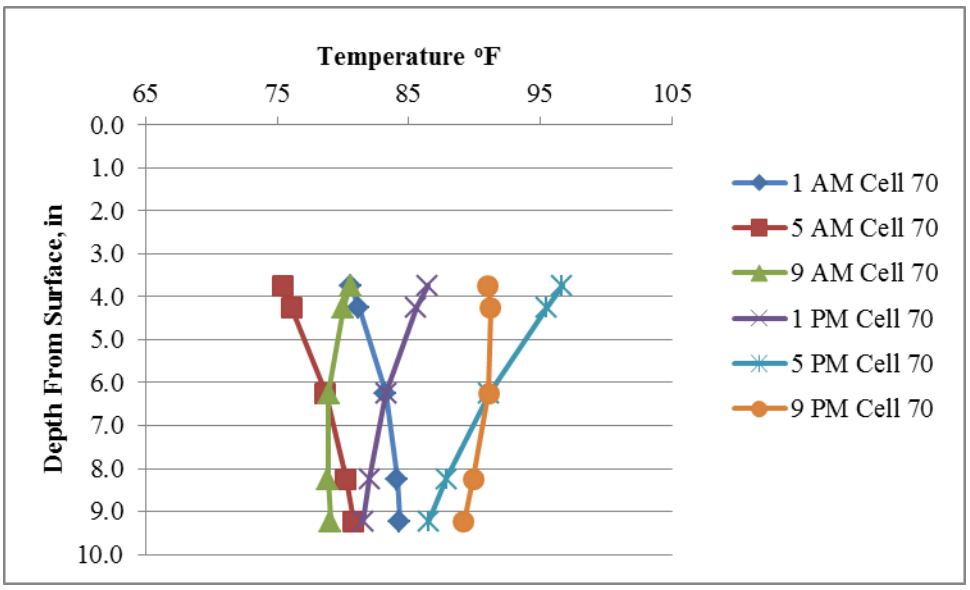

Figure 4.52: Temperature Gradients in Recycled Concrete Layer of Cell 70

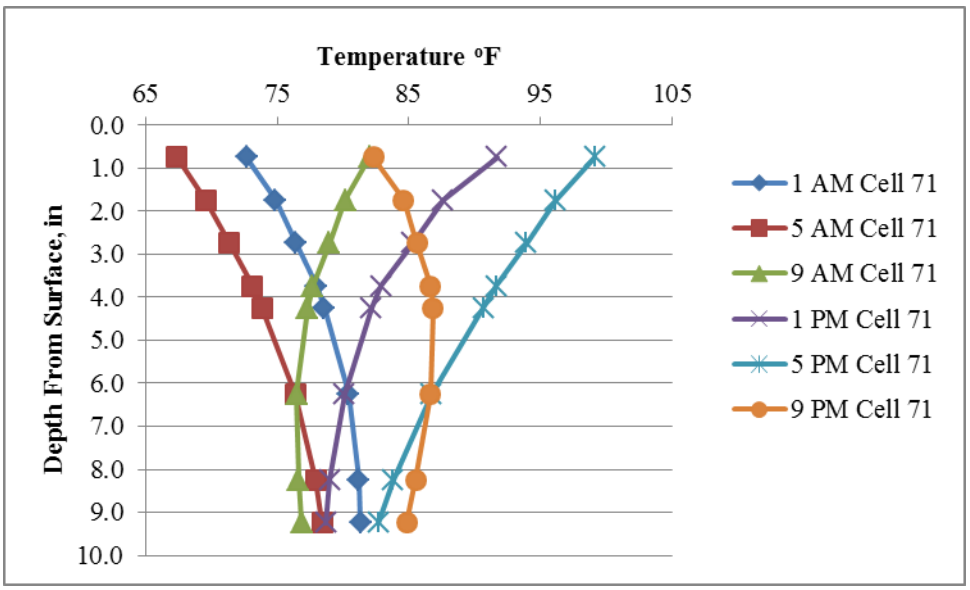

Figure 4.53: Temperature Gradients in Cell 71

The importance of the difference in the degree of linearity between the temperature profiles that developed in Cell 70 and Cell 71 can be captured by an assessment of the equivalent linear temperature gradient. Both the linear and equivalent linear temperature gradients that developed for a summer day in Cell 70 and Cell 71 are shown in Figure 4.54. A comparison between the linear temperature gradient and the equivalent linear temperature gradient for Cell 70 shows relatively close agreement. For Cell 71, two series were generated for defining the equivalent linear temperature gradient. The "Cell 71 Homog" series was generated considering a homogeneous pavement with one reference temperature throughout the depth. The "Cell 71 Comp" series was generated considering the actual material properties and built-in temperature gradient measured for Cell 71 as well as the respective layer reference temperatures at the zero stress time. Neither the Cell 71 "Homog" or "Comp" series shows as good agreement to the Cell 71 LTG as is observed between the Cell 70 ELTG and LTG.

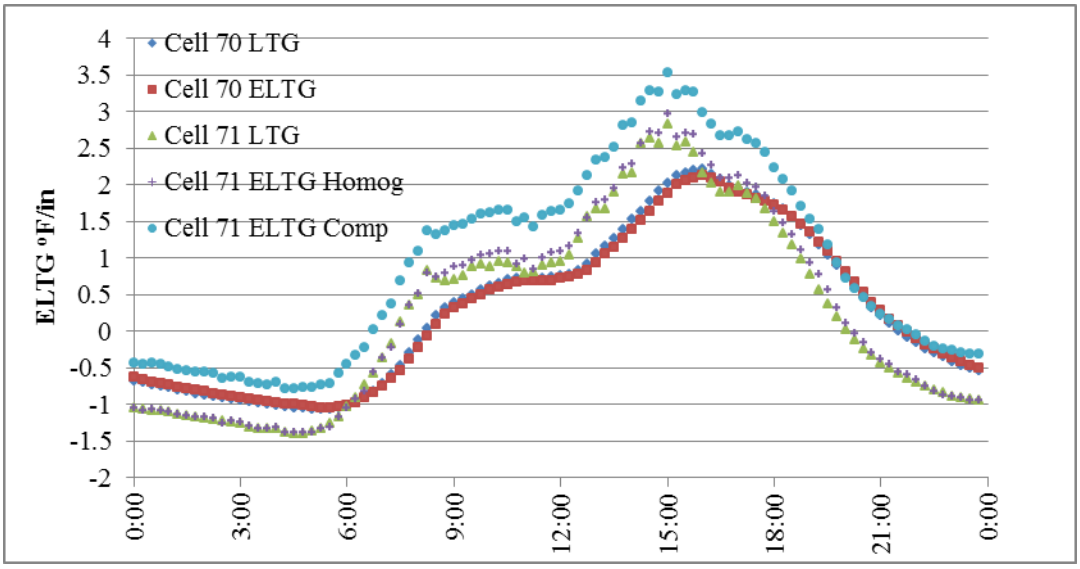

Figure 4.54: Comparison of Linear and Equivalent Linear Temperature Gradients for Cell 70 and Cell 71

For the three composite pavements, histograms of the ELTGs that developed over the entire eleven month analysis period are shown in Figure 4.55. It is apparent from this figure that with respect to both the positive and negative ELTGs, Cell 70 has less severe gradients than the composite concrete pavements that do not have a HMA surface layer. There is also a noticeable difference between the ELTGs that developed in the two composite concrete pavements.

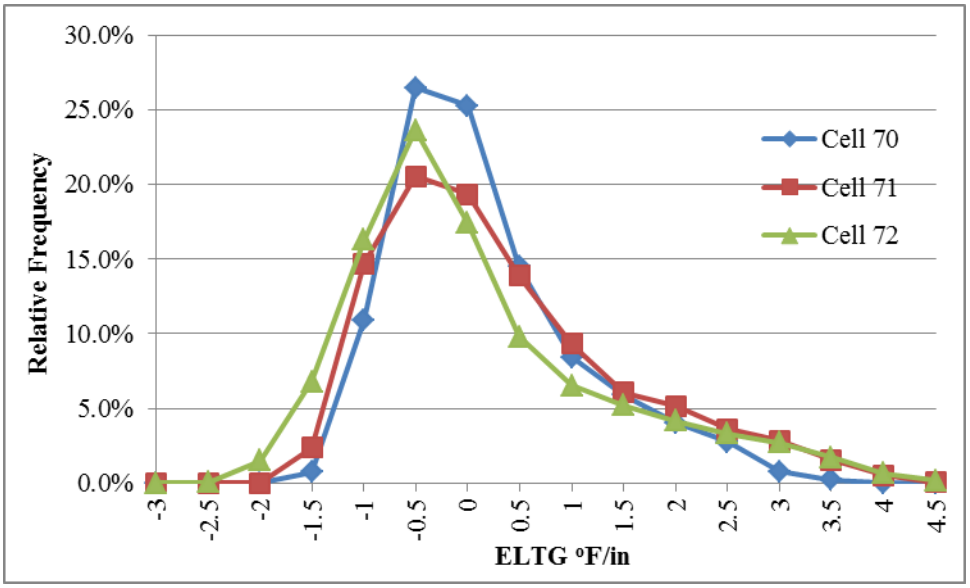

Figure 4.55: Histograms of ELTGs between Cell 70, 71 and 72

For Cell 71, 57 percent of the equivalent linear temperature gradients were negative. This is compared with 66 percent for Cell 72 and 63 percent for Cell 70. This means that the curling induced by temperature effects is more evenly distributed amongst both positive and negative ELTGs for Cell 71. While the split between positive and negative temperature gradients is more even for Cell 71, the magnitude must also be considered and a comparison of the frequency of relatively extreme temperature gradients was made.

An assessment of the linear temperature gradient magnitude discussed in Section 4.2.2 revealed that Cell 71 and Cell 72, which were represented by the same linear temperature gradients, had approximately twice as many positive linear temperature gradients greater than 2.0°F/in and approximately twice as many negative gradients with magnitude greater than 1°F/in. Extending this analysis to the equivalent linear temperature gradient, it was found that difference between the gradients of Cell 70 and the composite concrete pavement increased significantly.

Additionally, unlike in the assessment of the linear temperature gradient, a significant difference was noted between the two different composite concrete pavements.

Considering the equivalent linear temperature gradient, Cell 71 had 216 percent more positive temperature gradients above 2^{o}F/in and 77 percent more negative temperature gradients with magnitude greater than 1^{o}F/in relative to Cell 70. Cell 72 had over 1000 percent more positive temperature gradients above 2^{o}F/in and 64 percent more negative temperature gradients with magnitude above 1^{o}F/in relative to Cell 70.

A comparison of Cell 71 and Cell 72 found that the occurrence of positive equivalent linear temperature gradients with magnitude greater than 2^{o}F/in was similar and that Cell 71 had only eight percent more of these gradients relative to Cell 72. For negative gradients with magnitude greater than 1^{o}F/in however, Cell 71 had only 28 percent of the number of occurrences that Cell 72 had.

From this analysis, it is apparent that for both negative and positive temperature gradients, Cell 70 has the most favorable occurrence of relatively extreme temperature gradients. It is also apparent that for composite pavements, the consideration of the equivalent linear temperature gradient, rather than simply the linear temperature gradient, is more critical to drawing meaningful assessments of pavement curvature and performance.

4.3 CHARACTERIZATION OF MOISTURE GRADIENTS

As discussed in Section 2.3.2.2, the influence of moisture in concrete slabs is that it influences the propensity for drying shrinkage to occur. Drying shrinkage, when it occurs differentially

throughout the depth of the slab, causes slab warping. Warping associated with differential drying shrinkage causes the slab to assume a positive curvature.

In the three composite pavement cells at MnROAD, a total of 108 relative humidity sensors were installed. Despite the number of sensors installed, the information obtained from these sensors could not be processed to directly relate the relative humidity conditions in the concrete to differential drying shrinkage and slab curvature. The primary reason for this difficulty was the observed variability in the data and the questionable quality of the data obtained from the sensors.

In assessing the relative humidity measurements obtained from the cells at MnROAD, it is important to consider what has already been discovered about the relative humidity in concrete slabs. Janssen concluded that the moisture content of concrete slabs does not vary much throughout the depth of the concrete except for in the top two inches of the concrete [30]. Kim and Lee have shown the changes in relative humidity in concrete to be attributable to both self-dessication due to the hydration reaction and moisture diffusion through the slab [31]. Based on the fundamental law of moisture diffusion, Fick's second law, the rate of moisture diffusion from the concrete is also a function of the differential relative humidity between the slab surface and the environment.

The change in the differential relative humidity between the slab and the environment can be considered using Figure 4.56. This figure illustrates the variation in ambient relative humidity with temperature over a two day period. As the temperature increases, the relative humidity decreases. This is the result of the fact that for a relatively fixed amount of moisture in the air, the amount relative to the saturation moisture content changes with temperature. When the temperature is warmer, and the ambient vapor pressure is low relative to the saturation vapor

pressure, the moisture in the concrete has a greater propensity for evaporating from the concrete and resulting in drying shrinkage.

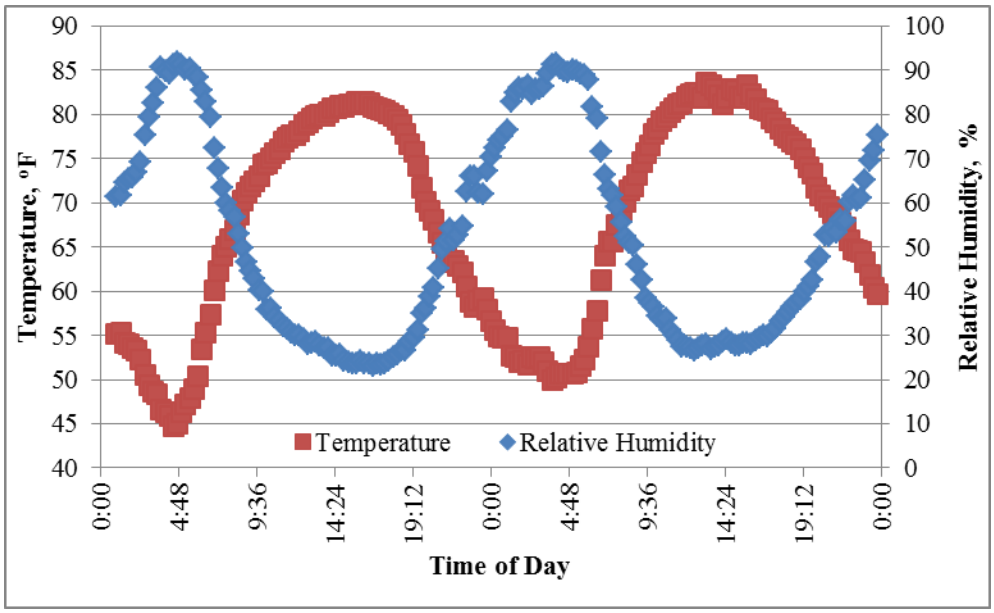

Figure 4.56: Typical Variation of Ambient Relative Humidity with Temperature

Considering these observations, the ambient relative humidity measurements and the relative humidity measurements from the three cells at MnROAD will now be discussed. The variation in the daily average ambient relative humidity at MnROAD can be seen in Figure 4.57. The range of the average daily ambient relative humidity is between 50 and 100 percent. Although the variation in the relative humidity of the concrete at very shallow depths might show a similar variation in relative humidity with time, it is more likely that the variation of relative humidity in the concrete will follow seasonal trends. The nature of this relationship is the result of the slow diffusion of water through the concrete due to its low permeability and other temperature effects.

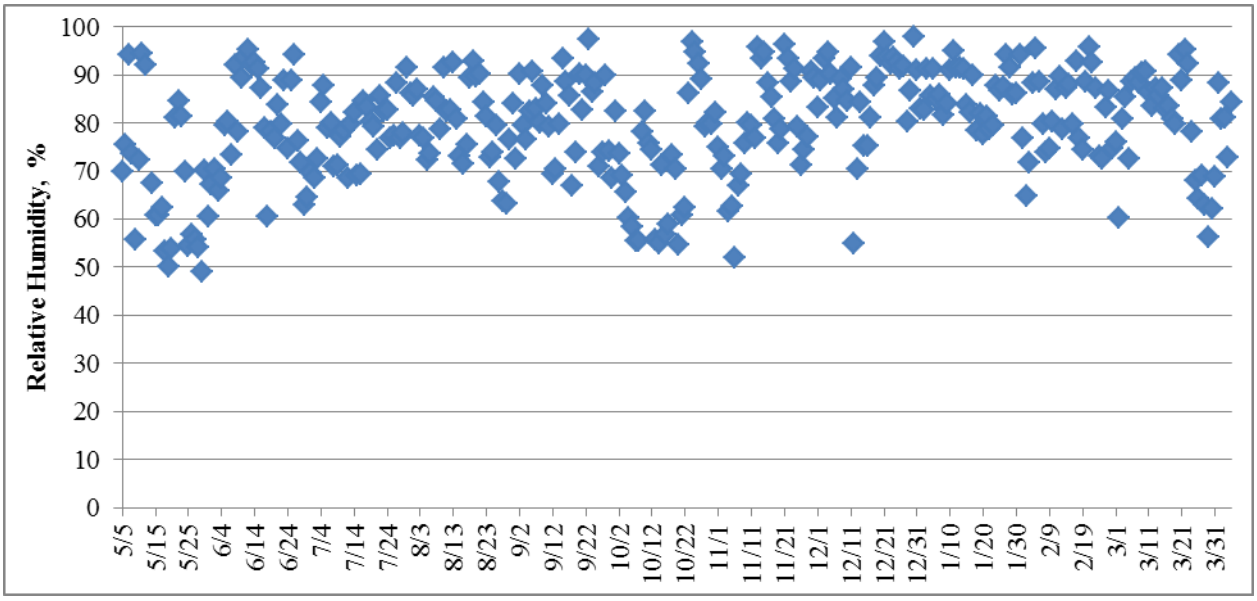

Figure 4.57: Variation in Daily Average Ambient Relative Humidity at MnROAD

Figure 4.58 captures seasonal effects by averaging the relative humidity over the entire month. In Figure 4.58, it can be seen that the ambient relative humidity increases in the winter. Winter months are generally prone to a higher rate of drying shrinkage occurring in the concrete. This is because, although the relative humidity is high in the winter, less moisture is in the air during the winter due to the suppression of the saturation vapor pressure at low temperatures.

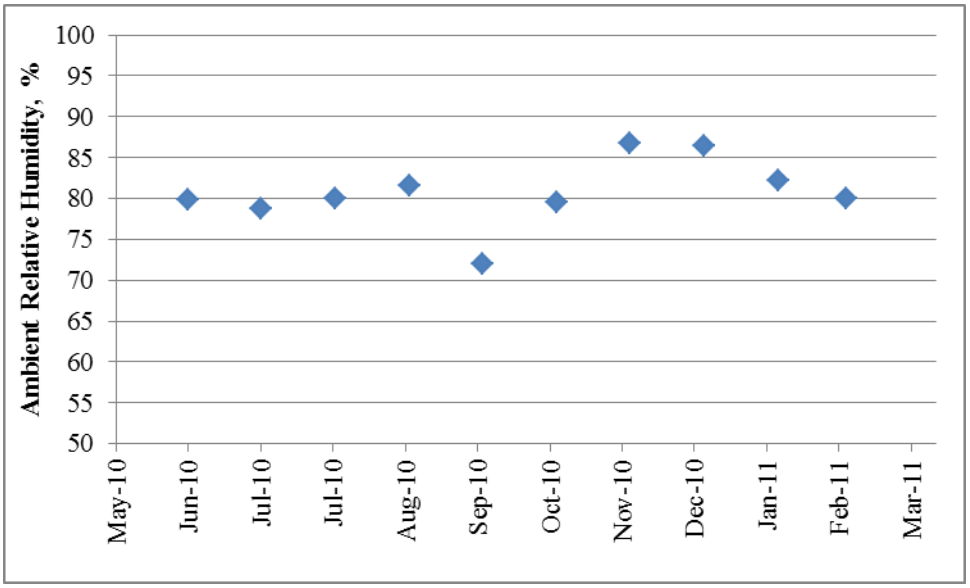

Figure 4.58: Variation in Monthly Average Ambient Relative Humidity at MnROAD

Figure 4.59 shows the variation in the concrete relative humidity measurements over the span of a week. Figure 4.59 was produced using data from Cell 70 and depicts the period of time approximately four days before and three days after the HMA overlay was placed on top of the underlying recycled concrete layer. The spike in the measured temperature on the morning of May 20th is indicative of the time that the HMA overlay was placed on the underlying recycled concrete.

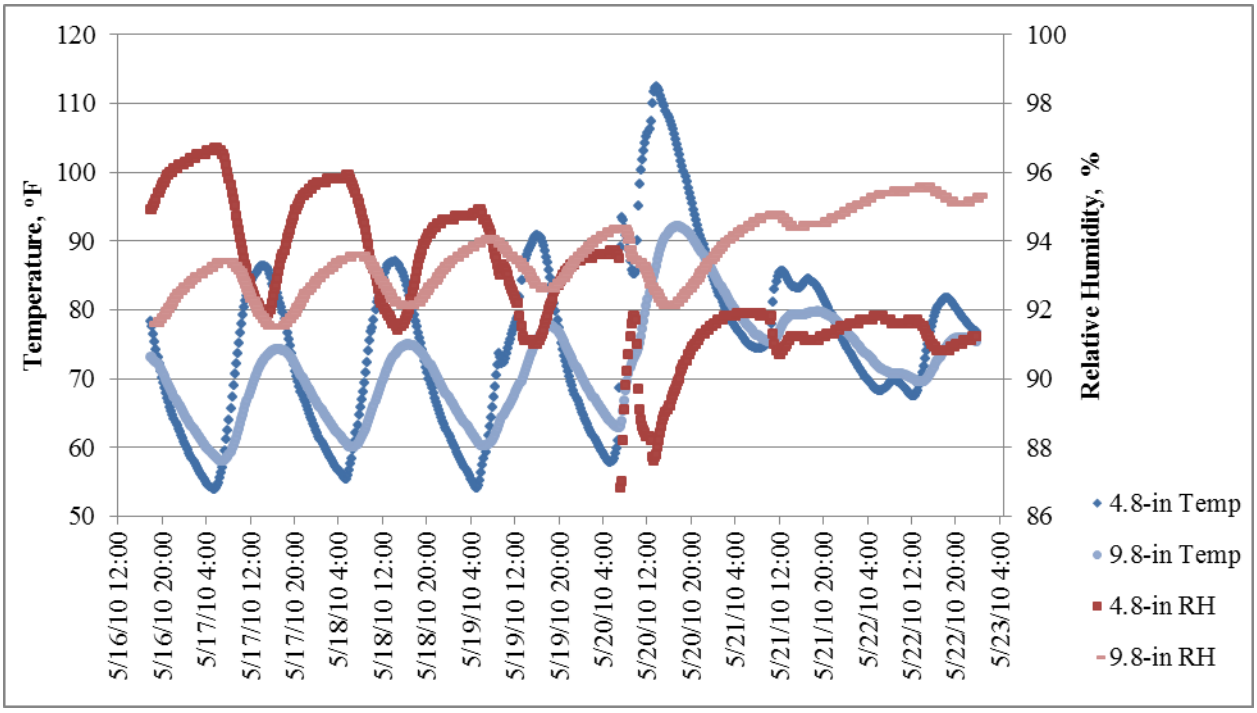

Figure 4.59: Variation of Concrete RH with Temperature

Unlike the ambient relative humidity, the relative humidity in the concrete does not fluctuate nearly as much with a given change in temperature. Suppression of the fluctuation of relative humidity with temperature is due to the effects of the surface tension in the concrete pore water. As the temperature increases, more kinetic energy is imparted to the water molecules in the concrete pore space. This results in these water molecules being more prone to escaping into the air surrounding the pore water and driving up the relative humidity. The opposite trend is true when temperature decreases and water molecules return from the gaseous to the liquid phase. This prevents the relative humidity from increasing too much in the pore space.

In Figure 4.59, it can be seen that there is more daily variation in the temperature and relative humidity measurements of the sensor located closer to the surface. The sensor depths shown in Figure 4.59 are relative to the surface of the HMA layer and therefore, in the beginning

of the time series shown in Figure 4.59, the top sensor is closer to the ambient environment than it is after the HMA overlay is placed.

Examining the relative humidity data for each of the three cells over the entire analysis period can be done with the help of Figure 4.60 through Figure 4.65. This collection of figures includes two plots of data from each cell. The location within the slab selected for presentation was based on the completeness of the data. Two figures were selected from each cell to show that conclusions drawn from one figure may be refuted with another figure presenting data from within the same cell. Figure 4.60 and Figure 4.61 represent Cell 70.

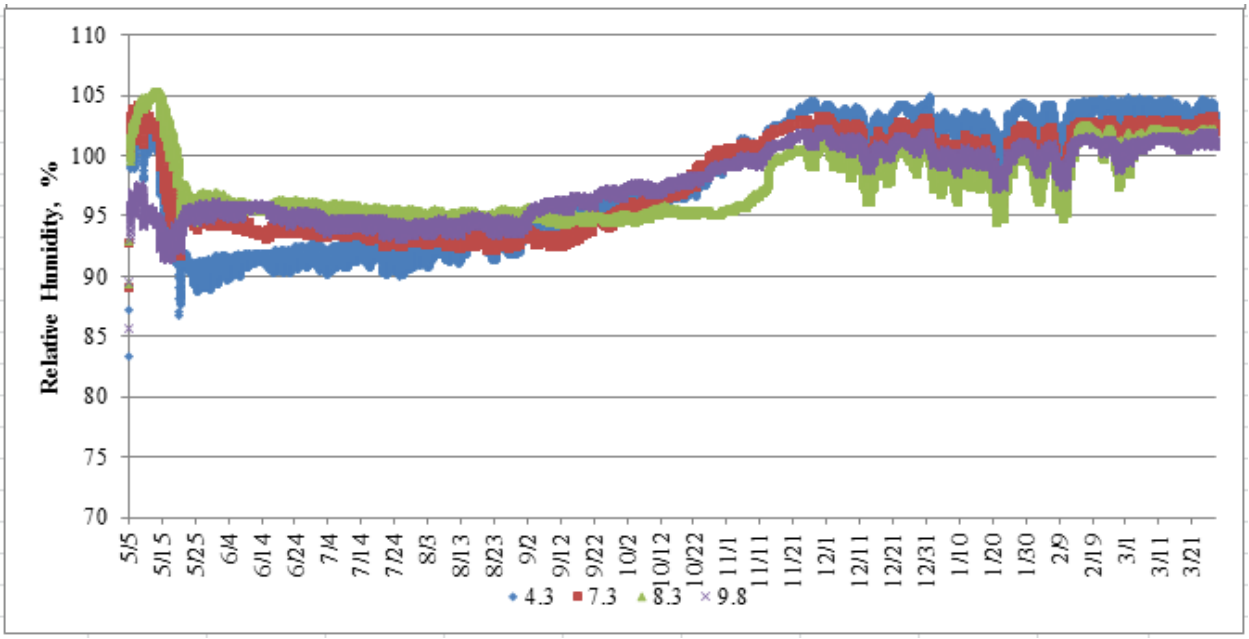

Figure 4.60: Variation of Relative Humidity with Depth for the Corner Location of Panel 2 in Cell 70

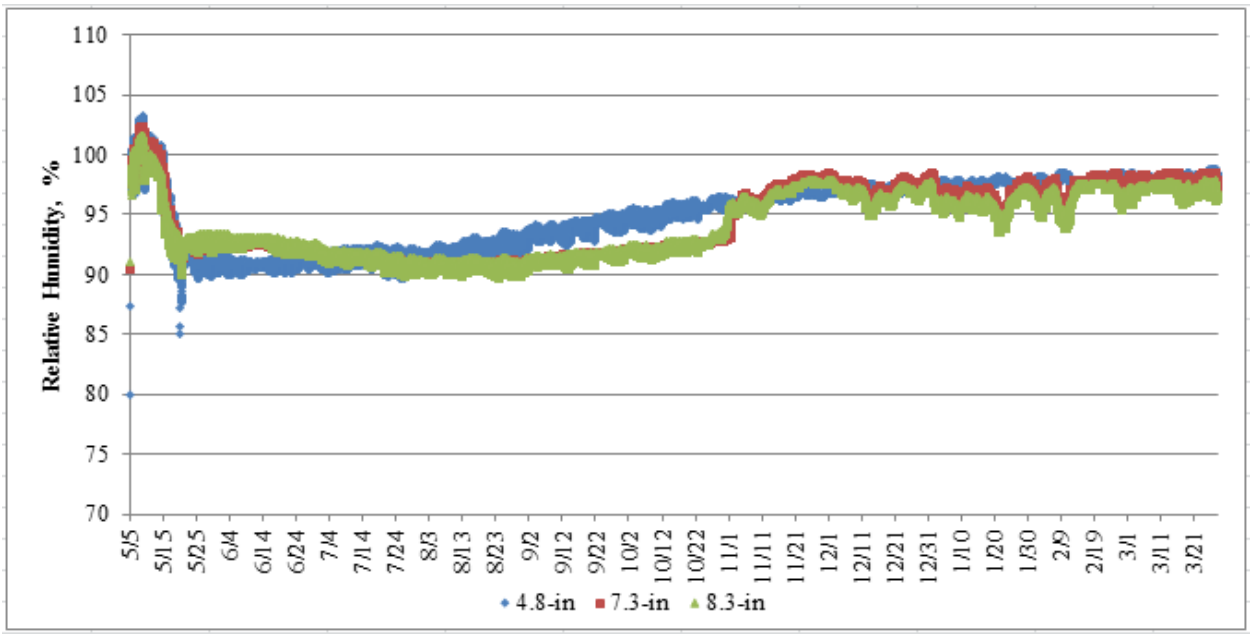

Figure 4.61: Variation of Relative Humidity with Depth for the Edge Location of Panel 2 in Cell 70

In Cell 70, it can be seen that the end of the initial drop in relative humidity after paving approximately corresponds with the time that the HMA overlay was placed on May 20th. After the time of the placement of the HMA overlay, the relative humidity of the sensor at the top of the concrete layer gradually trends towards the other sensor measurements. Although the difference in the measured values of relative humidity are small, this observation is considered to be due to the fact that the HMA overlay seals the concrete with respect to moisture loss. This sealing effect prevents differential drying shrinkage between the top and bottom of the slab from occurring. Eventually, moisture could become trapped in this location and provide more uniform moisture conditions throughout the slab relative to a full-depth concrete pavement.

Figure 4.62 and Figure 4.63 show the variation in the relative humidity with depth at two locations within Cell 71. Perhaps the most notable feature from these figures is that there seems to be no systematic variation in the relative humidity measurements with depth. Figure 4.62 and

Figure 4.63 also show a similar trend for Cell 70 in the sense that the relative humidity in the concrete increases as the ambient temperature decreases in the fall and through the winter and early spring months.

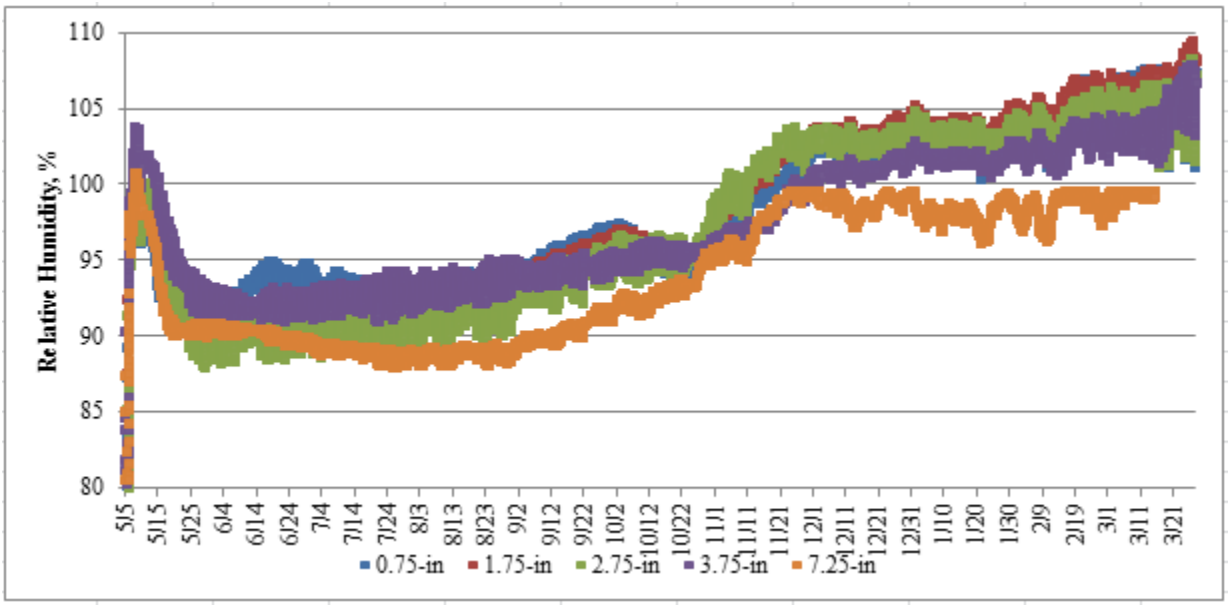

Figure 4.62: Variation of Relative Humidity with Depth for Midslab Location of Panel 2 Cell 71

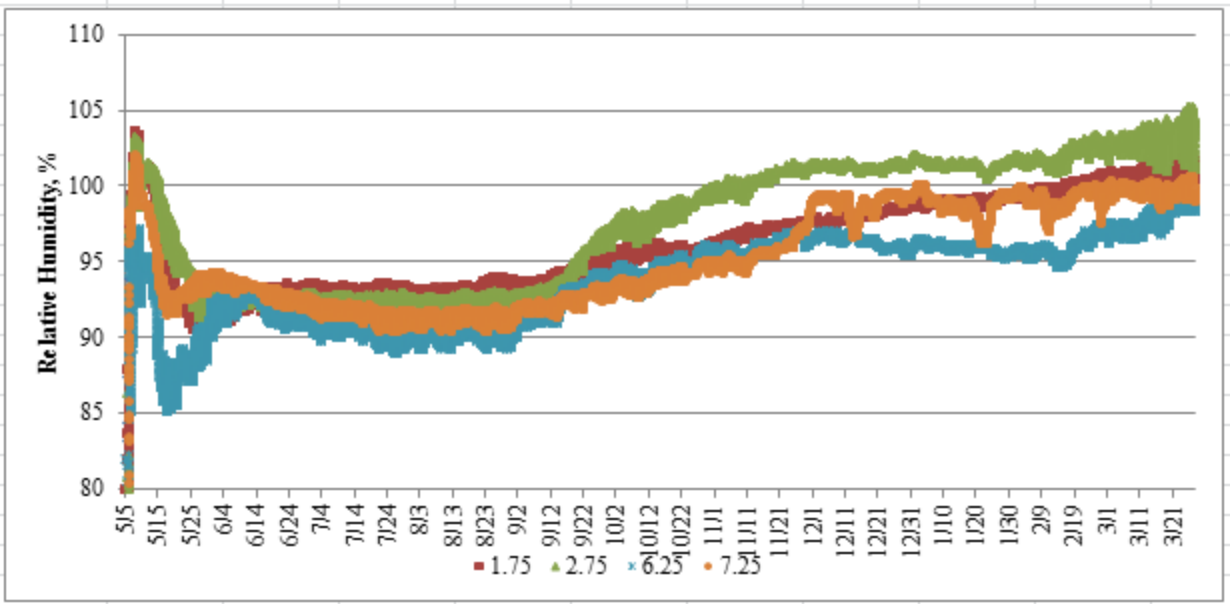

Figure 4.63: Variation of Relative Humidity with Depth for Edge Location of Panel 2 of Cell 71

Of all of the trends regarding the relative humidity in the concrete over time, perhaps the most reasonable measurements were obtained from Cell 72. These measurements are shown in Figure 4.64 and Figure 4.65 and were taken from the edge locations of Panel 1 and Panel 2 in Cell 72, respectively.

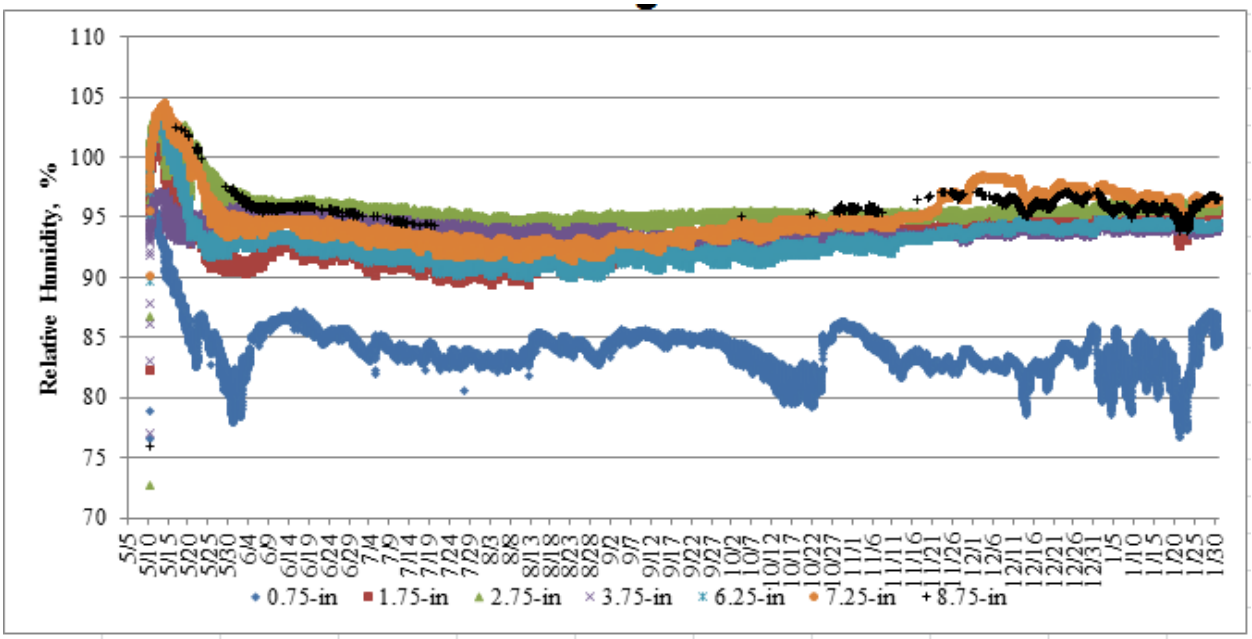

Figure 4.64: Variation of Relative Humidity with Depth for Edge Location of Panel 1 of Cell 72

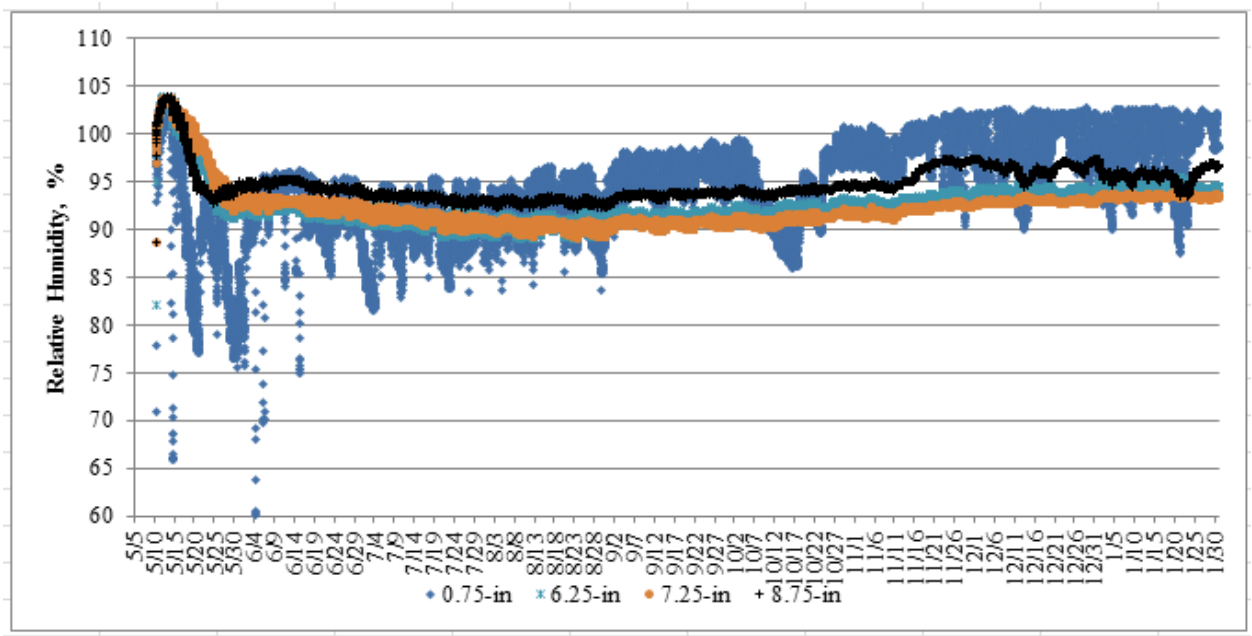

Figure 4.65: Variation of Relative Humidity with Depth for Edge Location of Panel 2 of Cell 72

Both figures show that the drop in relative humidity associated with the first drying period was proportionately greater in the top sensor located at a depth of 0.75 in from the concrete surface. The remaining sensors for which usable data was available all show that the relative humidity in the concrete remains essentially constant throughout the analysis period after the initial drying of the concrete.

Even though the trends in the relative humidity data for the two locations in Cell 72 are more intuitively reasonable, if taken at face value they could lead to different conclusions. In Figure 4.64, the relative humidity of the top sensor suggests that the relative humidity at this location is always lower than the relative humidity throughout the depth of the concrete. Figure 4.65, suggests that although the top of the slab initially experiences a larger drop in relative humidity, the relative humidity at the top of the slab eventually becomes higher than the relative humidity throughout the depth. In Figure 4.64, it can be seen that the initial value of the relative humidity at a depth of 0.75 in shortly after casting does not go as high as the relative humidity in the other locations. This is not observed in Figure 4.65. The reason for this is unknown and further complicates the assessment of the validity of the measurements.

Common to all of the relative humidity measurement figures presented is that from the time of paving through the first two to three weeks after paving there is a relatively significant drop in relative humidity. This is uniform for all sensors throughout the depth of the concrete. This is likely due to the hydration of the concrete using the capillary pore water and dropping the internal relative humidity.

4.4 ENVIRONMENTAL COMPSITE SLAB CURVATURE RESPONSE

In the previous three sections, the initial conditions in the slab, the temperature gradients that develop, and the relative humidity conditions were analyzed. These factors were assessed so that they could be related to the curvature of the slab. The curvature of the slab, as discussed throughout Chapter 2, will influence both the location and magnitude of the critical stress when wheel loads are applied. The location and magnitude of the critical stress relative to the strength of the concrete is ultimately what controls the fatigue life of the pavement.

The readings from the vibrating wire strain gauges in the slab afford the ability to calculate the strain in the concrete using Equation 30. Using the measurements from the vibrating wire strain gauges throughout the depth of the slab, the curvature in the slab can be determined using Equation 31. Equation 30 represents the total strain in the concrete and accounts for the strain due to temperature changes as well as the strain due to other sources. If the CTE of the concrete is known, the strain readings can also be corrected to subtract out the effects of temperature. This is done using Equation 32 and represents strain due to the effects of drying shrinkage, creep, and static applied loads such as the self-weight of the slab, the lockup of the joints in hot weather, and other restraint effects. Due to the complicated nature of the modeling associated with all of these effects, the static strain gages are used to directly measure their effects. This is done by taking the total strain readings and subtracting out the influence of temperature effects.

With respect to the correction required for temperature effects, the CTE of hydrated cement paste is known to vary with relative humidity. The CTE of concrete therefore also varies with relative humidity. Because of the difficulties associated with adjusting the CTE of the concrete for the actual relative humidity condition, a correction for relative humidity was not

made to the data when calculating the strain due to non-temperature effects. When correcting the strain gage readings to account for temperature effects, the saturated CTE value obtained from lab testing of each of the concrete mixes was used.

Relative humidity measurements obtained throughout the concrete slab and discussed in the last section showed that the relative humidity in the concrete did not drop significantly below saturation levels and mostly remained above 90 percent. Based on the range of the measured relative humidity encountered in the concrete slab, the CTE of the concrete is believed to not vary significantly from the saturated CTE value.

The CTE of the concrete mixtures used in the construction of the three composite pavements are shown in Table 4.8. These values were measured by the FHWA Mobile Concrete Laboratory according to AASHTO specification T336-09 "Coefficient of Thermal Expansion of Hydraulic Cement Concrete." These values are the average of at least two tests.

Table 4.8: Composite Pavement Concrete Mix CTEs

	Recycled Concrete Mix	Exposed Aggregate Concrete Mix	Economic Mix
CTE με/^{o}F	5.78	5.57	5.36

$$\varepsilon_{conc} = \left(R_1 - R_0\right)\cdot B + CTE_{steel}\cdot\left(T_1 - T_0\right) \qquad \text{Equation 30}$$

$$\rho = \frac{1}{R} = \frac{-\left(\varepsilon_{top} - \varepsilon_{bot}\right)}{D\cdot\left(1 + \varepsilon_{top} + \varepsilon_{bot}\right)} \qquad \text{Equation 31}$$

$$= \left(R_1 - R_0\right)\cdot B + \left(CTE_{steel} - CTE_{concrete}\right)\cdot\left(T_1 - T_0\right) \qquad \text{Equation 32}$$

For the three composite pavement cells, the restraint conditions with respect to dowel bars, tie bars, shoulder restraint, and base type are the same. Additionally, all three cells have

sawed and sealed joints with the same joint spacing. All three cells also have the same design thickness contributing to slab self-weight. Table 4.9 shows the unit weights of the various composite pavement layers. These values were obtained as part of the quality control testing during construction. From Table 4.9, it can be seen that the unit weight for all of the paving layers is significant.

Table 4.9: Unit Weights of Composite Pavement Layers

	HMA	Recycled Concrete Mix	Economic Concrete Mix	Exposed Aggregate Concrete
Unit Weight, pcf	153	146	148	144

Because strain readings are available at different locations in each slab and each location is reproduced twice in each cell, the variability in the curvature calculation at each location can be assessed. Considering that variability between locations, the location that most accurately represents the entire slab, or whether or not the curvature is uniform in the slab can also be determined. Because there are duplicate locations, an assessment of variability in curvature between cells can be made while also considering the variability between panels in each cell.

In comparing the curvature of the slabs, the strain gauges are first zeroed to the zero stress time. This is the time at which the slabs are flat and subsequently start responding to changes in temperature gradients and other conditions. Although the zero stress time, discussed in Section 4.1.3, varied somewhat between panels and between locations, there was no systematic variation to suggest that one zero stress time determined in Section 4.1.3 was particularly more accurate than another. Therefore, the interpretation of strain data with respect to curvature was performed based on the average zero stress time determined for the panels in each of the three cells. The time used to zero the strain readings for Cell 70 and Cell 72 was 18

hours after paving and the time to zero the strain gauges for Cell 71 was at 15 hours after paving. As presented in Section 4.1.3, the selection of a specific zero stress time and zero stress temperature did not have a significant influence on the set conditions of the cells at MnROAD. For the range of times presented in Section 4.1.3 there was a relatively small variation of the average slab temperature and temperature gradient.

Additionally, for all of the vibrating wire strain gauges in Cell 72, and ten of the vibrating wire strain gauges in Cell 71, strain and thermistor data was not available until after the zero stress time. Therefore, the T_o and R_o used in Equation 30 could not be established from the vibrating wire strain gage and temperature measurements. In the case of the ten sensors in Cell 71, the temperature at the zero stress time and the strain that had occurred in the gauge between the zero stress time and the time that the data began being collected was approximated. This was performed by equating these quantities to the corresponding values in Panel 1 for which data was available.

For Cell 72, no strain and vibrating wire thermistor data was available for either Panel until 52.0 hours after paving. T_o was determined for each vibrating wire sensor in Cell 72 using the nearest zero stress time thermocouple temperature. Since there were not thermocouples installed at all the locations of the strain gauges, the temperatures at the centerline, midslab, and transverse strain gauge locations were approximated using the thermocouple measurements from midslab location at the hypothesized zero stress time. The temperatures at the zero stress time for the edge and diagonal vibrating wires were approximated using thermocouple measurements at the slab edge. The zero stress temperatures for each vibrating wire gauge in Cell 72 are shown in Table 4.10. As can be seen, there is a significant difference between the temperature at the edge

of the slab and the midslab location at the zero stress time. This was also observed for the other cells as shown in Section 4.1.3.

Table 4.10: Zero Stress Temperatures for Strain Gauges in Cell 72 from Thermocouple Measurements

	Edge	Midslab	Centerline	Transverse	Diagonal
Bottom ^{o}F	58	65	65	65	58
Middle ^{o}F	57	64	64	64	57
Top ^{o}F	55	61	61	61	55

The reference strain, R_o, in Equation 30 was approximated for Cell 72 by determining the amount of drying shrinkage strain that elapsed between the zero stress time and approximately 34 hours after the zero stress time (52 hours after paving) when data recording began.

To determine the amount of drying shrinkage-related strain that took place between the zero stress time and approximately 52 hours after paving in Cell 71, a time period was selected near 52 hours where the linear temperature gradient was close to or the same as the linear temperature gradient that occurred at the zero stress time. By selecting a time when the temperature gradient is the same as what was present at the zero stress time, the load related strain calculated using Equation 32 should be due primarily to drying shrinkage and without temperature induced curling. Although less than ideal, this was believed to be the most reasonable approach in terms of selecting an initial strain value for Cell 72.

Table 4.11 shows the load-related strain at various locations in Panel 1, approximately 50 hours after paving and 35 hours after the zero stress time for Cell 71. The sign convention for strain with the vibrating wire strain gauge is that negative values represent compression while positive values represent tension. Although drying shrinkage induces a tensile stress in the concrete, it manifests itself as a compressive strain in the vibrating wire strain gauge. Because

drying shrinkage causes a reduction in the length of concrete between the gauge ends, it generates a compressive strain in the gauge. In Table 4.11, bottom, middle, and top reference the relative location of the strain gauge throughout the slab depth. LTG_{ZST} and LTG_{DS} represent the linear temperature gradient calculated using the vibrating wire thermistor measurements at the zero stress time and the linear temperature gradient at the time used to determine the effect of drying shrinkage in the slab. The time, $LTG_{DS,}$ represents the time after paving that the LTG_{DS} occurred and fortunately occurred around 50 hours after paving.

Table 4.11: Non-Temperature Related Strain Approximately 50 Hours after the Zero Stress Time for Cell 71

	Edge	**Midslab**	**Centerline**	**Transverse**	**Diagonal**
Bottom (με)	16.3	33.9	22.3	3.5	32.4
Middle (με)	1.7	42.7	23.2	13	40.6
Top (με)	-35.9	-6.5	-19.5	-19.6	3.3
LTG_{ZST} °F/in	-0.4	-0.6	-0.9	-0.5	-0.2
LTG_{DS} °F/in	-0.4	-0.6	-0.9	-0.5	-0.1
Time LTG_{DS} (hrs)	48	48.25	47.8	48.5	49.5

In Table 4.11, the load related strain at each location is much more compressive in nature at the top of the slab relative to the bottom of the slab. Because of the compressive nature in the gage, this indicates the influence of drying shrinkage on this value. The positive (tensile) values for the load related strain in the other locations suggest that the slab is being restrained from contracting somewhat. This could be due to the effects of the base or other slab restraints such as dowel or tie bars. This suggestion is bolstered by the fact that the least tensile load related strain occurs at the locations with the least restraint, namely the transverse and edge location. For Cell 72, the values shown in Table 4.11 were subtracted from the R_1 values when the strain gauges started recording data to obtain the R_o values for Cell 72.

In the following three sections, a comparison between the panels in each cell will be made with respect to trends in the calculated curvature and strain components. Differences in the calculated curvature with respect to location and panel for each cell will be highlighted and hypothesized reasons for the differences will be presented.

4.4.1 Cell 70 Slab Curvature Measurements

Figure 4.66 through Figure 4.70 shows a comparison by location of the Cell 70 curvatures calculated based on the strain gauge measurements. The calculated curvature is quite disparate between the two panels in Cell 70 with Panel 1 generally exhibiting more curvature than Panel 2. This disparity in the measured curvature is particularly obvious for sensors oriented in the longitudinal direction. The measured curvatures in the transverse direction agree well between the panels. The calculated curvature in the diagonal direction, which is a function of curvature in both the transverse and longitudinal direction, shows some disparity between panels but not as much as the longitudinally oriented sensors.

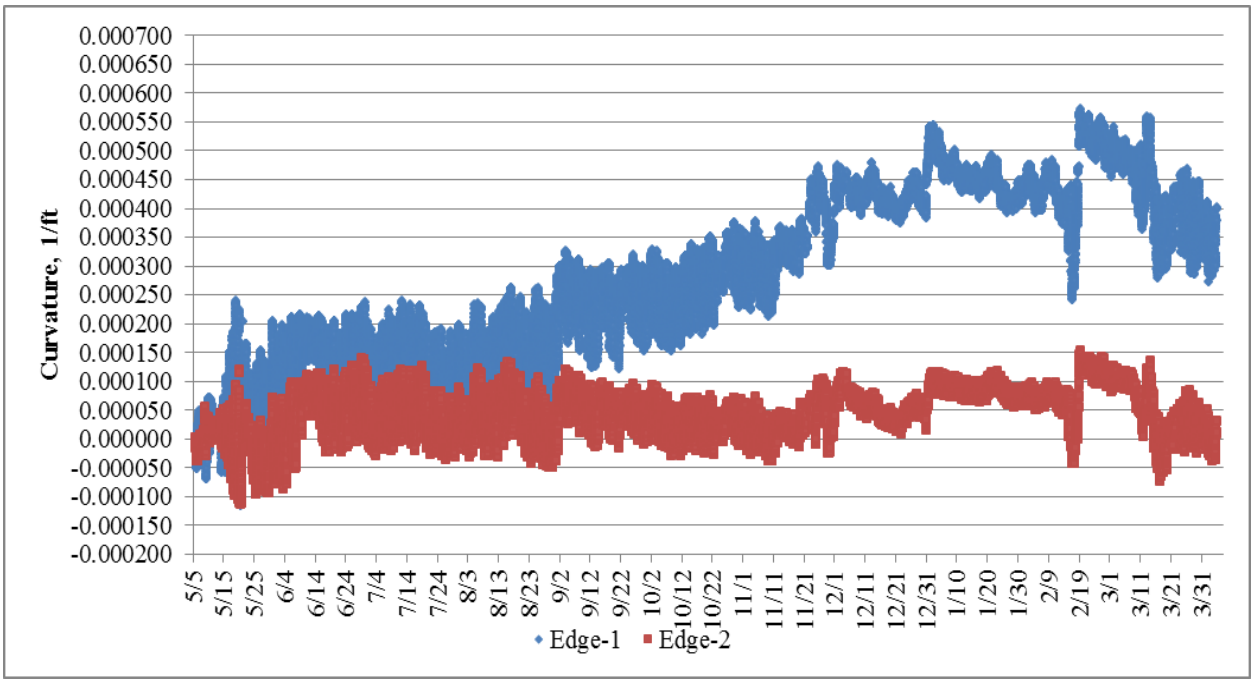

Figure 4.66: Comparison of Curvature at the Edge Location for Cell 70

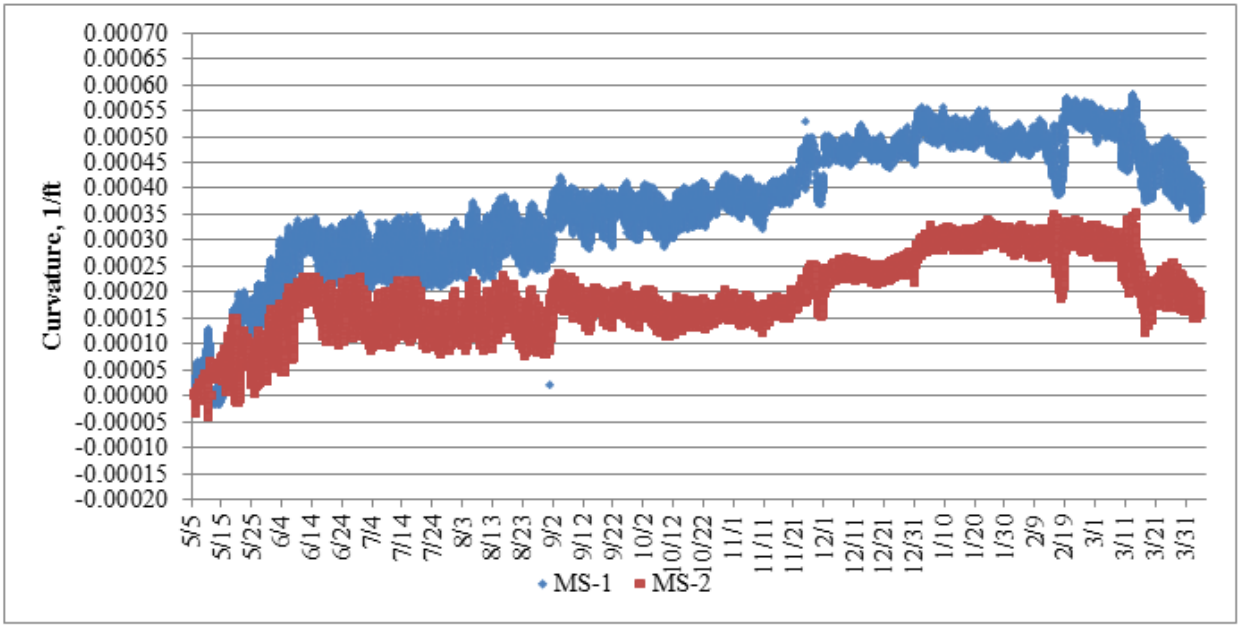

Figure 4.67: Comparison of Curvature at the Midslab Location for Cell 70

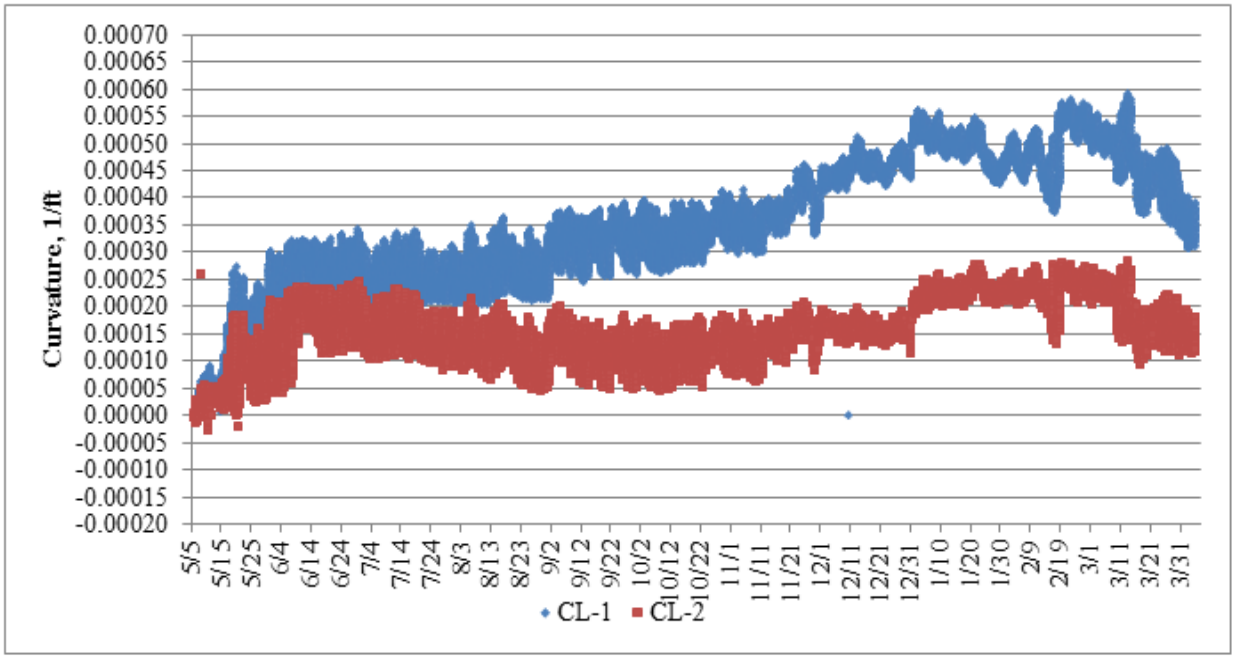

Figure 4.68: Comparison of Curvature at the Centerline Location for Cell 70

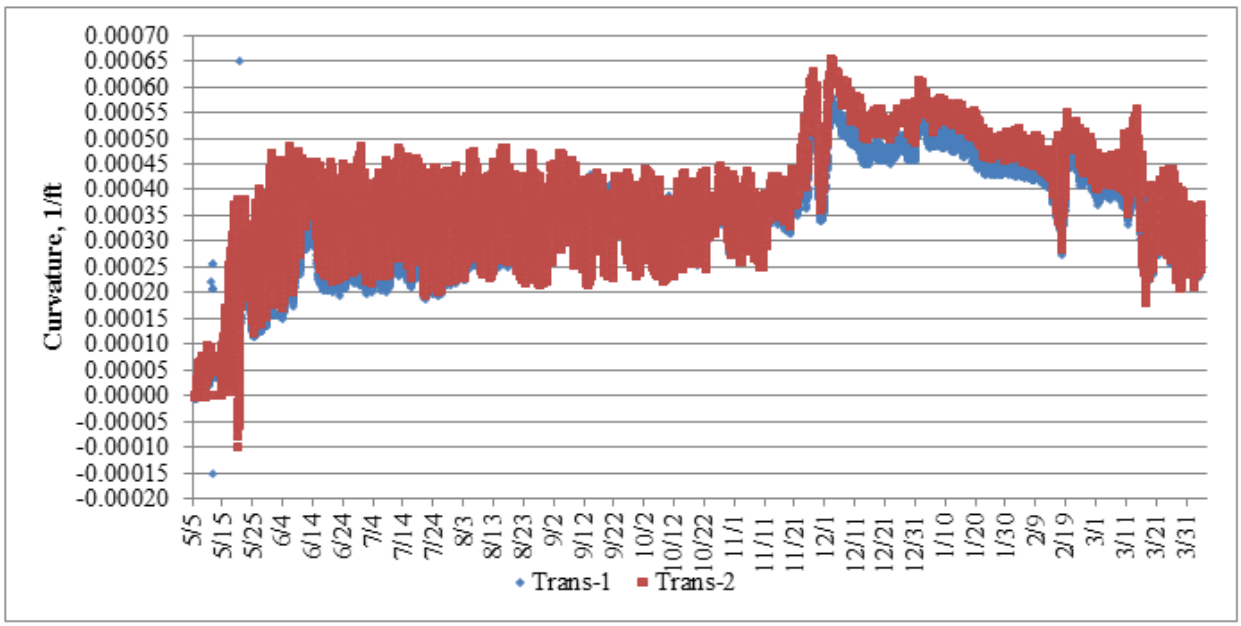

Figure 4.69: Comparison of Curvature at the Transverse Location for Cell 70

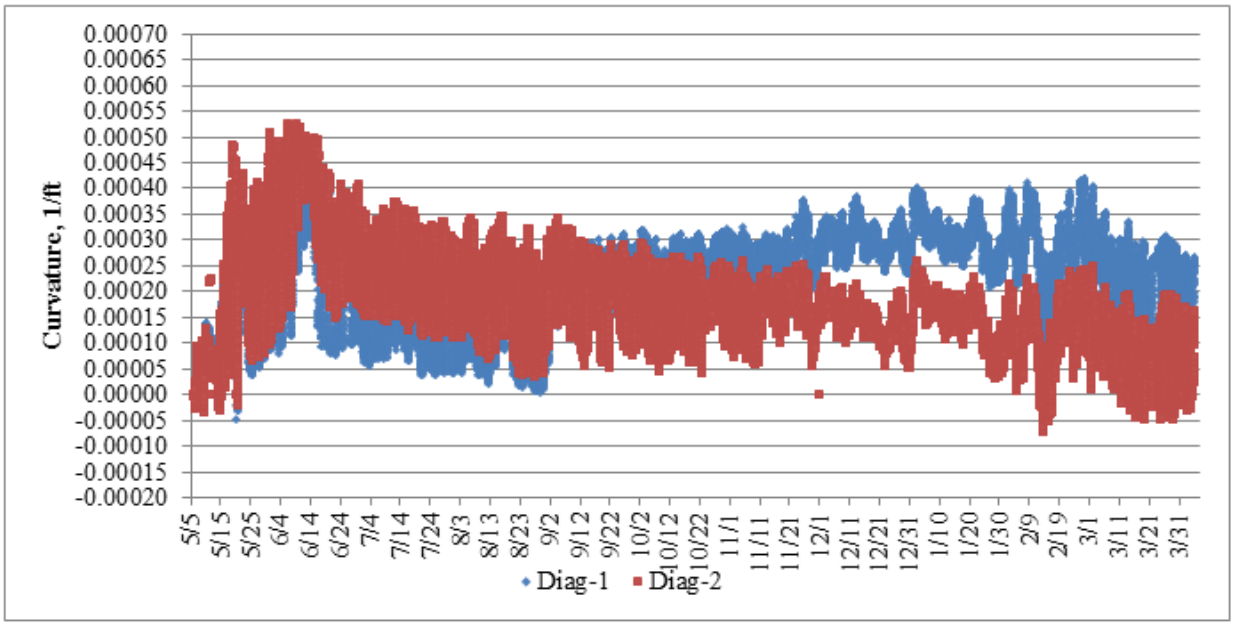

Figure 4.70: Comparison of Curvature at the Diagonal Location for Cell 70

The majority of the locations shown in Figure 4.66 through Figure 4.70 have positive upward curvature for the first 11 months after construction. The upward curvature is generally more pronounced in Panel 1. It can also be noticed that the largest positive curvature occurs in the winter when the temperature gradients are mostly negative. The range of curvatures exhibited over any given time period reflects the range in the temperature gradients over that time period. Comparing Figure 4.71 with Figure 4.66 through Figure 4.70 reveals the times in which there is a greater fluctuation in curvature corresponds to a time in which there is the greatest fluctuation in temperature gradient.

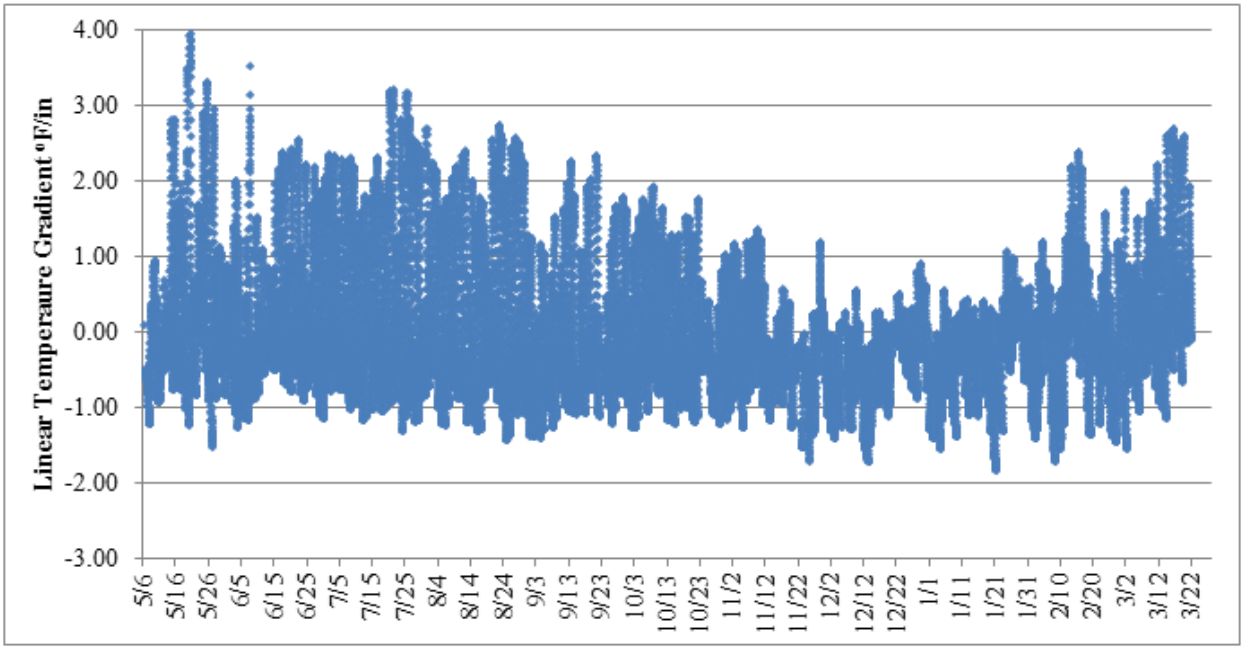

Figure 4.71: Linear Temperature Gradients over Analysis Period in Cell 70

Since the two panels are identical with respect to structure, the disparity in the curvature is an interesting observation and is problematic in assessing the curvature of Cell 70 for comparison with the other cells. To assess the difference in the curvature between the two panels, the strain associated with drying shrinkage, restraint, and creep, was separated from the total strain. This strain was calculated using Equation 32 and is hereby referred to as the non-temperature related strain. The non-temperature related strain at the top and bottom sensor locations is shown in Figure 4.72 and Figure 4.73. The total strain is shown in Figure 4.74 and Figure 4.75. Each pair or figures represents Panel 1 and Panel 2, respectively. In these figures, a negative strain represents compression of the gauge relative to its initial length in the fresh concrete. The depths of the sensors relative to the pavement surface are indicated by the number in the series name.

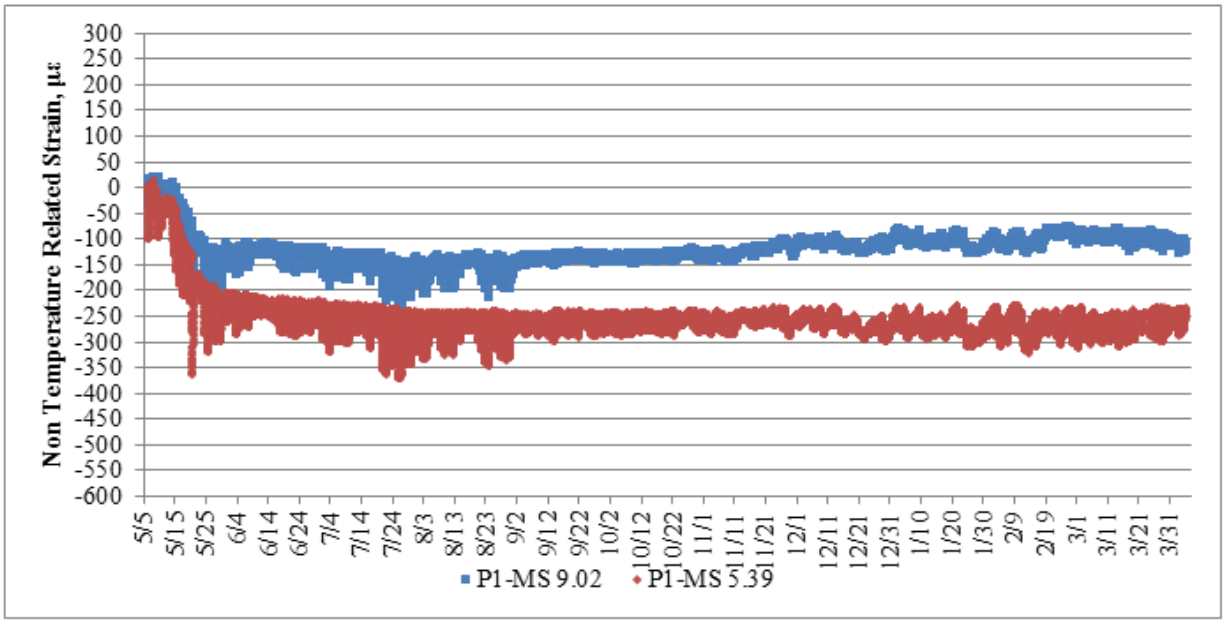

Figure 4.72: Non-Temperature Related Strain at the Midslab Location of Panel 1 in Cell 70

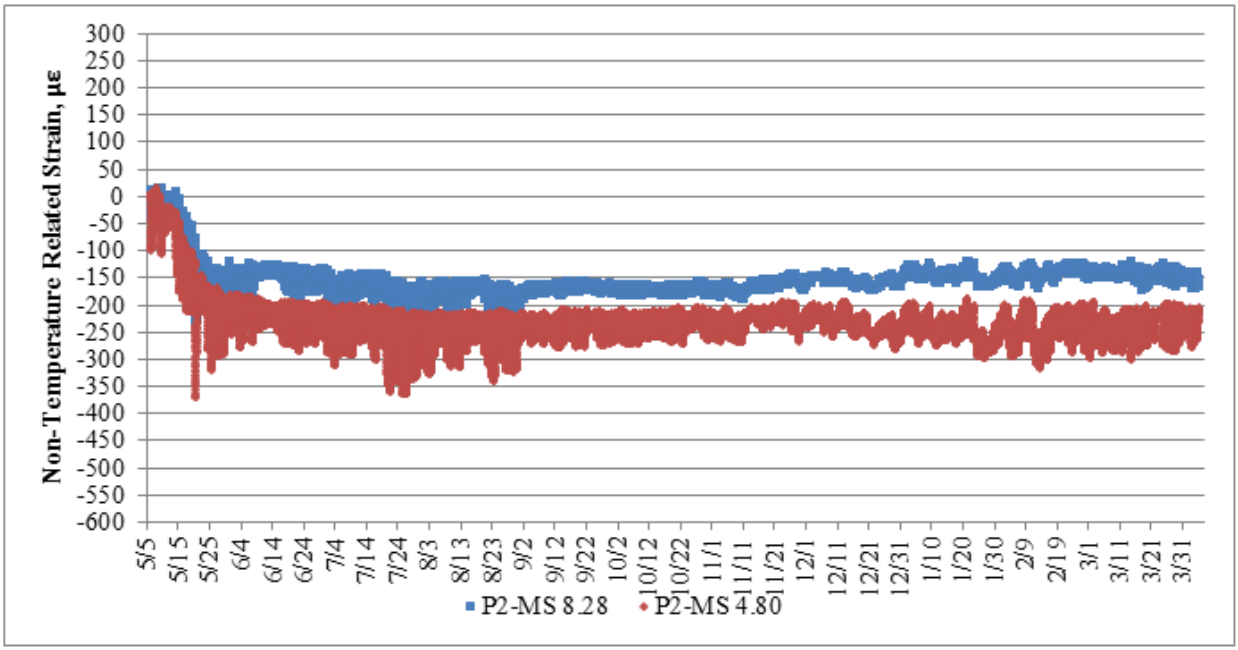

Figure 4.73: Non-Temperature Related Strain at the Midslab Location of Panel 2 in Cell 70

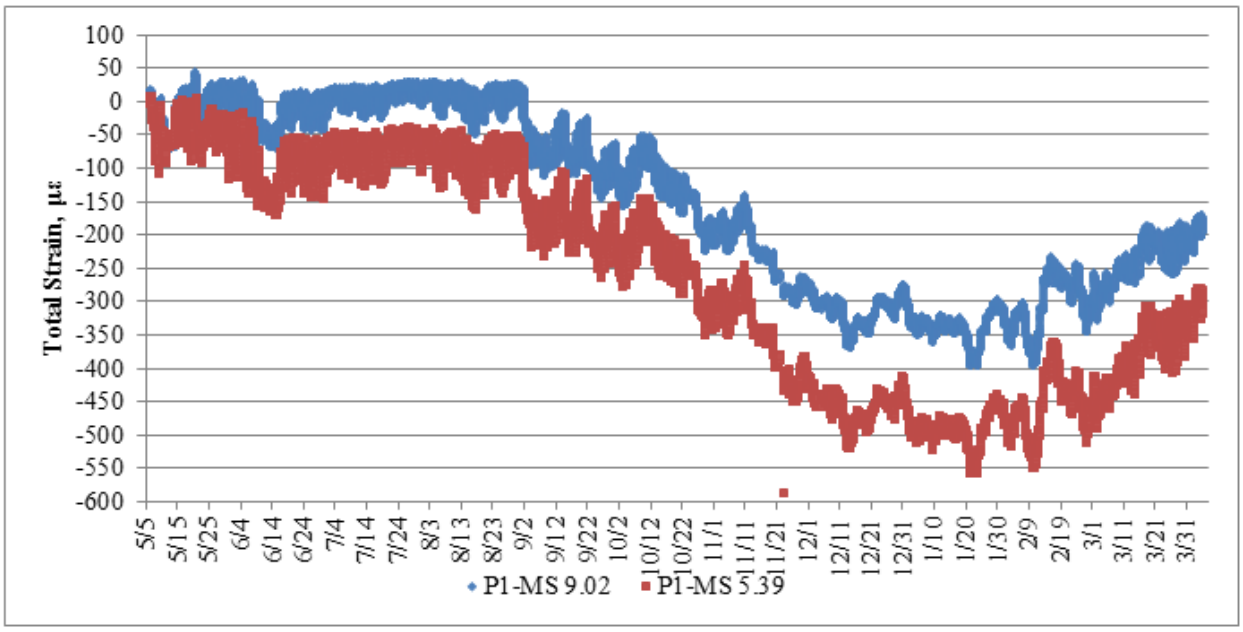

Figure 4.74: Total Strain at Midslab Location of Panel 1 in Cell 70

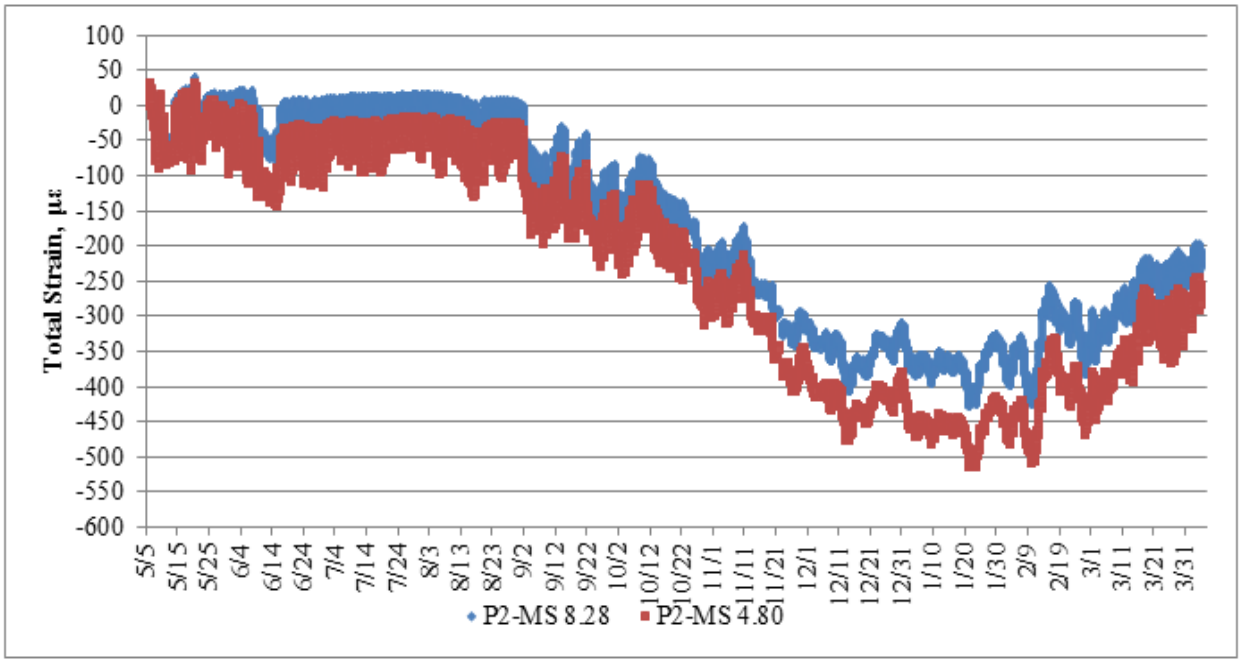

Figure 4.75: Total Strain at Midslab Location of Panel 2 in Cell 70

When looking at Figure 4.72 through Figure 4.75, the difference between the reading at the top and the bottom sensor is representative of the calculated curvature in the slab. In the case of Figure 4.72 and Figure 4.73 it can be seen that in Panel 1, at the midslab location, there is more curvature induced as a result of non-temperature effects than the corresponding location in Panel 2. Comparing the magnitude of the non- temperature related strains at the top and bottom of the slab, it can be seen that in Panel 1 there is less compressive strain at the bottom of the slab relative to Panel 2 and more compressive strain at the top of the slab relative to Panel 2. Both of these observations serves to increase the disparity in the measured curvature.

One distinct feature of Figure 4.74 and Figure 4.75 is that in the hot summer months there is a distinct ceiling on the amount of total strain in the slab. This can be considered due to the lock up of the joints. When the joints lock up, the slab, as well as the strain gages, can no longer expand. It can also be seen in the non-temperature related strain figures, Figure 4.72 and Figure 4.73 that the compressive strain due to non-temperature effects increases in the summer. This increase in compressive, non-temperature related strain reflects the degree of restrained thermal expansion due to the lockup of the joints. One thing that is unclear from Figure 4.74 and Figure 4.75 is that the magnitude of the total strain at joint lockup is different for the top and the bottom sensors and occurs at a lower value for the top sensor. This is especially pronounced in Figure 4.74 which represents Panel 1.

During the first month after paving there is a relatively large increase in both the total and non-temperature related strain between the top and bottom strain gages. This difference subsequently remains relatively constant throughout the rest of the year. For the longitudinally oriented sensors depicted in Figure 4.72 through Figure 4.75, the increase in the compressive non-temperature related strain occurs in both the top and bottom sensors. Figure 4.76 and Figure

4.77 depicts the non-temperature related strain in the transverse direction. In this orientation, the increase in the non-temperature related strain mainly occurs only in the upper sensor. The evolution of the total strain in the transverse direction is also different than the total strain in the longitudinal direction. In the transverse direction, the aforementioned phenomenon of joint lock-up does not occur. This is shown in Figure 4.78 and Figure 4.79. These figures depict the gage being allowed to expand freely throughout the summer months despite expansion in the longitudinal direction being limited.

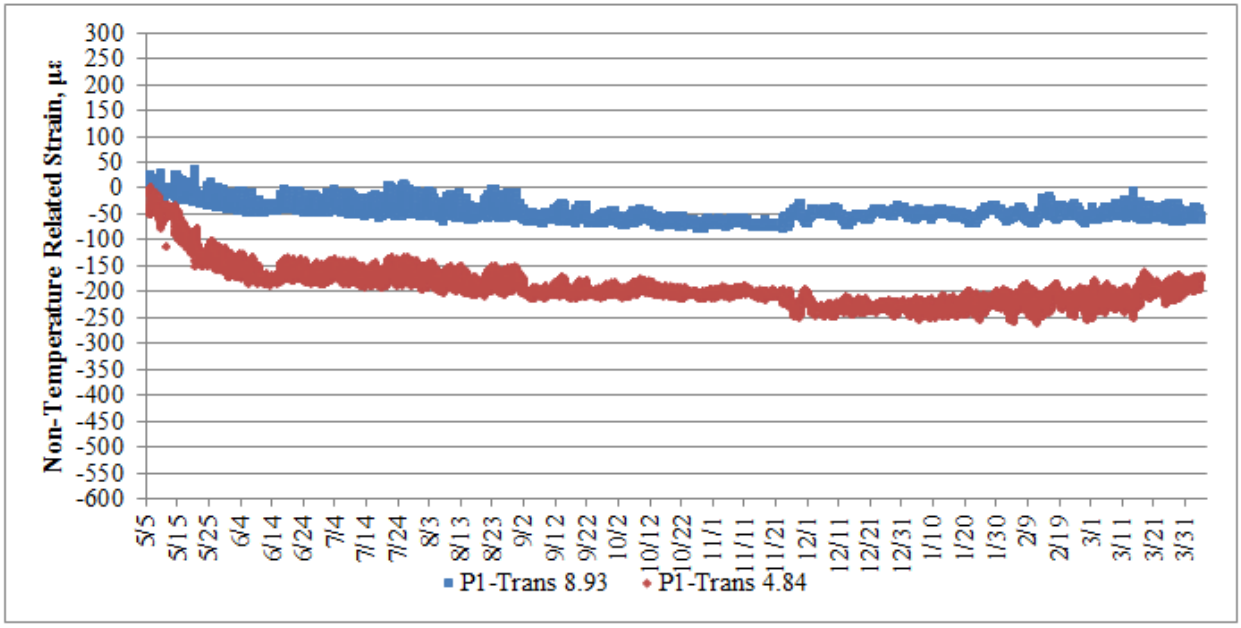

Figure 4.76: Non-Temperature Related Strain at the Transverse Location of Panel 1 in Cell 70

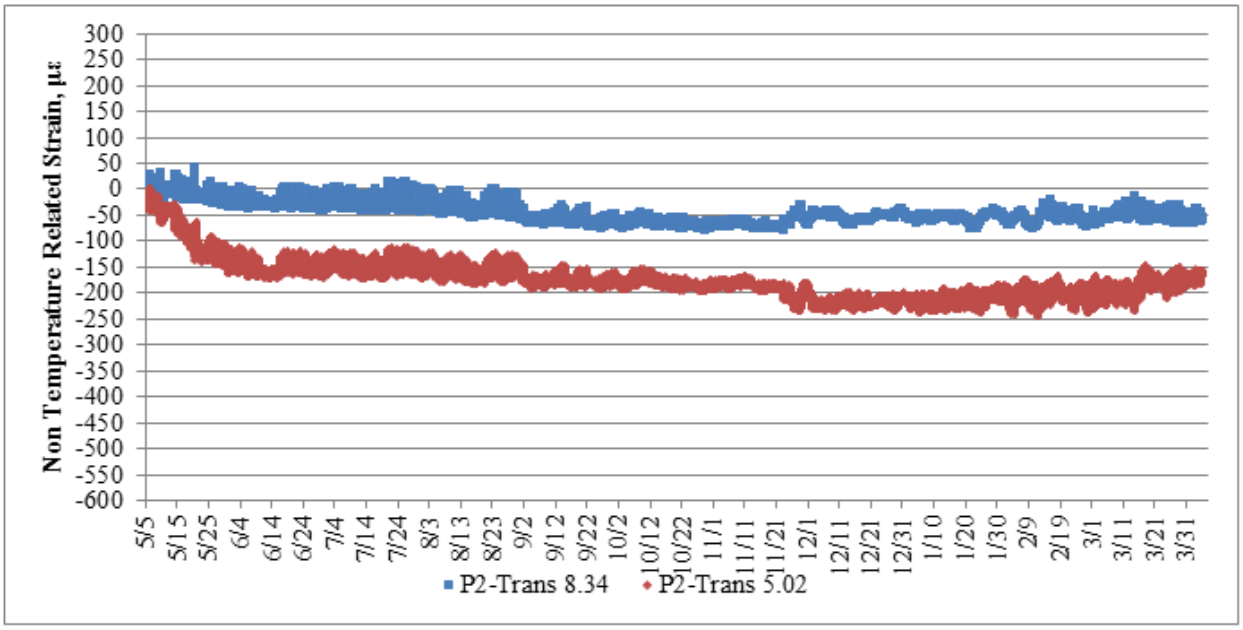

Figure 4.77: Non-Temperature Related Strain at the Transverse Location of Panel 2 in Cell 70

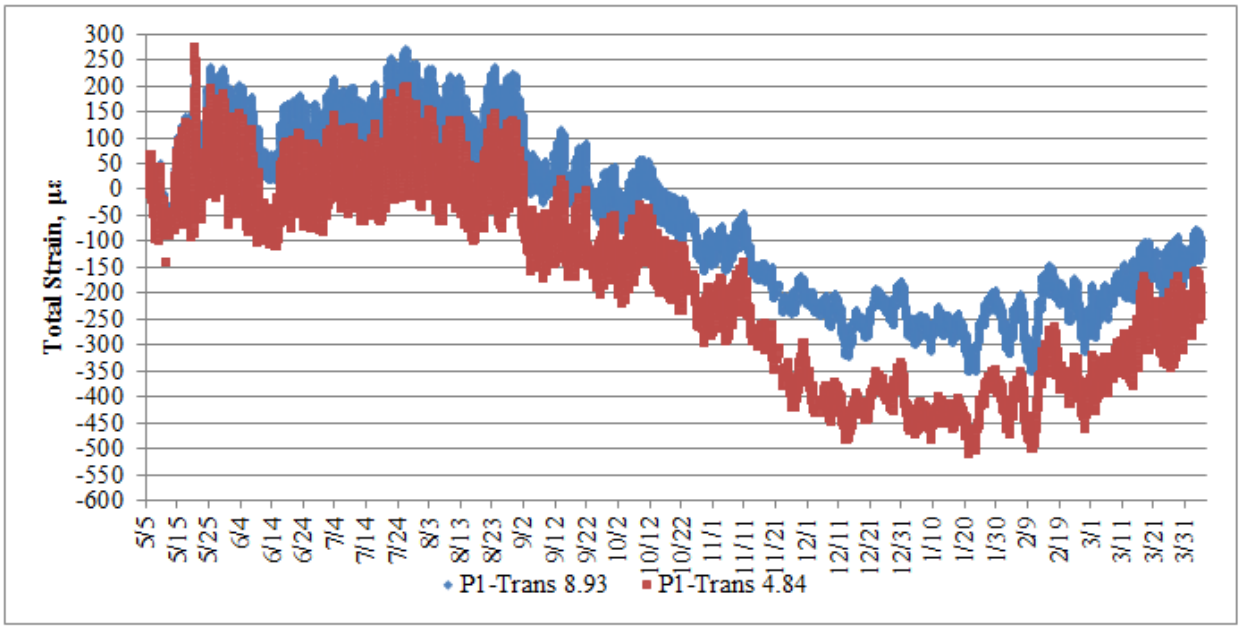

Figure 4.78: Total Strain in the Transverse Direction of Panel 1 in Cell 70

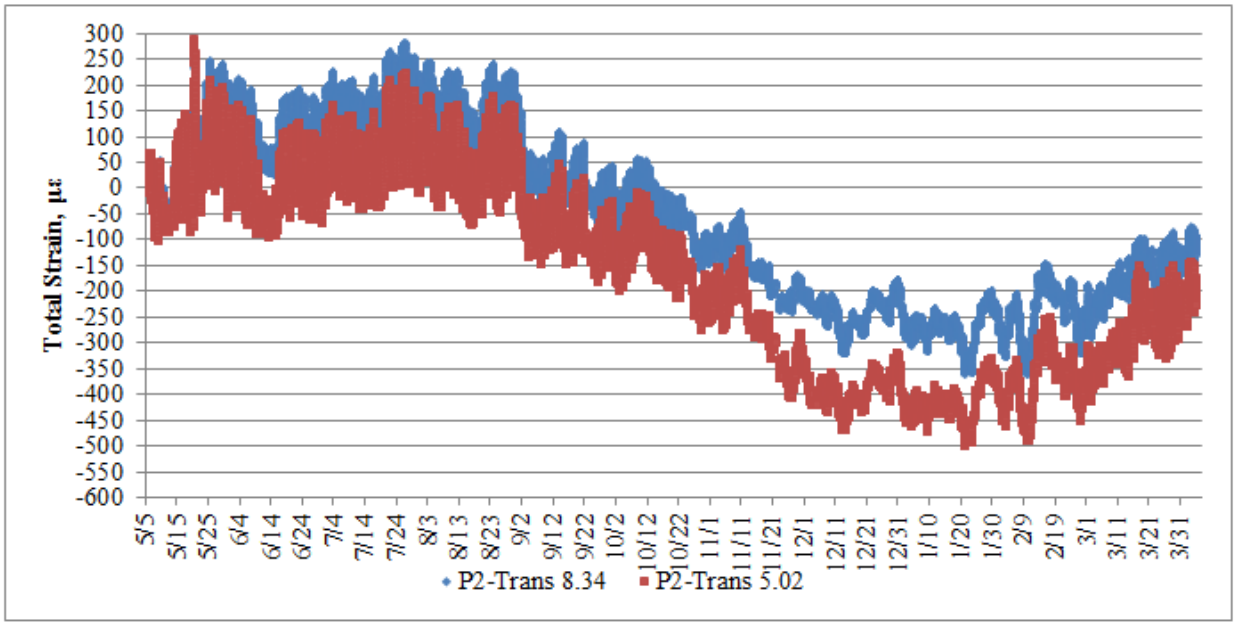

Figure 4.79: Total Strain in the Transverse Direction of Panel 2 in Cell 70

Because the transverse bottom sensors show little non-temperature related strain, it can be surmised that the reason for the difference in the non-temperature related strain between the depths is due primarily to drying shrinkage. The reason that the compressive, non-temperature related, strain at the bottom of the slab increases more in the longitudinal and diagonally oriented sensors relative to the transversely oriented sensors is unknown.

Based on the general trend in the relative humidity measurements in the slab presented in Section 4.3 it is believed that the increase in compressive strains for the bottom sensor is due to autogenous shrinkage of the concrete slab. This conclusion is supported considering the relatively low w/c ratio of 0.29 to 0.39 used in the paving mixes. Despite the disparity in strain magnitude with respect to sensor orientation, both the time scale over which this phenomenon occurs and the fact that the compressive non-temperature related strain increases at the top more than at the bottom suggests it is related to drying shrinkage. It is also notably the first drying of

the concrete. The time period also corresponds well with value recommended by the American Concrete Institue (ACI). The MEPDG adopted the ACI recommendation of 35 days required to develop 50 percent of the ultimate drying shrinkage in its design software.

No plausible explanation for the observed general increase in curvature over time for Panel 1 could be determined. It was noted that the difference between the calculated curvature of the two panels is more pronounced in the longitudinal direction than in the transverse direction or diagonal direction. The curvature calculated in the transverse direction showed good agreement between the panels while the agreement of the local curvature in the diagonal direction between the panels showed a level of agreement between that seen in the longitudinal and transverse directions.

Figure 4.81 through Figure 4.83 show the evolution of the strain in the diagonal direction of Panel 70. It can be seen in Figure 4.82 that the non-temperature related strain in the top sensor of Panel 2 decreases beginning near the beginning of September. The reason for this disparity in the performance relative to Panel is unknown. It appears that this trend is responsible for the divergence of the curvature calculated between Panel 1 and Panel 2 in the diagonal direction and as shown in Figure 4.70.

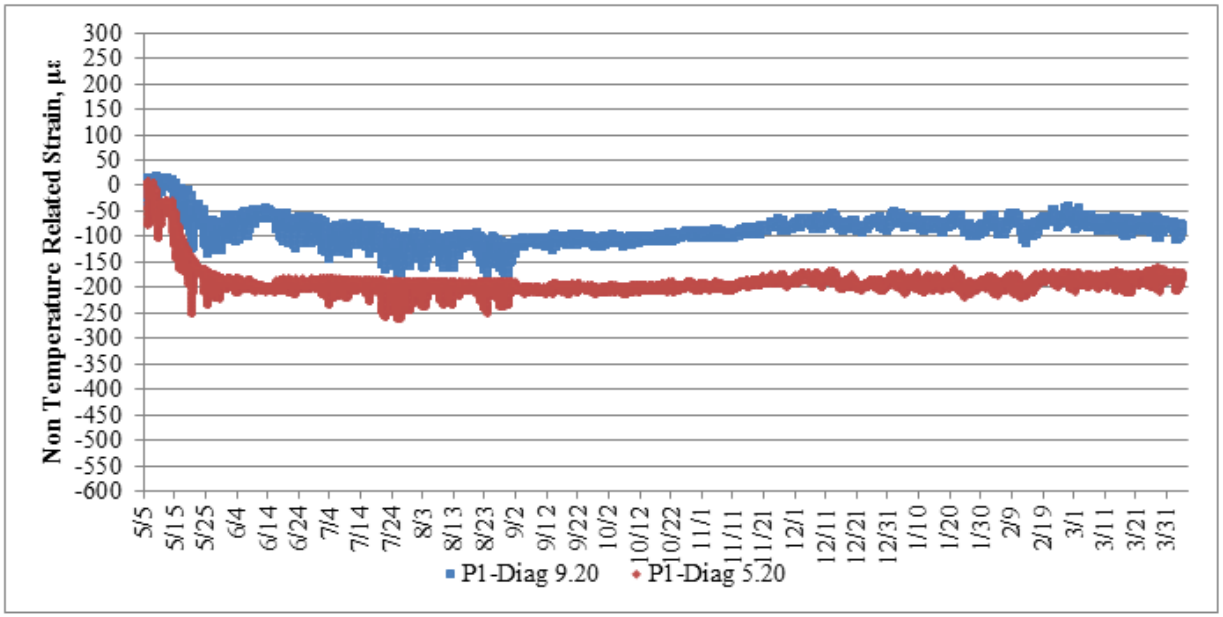

Figure 4.80: Non Temperature Related Strain at the Diagonal Location in Panel 1 of Cell 70

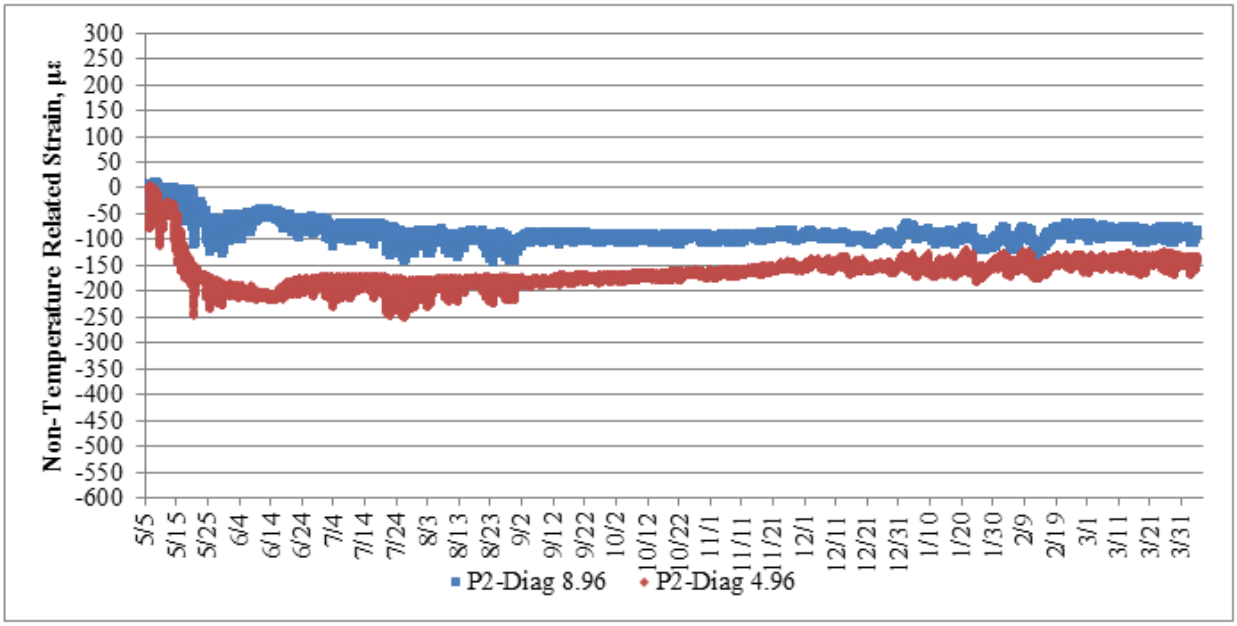

Figure 4.81: Non Temperature Related Strain at the Diagonal Location of Panel 2 in Cell 70

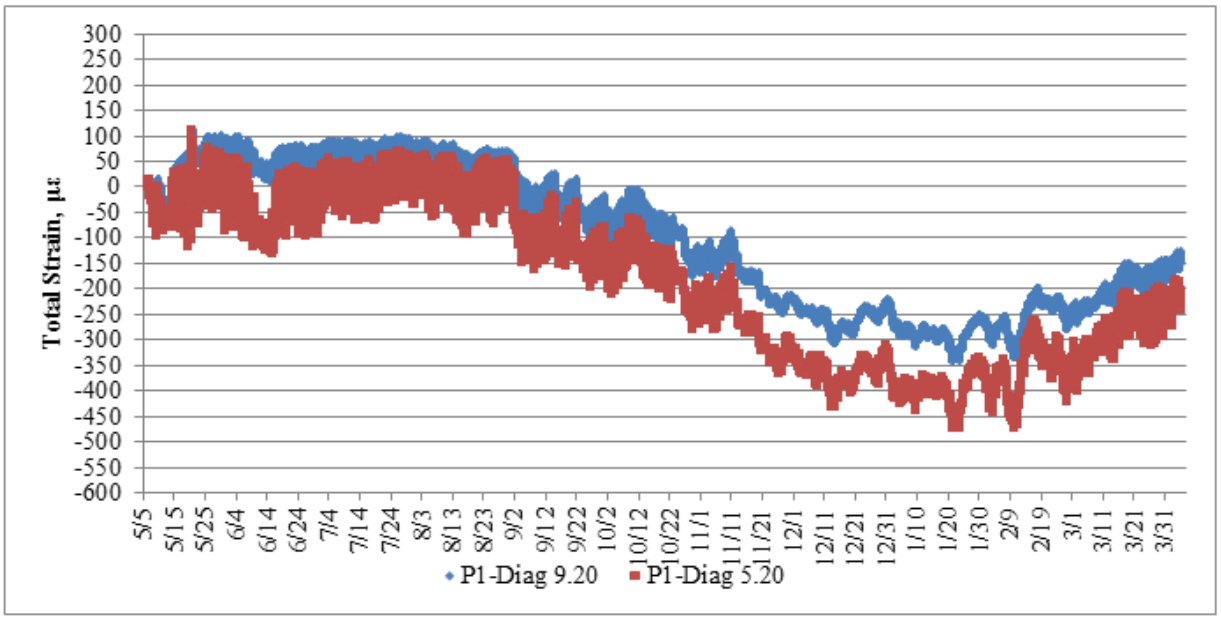

Figure 4.82: Total Strain at the Diagonal Location in Panel 1 of Cell 70

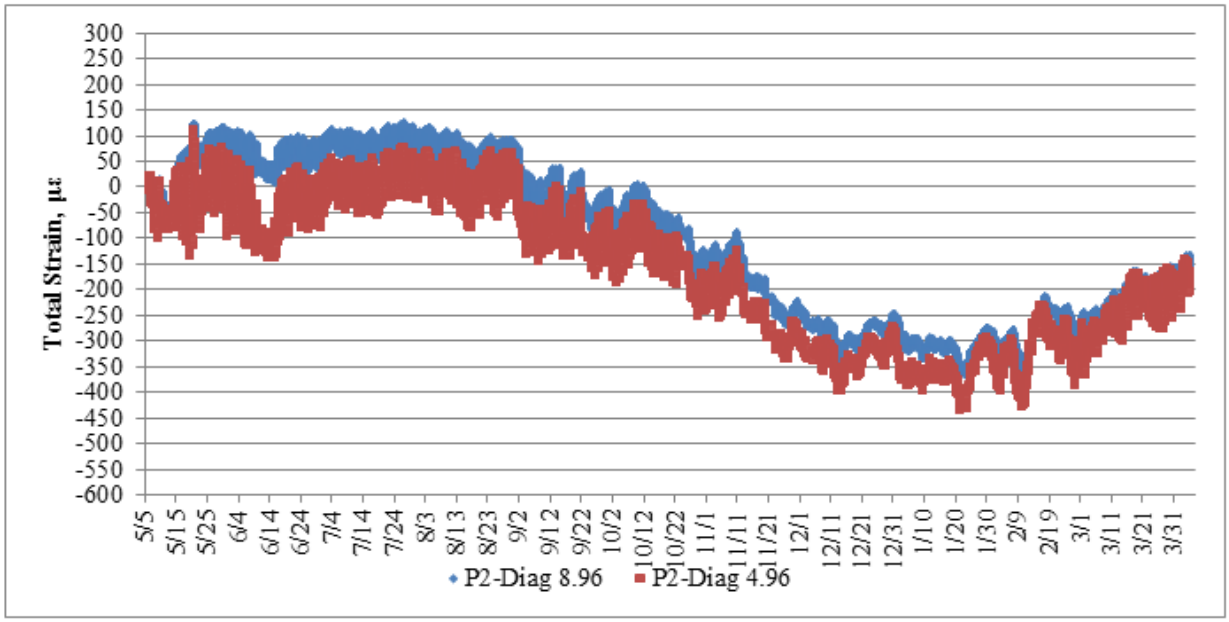

Figure 4.83: Total Strain at the Diagonal Location in Panel 2 of Cell 70

When comparing Figure 4.81 to the other non-temperature related strain figures presented in this section, it can be seen that this is the only location for which the top sensor shows such a trend of decreasing compressive strain. Since this trend is anomalous relative to the other locations, further comparisons for Cell 70 curvature measurements are based on measurements obtained from Panel 1.

In Cell 70, it was also desired to assess the effect of placing the HMA overlay on the curvature in the slab. Figure 4.84 through Figure 4.86 show the curvature and temperature gradient in the longitudinal, transverse, and diagonal direction, respectively. These figures are representative of the period of time three days prior and eleven days after paving the HMA overlay on May 20th. Despite a limited amount of pre-HMA overlay placement data, it seems that the effect of the overlay placement on the curvature and temperature gradients is not particularly pronounced.

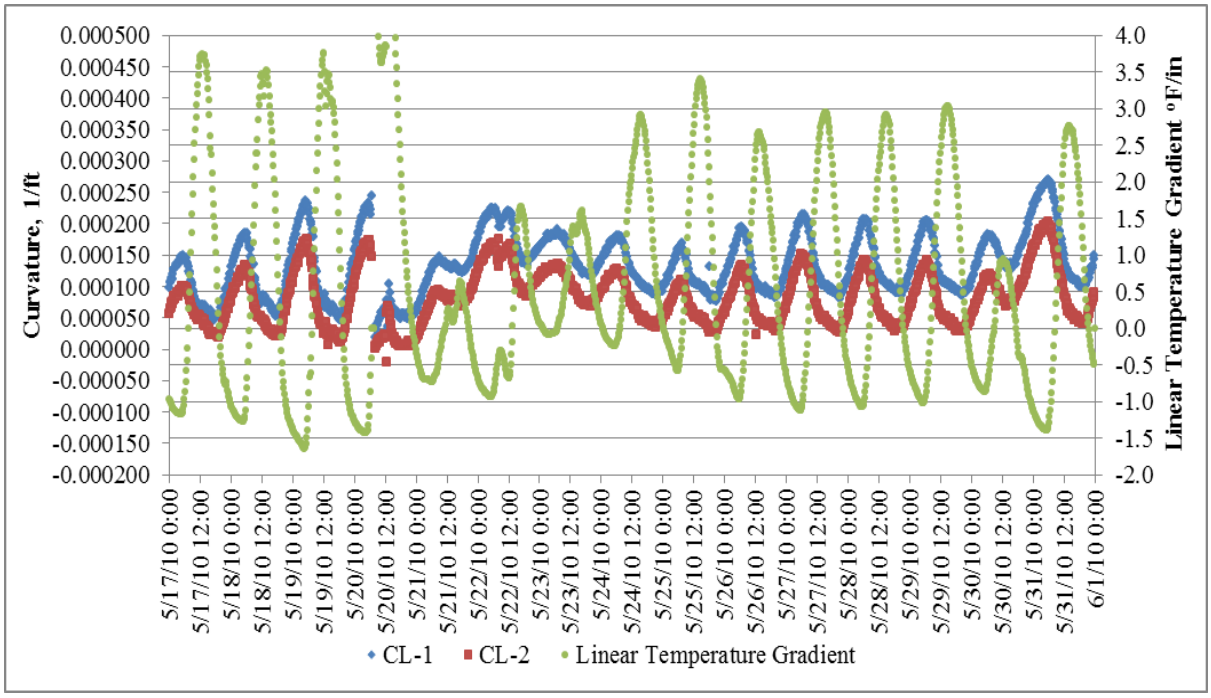

Figure 4.84: Centerline Curvature and Temperature Gradient - Cell 70 before and after the HMA Overlay

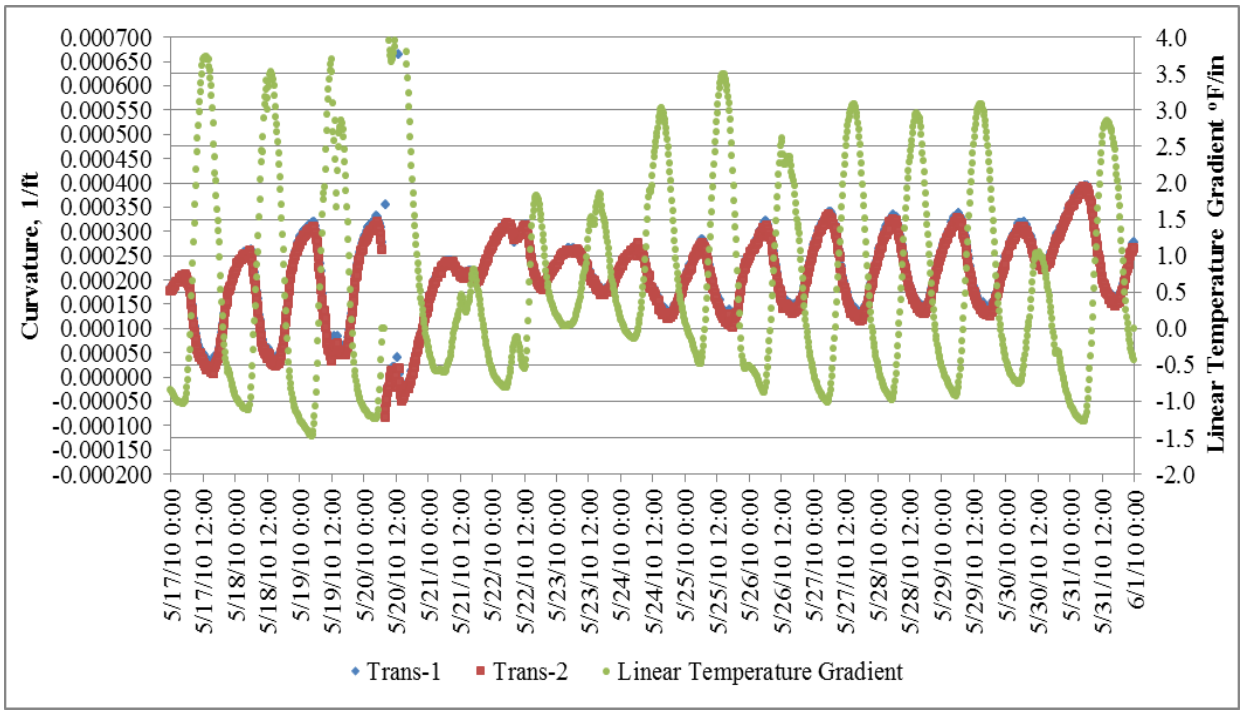

Figure 4.85: Transverse Curvature and Temperature Gradient - Cell 70 before and after the HMA Overlay

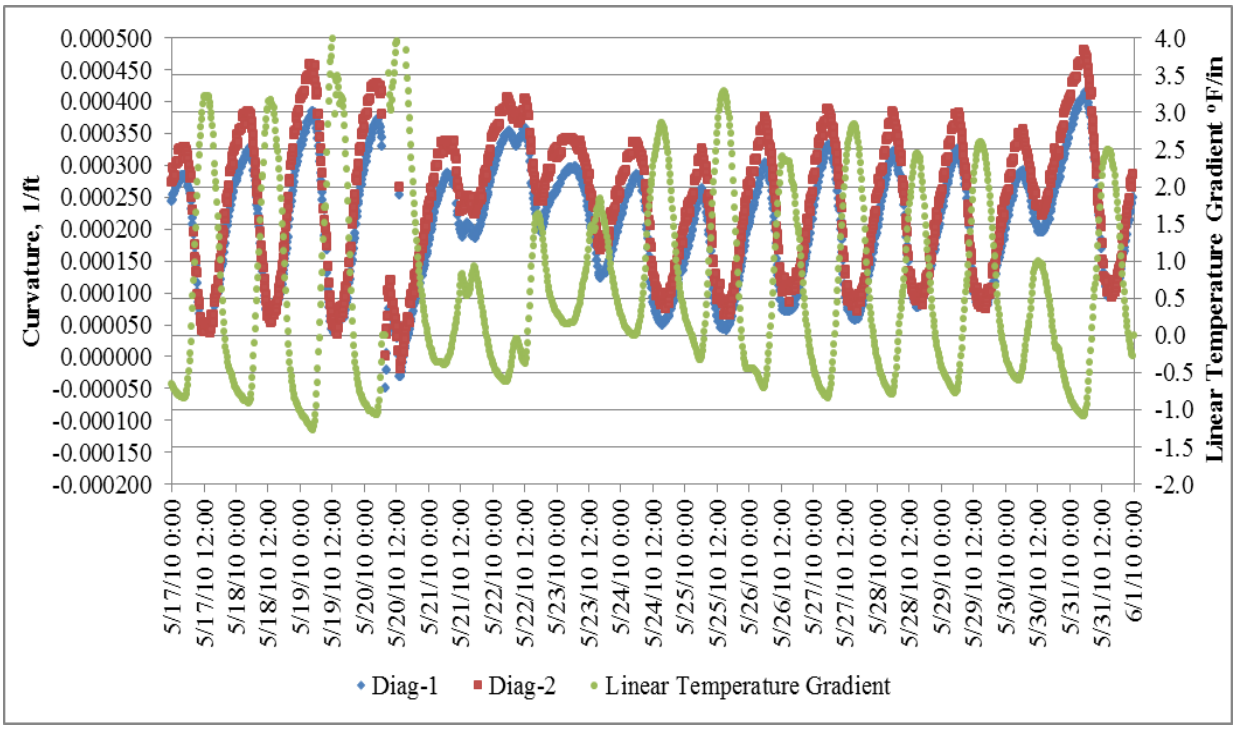

Figure 4.86: Diagonal Curvature and Temperature Gradient - Cell 70 before and after the HMA Overlay

Other times of interest from Figure 4.66 through Figure 4.70 were also evaluated. This effort was undertaken in an attempt to explain some of the inflection points in the curvature vs. time series at each location. Based on the curvature figures, perhaps the two most notable time periods to examine the relationship between curvature and temperature gradient are at the end of November and the middle of February. At the end of November, there is a disproportionately large fluctuation in the curvature in the transverse direction in both panels. In the middle of February, all panels seem to show a large fluctuation in curvature. Figure 4.87 through Figure 4.89 show the curvature and temperature gradients in the slab in late November. These figures are representative of the longitudinal, transverse, and diagonal directions respectively. Figure 4.90 through Figure 4.92 present the same figures for mid-February.

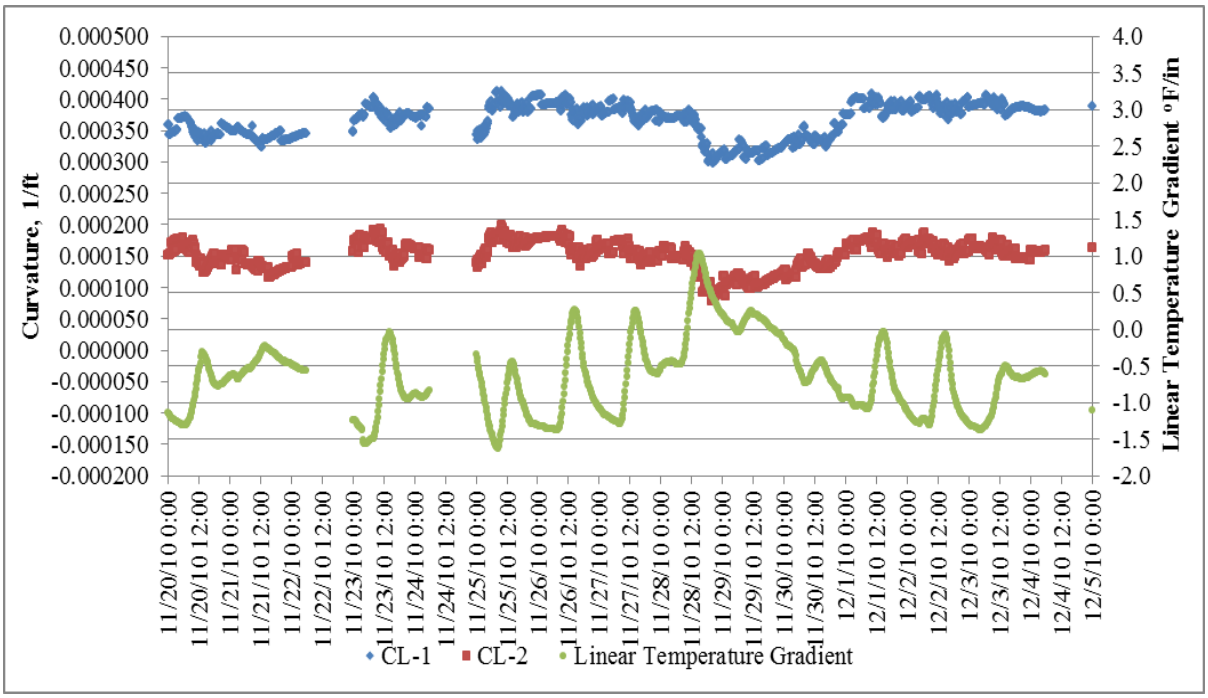

Figure 4.87: Centerline Curvature and Temperature Gradient in Cell 70 during Late November

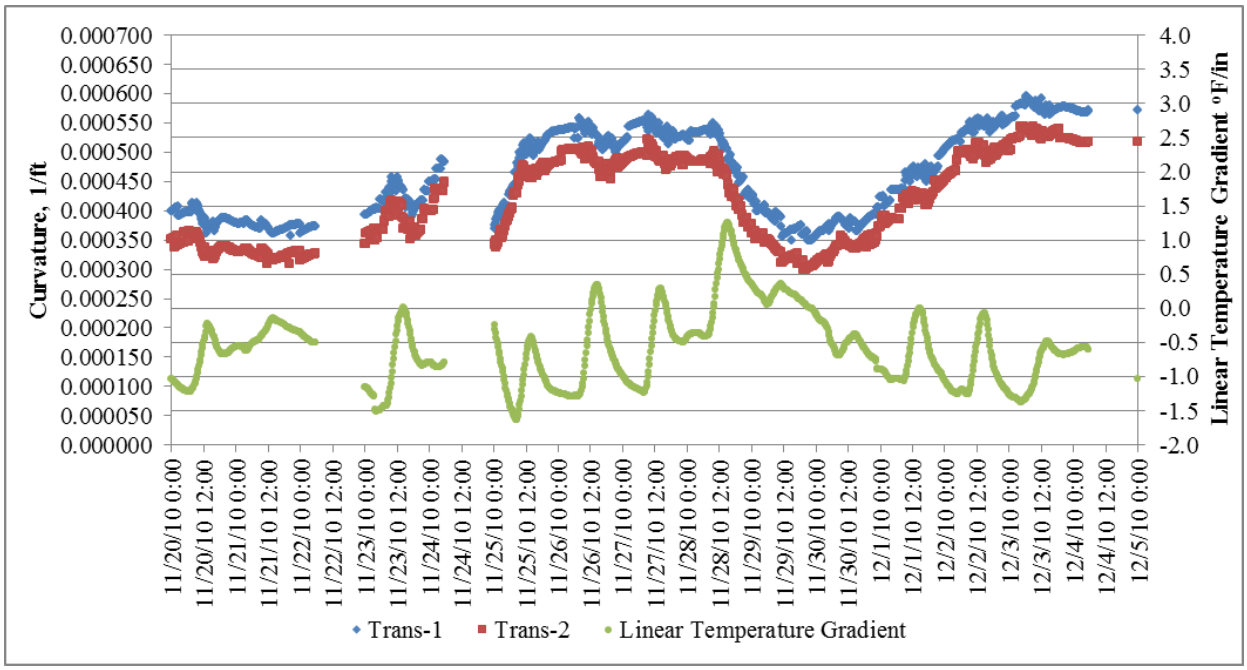

Figure 4.88: Transverse Curvature and Temperature Gradient in Cell 70 during Late November

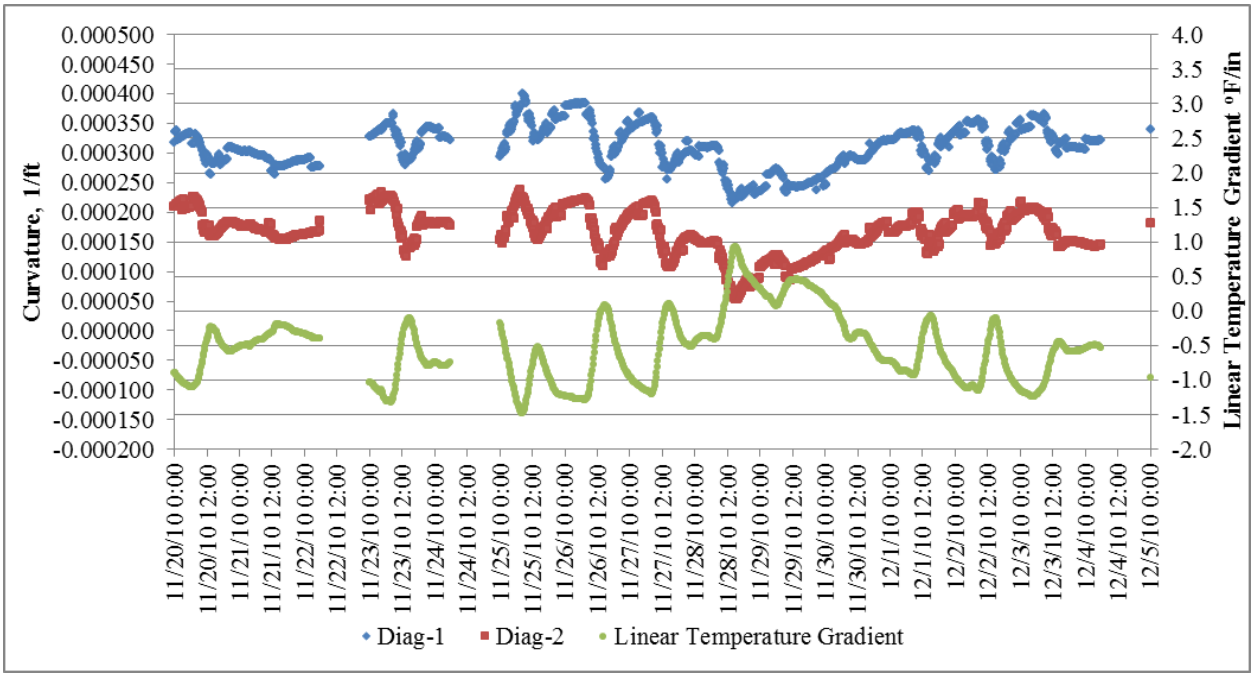

Figure 4.89: Diagonal Curvature \ and Temperature Gradient in Cell 70 during Late November

From Figure 4.87 through Figure 4.89 it can be seen that there is the most daily fluctuation in curvature at the diagonal location. It can also be seen that this location has the best response in curvature for a given temperature gradient. In the transverse direction, although there is some response in curvature for a given change in temperature gradient, the general trend of curvature from the beginning of November 28th to November 30th is opposite to what would be expected. This is also opposite to what is shown in the longitudinal and diagonal direction. Figure 4.90 through Figure 4.92 show a similar trend to Figure 4.87 through Figure 4.89. The transverse direction shows opposite trends to what would be expected while the longitudinal and diagonal directions show expected trends. The diagonal direction also curls more in response to a given temperature gradient.

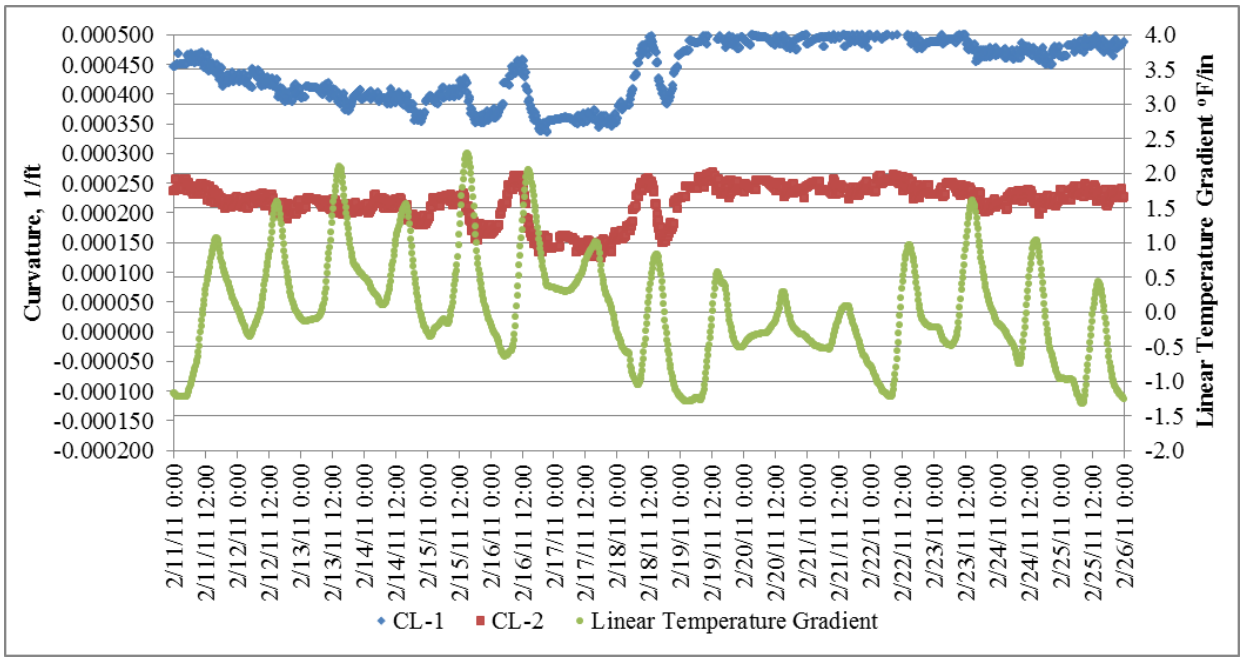

Figure 4.90: Centerline Curvature and Temperature Gradient in Cell 70 during Mid-February

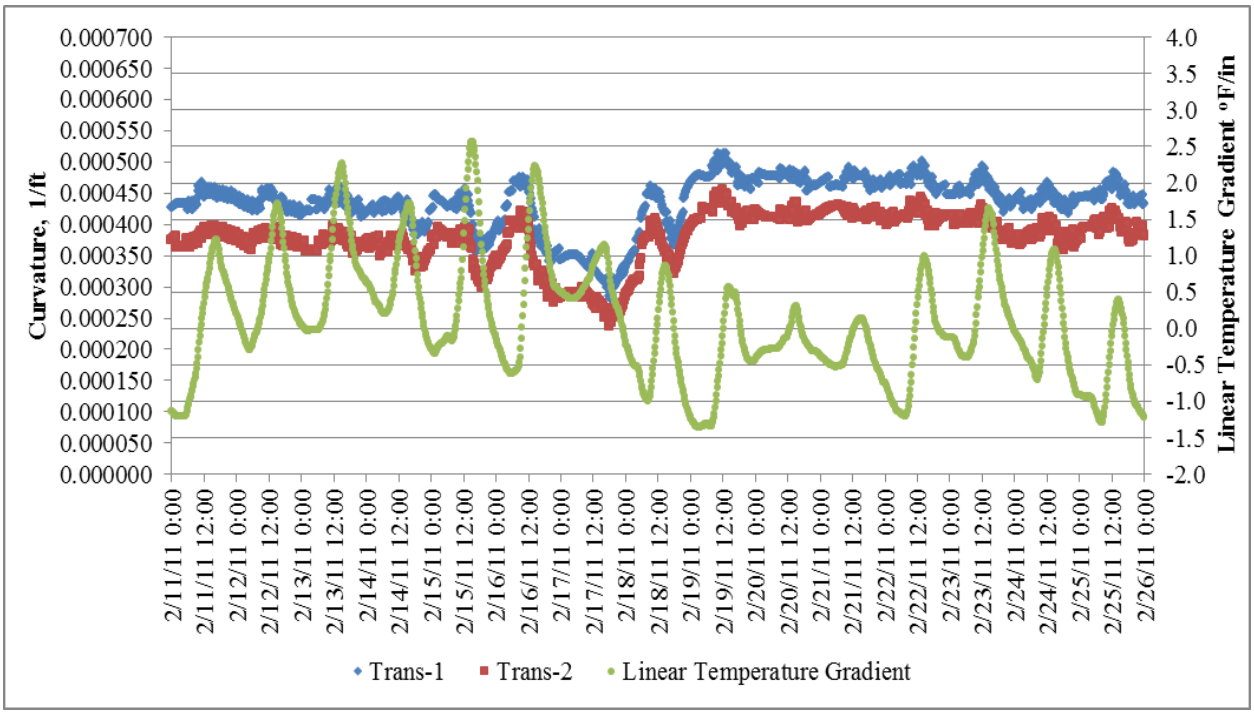

Figure 4.91: Transverse Curvature and Temperature Gradient in Cell 70 during Mid-February

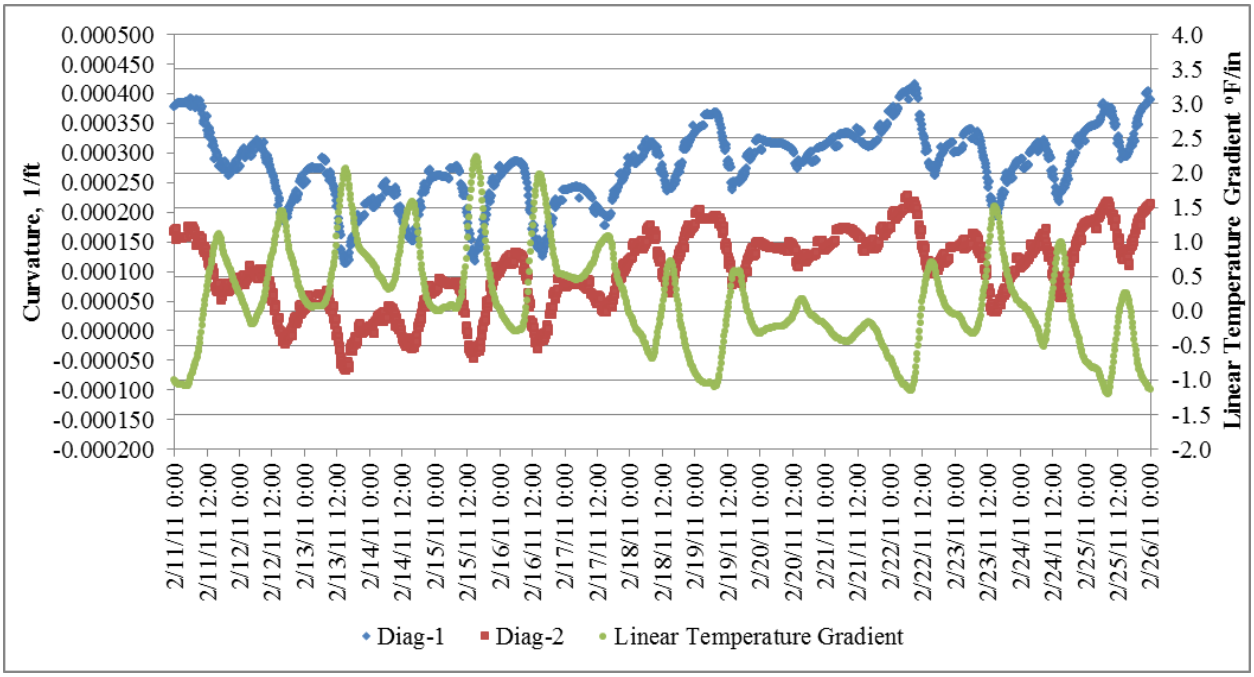

Figure 4.92: Diagonal Curvature and Temperature Gradient in Cell 70 during Mid-February

In summary, for Cell 70, it can be seen that while the transverse direction has good agreement between the panels, its response to temperature gradient is not always as expected. The diagonal location responds the most with respect to curvature induced by a given temperature gradient. The disagreement between panels in the non-transverse locations seems to be related to the variation in the development of the non-temperature related strain. The reason for this discrepancy could not be explained and a further examination of data beyond the time frame studied in this work may resolve the discrepancy between the two panels.

4.4.2 Cell 71 Slab Curvature Measurements

For Cell 71, a comparison of the calculated curvature between the panels at each location is shown in Figure 4.93 through Figure 4.97. As can be seen from these figures, there is much

better agreement in general between the two panels in Cell 71 than was seen between the two panels in Cell 70. Curvature in the longitudinal direction for Cell 71 was such that it was almost always curled up throughout the analysis period. In the transverse and diagonal directions, both positive and negative curvatures were observed.

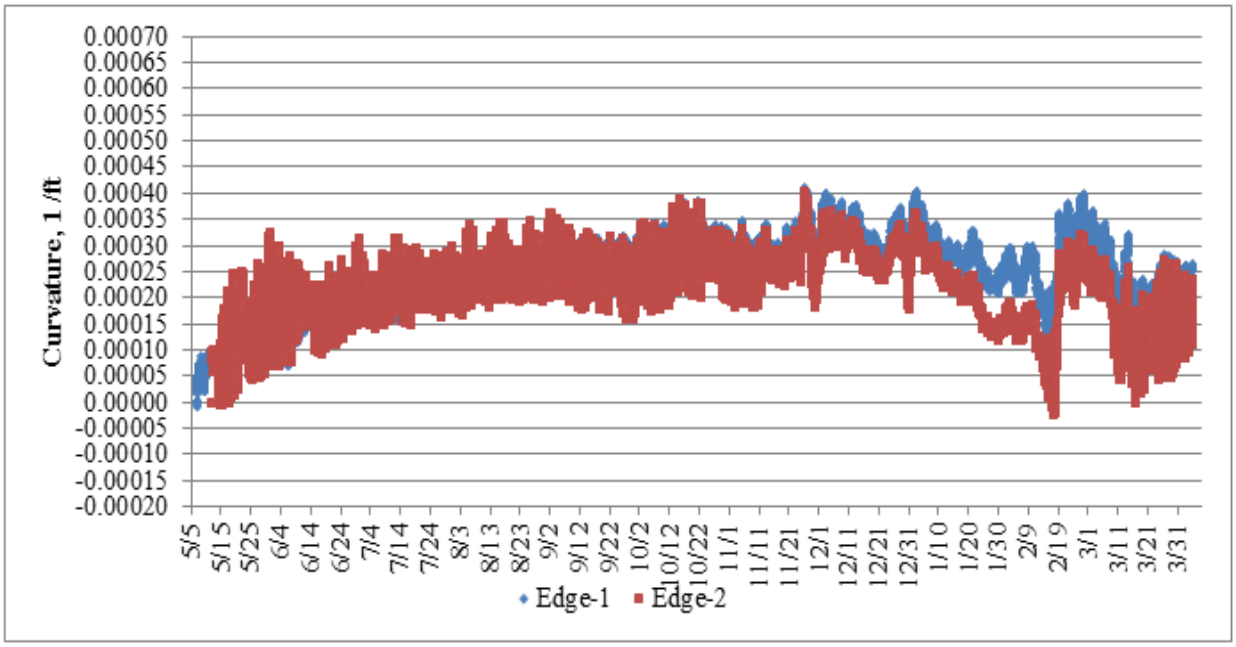

Figure 4.93: Comparison of Curvature at the Edge Location of Cell 71

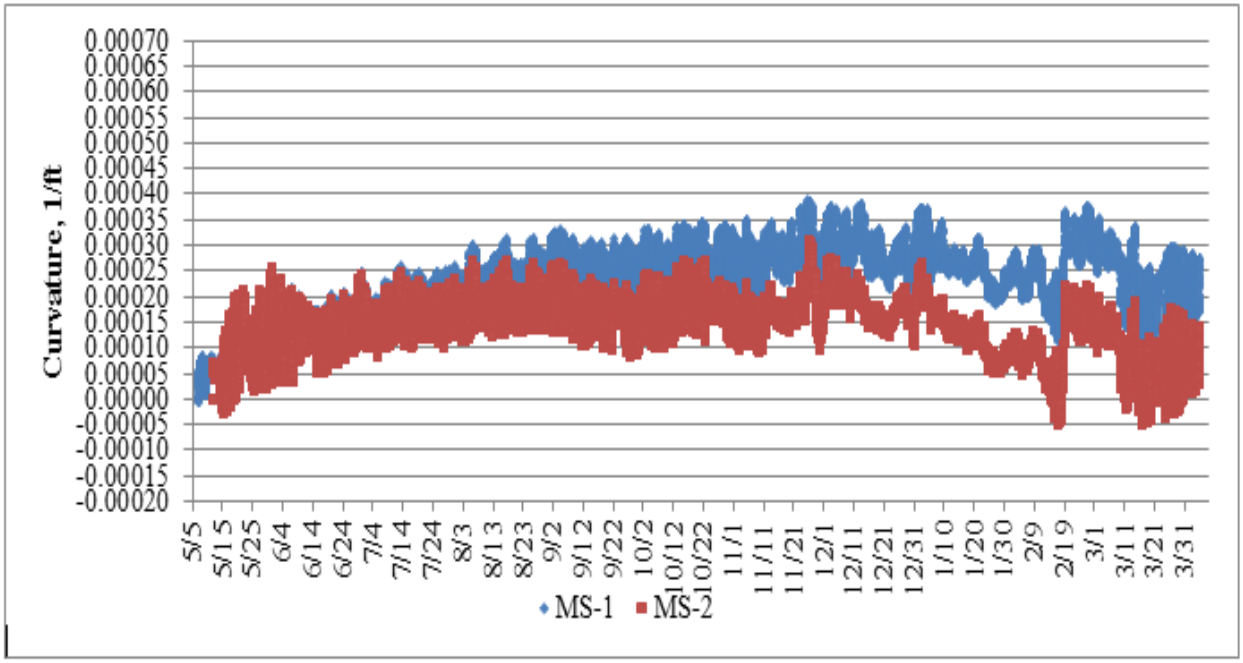

Figure 4.94: Comparison of Curvature at the Midslab Location of Cell 71

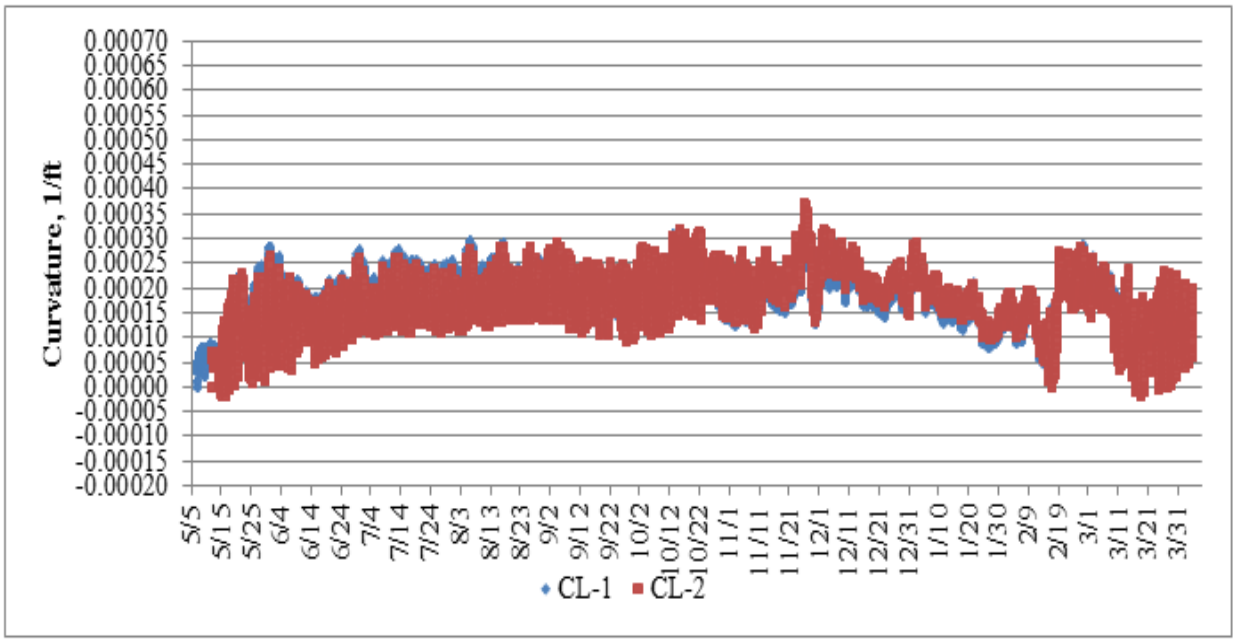

Figure 4.95: Comparison of Curvature at the Centerline Location of Cell 71

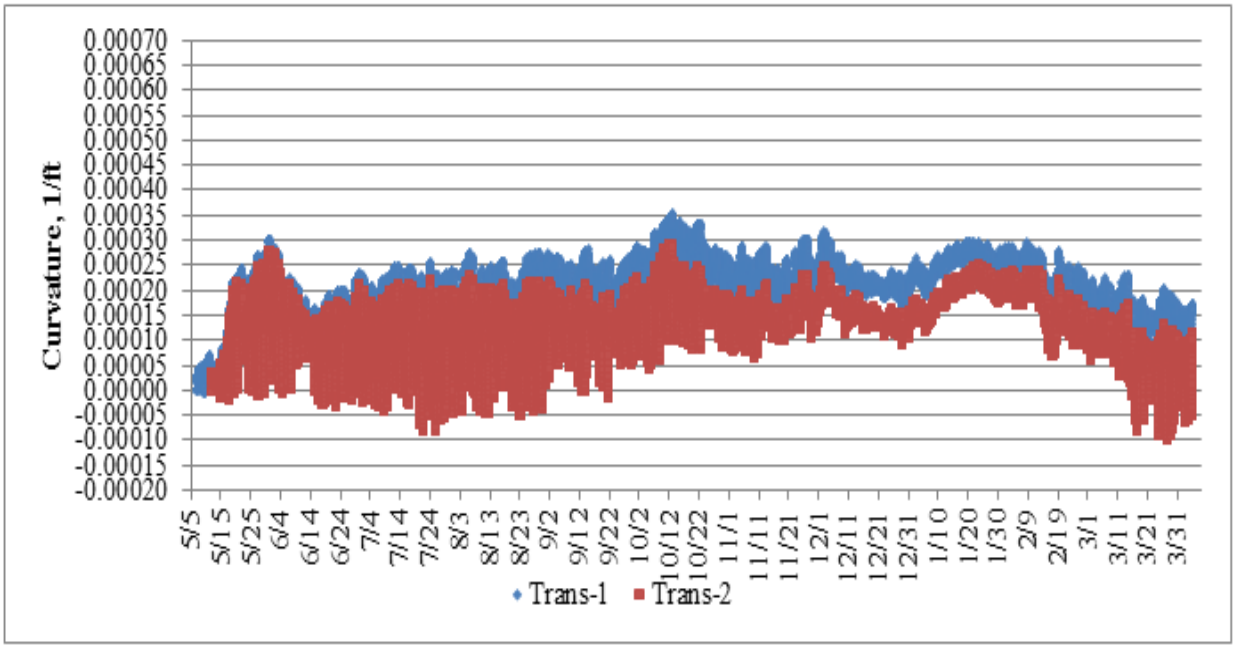

Figure 4.96: Comparison of Curvature at the Transverse Location of Cell 71

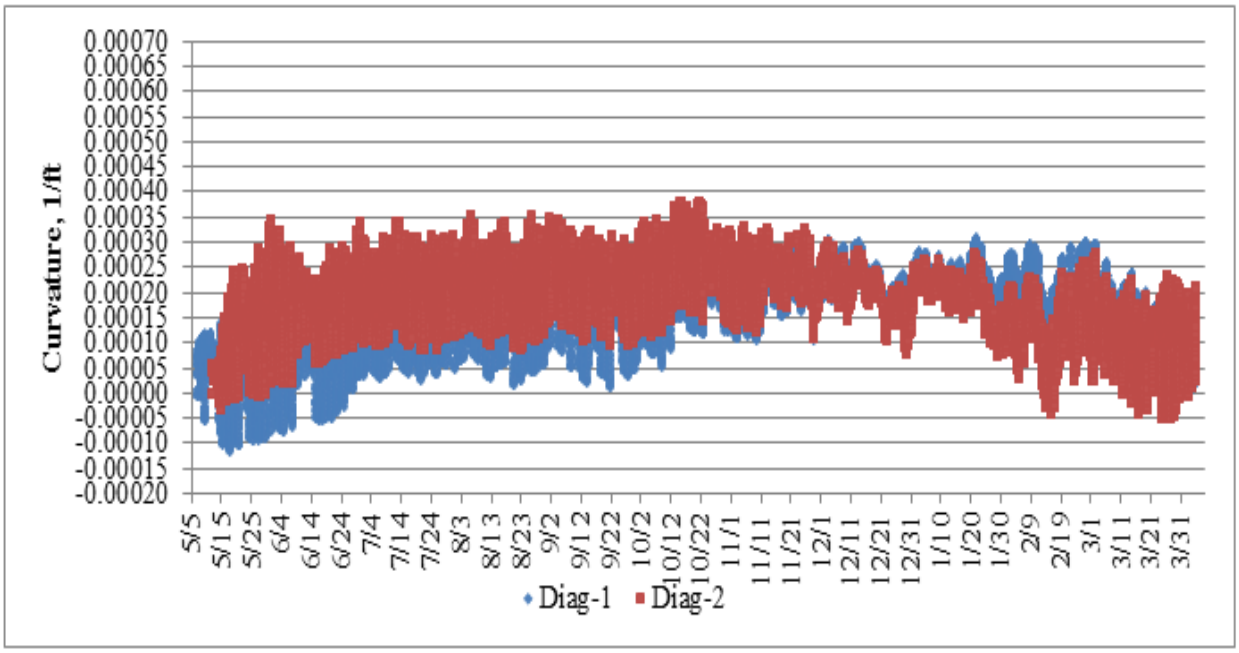

Figure 4.97: Comparison of Curvature at the Diagonal Location of Cell 71

The total strain and non-temperature related strain at the diagonal location are shown in Figure 4.98 through Figure 4.101. In general, both the non-temperature related and total strain at other locations shows good agreement between the two panels. Comparing Figure 4.98 and Figure 4.99, it can be seen that the bottom sensor in Panel 1 of Cell 71 shows somewhat erratic behavior initially. Since the strain at the bottom of the slab is used in the calculation of slab curvature, it is believed to be more beneficial to draw conclusions based on the curvature calculated from Panel 2.

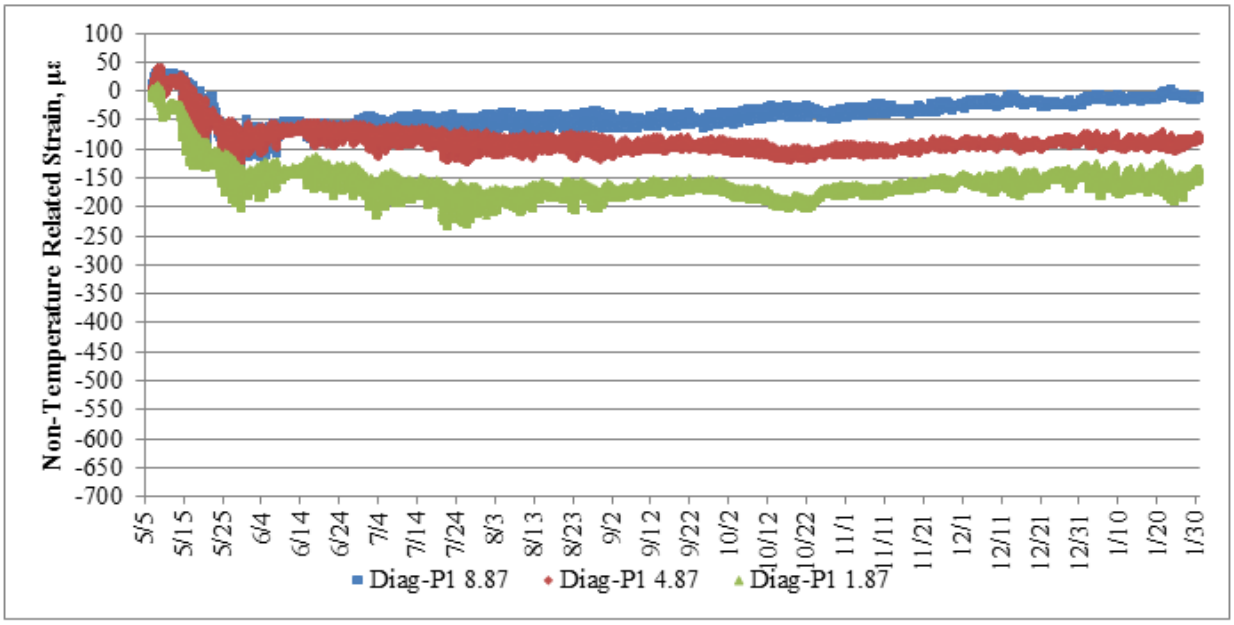

Figure 4.98: Non Temperature Related Strain at the Diagonal Location of Panel 1 in Cell 71

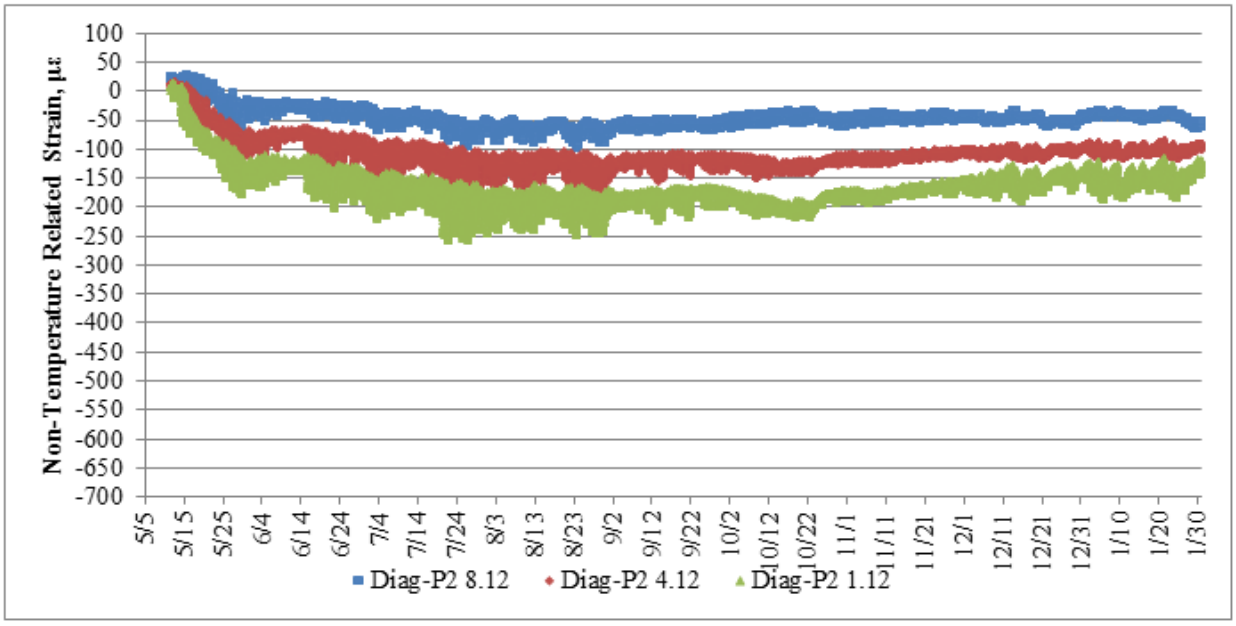

Figure 4.99: Non Temperature Related Strain at the Diagonal Location of Panel 2 in Cell 71

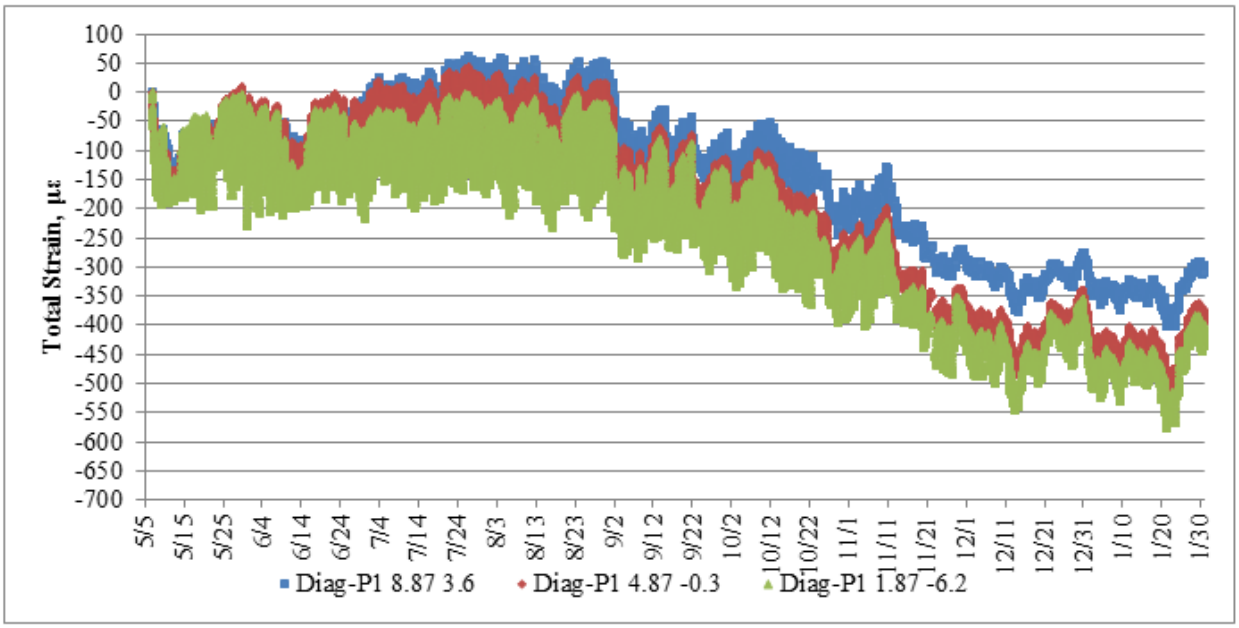

Figure 4.100: Total Strain at the Diagonal Location of Panel 1 in Cell 71

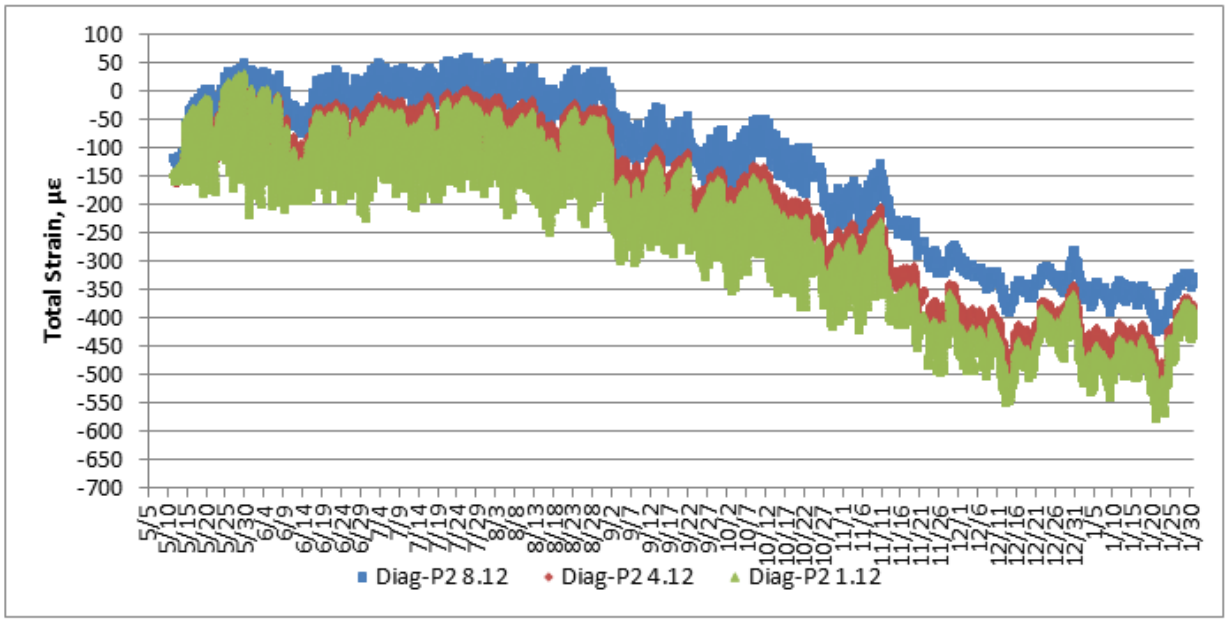

Figure 4.101: Total Strain in the Diagonal Location of Panel 2 in Cell 71

As was done in Figure 4.84 through Figure 4.92 for Cell 70, it was also desired to assess the relationship between curvature and the linear temperature gradient for Cell 71. This was done partly to see if the same trend was observed with respect to location as was seen for Cell 70. Additionally, this analysis was also performed to see if the same disagreement between the curvature and the transient temperature gradient at the transverse location was observed. Curvature and temperature gradients at each of the desired locations are shown in Figure 4.102 through Figure 4.104. While there is still some time lag between the peak temperature gradient and peak curvature for the transverse direction, these figures show that the curvature and temperature gradients agree much better in the transverse location for Cell 71 relative to Cell 70. The relationship between curvature and linear temperature gradient is strongest in the diagonal location however.

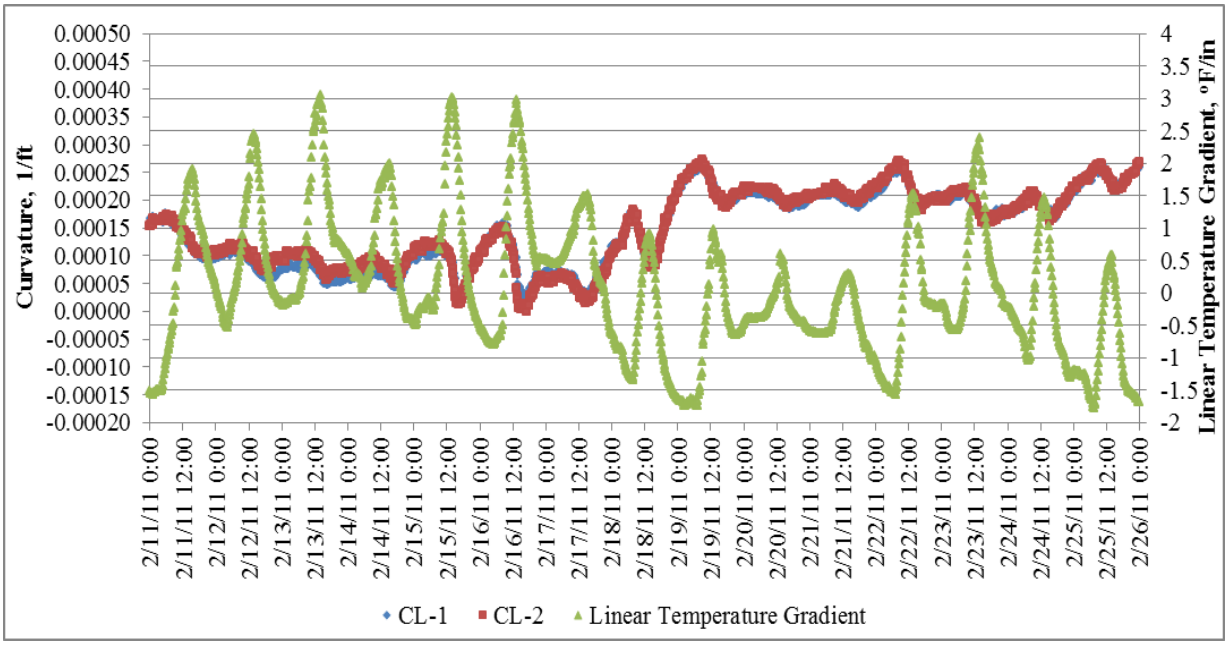

Figure 4.102: Centerline Curvature and Temperature Gradient in Cell 71 during Mid-February

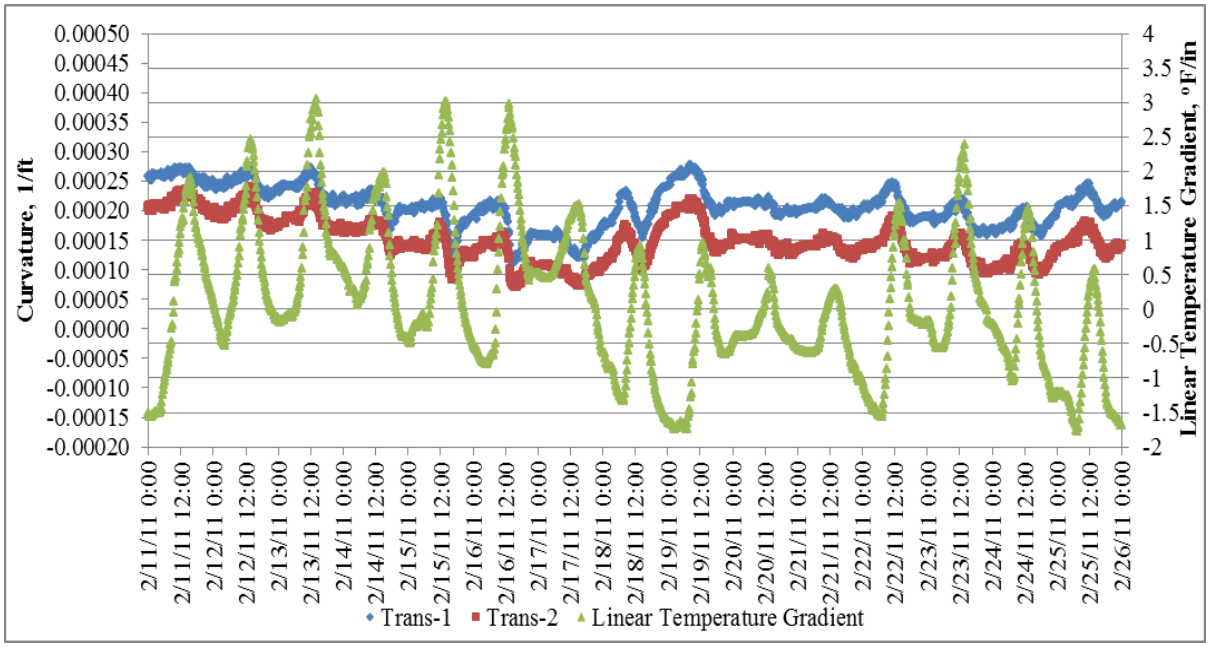

Figure 4.103: Transverse Curvature and Temperature Gradient in Cell 71 during Mid-February

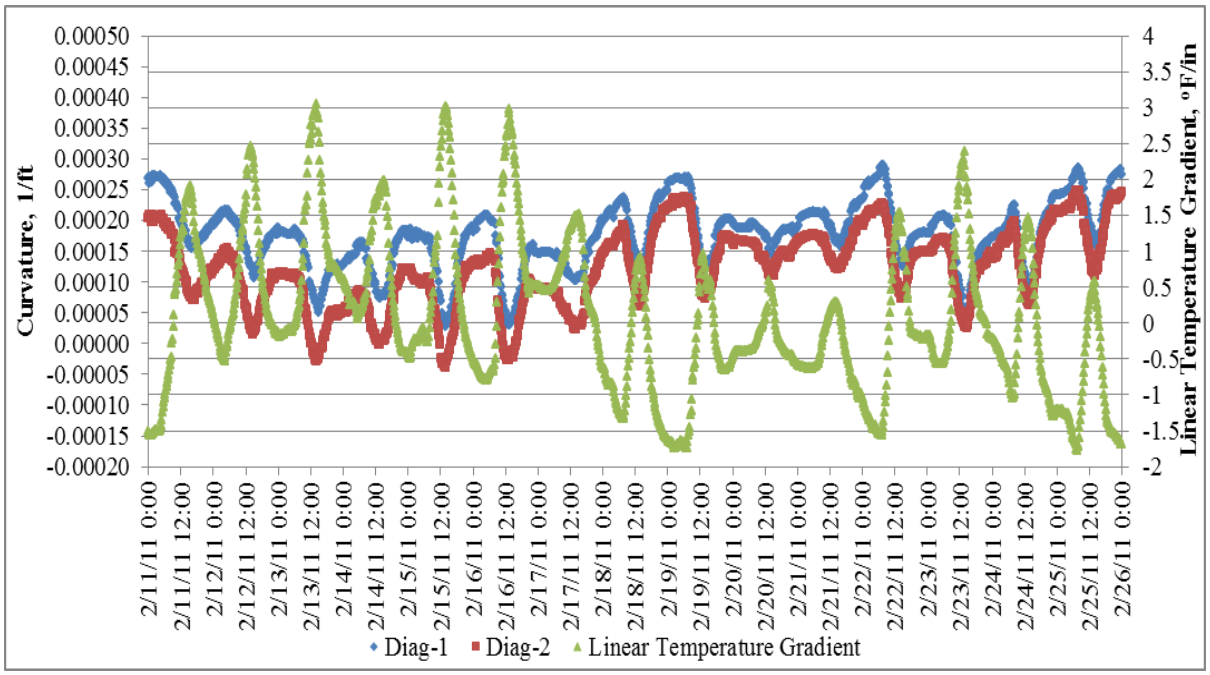

Figure 4.104: Diagonal Curvature and Temperature Gradients in Cell 71 during Mid-February

4.4.3 Cell 72 Slab Curvature Measurements

A comparison of the curvature in Cell 72 between the five locations in each panel can be seen in Figure 4.105 through Figure 4.109. Most locations, perhaps with the exception of the centerline and diagonal location, show good agreement between the panels. A closer examination of the non-temperature related and total strain at the diagonal location for each panel can be seen in Figure 4.110 through Figure 4.113.

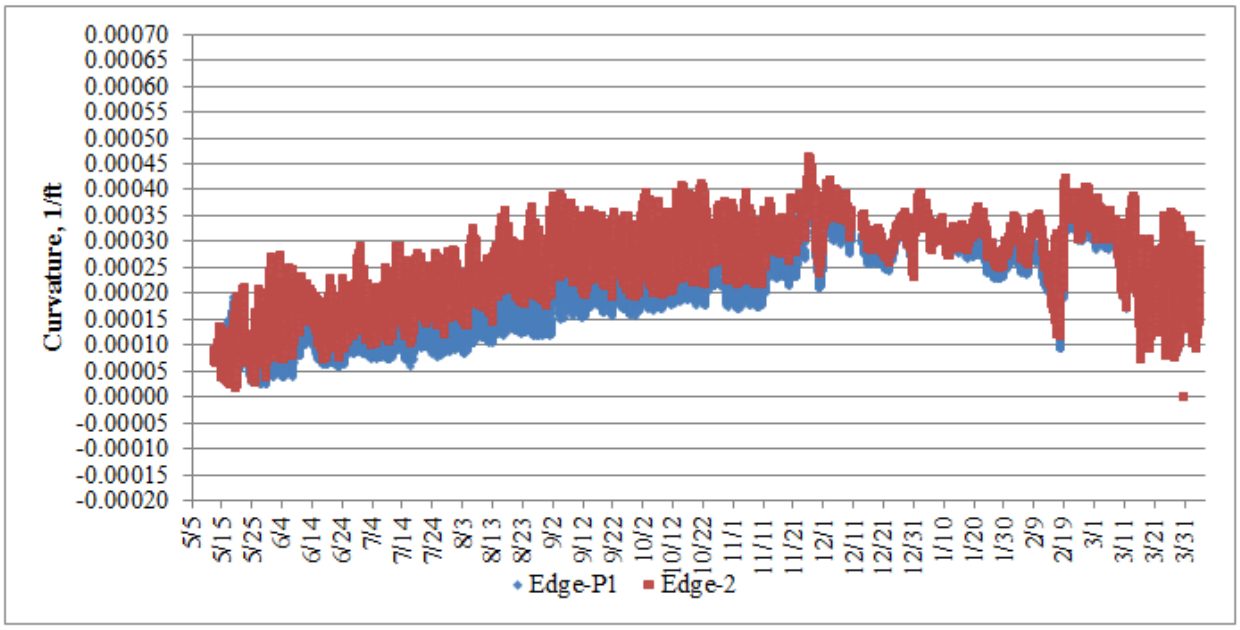

Figure 4.105: Comparison of Curvature at the Edge Location of Cell 72

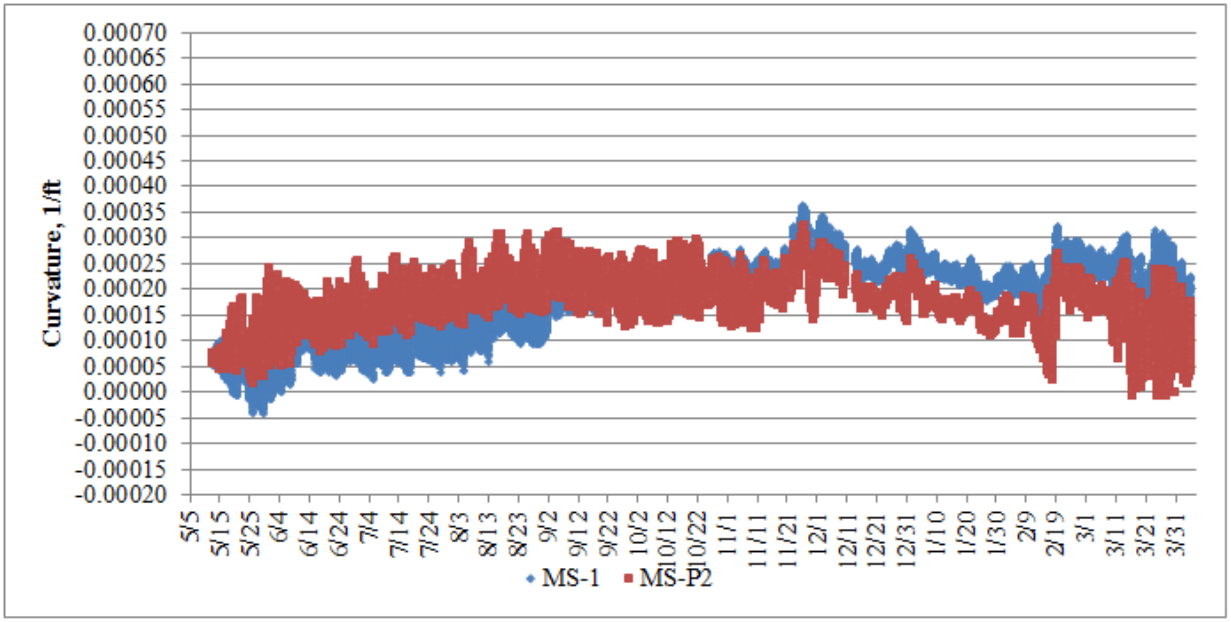

Figure 4.106: Comparison of Curvature at the Midslab Location of Cell 72

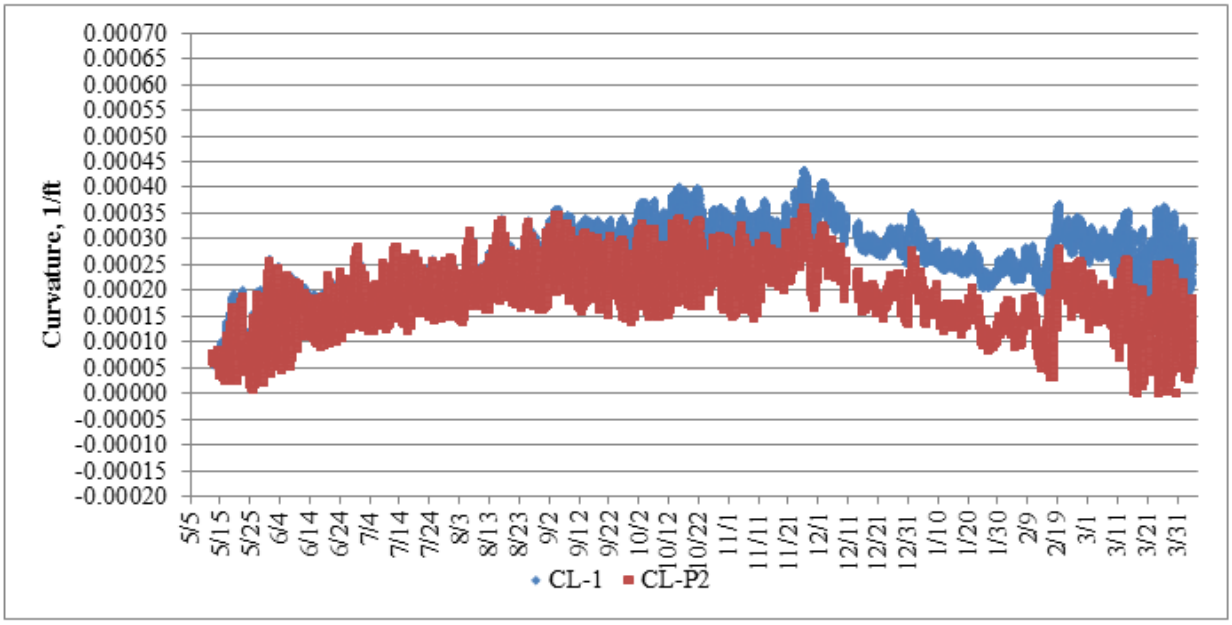

Figure 4.107: Comparison of Curvature at the Centerline Location of Cell 72

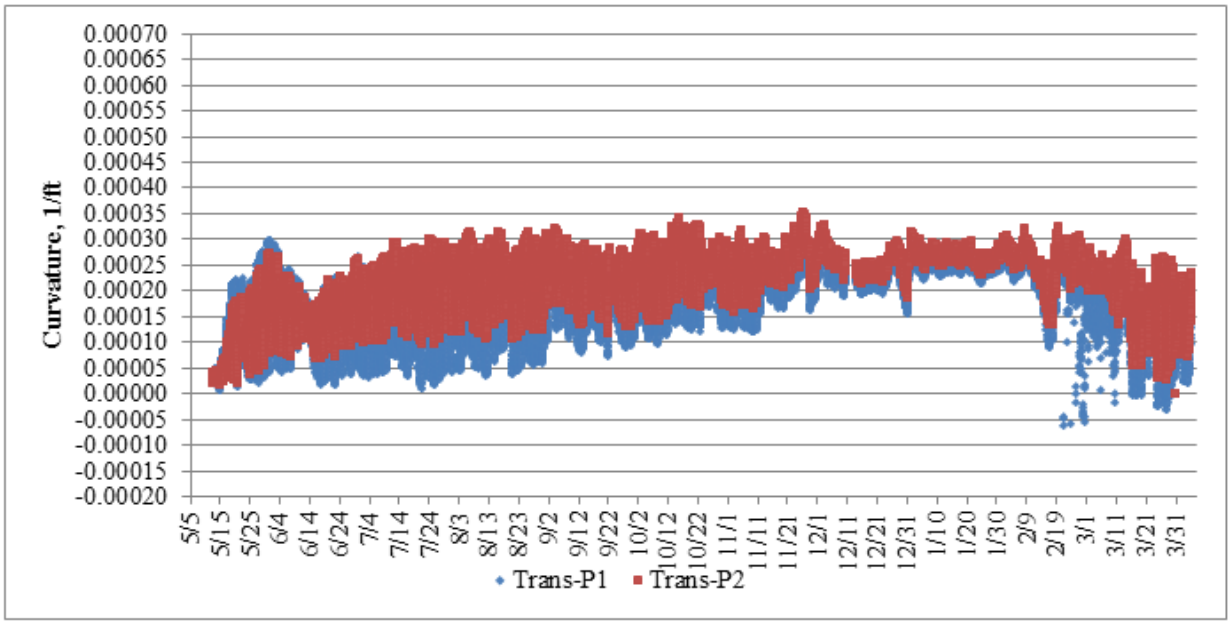

Figure 4.108: Comparison of Curvature at the Transverse Location of Cell 72

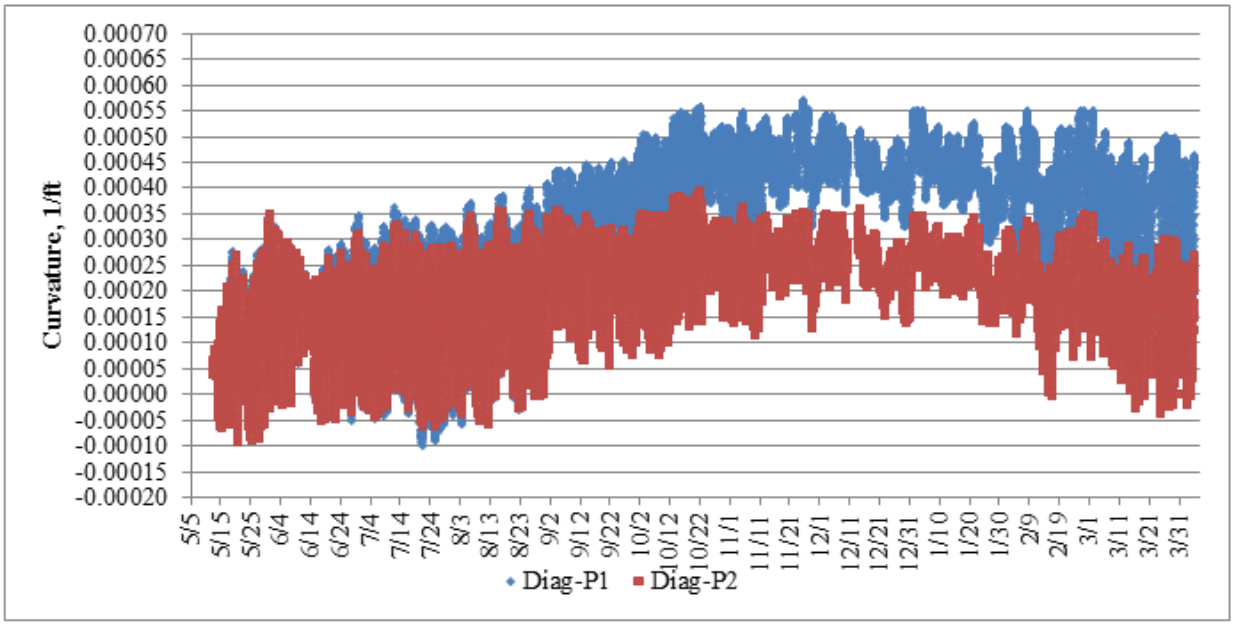

Figure 4.109: Comparison of Curvature at the Diagonal Location of Cell 72

Figure 4.110 through Figure 4.113 depict the non-temperature related and total strain at the diagonal location of the two panels in Cell 72.

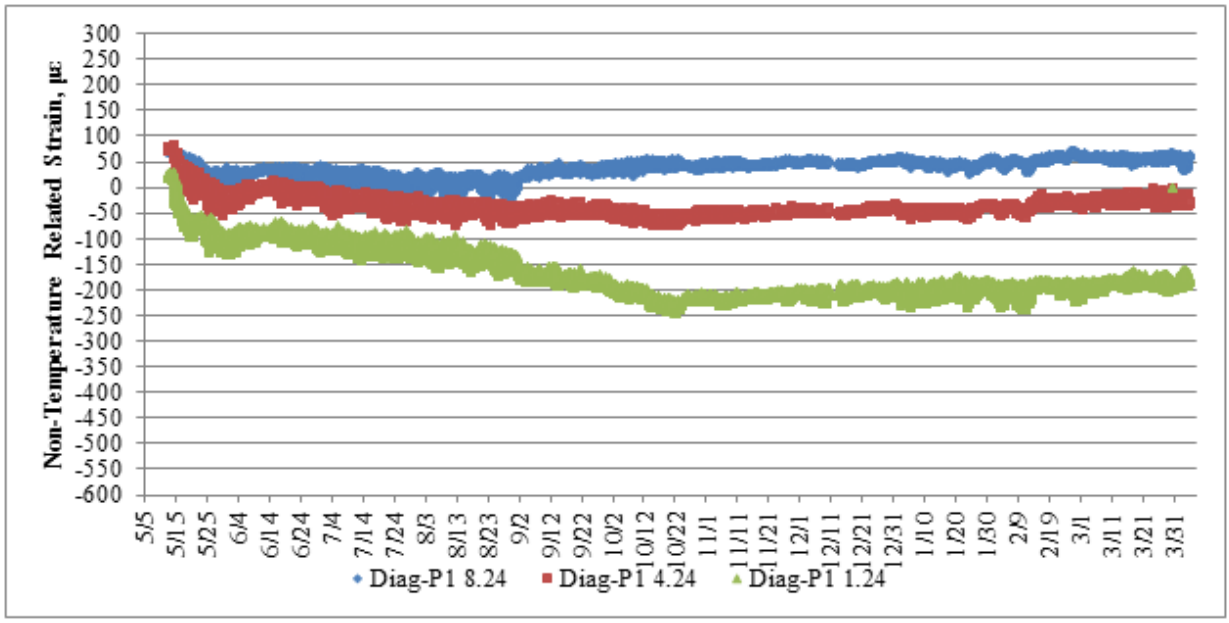

Figure 4.110: Non Temperature Related Strain at the Diagonal Location of Panel 1 in Cell 72

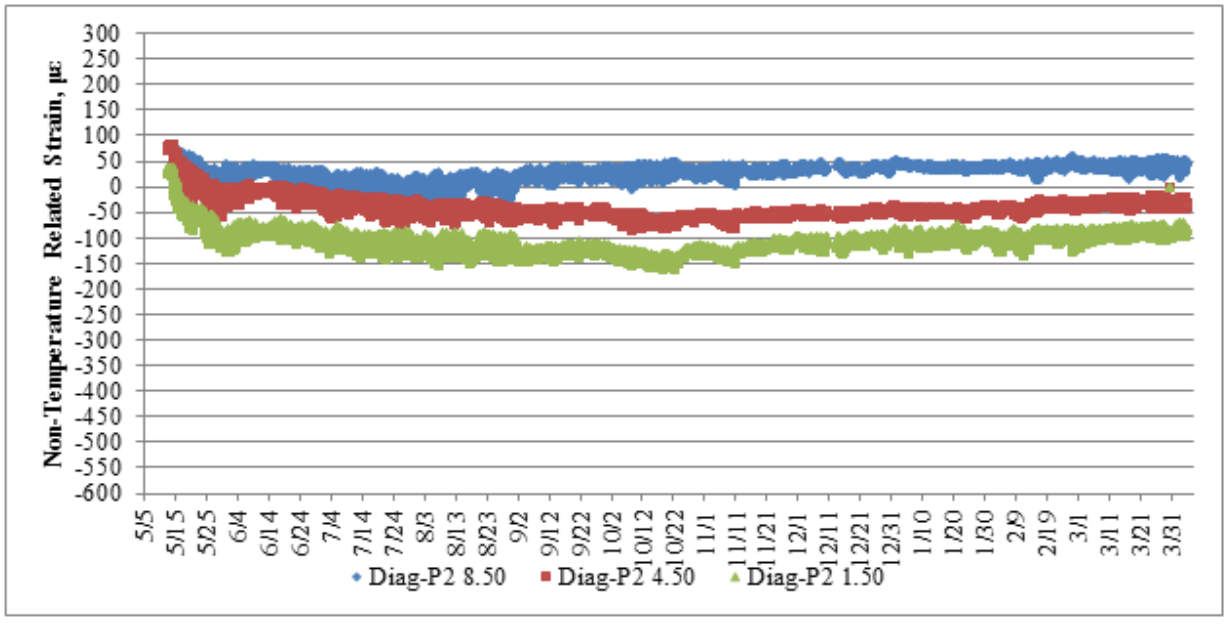

Figure 4.111: Non Temperature Related Strain at the Diagonal Location of Panel 2 in Cell 72

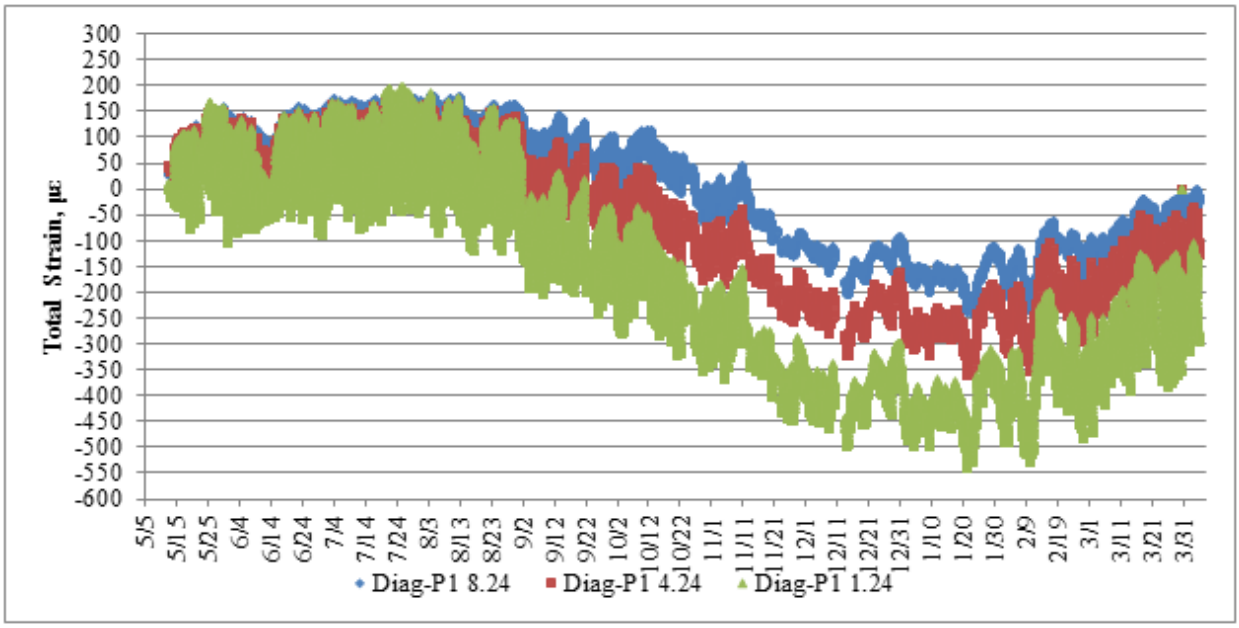

Figure 4.112: Total Strain at the Diagonal Location of Panel 1 in Cell 72

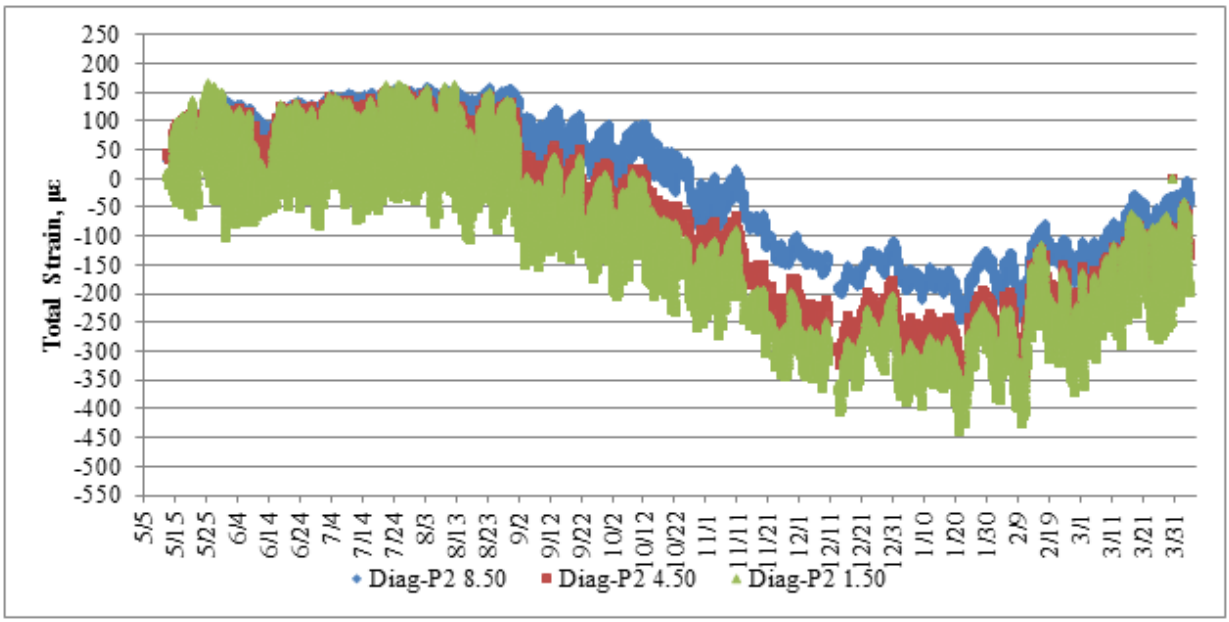

Figure 4.113: Total Strain at the Diagonal Location of Panel 2 in Cell 72

The discrepancy in the diagonal direction curvature between the two panels of Cell 72 can be shown to be a result of observations from Figure 4.110. In Figure 4.110, the non-temperature related strain in Panel 1 starts to become more compressive in the beginning of September and ending at the end of October. After the end of October, the compressive non-temperature related strain starts to increase. While there is a correlation between the maximum non-temperature related strain and the lowest relative humidity in October, the non-temperature related strain does not increase again as relative humidity levels rebound in the winter. Panel 2, therefore, is believed to be more beneficial with respect to assessing the behavior of the curvature between the cells.

The analysis performed in this and the previous two sections focused on establishing the variation between the panels of each cell. A qualitative evaluation of which panel in each cell provided better data was also performed. Interpretation of the strain readings with respect to curvature, non-temperature related strain, and total strain was also performed. It was generally found that differences in curvature between panels were the result of trends in the non-temperature related portion of the strain readings. This portion includes strain due to drying shrinkage, creep, self-weight, and restrained thermal expansion. It was also noted that the curvature response to a given temperature gradient was different at different locations and that the curvature at the diagonal location was the most in-sync with the transient temperature gradients.

The most common feature between all of the sensor locations was the differential increase in the non-temperature related strain between the top and bottom gages over the first month after paving. This is believed to be due to the effects of autogeneous drying shrinkage and the first drying event. This time period corresponds well with the initial drop in uniform relative

humidity throughout the slab, as discussed in Section 4.3. The residual non-temperature related strain in each of the gauges, beyond the first month after paving, could represent the portion of drying shrinkage that is irrecoverable.

4.4.4 Comparison of Curvature between Cells

Figure 4.114 through Figure 4.118 shows the curvature calculated at each location in all six instrumented panels. In Figure 4.114 through Figure 4.116 it can be seen that the two composite pavements comprised of PCC agree fairly well in the longitudinal direction. Panel 1 of Cell 70 generally shows more curvature relative to Cell 71 and 72, and Panel 2 of Cell 70 generally shows less curvature relative to Cell 71 and Cell 72. The curvature in the transverse direction for all cells is illustrated in Figure 4.117. In the transverse direction, both panels in Cell 70 show more curvature relative to Cells 71 and 72. Figure 4.118 shows that in the diagonal direction, Cell 70 shows more curvature than Cell 71 and Cell 72 initially but that after the first couple of months, it is difficult to interpret a trend in the relative magnitudes of the curvature between the panels of the three cells.

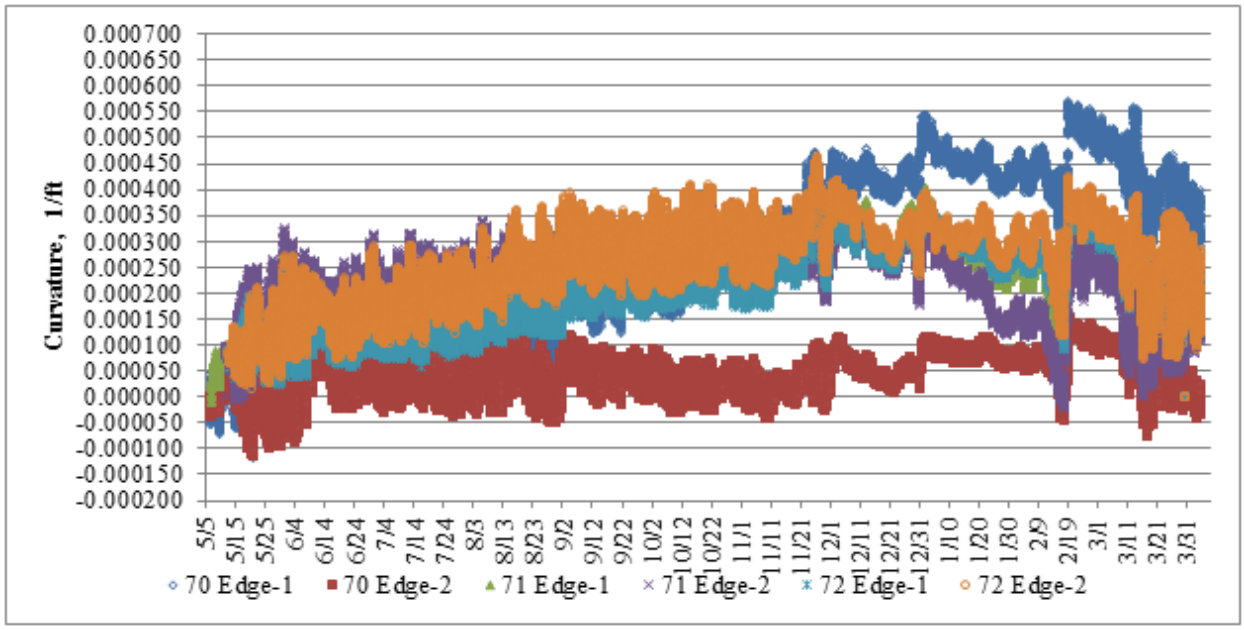

Figure 4.114: Comparison of Curvatures at the Edge Location of All Cells

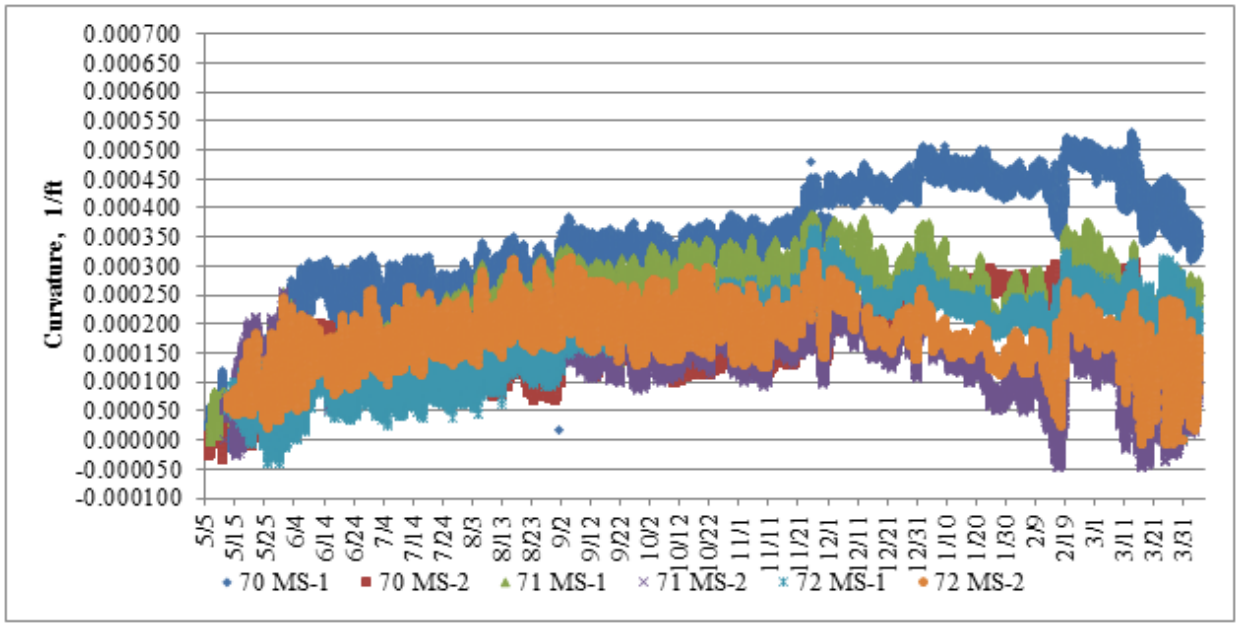

Figure 4.115: Comparison of Curvatures at the Midslab Location of All Cells

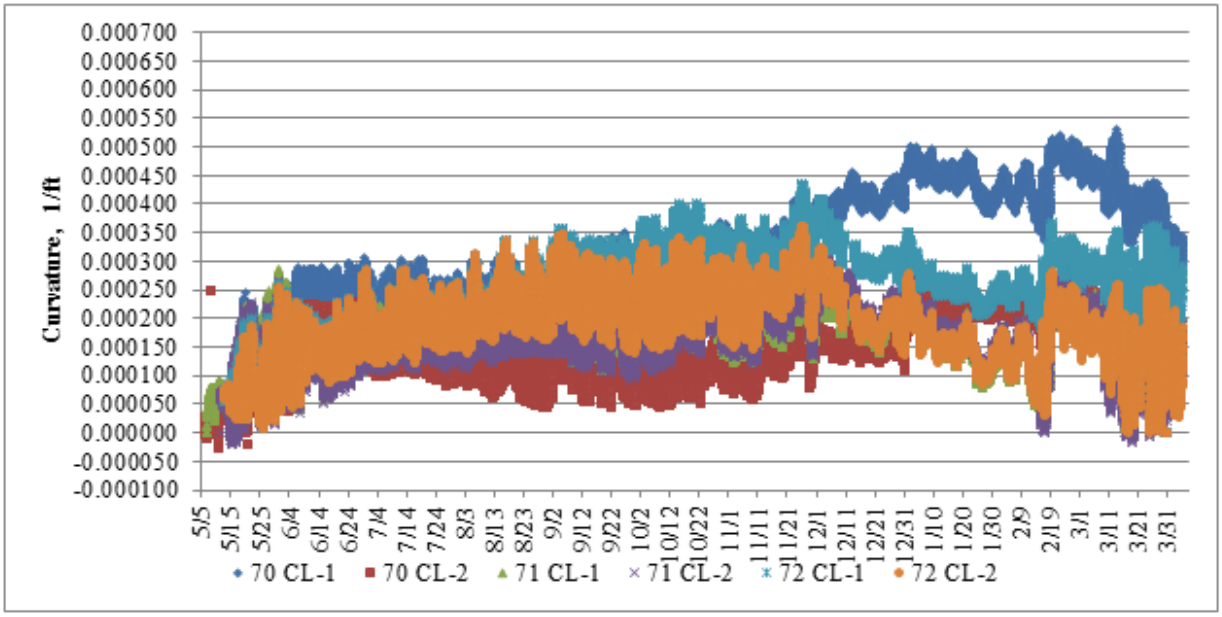

Figure 4.116: Comparison of Curvatures at the Centerline Location of All Cells

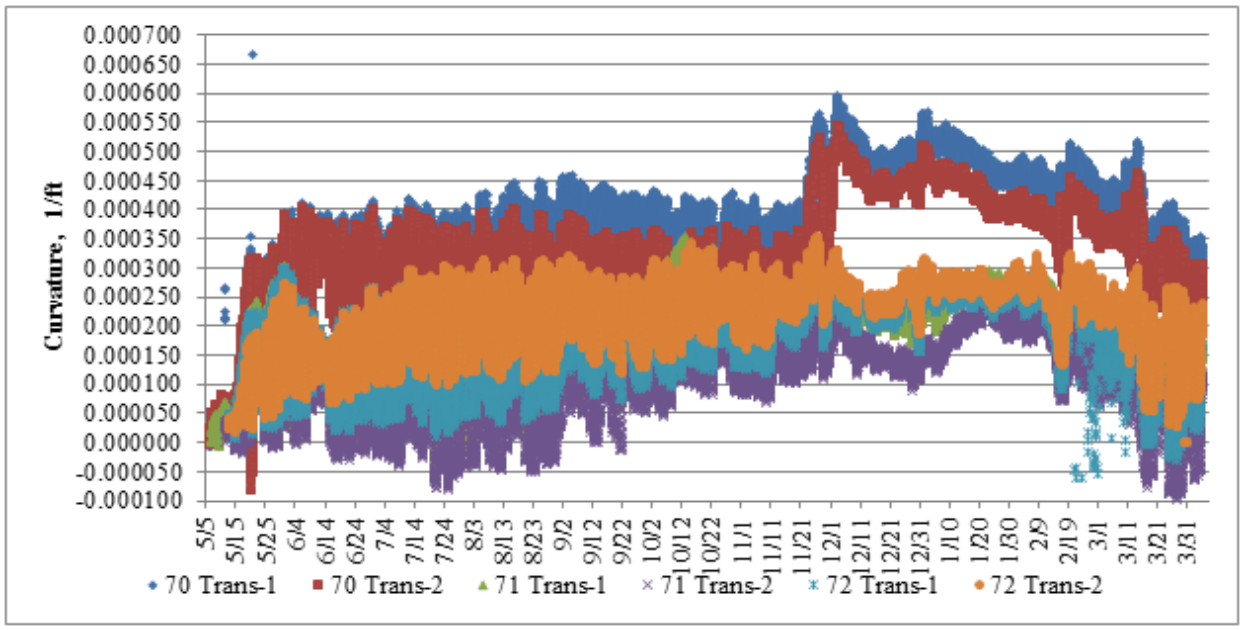

Figure 4.117: Comparison of Curvatures at the Transverse Location of All Cells

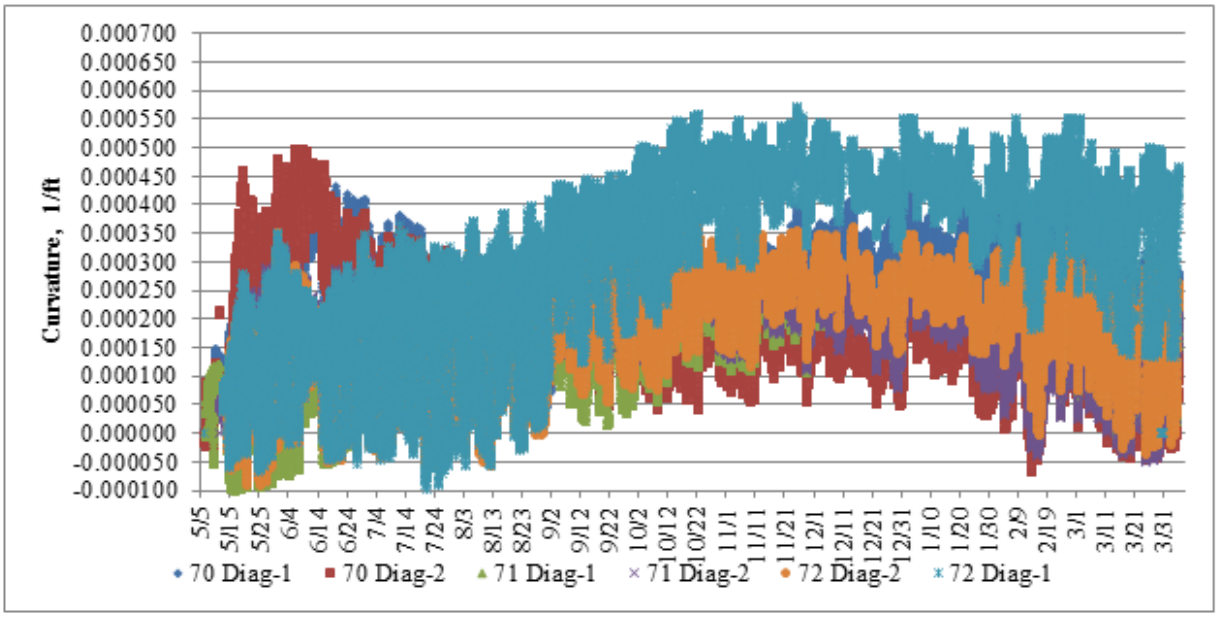

Figure 4.118: Comparison of Curvatures at the Diagonal Location of All Cells

Although the structural design and materials between the two adjacent panels in each cell are the same, there is still some inherent variability in the curvature calculations shown in the previous five figures. In general, the cause of the deviation was related to the deviation in the non-temperature related strain.

In the previous subsections the diagonal sensor location was generally highlighted as a representative location for assessing slab curvature. At the corner location, the vibrating wire sensors are positioned to capture a portion of the curling in both the longitudinal and transverse direction. This is also the location where curvature is most likely to be exacerbated since it is the farthest location from midslab. In each of the previous three sub-sections, the corner location curvature was assessed for the panel whose results produced more realistic measurements. A brief discussion was provided as to the specific panel whose curvature measurements might be

more representative. These panels were delineated based on comparing the trends in the non-temperature related strain at the corner and other locations.

Based on the trends shown in each panel, it is believed that a comparison of the curvature in Panel 2 of Cell 71 and 72 and Panel 1 in Cell 70 will provide the most reasonable results. The reasons for choosing these panels were discussed in Sections 4.4.1, 4.4.2, and 4.4.3 for Cells 70, 71, and 72 respectively. The curvature in Panel 1 of Cell 70 and Panel 2 of Cells 71 and 72 is shown in Figure 4.119.

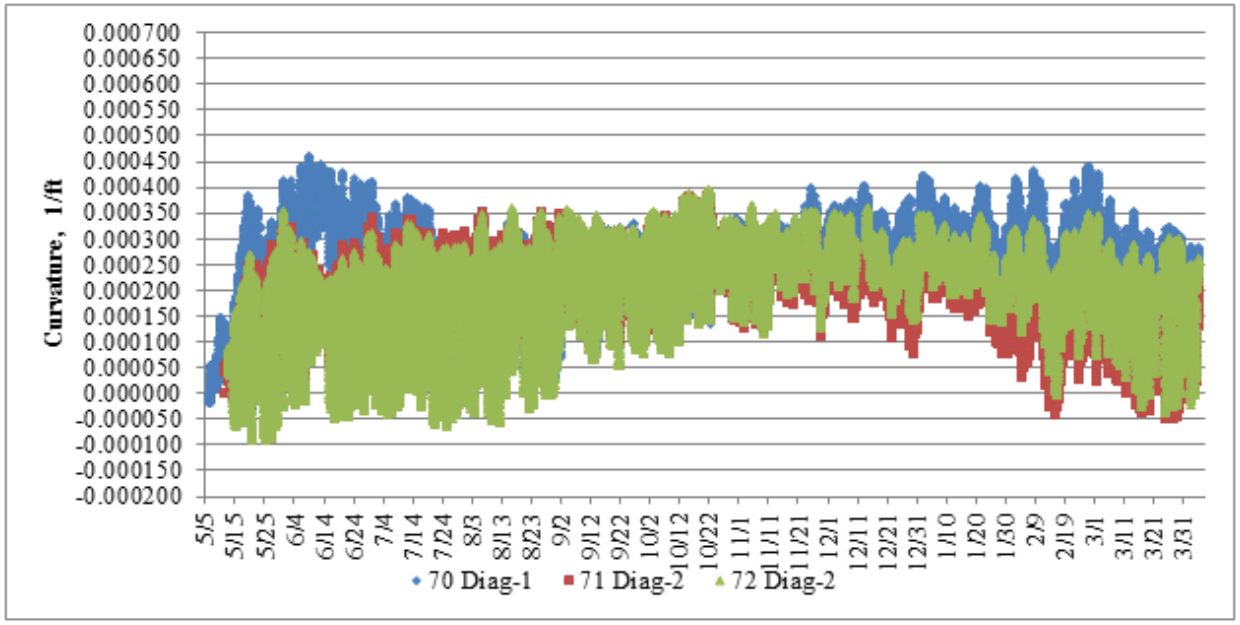

Figure 4.119: Curvatures at Diagonal Location from Representative Panels in Each Cell

From Figure 4.119, it is clear that initially the curvature in the diagonal direction is greatest in Cell 70 with the curvature peaking in the middle of June and decreasing thereafter. Between the beginning of July and the beginning of December, the curvature in Cell 70 is within

the range of curvatures encountered in Cell 71 and Cell 72. After December, the curvature is again highest in Cell 70.

Figure 4.120 shows the non-temperature related strain at the diagonal location of Cell 70 over the first two months after paving. Figure 4.120 shows that there is a decrease in the compressive strain in the bottom vibrating wire gauge. This is responsible for the increased curvature predictions for the time period in the beginning of June where Cell 70 has relatively higher slab curvature than Cell 71 and Cell 72. The increased curvature seems to be due to a decrease in the non-temperature related strain at the bottom of the slab, rather than an increase in the compressive non-temperature related strain at the top of the slab. This increased curvature is therefore likely not due to drying shrinkage strain. Another anomalous feature of this observation is that shortly after mid-June the strain in bottom sensor seems to return to oscillate around a relatively constant value of approximately -100 microstrain. Upon review, no reason was found to question the quality of this particular subset of data.

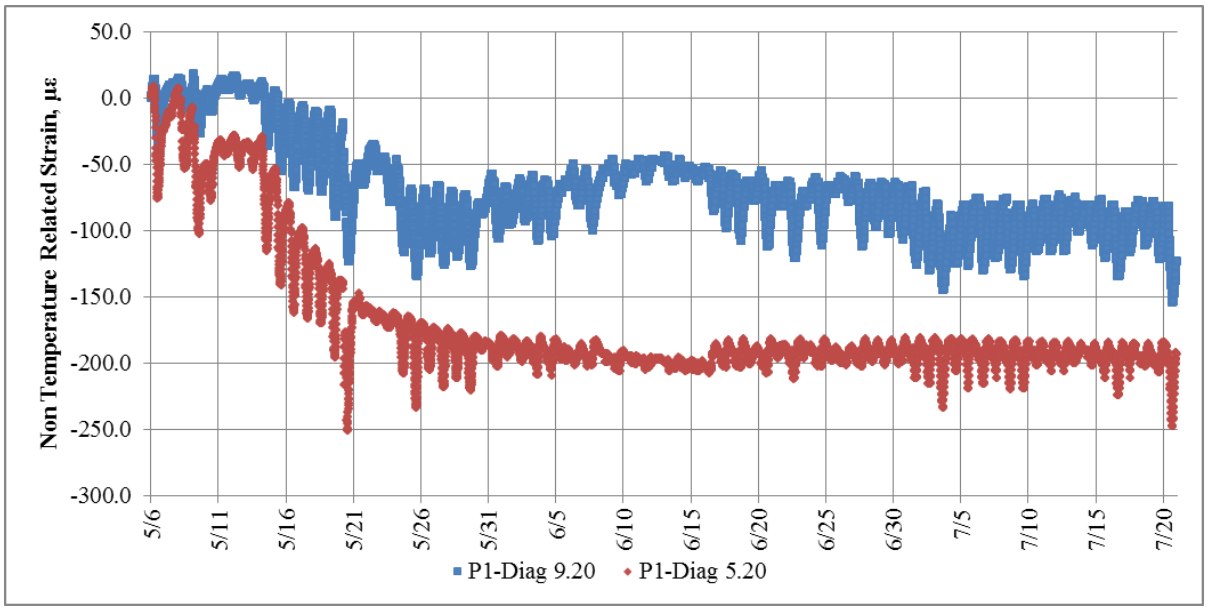

Figure 4.120: Non-Temperature Related Strain at Diagonal Location of Panel 1 in Cell 70

At the beginning of the winter, there is a slight increase in the curvature in Cell 70 causing it to exhibit more curvature relative to Cells 71 and 72. The beginning of winter also approximately corresponds with a significant increase in the curvature in both the longitudinal and transverse direction in Panel 1, as shown in Figure 4.67 and Figure 4.69. This correlates with an increase in curvature in the diagonal direction over this time period as well. Figure 4.71 shows that this time period corresponds with some of the most negative temperature gradients experienced over the analysis period. The fact that this period of time exhibits the most positive curvature outside of the time after the initial drying is therefore not surprising.

The relative curvature of Cell 70 compared to Cell 71 and 72 during the winter can also be explained by considering the magnitude of the temperature gradients that develop over the analysis period. Figure 4.121 and Figure 4.122 present the variation of the linear temperature gradient during the winter for Cell 70 and 71 respectively. It can be seen by comparing these figures that the positive temperature gradients in Cell 71 are of a larger magnitude than in Cell 70. Therefore, the curvature in Cell 71 should be less positive than Cell 70 at the corresponding time.

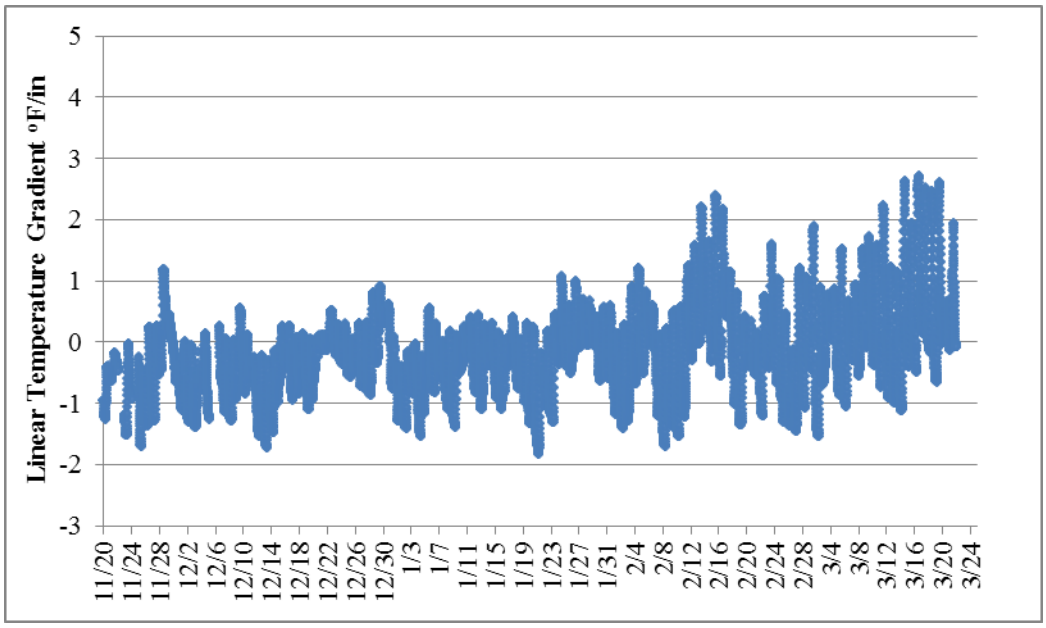

Figure 4.121: Winter Temperature Gradients in Cell 70

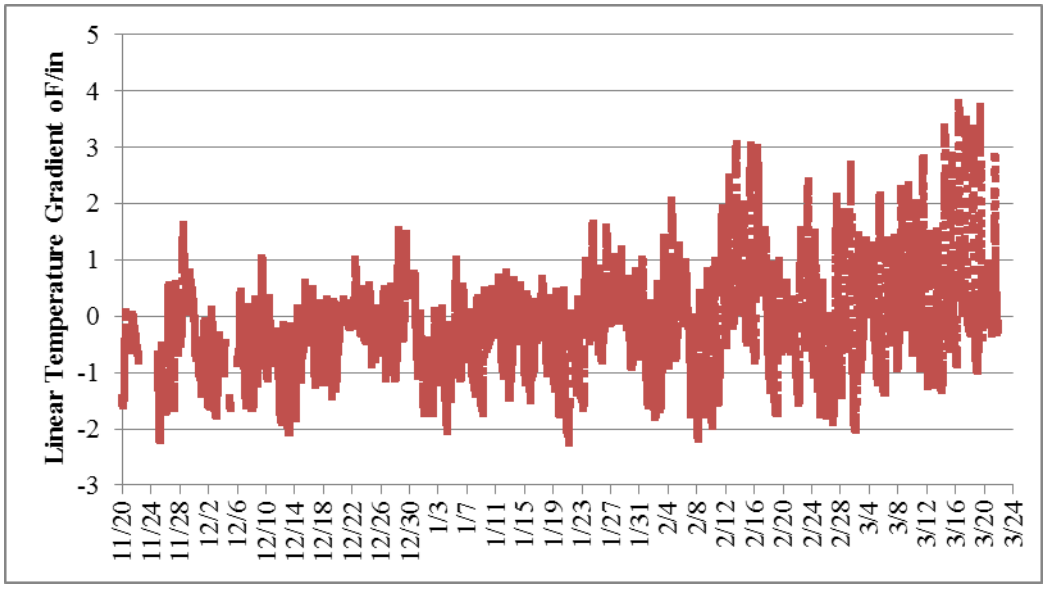

Figure 4.122: Winter Temperature Gradients in Cell 71

Comparing the curvatures in Cell 71 and Cell 72 it can be seen that the curvature in Cell 71 is slightly higher than the curvature in Cell 72 in the warmest months, (June, July, August) and less than the curvature in Cell 71 in the coldest months (November, December, January, February, March). This trend can be explained by considering Figure 4.123 and the relative CTEs of the two pavement layers. Unlike plain Portland cement concrete pavements, composite pavements do not experience only a uniform expansion or contraction when the weighted average temperature changes. The fact that each layer in a composite pavement is restrained from expanding and contracting with temperature changes results in curvature being induced in the slab. The curvature induced depends on whether the current temperature is higher or lower than the reference temperature. It is also dependent on the relative CTEs of the two layers. The curvature calculated at the diagonal location of Panel 2 in Cells 71 and 72 supports this theory. The positive curvature is higher in Cell 71 during the warmest periods of the year and lower in the coldest months of the year. This effect would likely be more pronounced if the CTEs of the two layers in each of the composite concrete pavements were more disparate.

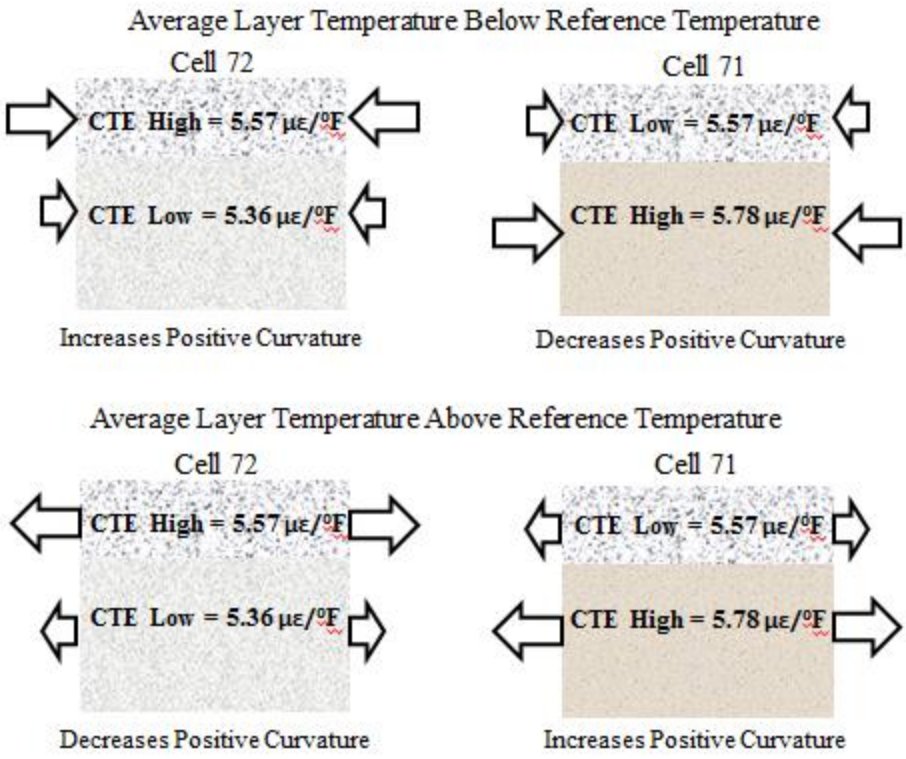

Figure 4.123: Curvature Induced in Composite Pavements Due to Uniform Changes in Temperature

4.5 CONCLUSIONS FROM SENSOR MEASUREMENTS

In the previous four sections, thermocouple temperature, relative humidity, and vibrating wire strain data collected over the first 11 months after paving three different composite pavement cells was analyzed. This data was used to establish the initial temperature and moisture conditions in the slab at the zero stress time. The temperature gradients at the zero stress time of the composite pavement cells were all negative. Specifically, the values for the three cells were -1.0°F/in for Cell 70, -0.5°F/in for Cell 71. The temperature gradient at the zero stress time for Cell 72 was estimated to be -0.6°F/in. The temperature equivalent of the moisture gradients at the zero stress time was 0°F/in since the slabs were still saturated at the zero stress time.

The temperature data, relative humidity data, and strain data collected over the first 11 months after construction were also analyzed. The intent of this analysis was to find differences in the way the composite pavement structure affects the temperature and moisture regimes in the pavement. Temperature data was available at multiple locations throughout the slabs. This data was used to determine that at the zero stress time, the temperature varied with location due to the thermal boundary conditions at the zero stress time. The entirety of the thermocouple data was assessed to see if there was any systematic variation in the temperature measurements in the slab with location. It was found that after the completion of shoulder construction, there was no systematic spatial variation in temperature within the slab.

Since the primary concern with respect to temperature in the slab is the temperature gradient that develops in the concrete, the temperature gradients that were calculated based on thermocouple measurements were compared. Although it was shown that the measured temperatures were different in Cell 72 relative to Cell 71, it was also found that this variation is most likely due to variation in the depths of the sensors. It is likely that the temperature measurements that developed in Cell 71 and Cell 72 were actually the same. Because thermocouple temperature data was not available for a significant part of the analysis period in Cell 72, the temperature regimes that developed in Cell 71 were compared to those in Cell 70 to comment on the insulating effect of the HMA layer with respect to the linear temperature gradients that develop in the underlying concrete.

Both the severity of the linear temperature gradients, and the frequency with which relatively severe temperature gradients developed in Cell 70, were less than in Cell 71. Comparing the temperature gradients that developed between Cell 70 and Cells 71 and 72 was also extended to the equivalent linear temperature gradient. The equivalent linear temperature

gradient comparison revealed that the difference in the occurrence of relatively extreme temperature gradients between Cell 70 and Cells 71 and 72 increased. Cells 71 and 72 were found to experience even more relatively extreme temperature gradients relative to Cell 70. Furthermore, a significant difference in the equivalent linear temperature gradients that developed between the two composite concrete over concrete cells was also observed.

Despite the fact that the slabs were heavily instrumented with relative humidity sensors, the data obtained from the various cells over this analysis period were not used in a quantitative analysis. No quantitative analysis was performed due to the inconsistency in the relationship between relative humidity and depth at the various locations, the magnitude of the measured relative humidity, and the fact that the relative humidity readings were in the relative humidity range for which there is the lowest accuracy in the sensor readings.

There were however general trends in the relative humidity measurements that were discussed. These include the observation that the slab seemed to remain saturated for a period of a few days after paving and was followed by a significant drop in relative humidity at all depths in the slab over the period of a month. In some cases, it was found that the sensor that was at the top of the slab recorded the largest drop in relative humidity over this time period. Together these observations suggest that there was some differential drying shrinkage occurring between the top and bottom of the slab as well as some autogenous shrinkage occurring. The autogenous shrinkage was also deemed reasonable considering the low w/c ratio of the paving mixes. The time period over which this phenomenon occurred also correlated with the approximate time required to achieve 50 percent of the ultimate drying shrinkage.

Due to the difficulty in interpreting the relative humidity data within a given cell, no specific difference between the cells could be determined. It was however noticed that the

relative humidity at the top senor in Cell 70 continued to decrease for a short while after placing the HMA overlay. It then started to trend towards the relative humidity at the other sensors. This was interpreted as meaning that although the HMA overlay initially aided in drying out the top of the concrete slab, it eventually served to saturate this region to a similar level seen throughout the rest of the slab depth.

The strain data obtained from the instrumented composite pavement panels was primarily used to compare the curvature in the different cells. The analysis of this data consisted of two parts. The first part assessed the variability in the data within a given cell while the second part assessed the differences between the cells. Very disparate calculated curvatures were observed between panels within a cell. This was especially true for Cell 70, which showed poor agreement between panels. Cell 71 and Cell 72 showed adequate agreement in calculated curvature at most locations between panels. To investigate the cause of the between panel variation, the non-temperature related strain, which considers strain due to drying shrinkage, loading effects such as compressive strains generated by joint lockup, and creep was separated from the total strain. It was found that the variation in the curvature between panels could be explained by variation in the non-temperature related strain.

In general, analysis of the non-temperature related strain showed that there was an increase in the compressive non-temperature related strain and that this increase corresponded with the time the relative humidity dropped in the slab from saturation levels. Once a relatively lower relative humidity level was achieved and maintained, the increase in the non-temperature related strain also generally stabilized. A larger increase in the compressive non-temperature related strain at the top of the slab relative to the bottom was observed. Together, this

observation, along with the trends found in the relative humidity data, were believed to indicate that differential drying shrinkage and autogenous shrinkage were occurring in the slabs.

In Cell 70, the effect of constructing the HMA overlay and the cause of other apparent anomalies in the calculated curvature were investigated. It was determined that while constructing the HMA layer did not seem to influence the curvature of the concrete slab for a given temperature gradient, the indirect effect of the HMA overlay was to reduce the temperature gradients that develop in the underlying concrete slab. It was observed that the curvature in the slab as a response to temperature gradients was most instantaneous at the diagonal location. It was somewhat delayed at the longitudinal and transverse locations. This delay was especially pronounced in Cell 70. In some cases, the transverse location showed decreasing curvature in response to an increasingly negative temperature gradient.

Slab curvature variation in the different panels of Cell 70 made drawing conclusions about the curvature in Cell 70 relative to Cells 71 and Cells 72 difficult. It was also difficult to draw conclusions with respect to the calculated curvature in Cell 71 relative to Cell 72. Ultimately, curvature calculated at one panel in the diagonal direction of each cell was used to compare curvatures between cells and draw conclusions. Based on this analysis, it was found that the curvature in Cell 70 remained positive in the spring for a longer period of time relative to Cell 71 and Cell 72. Additionally, more positive temperature gradients developed in Cell 71 and Cell 72 relative to Cell 70. Based on seasonal differences in the relative magnitude of the curvature calculated in Cell 71 and Cell 72, two hypotheses were made regarding composite pavement behavior. It was postulated that the variation in curvature between the two cells was due to both the variation in the relative CTEs of the top and bottom layers and the effect that changes in weighted average temperature have on the curvature of a composite pavement.

5.0 STRESS CONDITIONS IN MNROAD COMPOSITE PAVEMENTS

In the previous chapter, the data obtained from the three composite pavement cells at MnROAD was presented. Conclusions were also drawn regarding the relationship between the environment, composite pavement structure, and material properties. While general conclusions can be drawn regarding the stress conditions in the pavement slabs based on the sensor measurements, only relatively rough estimates of the stress magnitude can be made.

This chapter presents the attempt to quantify the stress conditions in slab. The measured environmental conditions in the slab at a given instant were input into a composite pavement model created using the pavement finite element program ISLAB. The predicted slab curvature was then compared with the measured curvature. The next two sections elaborate upon the determination of the model input parameters and present the results of the comparison between measured and predicted pavement curvatures.

5.1 MNROAD MODEL INPUT PARAMETERS

The ISLAB input parameters needed for this assessment can generally be broken down into three groups, structural parameters, material parameters, and loads. Structural parameters include slab geometry and mesh size, layer thickness, foundation type and modulus of subgrade reaction, longitudinal and transverse joint transfer conditions, and the interface condition between the two

pavement layers. Material parameters for each layer include elastic modulus, Poisson's ratio, CTE, and unit weight. An environmental load input into ISLAB is restricted to a temperature gradient. Curvature induced by moisture effects must also be represented by a temperature gradient. Because of the myriad unique temperature gradients that were measured in the cells throughout the analysis period, eight representative temperature conditions were selected for each cell as a representative sample. The representative sample consists of a positive ("+") and negative ("-") temperature gradient from each of the four seasons.

5.1.1 Finite Element Model Structural Parameters

ISLAB structural parameters that need to be specified include slab geometry and mesh size, layer thickness, foundation type, joint transfer parameters, and the interface condition between adjacent layers. The slab geometry consists of specifying the number of slabs in each direction as well as the dimensions of the slabs. For the three models used in this analysis, the number of slabs in the longitudinal direction is three while the number in the transverse direction is two. The dimensions of each of the slabs are 15-ft. long by 12-ft. wide.

The mesh chosen for each model includes six inch square elements resulting in 30 elements in the longitudinal direction of each slab and 24 elements in the transverse direction. The pavement/subgrade system utilized in the model is a plate resting on a Winkler foundation. This model is shown in Figure 5.1. A Winkler foundation consists of a series of springs attached to the plate. These springs do not transfer shear forces so deflection is limited to the area directly beneath the slab.

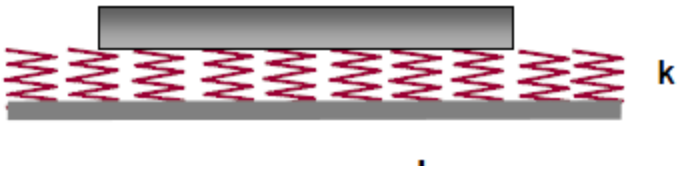

Figure 5.1: Illustration of Winkler Dense Liquid Foundation Model [20]

Measured data in the form of FWD test results were not available for determining the k-value directly for the cells at MnROAD. Experience at MnROAD however has shown that a k-value of 180 psi/in is a representative summer modulus value for representing the composite stiffness of all layers below the composite slabs. In lieu of seasonal FWD data, this summer modulus value was adjusted for seasonal effects using typical ratios of the modulus of subgrade reaction in the summer to the modulus of subgrade reaction in other months.

The remaining two structural parameters that need to be specified are the joint load transfer conditions and the interface condition of the two layers. A deflection LTE of 95 percent was assumed across all longitudinal joints and 100 percent was assumed across all transverse joints. These values are commonly used when modeling the joints for a newly paved joint plain concrete pavement.

As discussed in Section 2.0 debonding of the concrete layers of composite concrete pavements paved wet on wet has not been observed and does not seem to be a problem. In cases where debonding between two concrete layers was observed, it was attributed to conditions such as different reference temperatures between the old and new concrete or the restraint of differential drying shrinkage. Differential drying shrinkage and large differences in set temperatures between the two layers are not prevalent with composite concrete pavements. This is a residual effect from the fact that these pavements are paved wet on wet. For these reasons,

and because there were no observations of distresses at the layer interface, the interface between the two pavement layers was considered bonded. For Cell 70, no debonding was observed between the HMA and the concrete up though ten months after construction.

5.1.2 Model Material Parameters

The material parameters that need to be specified in the finite element slab models include the modulus of elasticity, Poisson's ratio, CTE, and unit weight. Information regarding the direct measurements of the modulus of elasticity and Poisson's ratio of the concrete was not available. Therefore, the modulus of elasticity was obtained using a correlation between the modulus of elasticity of the concrete and its compressive strength while a typical value of 0.19 was used for the Poisson's ratio. Compressive strength data was obtained from two different testing laboratories. The results for cylinders from the various paving mixes are shown in Table 5.1.

Table 5.1: 28-Day Compressive Strength Statistics for Composite Pavement Paving Mixes

Cell	Layer	Average 28-Day Compressive Strength, psi	Compressive Strength Standard Deviation, psi	Compressive Strength Coefficient of Variation	Number of Tests
70	Recycled Concrete	5300	310	5.8%	3
71	Recycled Concrete	3650	1550	42.5%	3
71	Exposed Aggregate Concrete	6150	385	6.3%	3
72	Cheap Mix Concrete	5600	730	13.0%	2
72	Exposed Aggregate Concrete	6000	280	4.7%	2

ASTM C39-10, "Standard Test Method for Compressive Strength of Cylindrical Concrete Specimens" states that it has been found that between laboratory variation should not lead to a coefficient of variation of more than 5 percent. Considering that the samples for a given day were not all obtained from the same truck, the results in Table 5.1 seem mostly reasonable considering the limited number of tests performed. For the recycled concrete mixture used in Cell 71, the average compressive strength is relatively low and the coefficient of variation is high. This is the result of one of the 28-day strength tests being 2000 psi. If this result is eliminated, the average 28-day compressive strength is 4500 psi with a coefficient of variation of six percent.

In order to relate the 28-day compressive strength to the elastic modulus of the concrete, the relationship used in the MEPDG and established by the American Concrete Institute was used. This relationship is shown in Equation 33.

$$E_c = 33 \cdot \rho^{\frac{3}{2}} \cdot \left(f_c\right)^{\frac{1}{2}} \qquad \text{Equation 33}$$

Combining the results of the compressive strength testing and using Equation 33 with the concrete units weights shown in Table 4.9, the elastic moduli of the concrete layers used in the finite element modeling are shown in Table 5.2.

Table 5.2: Concrete Elastic Moduli Values Used in Finite Element Modeling

Cell	Layer	Elastic Modulus, psi
70	Recycled Concrete	4250000
71	Recycled Concrete	3900000
71	Exposed Aggregate Concrete	4450000
72	Cheap Mix Concrete	4450000
72	Exposed Aggregate Concrete	4400000

For the elastic modulus of the HMA in Cell 70, the temperature dependence of the elastic modulus for unloaded conditions was considered. A base elastic modulus of 350,000 psi was assumed for the HMA. The Shell equation was then used to adjust the elastic modulus for the effects of temperature.

Adjusting the base elastic modulus of the HMA layer of 350,000 psi based on the Shell equation resulted in the elastic moduli shown in Table 5.3. These moduli were used to represent the stiffness of the HMA in the ISLAB model of Cell 70.

Table 5.3: HMA Elastic Moduli Used in Finite Element Model

Temperature Condition	E (psi)	Ave Temp (^{o}F)
Summer "-"	250000	77.3
Summer "+"	100000	110.2
Fall "-"	750000	33.1
Fall "+"	450000	53.5
Winter "-"	1750000	-0.5
Winter "+"	1400000	9.0
Spring "-"	1000000	20.3
Spring "+"	400000	57.3

The results of CTE testing, unit weight testing for the three concrete mixes, and the unit weight testing of the HMA were presented in Table 4.8 and Table 4.9 respectively. The CTE of the HMA was assumed to be 13.9 με/^{o}F [32] while the Poisson's ratio was assumed to be 0.35.

5.1.3 Model Environmental Loads

The environmental loads used in the MnROAD composite pavement models are based on measured temperatures and an approximation of an ELTG to account for moisture and other effects. The selection of representative conditions to simulate in ISLAB resulted in the selection of a day with relatively large, positive and negative temperature gradients, from each of the four seasons. The measured temperature profiles for each representative condition are shown in Figure 5.2 for Cell 70 and in Figure 5.3 for Cells 71 and 72.

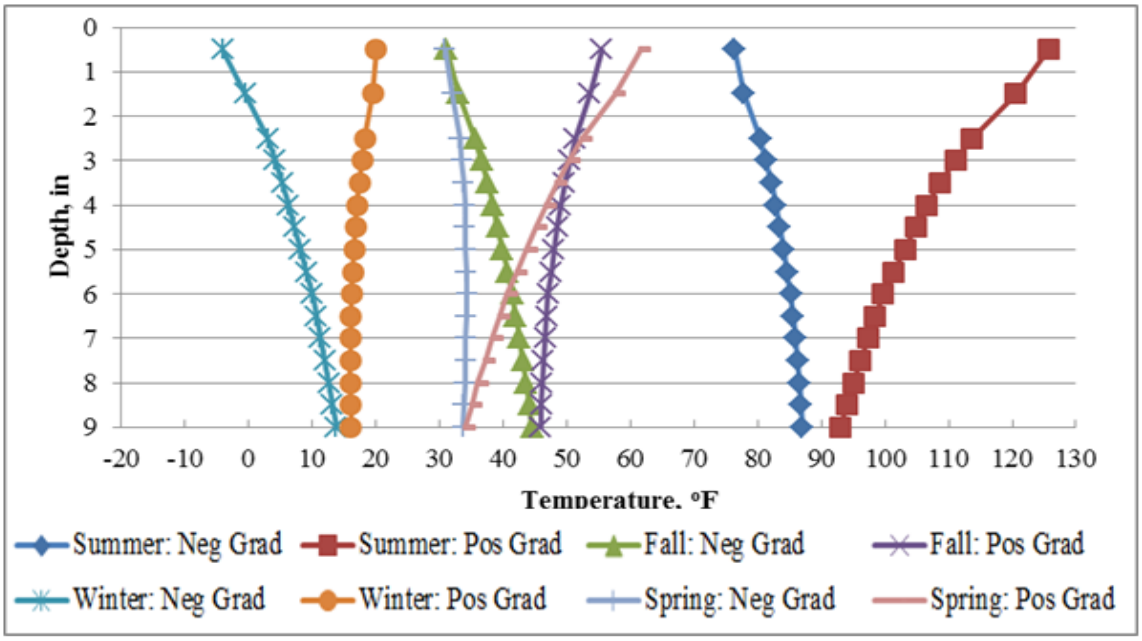

Figure 5.2: Temperature Profiles Considered for Cell 70

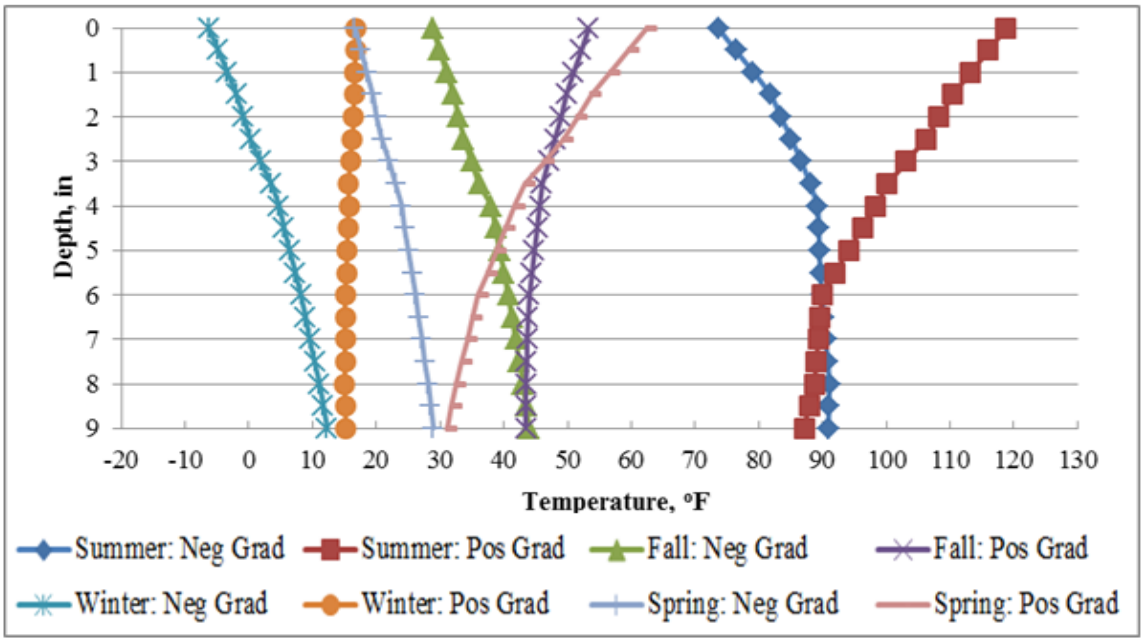

Figure 5.3: Temperature Profiles Considered for Cell 71 and 72

The temperature profiles shown in Figure 5.2 and Figure 5.3 were further adjusted to account for the effects of the built-in temperature gradient. To account for these effects, the difference between the actual temperatures and the weighted average temperature of the pavement layer at the zero stress time were first calculated. Each layer's reference temperature and weighted average temperature at the zero stress time were determined and discussed in Section 4.1.3. These values are re-iterated in Table 5.4.

Table 5.4: Finite Element Model Layer Reference Temperatures

	Cell 70	**Cell 71**	**Cell 72**
Top	Varies	75	61
Bottom	59	79	65

For the pavement layers not constructed with HMA, the difference between the actual temperature and the weighted average temperature at the zero stress time was determined. This value was then added to the measured temperature at each depth to obtain the composite temperature profile input into ISLAB. The resulting temperature profile accounts for the effects of the temperature gradient and the built-in temperature gradient. The reference temperature for the HMA layer was varied. This was done because a reference temperature is not applicable for HMA. Due to its nature as a viscoelastic material, thermal stresses would likely creep out. Since this input is required by ISLAB, the weighted average temperature for each temperature loading was used as the reference temperature. The resulting temperature profiles after considering the built-in temperature gradient for all of the Cells are shown in Figure 5.4 for Cell 70, Figure 5.5 for Cell 71, and Figure 5.6 for Cell 72.

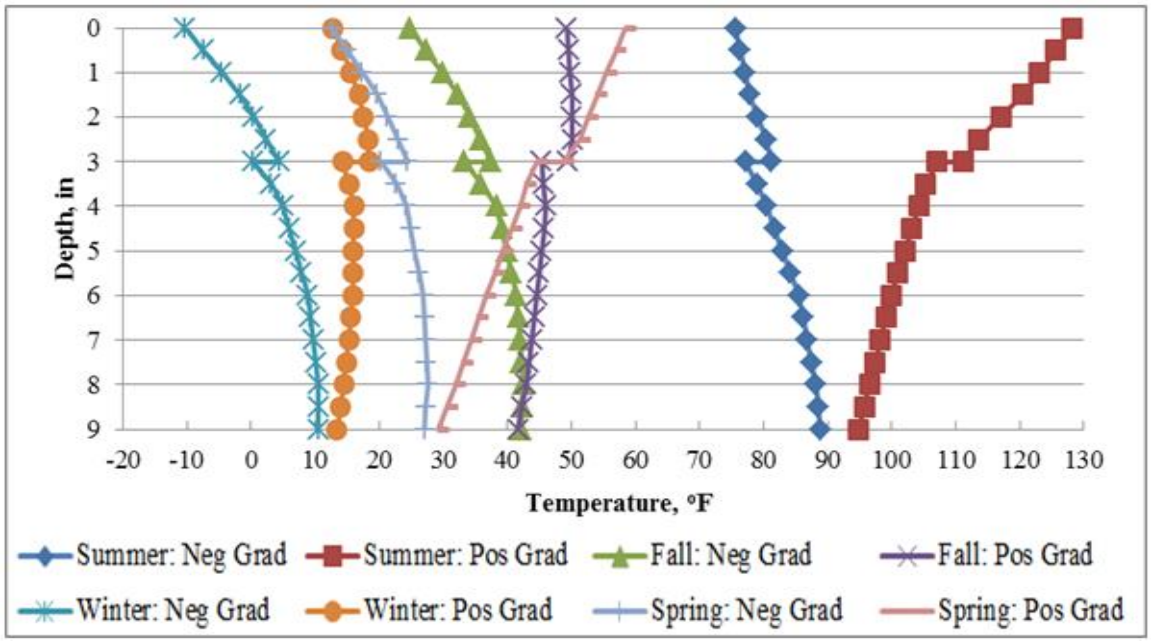

Figure 5.4: Temperature Profiles that Account for the Built-in Temperature Gradient for Cell 70

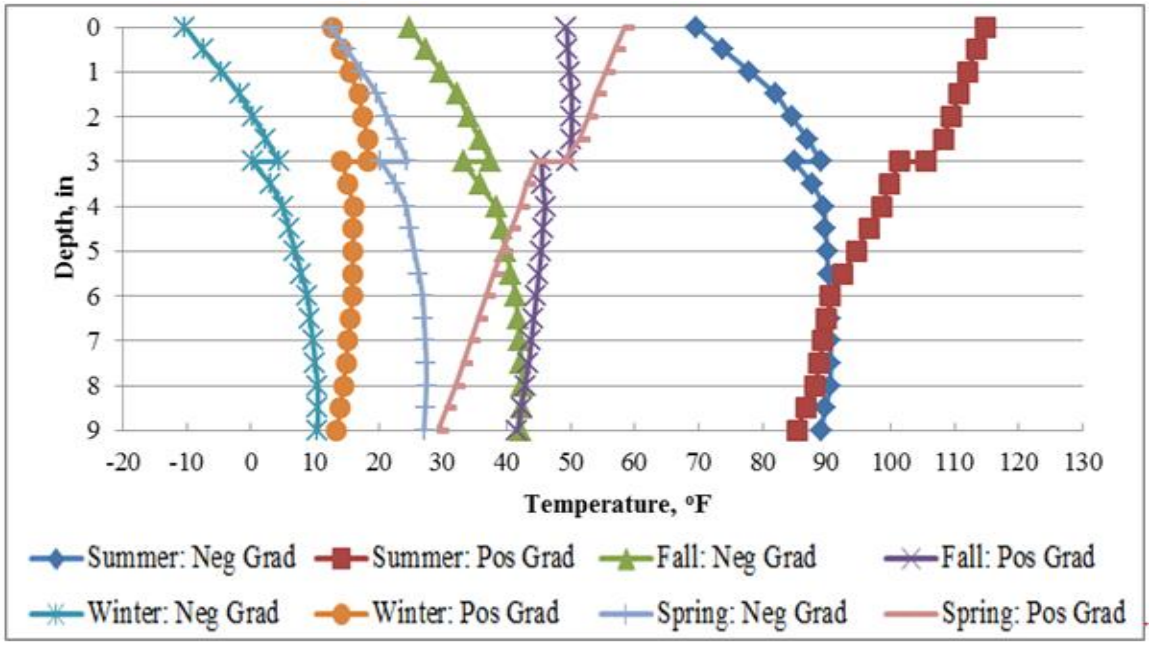

Figure 5.5: Temperature Profiles that Account for the Built-in Temperature Gradient for Cell 71

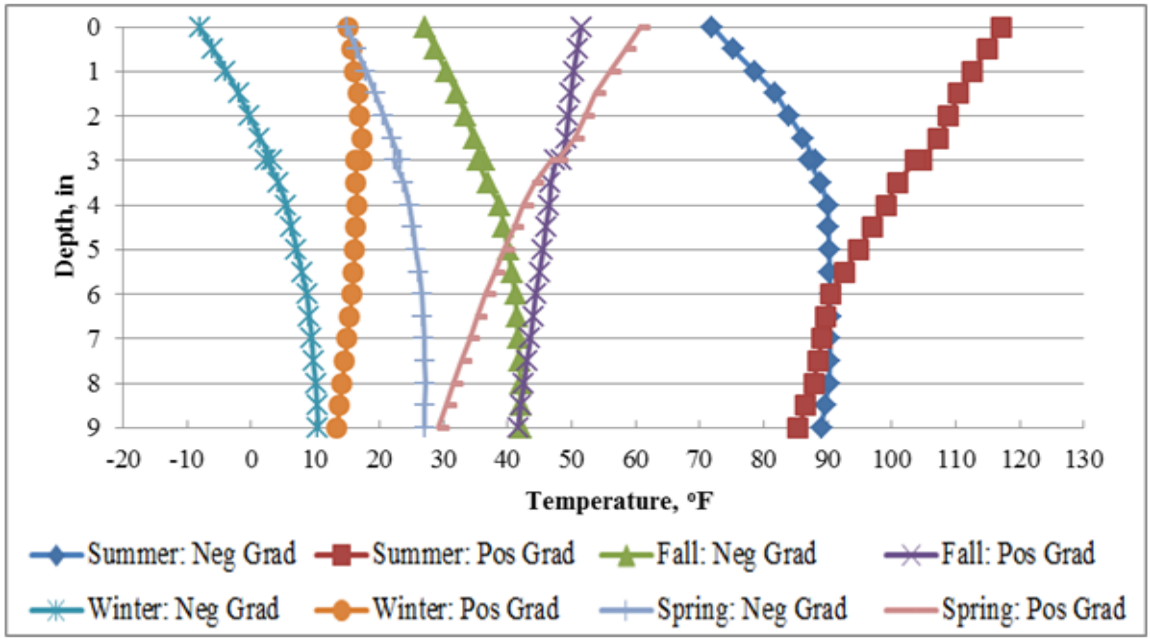

Figure 5.6: Temperature Profiles that Account for the Built-in Temperature Gradient for Cell 72

Because of the difficulty associated with the measurement of relative humidity, an alternative method was established to estimate the slab curvature due to drying shrinkage. This method relies on the fact that at a given moment, the strain gauges in the slab are measuring total strain. This total strain is due to both temperature and "other" effects. Since, the static strain gauges installed in the pavement do not measure strain induced by vehicle loads, the "other" effects primarily consist of the effects of drying shrinkage.

A novel approach to develop an ELTG associated with these "other effects" at the specific conditions of interest was developed using the two constituent components of the total strain measured by the vibrating wire strain gauges and the ELTG for the slabs calculated from thermocouple data. A conceptual diagram illustrating the methodology used to develop the ELTG to account for "other" effects is illustrated in Figure 5.7. While not ideal, this approach is believed to be the most reasonable approach to account for moisture effects specific to the particular times of interest. This is especially true in lieu of dependable moisture data that could be used to calculate an appropriate equivalent linear temperature gradient directly.

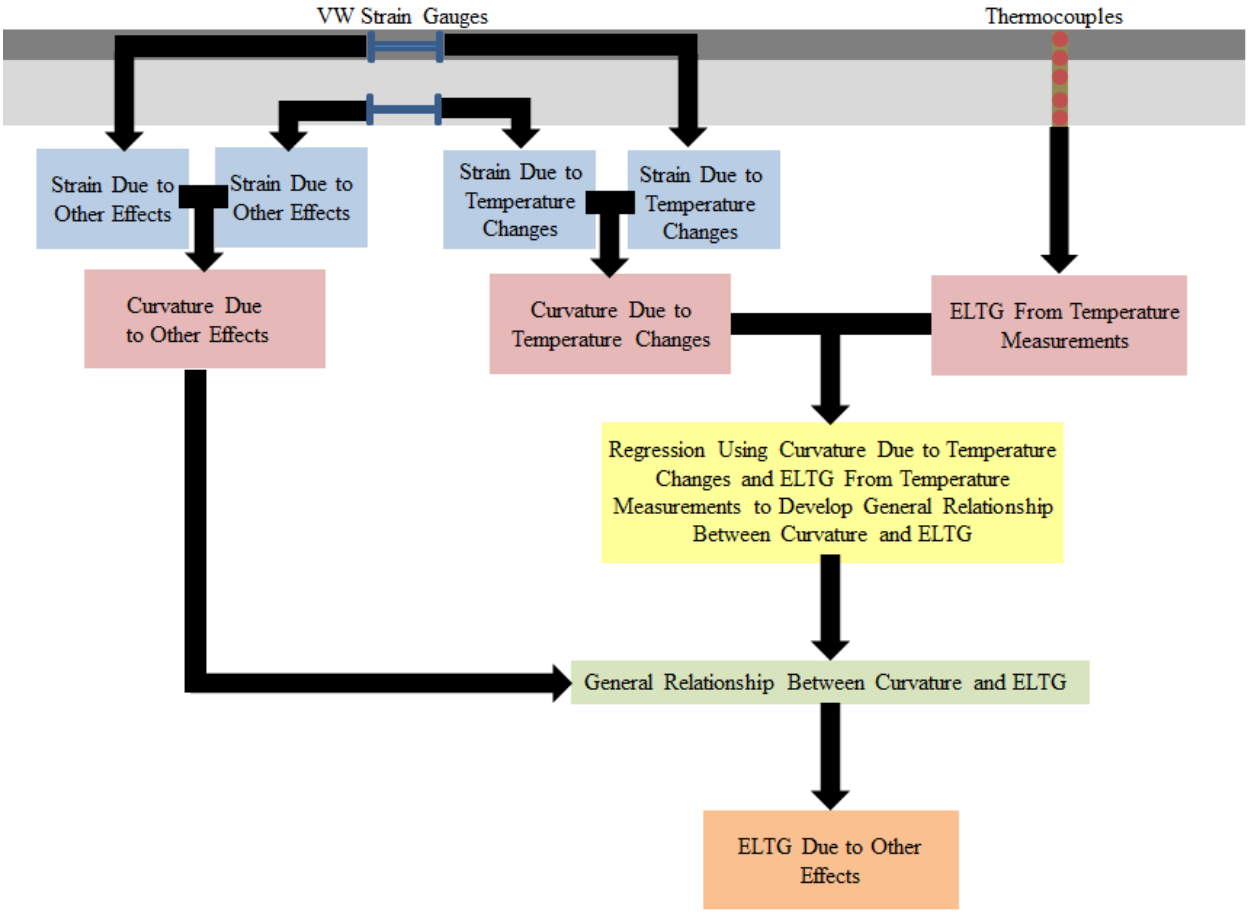

Figure 5.7: Flow Chart to Develop ELTG Due to Other Effects

The general relationship between ELTG and curvature developed through linear regression of the temperature related curvature and ELTGs from the thermocouple data is shown in Figure 5.8 through Figure 5.10 for Cells 70, through 72 respectively. The input data for the relationship derived for Cell 70 consists of data beginning the day after the placement of the HMA layer and continuing through the end of the analysis period March 2011. The input data for the relationship derived for Cell 71 and Cell 72 consists of data from a few days after paving through the end of the analysis period in March 2011. The vast majority of the data falls within a relatively narrow band around the best-fit linear regression line. Data relatively divergent from

the best-fit linear regression trendline, such as is seen in Figure 5.8, represents a small portion of the total sample from a few days in early June 2010. This sub-sample is relatively insignificant, statistically speaking. It is noteworthy, however, that in many instances, the ELTG estimated to account for the "other" effects involved extrapolation of the relationships shown in Figure 5.8 through Figure 5.10.

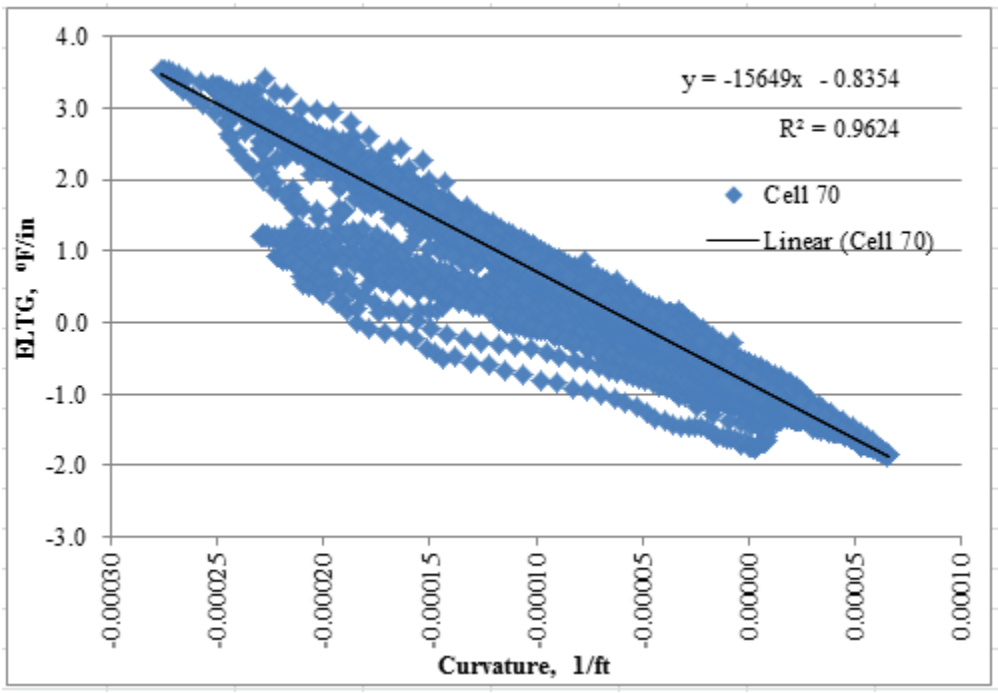

Figure 5.8: Relationship between Curvature and Equivalent Linear Temperature Gradient for Cell 70

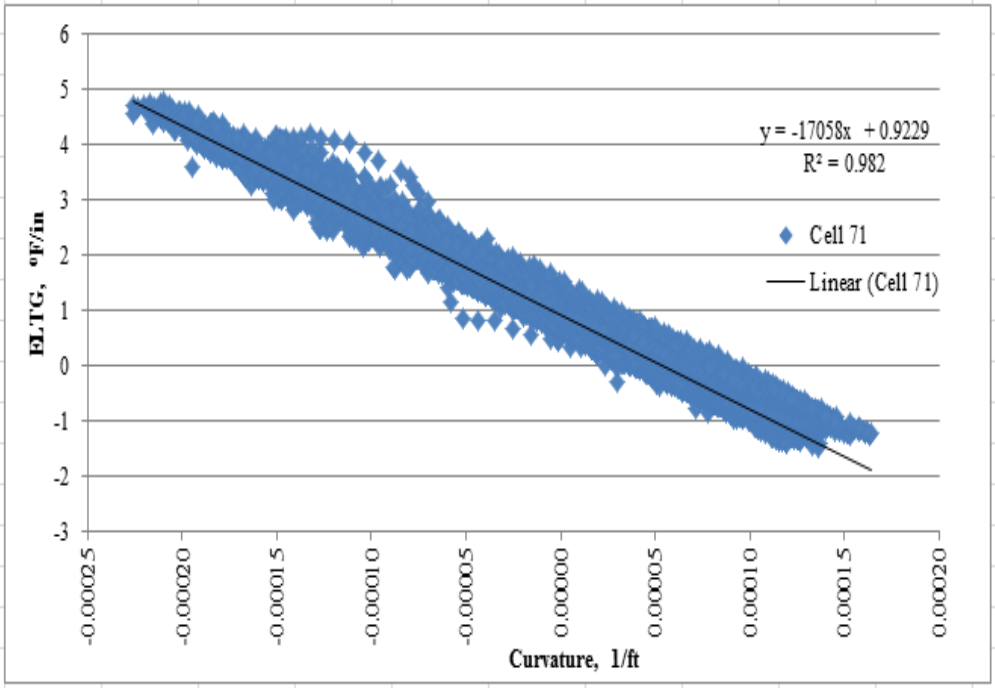

Figure 5.9: Relationship between Curvature and Equivalent Linear Temperature Gradient for Cell 71

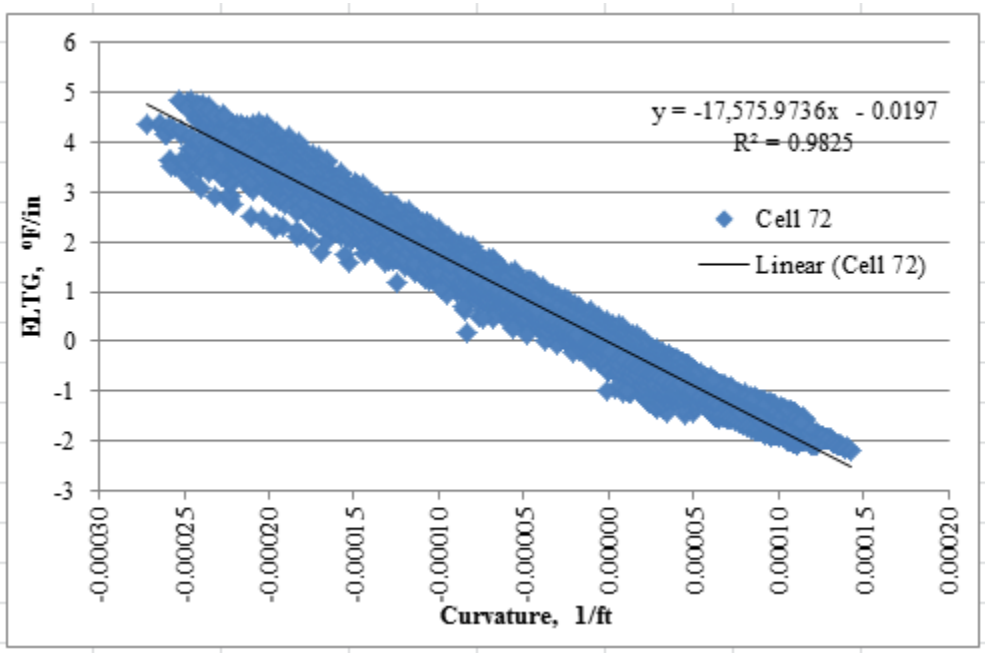

Figure 5.10: Relationship between Curvature and Equivalent Linear Temperature Gradient for Cell 72

Based on the best-fit linear regression equations shown in Figure 5.8 through Figure 5.10 and the curvature calculated from the measurement of the strain due to "other" effects, an ELTG can be estimated to represent the effects of drying shrinkage. This was done for the specific conditions at the eight representative conditions mentioned previously. The ELTG at each of these conditions is shown in Table 5.5.

Examination of Table 5.5 reveals that the ELTG associated with non-temperature related effects generally varies more seasonally than it does diurnally. For Cell 71 and 72, the highest ELTGs associated with non-temperature related effects occur in the fall when the ambient relative humidity was shown to be the lowest. For Cell 70, there is more curvature associated with non-temperature related effects. There is also less seasonal variation in the non-temperature associated curvature for Cell 70 than there is for Cell 71 and 72. This relatively smaller seasonal variation is most likely due to the effect of the HMA layer on top of Cell 70. Placement of the HMA layer initially dries the concrete and afterwards serves to enhance drying shrinkage by preventing the rewetting of the underlying concrete. The HMA layer would also serve to dampen seasonal variation in moisture conditions in the slab. Together these observations are believed to indicate that this methodology of assessing the effects of drying shrinkage on curvature at a given instant is reasonable.

Table 5.5: ELTGs Accounting for Non-Temperature Related Strain

	Temperature Gradient Sign	Cell 70	Cell 71	Cell 72
		ELTG ^{o}F/in (Accounting for Non-Temperature Effects)		
Summer	"-"	-5.01	-1.97	-3.09
	"+"	-5.48	-4.15	-3
Fall	"-"	-5.36	-3.1	-5.02
	"+"	-5.89	-2.87	-4.75
Winter	"-"	-5.96	-1.4	-3.67
	"+"	-6.78	-2.5	-4.32
Spring	"-"	-5.86	-1.29	-3.96
	"+"	-6.62	-2.1	-4.19

The temperatures at the eight representative conditions were then further adjusted to consider the ELTGs shown in Table 5.5. The resultant temperature profiles were used as the model temperature profiles. Based on the discussion in the aforementioned sections, these profiles account for temperature effects, built-in effects, and drying shrinkage effects. The eight test conditions after the final adjustment for drying shrinkage effects are shown in Figure 5.11 Figure 5.12 and Figure 5.13 for Cell 70, 71, and 72 respectively. In Figure 5.11 is an inflection point at the 3-in depth in the temperature profiles for Cell 70. This inflection point is due to the fact that no adjustment was made to the temperatures in the HMA layer.

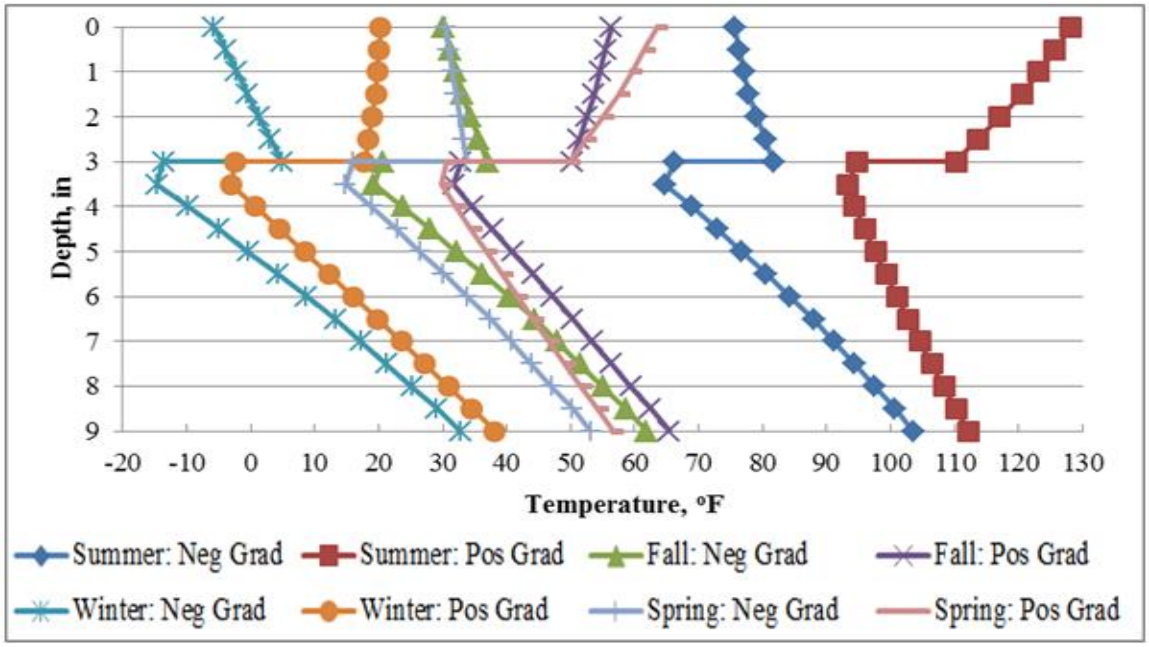

Figure 5.11: Temperatures with Built-in Conditions and Non-Temperature Related Curvature for Cell 70

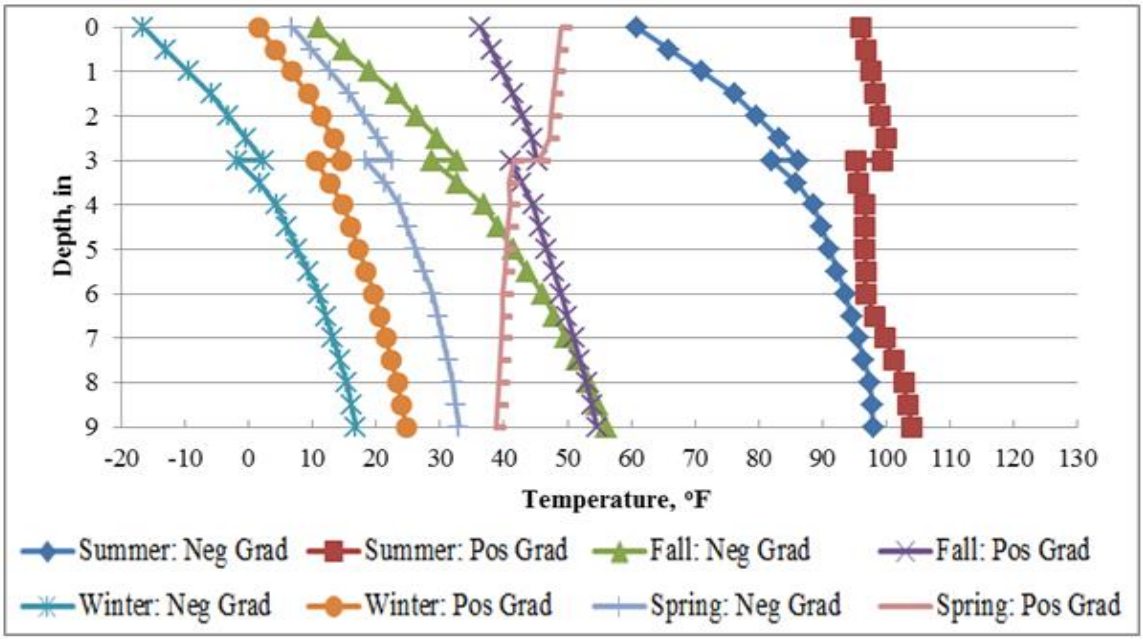

Figure 5.12: Temperatures with Built-in Conditions and Non-Temperature Related Curvature for Cell 71

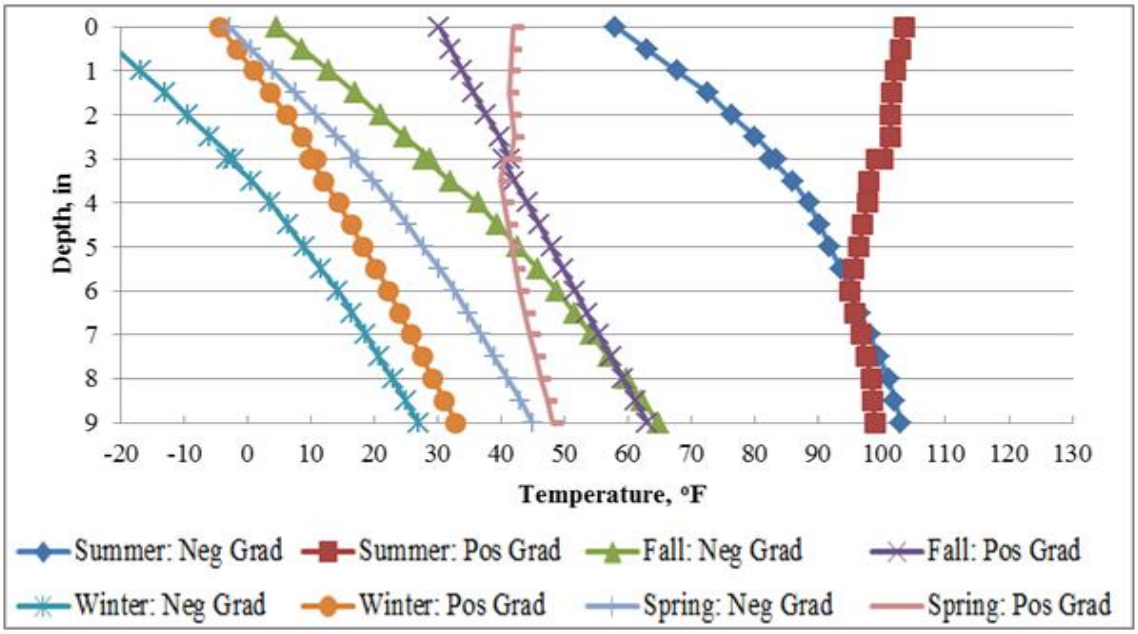

Figure 5.13 Temperatures with Built-in Conditions and Non-Temperature Related Curvature for Cell 72

5.2 COMPARISON OF MEASURED AND PREDICTED RESPONSE

Using the input parameters discussed in Section 5.2, ISLAB runs were executed so that the predicted curvature could be compared to the measured curvature. A typical visual output showing slab deflection is shown in Figure 5.14.

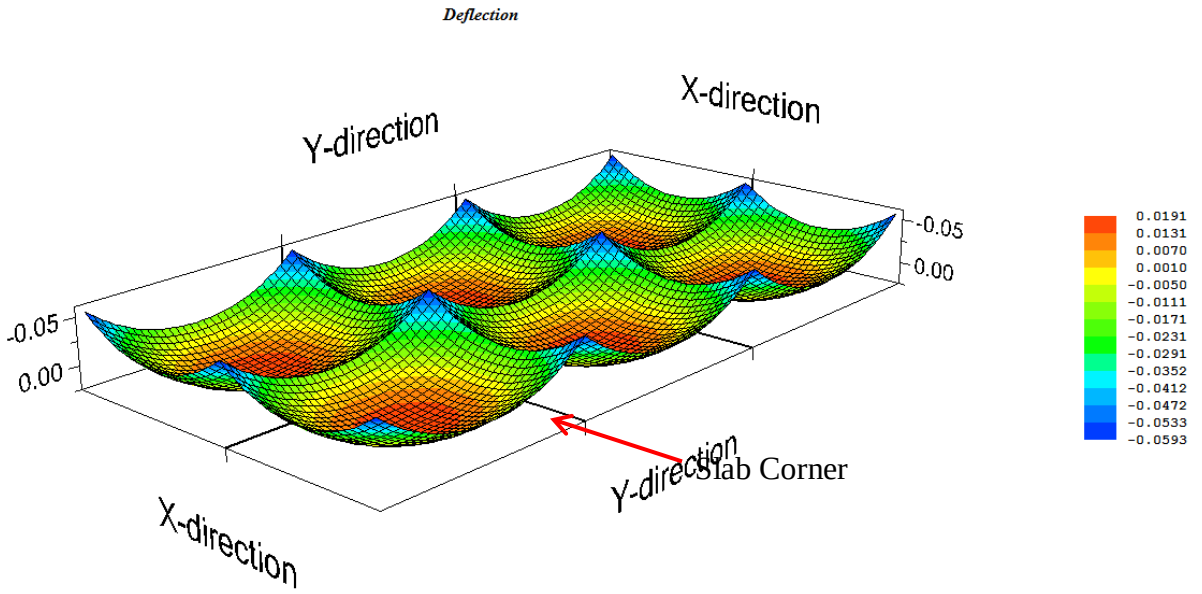

Figure 5.14: ISLAB Deflection Output

Model deflections were then obtained along a diagonal path originating at the slab corner indicated in Figure 5.14 and progressing towards mid-slab. Deflections were obtained at every model node along this path and a relationship between deflection (y-variable) and distance from the slab corner (x-variable) was established. The resulting relationship was fitted with a quadratic polynomial. Using this polynomial, the curvature to compare with the curvature obtained based on strain gauge measurements was obtained using Equation 34 and evaluated at the location of the diagonal strain gauge. A comparison of the measured and predicted curvature for Cell 70 is shown in Figure 5.15.

Equation 34

$$\kappa = \frac{\frac{d^2}{dx^2}y}{\left[1 + \left(\frac{d}{dx}y\right)^2\right]^{\frac{3}{2}}}$$

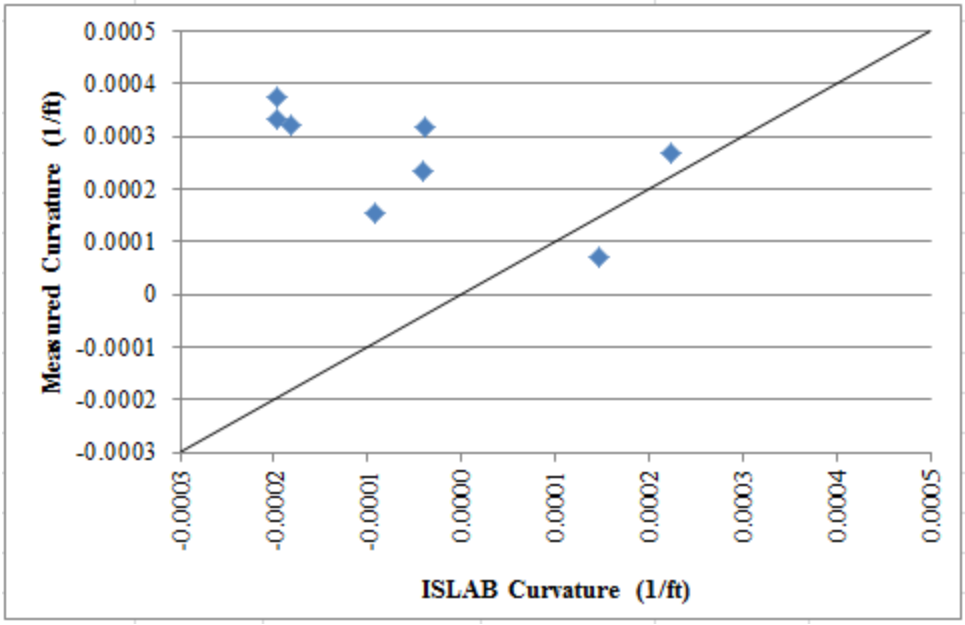

Figure 5.15: Comparison of Measured and Predicted Curvatures for Cell 70

For Cell 70 there is no discernible trend in the relationship between measured and predicted curvature and that the ISLAB model, even on a qualitative basis, does not predict well the measured curvature. Specifically, ISLAB is underestimating the measured curvature and in some cases is predicting the opposite curvature to what was observed with the strain gauges. Potential reasons for this discrepancy are believed to be due to the way that the HMA layer was accounted for in the model. It is noteworthy that the two closest predictions are both representative of the summer when the assigned elastic modulus of the HMA was lowest and that the two most erroneous predictions are representative of winter conditions when the elastic modulus of the HMA was largest. When the HMA elastic modulus is lower, it is less structurally significant in the model's prediction of curvature.

To further examine this hypothesis, runs were performed with the stiffness of the HMA set to a nominal value of 100,000 psi and seasonal adjustment of the moduli of subgrade reaction

was considered. Using these parameters, the results provided in Figure 5.16 were obtained. While decreasing the stiffness of the HMA improves the results, it can still be seen that there is a poor fit between the measured curvature and that predicted using ISLAB.

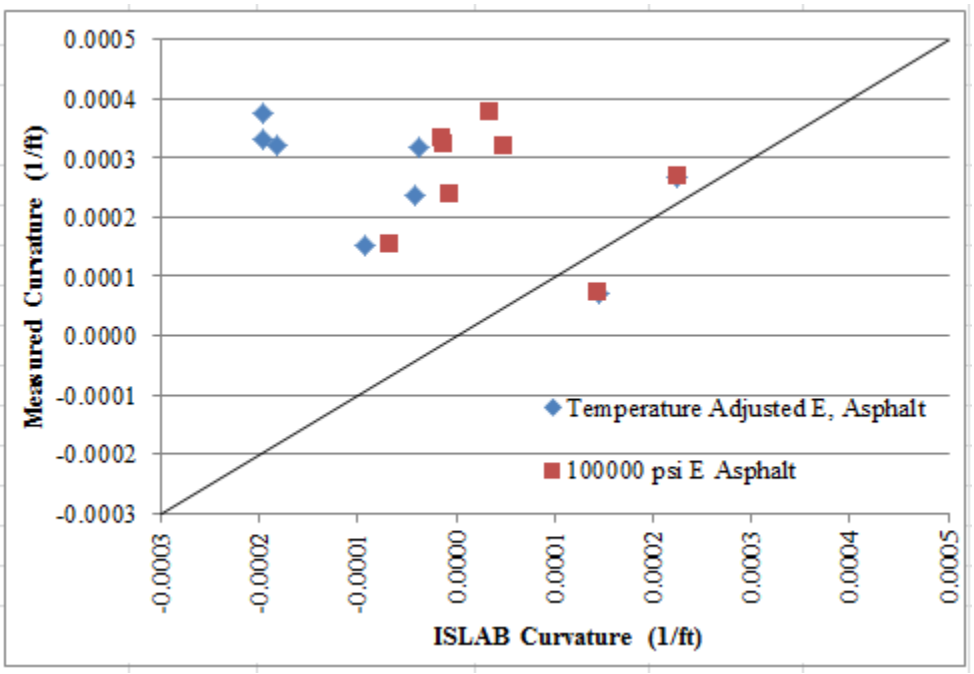

Figure 5.16: Evaluation of the Effect of Lower HMA Moduli on Measured vs Finite Element Curvature

A comparison of the measured and predicted curvatures for Cell 71 is shown in Figure 5.17. From Figure 5.17, there is an increasing disparity in the curvature estimated with the strain gauges and the curvature predicted using ISLAB as the measured curvature increases. As with Cell 70, ISLAB under-predicts the measured curvature for Cell 71. Unlike in Cell 70, however, the consistency in the trend of the predicted curvature for Cell 71 suggests that there might be some factor that could shift the predicted results and allow better agreement to be achieved with the measured curvature. Potential influences on the agreement between the predicted and measured curvature will be discussed after the results from Cell 72 are presented.

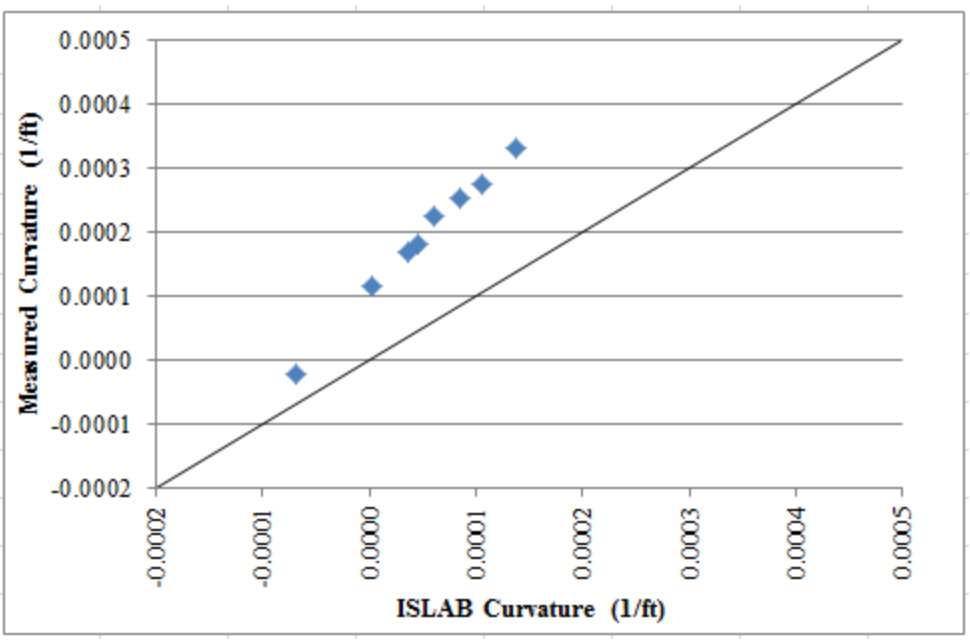

Figure 5.17: Comparison of Measured and Predicted Curvature for Cell 71

From a qualitative perspective, the fit of the predicted and measured curvature as shown in Figure 5.18 is best for Cell 72. In fact, two of the predicted curvatures match the measured curvature very well. These two particular curvatures are representative of curvatures measured in the winter and summer seasons during times when there was a maximum negative ELTG in the pavement. While this finding seems to suggest that there is no seasonal correlation, it is in agreement with the finding for Cell 71 that the best agreement between measured and predicted curvature occurs at smaller curvatures. Like Cell 71, Cell 72 also displays an increasing disparity between measured and predicted curvature as the measured curvature increases.

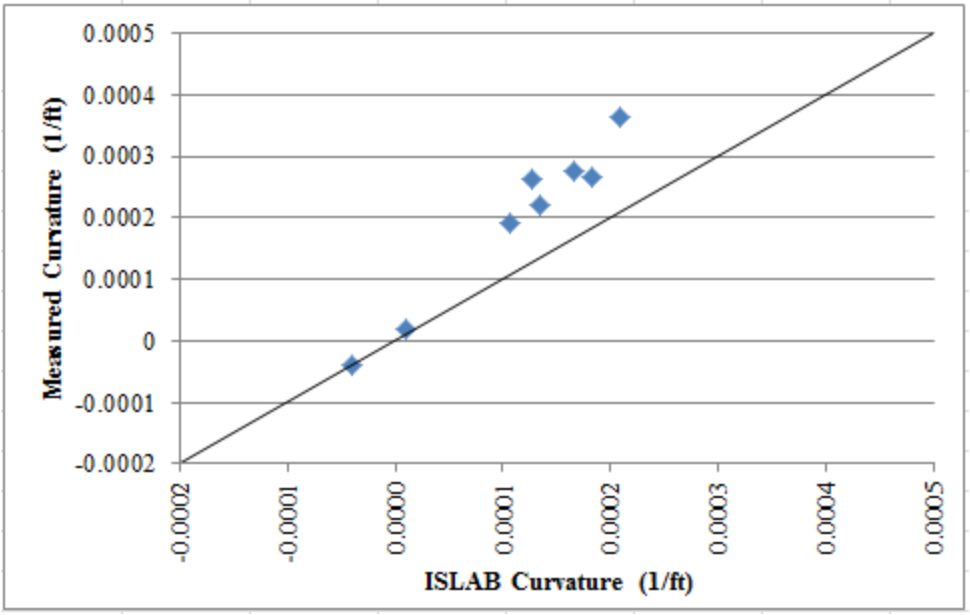

Figure 5.18: Comparison of Measured and Predicted Curvature for Cell 72

Two observations were made regarding potential explanations for the disparity between the measured and predicted curvature in Cell 71 and Cell 72. The first observation involves the accuracy of the inputs. In Table 5.5, higher ELTGs are prescribed to account for the non-temperature related strain in the pavement for Cell 72 relative to Cell 71. The more negative ELTGs will subsequently result in higher curvature and hence better agreement between the predicted and measured since it was generally found that ISLAB is underestimating curvatures. The reason for the disparity in the ELTGs assigned to Cell 71 and Cell 72 is due, in part, to the relationship used to assign the ELTG to the non-temperature related curvature and as shown in Figure 5.9 and Figure 5.10. Implicit in these relationships are the CTE and the elastic modulus of each of the concrete layers. The CTE is used as an input in both the calculation of the temperature related curvature measured from the strain gauges while the elastic modulus is significant in the calculation of the ELTG. Measured values of the CTE for the different concrete mixtures showed variation only as large as .03ε/^{o}F for the same mix tested on different days and

at an age of 28 days. The elastic modulus, on the other hand, was obtained through an approximation. The compressive strength input into this approximation was obtained from only a few test results at one age in each instance.

The second observation made in regards to an explanation of the variability in the measured and predicted performance is also related to Figure 5.9 and Figure 5.10. The ELTG values input into the model to account for drying shrinkage effects are based on the best-fit relationship to the data between temperature related curvature and ELTG. At each curvature value in these figures, a range of curvatures were observed at the same ELTGs. While the source of this variation is unknown, it is certain that this variability plays some role in the accuracy of the prediction seen for the eight test conditions.

5.2.1 Traditional Analysis for Determination of the Built-in Gradient

Based on the analysis presented in the previous section, the ELTG assigned to the pavement to account for shrinkage and other non-temperature related effects appears to be one of the more critical parameters dictating the ability to reproduce the measured slab response using ISLAB. The impetus of using this methodology to estimate this value for incorporation into the ISLAB temperature profiles was based on the desire to determine an ELTG to account for non-temperature related effects at a single point in time in lieu of reliable relative humidity data that could be used to generate such a value.

One limitation of the ELTGs used to account for non-temperature related effects in this manner is that in some instances there are significant differences in the ELTG value calculated at different times on the same day. This daily variation in ELTG to account for non-temperature related effects is contradictory to relative humidity measurements obtained in the slab.

Regardless of the confidence in the specific magnitude of the measured relative humidity in the slab, it can be confidently stated that the relative humidity, and therefore drying shrinkage strain, did not vary significantly on a daily basis. This is most likely the result of assuming that the relationship between temperature related curvature and the ELTG is the same as non-temperature related curvature and the ELTG.

Other researchers have found drying shrinkage to vary on a seasonal basis [33]. With this realization, researchers have established a method for estimating the built-in gradient, defined as the composite effect of drying shrinkage and the built-in temperature gradient, by looking at the intercept of plots of curvature using vibrating wire total strain measurements vs ELTG [7]. By definition, any curvature in the slab when there is no temperature gradient in the slab is due to other effects. Conversely, the temperature gradient present at the time that the slab is flat on the ELTG vs curvature plot represents the built-in temperature gradient. Although the intercept is a positive value, it must be subtracted from any temperature profile used in a finite element analysis. Based on this distinction the application of these positive intercept values can be considered as similar to applying a negative built-in temperature gradient.

Plots of curvature calculated utilizing total strain measurements and ELTG were generated, as in Figure 5.19. Figure 5.19 represents a plot generated for Cell 72 using curvature calculated from total strain measurements and ELTGs in the month of March, 2010. The y-intercept (+3.62) provides an estimate of the built-in gradient

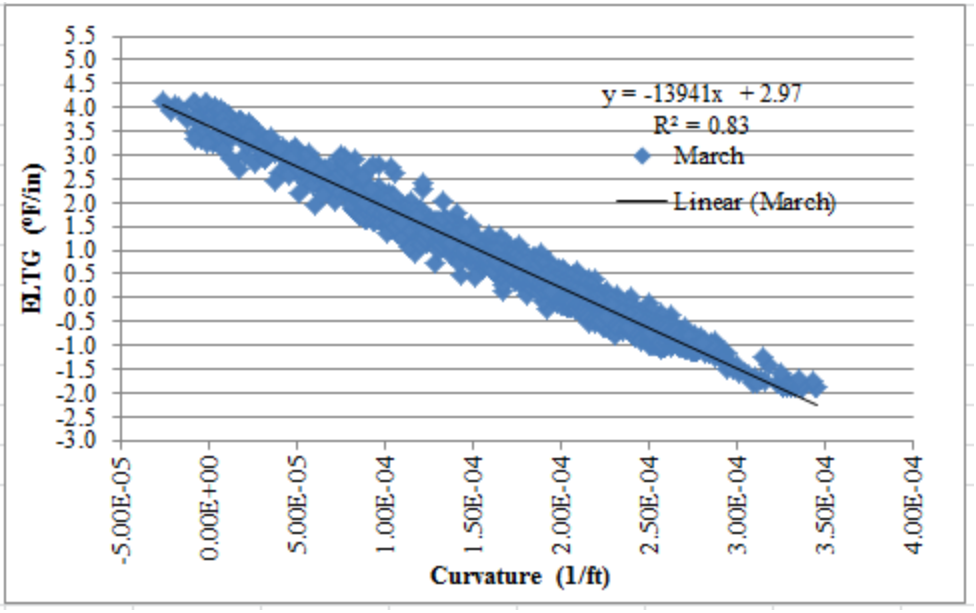

Figure 5.19: Typical Curvature from Total Strain Measurements vs ELTG Plot

A similar plot was generated for each cell and for each month between July and March, 2010. These plots can be found in APPENDIX B. Curvature values calculated in May and June, 2010 were not analyzed because these months were dissimilar to the other months in the sense that the initial drying of the concrete was occurring. For each month, the intercept (estimate of the built-in gradient) as well as the coefficient of determination, R^2, was recorded. Table 5.6, Table 5.7, and Table 5.8 summarize these results for Cells 70, 71, and 72 respectively.

Table 5.6: Comparison of ELTGs to Account for Non-Temperature Related Effects - Cell 70

	Cell 70		Table 5.5 Negative Gradient to Account for Non-Temperature Effects	
Month	Intercept of Curvature from Total Strain vs ELTG Plot	Coefficient of Determination (R^2)	"-" Temperature Profile	"+" Temperature Profile
July	2.56	0.66	5.01	5.48
August	2.15	0.69		
September	3.39	0.91		
October	3.85	0.96		
November	3.83	0.89	5.36	5.89
December	4.27	0.70		
January	2.85	0.58	5.96	6.78
February	3.19	0.74		
March	4.15	0.85	5.86	6.62

Table 5.7: Comparison of ELTGs to Account for Non-Temperature Related Effects - Cell 71

	Cell 71		Table 5.5Negative Gradient to Account for Non-Temperature Effects	
Month	Intercept of Curvature from Total Strain vs ELTG Plot	Coefficient of Determination (R^2)	"-" Temperature Profile	"+" Temperature Profile
July	6.00*	0.89	1.97	4.15
August	5.72*	0.90		
September	5.06*	0.95		
October	4.73	0.89		
November	4.37	0.91	3.1	2.87
December	3.06	0.69		
January	2.81*	0.51	1.4	2.5
February	2.97	0.83		
March	3.47	0.93	1.3	2.1

*Plots exhibited questionable trends.

Table 5.8: Comparison of ELTGs to Account for Non-Temperature Related Effects - Cell 72

	Cell 72		Table 5.5 Negative Gradient to Account for Non-Temperature Effects	
Month	Intercept of Curvature from Total Strain vs ELTG Plot	Coefficient of Determination (R^2)	"-" Temperature Profile	"+" Temperature Profile
July	2.97	0.83	3.09	3
August	3.03	0.83		
September	4.31	0.96		
October	4.13	0.91		
November	4.03	0.92	5.02	4.75
December	3.38	0.89		
January	3.80	0.89	3.67	4.32
February	3.66	0.94		
March	3.61	0.97	3.96	4.19

Overall, the best relationship between curvature and the calculated ELTG, as evidenced by the coefficient of determination, was found for Cell 72. The coefficient of determination in the monthly plots for Cell 72 was greater than 0.8 for each month. The plots generated for the Cell 71 strain gages had a slight curvature in them for the months of July through September so the built-in gradient for each of these months is questionable even through the coefficient of determination is relatively high. The data for the month of January was also questionable, as indicated by the low coefficient of determination. Less than half of the months for Cell 70 had a coefficient of determination greater than 0.8.

For Cell 70, the ELTGs to account for non-temperature related effects determined through the intercept method are significantly lower than the ELTGs developed using the approach presented in Section 5.1.3. At face value, these ELTG values are more reasonable compared to those presented in Section 5.1.3. These gradients presented in Table 5.6 have the

lowest average and result in temperature differences between the top and bottom of the slab that are the most similar to the default value of 10°F used in the MEPDG. However, because the approach presented in Section 5.1.3 resulted in ISLAB under-predicting the curvature in the slab, using these temperature gradients to account for non-temperature related effects would only serve to decrease agreement between the measured and predicted values.

Contrary to Cell 70, the ELTG values shown in Table 5.7 for Cell 71 determined using the intercept method are significantly higher than those presented in Table 5.5. If these values were utilized to adjust the model nodal temperature in ISLAB, it may be that an improved relationship between predicted and measured curvature could be obtained. The ELTGs to account for non-temperature related curvature presented in Table 5.8 for Cell 72 are either relatively similar or slightly lower than those presented in Section 5.1.3 and Table 5.5. Due to the fact that these ELTGs are either similar or slightly less negative and ISLAB was under-predicting curvature in Cell 72, it is not likely that the incorporation of these ELTGs into the ISLAB models would significantly improve the relationship between the measured and predicted curvature.

The built-in gradients result in the temperature differences between the top and bottom of the slab ranging between and -12.9°F and -24.9°F for Cell 70, -26.7°F and -42.6°F for Cell 71 (excluding questionable data months), and -26.7°F to -38.8°F for Cell 72. The default built-in temperature difference used in the MEPDG is -10°F. This value is based on the gradient present throughout the design life while the temperature ranges above just represent the first year after construction. Significant creep, as well as additional drying shrinkage, will be exhibited over the years and therefore it would be beneficial to continue monitoring the sensor data as additional dad becomes available.

The analysis of a temporally expanded dataset from this project, data from the other panel within each Cell, or data from a different instrumented composite pavement would be beneficial. Now that additional years of data is available, a similar analysis could be performed which would allow the evaluation of the built-in gradient for within each month. It would also be beneficial to compare ELTGs accounting for non-temperature related effects determined by different methods such as models relating relative humidity measurements to drying shrinkage strain.

6.0 STRESSES IN COMPOSITE PAVEMENTS

In the previous section, a reasonable agreement between measured and predicted curvatures for the MnROAD composite pavements was unable to be obtained using the material properties established from the materials testing and the sensor data. Despite the lack of agreement for the specific inputs developed for the MnROAD site, the previous section did show a qualitative agreement between the measured and predicted performance for the composite concrete pavements constructed at MnROAD. For the three MnROAD cells, the fit of the measured and predicted curvature can be qualitatively placed in one of two groups.

For Cell 71 and Cell 72, ISLAB consistently under-estimated the measured slab curvature. However, it was postulated that better, and perhaps good, agreement could be obtained with modified input data. For Cell 70, however, there was no consistent relationship between the measured and predicted slab curvature. Although modifications to the input data in order to improve the fit were attempted, an adequate fit was not achieved. Without confidence in the ability of ISLAB to model the response of the HMA/concrete composite pavement, the sensitivity analysis performed in this section will focus on the influential parameters in the design of composite concrete pavements.

In order to determine which pavement parameters influence the performance of composite concrete pavements, this sensitivity analysis considers a broader range of variables

relative to those encountered at MnROAD. Within this sensitivity analysis, three assessments will be made.

The first assessment examines the location and magnitude of the critical tensile pavement stress determined using ISALB under temperature loading conditions alone. The second assessment looks at a loading condition in which both temperature and vehicle loads are applied. The specific temperature loads applied for the second assessment are extreme temperature gradients. The objective of this assessment is to determine the range of maximum stresses in composite pavements, especially relative to a homogeneous pavement.

The third assessment involves comparing the stresses in various composite pavements and a homogeneous pavement due to a vehicle load and more commonly encountered moderate temperature gradients. Stress will be calculated at critical points of interest that results in the initiation of pavement distress. Specifically, in-plane stresses parallel to the edges of the slab will be examined. These stresses are calculated by ISLAB at the top of the slab, immediately above and below the layer interface, and at the bottom of the slab. The directions of these stresses are such that a vertical crack would initiate from their application. The tensile stress at these critical locations will then be compared against the strength of the composite pavement material at that location. A comparison of the sum of the stress/strength ratios at the potential locations of distress initiation will provide a basis for assessing where each composite pavement would be likely to fail and the relative order in which the various composite and the homogeneous pavement considered in this sensitivity analysis might fail.

6.1 STRESS ANALYSIS INPUT PARAMETERS

The same parameters that needed to be determined in the assessment of the ability of ISLAB to predict the measured pavement response at MnROAD must also be established for the sensitivity analysis. As was done in Section 5.0 , these parameters will be grouped and discussed in three categories, structural parameters, material parameters, and environmental loads.

6.1.1 Stress Sensitivity Analysis Structural Input Parameters

The parameters that need to be specified in ISLAB include slab geometry and mesh size, layer thickness, foundation type, joint transfer parameters, and the interface condition between adjacent layers. The number of slabs in the longitudinal direction was chosen as three while the number in the transverse direction was two. The dimensions of each of the slabs are 15-ft long by 12-ft wide. The mesh chosen for each model includes six inch square elements.

With respect to the thickness of the upper layer, typical values used in Europe have been reported to be 2 inches in Austria and Germany and 3.5 inches in the Netherlands. Using a thinner layer poses construction issues while using a thicker layer generally incurs a higher cost because of its durable aggregates and high cement content. Based on this experience, the thickness of the upper layer in the stress sensitivity analysis will be varied between 2 and 4-in. As before, the pavement structure was modeled as two bonded plates resting on a Winkler foundation.

A special consideration for the homogeneous pavement modeled in this analysis is that it was modeled as two bonded plates, a 3-in plate on top of a 6-in plate. Each plate possessed the same thermal and structural properties. Because ISLAB's nodal thickness is always equal to the

plate thickness, stresses within the slab thickness cannot be readily determined. Defining the homogeneous pavement as two bonded plates with the same structural and material properties allows for determination of the stress at a point within the pavement thickness.

When performing the analysis presented in Section 5.0 , it was found that the k-value did not significantly influence the stress generated by temperature loads alone. For this reason, the k-value was not varied. A k-value of 180 psi/in was used throughout the analysis. The LTE of the joints, was selected as 95 percent and also held constant.

6.1.2 Stress Analysis Material Input Parameters

The material parameters that need to be specified in the slab models include the modulus of elasticity, Poisson's ratio, CTE, and unit weight for each layer within the composite slab. Poisson's ratio and the unit weight of the concrete, because of their relatively small influence, were not varied in the analysis. The unit weights and Poisson's ratio used in this analysis are the same as those measured and estimated for the construction materials used in constructing the MnROAD cells. These unit weight values were presented in Table 4.9 and Poisson's ratio was discussed in Section 5.1.2 .

The elastic modulus and CTE of the concrete were selected to represent composite pavements constructed using both virgin and recycled aggregates. Recycled aggregate in new pavement construction has been shown to influence both the elastic modulus and CTE. The following section will discuss the material constraints applied to the elastic modulus and CTE in the ISLAB stress analysis. These constraints were based on the European experience with recycled concrete,.

Composite pavements constructed in Europe typically have higher cementitious contents, stiffer and stronger aggregate, and a lower aggregate top size in the upper layer relative to the lower layer. These factors can contribute to a common situation where the strength and elastic modulus of the upper EAC layer is higher than that of the underlying layer. While a range of ratios of elastic modulus for the EAC with respect to the lower layer elastic modulus (E_{EAC}/E_{LOW}) was not available in the literature, it was desired to expand the analysis to ratios beyond those encountered at MnROAD. Ratios of 1.25/1, and 1.5/1 were used as part of the composite pavement design limitations for this stress analysis.

Water-to-cement ratios typically used in paving concrete dictate that the elastic modulus is controlled by the weaker paste constituent, especially for normal weight concretes [9]. In light of these observations, the expected range of elastic moduli for the upper EAC layer is likely to be similar to that for typical paving concretes. A study looking at the premature deterioration of JPCP pavements in Pennsylvania found a range of elastic moduli of mature paving concrete from different regions across the state to be between 3.4 and 6.2 million psi. The elastic modulus of the EAC layer in this stress analysis was subsequently kept within these bounds [34]. Values of the elastic modulus for the upper EAC layer were 4.5, 5.4, and 6.2 x 10^6 psi. These values are based on the E_{EAC}/E_{Low} ratios selected and the constraints for typical paving concrete elastic moduli.

The elastic modulus for the recycled concrete in the lower layer, $E_{Low,}$ was selected to be 25 percent lower than the homogeneous pavement consisting of the same virgin aggregate. This limitation was applied because elastic modulus values for concrete containing recycled concrete aggregate when compared to a virgin aggregate control can be between 1 and 50 percent lower than a mix containing only virgin aggregates [35]. A base elastic modulus of 4.8 x 10^6 psi was

selected for the homogeneous pavement, and therefore the base elastic modulus for the recycled concrete was 3.6 x 10^6 psi. An additional lower layer elastic modulus of 4.8 x 10^6 psi was also considered for additional variability.

The CTEs used in the sensitivity analysis were selected to reflect both the influence of aggregate type and residual mortar content on the recycled coarse aggregate. Using the mix designs from MnROAD as shown in Table 3.1, the volumetric proportion of coarse aggregate, cementitious material, and fine aggregate were obtained for each mix. Typical CTE values were assigned to each mix constituent and a volume weighted average CTE was determined. For the EAC mix, the parameter that was varied to influence the overall CTE of the mixture was the coarse aggregate type. Granite and quartzite, two coarse aggregate types typically used in the EAC in Europe, were selected. Only one recycled concrete coarse aggregate CTE, 4.5 x 10^{-6} in/in/^{o}F, was considered. The overall mix CTE was varied however by modifying the residual cement paste associated with the aggregate after crushing. Based on the recycled mix proportioning at MnROAD, the CTE for a concrete when no residual mortar is clinging to the aggregate is 4.8 x 10^{-6} in/in/^{o}F. If the coarse aggregate was assumed to have 10 and 30 percent residual mortar contents, the overall mix CTE changed to 5.1 x 10^{-6} in/in/^{o}F and 5.6 x 10^{-6} in/in/^{o}F, respectively.

Table 6.1 provides a summary of the various pavement material variables discussed in the preceding paragraphs and analyzed as part of the sensitivity analysis. The combinations of variables shown resulted in the analysis of 72 different composite pavement structures in addition to the homogeneous pavement structure modeled for comparison.

Table 6.1: Pavement Structures Considered as Part of Stress Sensitivity Analysis

EAC Thickness (in)	RCC Thickness (in)	EAC Elastic Modulus ($x10^6$ psi)	RCC Elastic Modulus ($x10^6$ psi)	EAC Coarse Agg CTE (10^{-6} in/in/^oF)	EAC Mix CTE (10^{-6} in/in/^oF)	RCC Coarse Agg CTE (10^{-6} in/in/^oF)	% Mortar	RCC Mix CTE (10^{-6} in/in/^oF)
2, 3, 4	5, 6, 7	4.5, 5.4, 6.2	3.6, 4.8	4.5, 6.7	4.7, 5.7	4.8	10, 30	5.1, 5.6

6.1.3 Stress Analysis Temperature Loading Input Parameters

As was done in Section 5.1.3, this sensitivity analysis utilized a non-linear temperature gradient to define thermal loads. Because the ELTG frequency distribution varies widely between pavements and the strain equivalent ELTG neglects the contribution of the residual stresses, actual temperature profiles were used in the sensitivity analysis assessment. The specific temperature profiles selected were based on MnROAD temperature profiles and were selected based on making two assessments with the resultant stress data.

The first assessment is an evaluation of the variation in the maximum stresses generated in the pavement from extreme temperature gradients. The second assessment is an evaluation of the stresses that are generated in the pavements from typical temperature gradients. A desire to assess seasonal effects was also incorporated by selecting gradients from the different seasons. In total, four sets of four temperature profiles were selected. To accomplish the aforementioned objectives, a mild and extreme positive and negative temperature gradient were selected from each of the four seasons. The sixteen separate temperature distributions selected are shown in Table 6.2.

Table 6.2: Temperature Loads Used in Composite Concrete Pavement Sensitivity Analysis

MnROAD Temperature Condition		Depth (in)/Temperatures in °F									
Date	**Time**	**0.0**	**1.0**	**2.0**	**3.0**	**4.0**	**5.0**	**6.0**	**7.0**	**8.0**	**9.0**
10/12	23:30	35.6	38.1	40.4	42.6	44.8	46.9	48.8	50.8	52.6	54.4
10/2	19:45	50.7	51.9	53.1	54.3	55.3	56.3	57.3	58.2	59	59.9
9/27	8:30	66.5	62.5	59.6	57.6	56.3	55.5	55.2	55.3	55.5	55.9
10/5	12:30	83.9	79.6	75.7	72.1	68.8	65.8	63	60.6	58.3	56.1
1/30	7:00	-15.7	-12.8	-10.1	-7.3	-4.6	-2	0.7	3.2	5.7	8.2
1/23	22:45	4.7	5.7	6.8	7.9	8.9	10	11	12.1	13.2	14.2
2/17	11:30	54.1	48.6	43.8	39.7	36.2	33.1	30.6	28.4	26.6	24.9
1/7	12:00	27.4	25.2	23.3	21.7	20.4	19.5	18.7	18.2	17.8	17.5
5/20	3:45	42.6	45.1	47.5	49.7	51.9	54	56	57.9	59.8	61.6
4/3	2:00	32	33.8	35.3	36.6	37.8	38.7	39.5	40.2	40.9	41.4
4/8	14:00	85.7	78.9	72.5	66.6	61.2	56.2	51.7	47.4	43.4	39.6
5/25	10:30	68.3	65.5	63.2	61.6	60.3	59.4	58.7	58.3	58	57.7
7/24	2:30	59.5	62	64.4	66.6	68.8	70.8	72.7	74.6	76.3	78
8/16	23:30	75.5	77	78.3	79.5	80.4	81.3	82	82.7	83.3	83.9
6/30	12:45	120.4	113.9	108.1	102.9	98.2	94	90.1	86.5	83.1	79.8
8/17	17:15	95.4	95.5	95.1	94.3	93.2	92	90.5	89	87.3	85.7

6.1.4 Vehicle Load

While the effects of environmental stresses on composite pavements are important, an overall assessment of pavement performance cannot be conducted without considering vehicle loads. It is also important to assess the magnitude of the stress induced by environmental loads relative to the stress induced by vehicle loads. For this reason, two loading conditions for the first three axles of a standard five-axle semi were considered. The single tire axle represents the steering axle and the tandem duals are on the rear of the tractor. The two locations of the single and dual axle tires that were considered are illustrated below in Figure 6.1. The magnitude of the load applied was 12,216 lbs for the steering axle and 33,677 lbs for the driving axle.

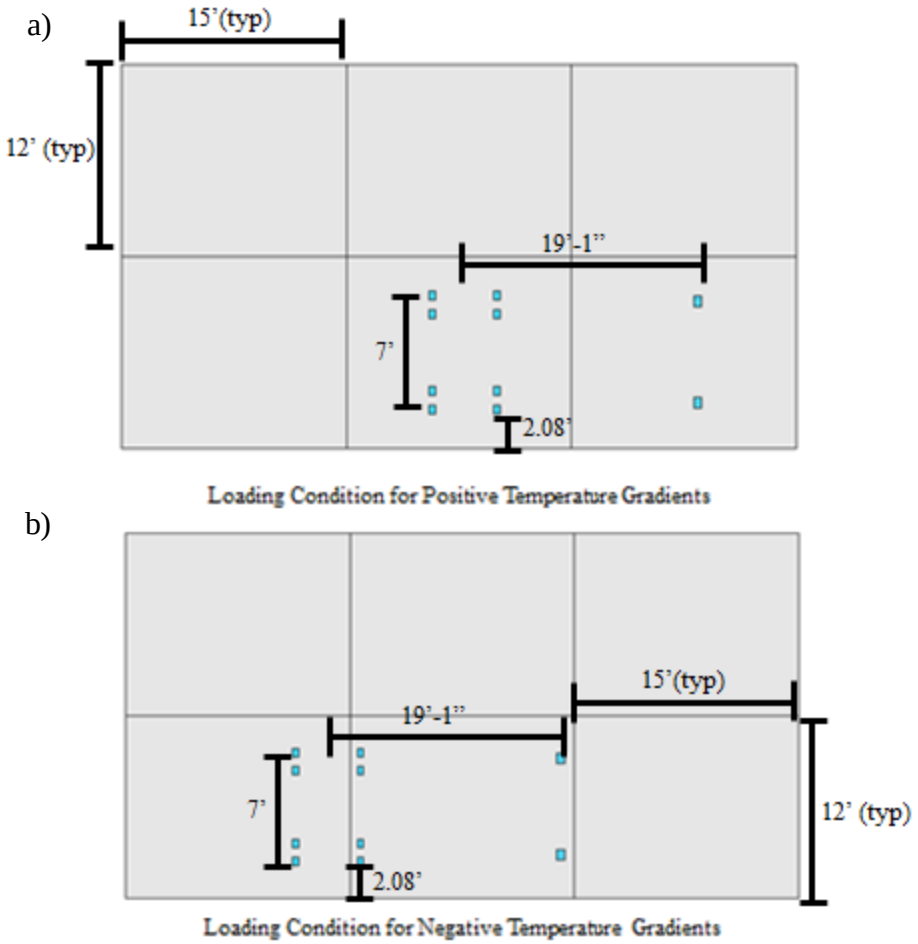

Figure 6.1: Vehicle Load Conditions Considered in Sensitivity Analysis

6.2 SENSITIVITY ANALYSIS RESULTS

Considering the range of temperature loads, pavement structure design parameters, and vehicle loads analyzed, a total of 6,912 ISLAB runs were processed to obtain the results presented in this section.

As mentioned in Section 6.0 the assessment of stress magnitude will focus on three objectives. The first assessment addresses the location of the critical stress in composite pavements subjected to only temperature loading conditions. The second assessment examines

composite pavements under only relatively extreme temperature gradients. The third assessment involves comparing the stresses in various composite pavements and a homogeneous pavement due to a vehicle load and more typical temperature loading conditions. For these analyses, the critical stress location was taken as the location with the highest tensile stress. The critical tensile stress location is simply referred to as critical stress location herein.

6.2.1 Critical Stress Location – Temperature Load Only

For the 2,304 ISLAB runs for which only a temperature loading was applied to the pavement, the distribution of the location of the critical tensile stress can be seen in Figure 6.2.

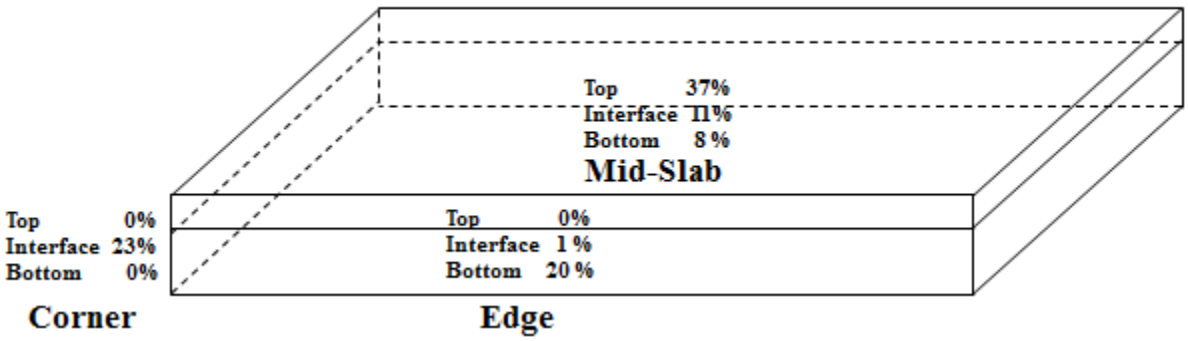

Figure 6.2: Distribution of Critical Stress for Composite Pavements Subjected to Temperature Loads

Figure 6.2 suggests that in addition to the typical mid-slab critical stress location seen in conventional concrete pavements, a third location of the critical stress is also common. This location is between the composite pavement layers. For the structures analyzed, the critical stress is between the layers in 34% of the conditions analyzed. For the homogeneous pavement analyzed, the location of the critical stress for the 16 temperature loadings conditions analyzed

can be seen in Figure 6.3. In Figure 6.3, the temperature gradients that correspond to the critical stress being at the top of the pavement at mid-slab are all negative temperature gradients. The 19 percent that are at the bottom of the pavement at mid-slab are due to the moderate positive temperature gradients while the 25 percent that are at the bottom of the pavement along the edge are due to the extreme positive temperature gradients. The six percent at the edge at the interface between the pavement layers represents a moderate positive temperature gradient occurring in the fall. The fact that the critical stress location occurred here, even for a homogeneous pavement, is due to the relatively high self-equilibrating stress created by the non-linearity in the fall moderately positive temperature gradient. Because of the relatively low magnitude of the temperature gradient, the magnitude of the stress at this corner location is relatively insignificant.

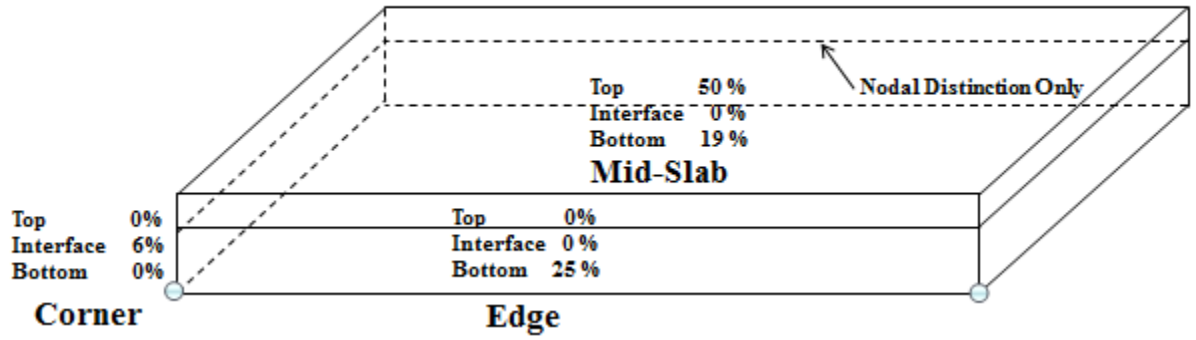

Figure 6.3: Distribution of Critical Stress for Homogeneous Pavement Subjected to Temperature Loads

A comparison of Figure 6.2 and Figure 6.3 reveals that for some of the composite pavement structures analyzed, the critical stress is at a different location relative to a homogeneous pavement subjected to the same temperature loads. In 13 and 22 percent of the

conditions that in the homogeneous slab would have produced the critical stress at the top and bottom of the slab respectively, the critical stress in the composite slab was at the layer interface.

An investigation of the causes of the critical stress being at the interface between the pavement layers was done separately for the corner and mid-slab location. Table 6.3 presents an analysis of all the runs for which the critical stress location was at the corner at the interface between the layers. Table 6.4 considers the critical stresses that occurred at mid-slab at the interface between the layers. From Table 6.3, the most influential pavement properties for the critical stress being at the interface in the corner location are the sign of the temperature gradient applied, the reference temperature, and the difference between the CTEs of the top and bottom layer. The layer thickness and relative elastic moduli of the two composite pavement layers seem to have a relatively minor influence on the critical stress being located at the interface for the range of parameters considered.

Table 6.3: Influence of Pavement Properties on the Critical Stress Being at the Interface in the Corner for Applied Temperature Loads

Temperature Gradients															
Extreme Negative Temperature Gradient				**Moderate Negative Temperature Gradient**				**Moderate Positive Temperature Gradient**				**Extreme Positive Temperature Gradient**			
Fall	**Winter**	**Spring**	**Summer**	**Fall**	**Winter**	**Spring**	**Summer**	**Fall**	**Winter**	**Spring**	**Summer**	**Fall**	**Winter**	**Spring**	**Summer**
0%	2%	0%	0%	2%	9%	3%	0%	25%	19%	16%	0%	1%	17%	3%	3%

Reference Temperature, ^{o}F	
65	**100**
40%	60%

Top Layer Thickness		
2-in	**3-in**	**4-in**
28%	38%	34%

Ratio of Top to Bottom Layer Elastic Moduli x10^{6}psi					
4.5/4.8 = 0.94	**4.5/3.6 = 1.25**	**5.4/4.8 = 1.13**	**5.4/3.6 = 1.5**	**6.2/4.8 = 1.29**	**6.2/3.6 = 1.75**
16%	16%	19%	17%	20%	13%

Ratio of Top to Bottom Layer Coefficient of Thermal Expansion x10^{-6}			
4.7/5.1 = 0.92	**4.7/5.6 = 0.84**	**5.7/5.1 = 1.12**	**5.7/5.6 = 1.02**
22%	38%	26%	14%

With respect to temperature gradients, positive temperature gradients create the critical stress at the interface between the composite pavement layers in the corner a disproportionate 84 percent of the time. Further analysis of this 84 percent reveals that 60 percent are from moderately positive temperature gradients and 24 percent are from extreme positive temperature gradients.

Contrary to the situations for which the critical stress is at the interface between the layers in the corner of the pavement, the critical stress occurs at the interface at mid-slab under mostly negative temperature gradients. A similar breakdown, as was shown in Table 6.3, is presented in Table 6.4 for the critical stress location at the interface at mid-slab. Forty-six percent of these situations occur for the extreme negative temperature gradient, 39 percent occur

for the moderate negative temperature gradients, and 14 percent occur for the moderate positive temperature gradients.

Table 6.4: Influence of Pavement Properties on the Critical Stress Being at the Interface at Mid-Slab for Applied Temperature Loads

Temperature Gradients															
Extreme Negative Temperature Gradient				**Moderate Negative Temperature Gradient**				**Moderate Positive Temperature Gradient**				**Extreme Positive Temperature Gradient**			
Fall	**Winter**	**Spring**	**Summer**	**Fall**	**Winter**	**Spring**	**Summer**	**Fall**	**Winter**	**Spring**	**Summer**	**Fall**	**Winter**	**Spring**	**Summer**
11%	24%	8%	3%	6%	22%	8%	3%	3%	9%	2%	0%	0%	0%	0%	0%

Reference Temperature ^{o}F	
65	**100**
33%	67%

Top Layer Thickness		
2-in	**3-in**	**4-in**
32%	39%	29%

Ratio of Top to Bottom Layer Elastic Moduli x10^{6}psi					
4.5/4.8 = 0.94	**4.5/3.6 = 1.25**	**5.4/4.8 = 1.13**	**5.4/3.6 = 1.5**	**6.2/4.8 = 1.29**	**6.2/3.6= 1.75**
19%	14%	17%	13%	17%	18%

Ratio of Top to Bottom Layer Coefficient of Thermal Expansion x10^{-6}			
4.7/5.1 = 0.92	**4.7/5.6 = 0.84**	**5.7/5.1 = 1.12**	**5.7/5.6 = 1.02**
29%	40%	29%	3%

The observations from Table 6.3 and Table 6.4, regarding influential parameters on critical stress location, are primarily a function of the nature of the curvature induced in the slab by each of the gradients. The typical curvature and the stresses generated between the pavement layers are shown in Figure 6.4 for both a typical positive and negative temperature gradient.

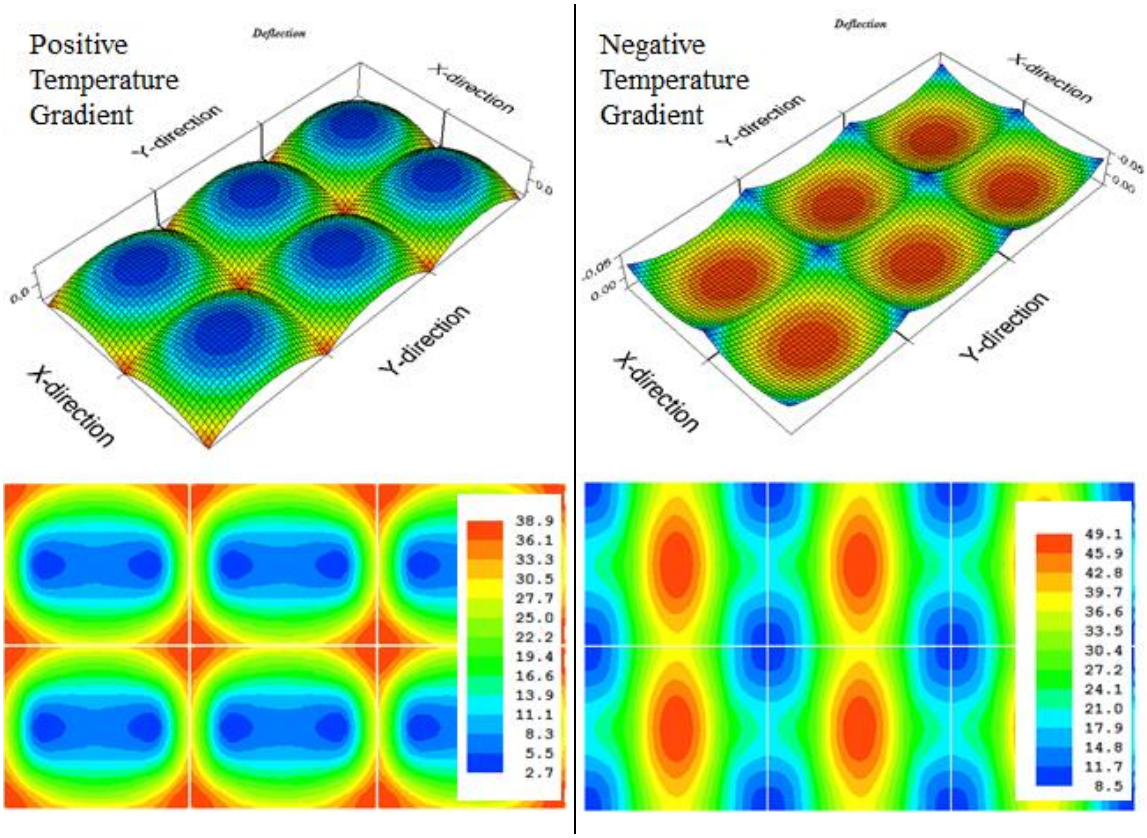

Figure 6.4: Typical Curvature and Principal Stresses at the Interface for Two Temperature Gradients

As Figure 6.4 illustrates, the induced curvature for a positive gradient is such that it tends to generate a higher tensile stress in the corner at the interface. For negative gradients, the critical stress location tends to be at the center of the slab and at the top of the slab. The distribution of stresses between the layers for a negative temperature gradient shows that the highest stress between the layers also occurs at the center of the slab. Accordingly, composite pavements have more instances with critical stresses at the corner for positive rather than negative temperature gradients.

While the positive temperature gradient shown in Figure 6.4 produces the critical stress at the corner location, Table 6.4 shows that positive temperature gradients are also capable of

producing the critical stress at the mid-slab location. Figure 6.5 shows one such situation where a positive temperature gradient produced the critical stress at the interface at mid-slab.

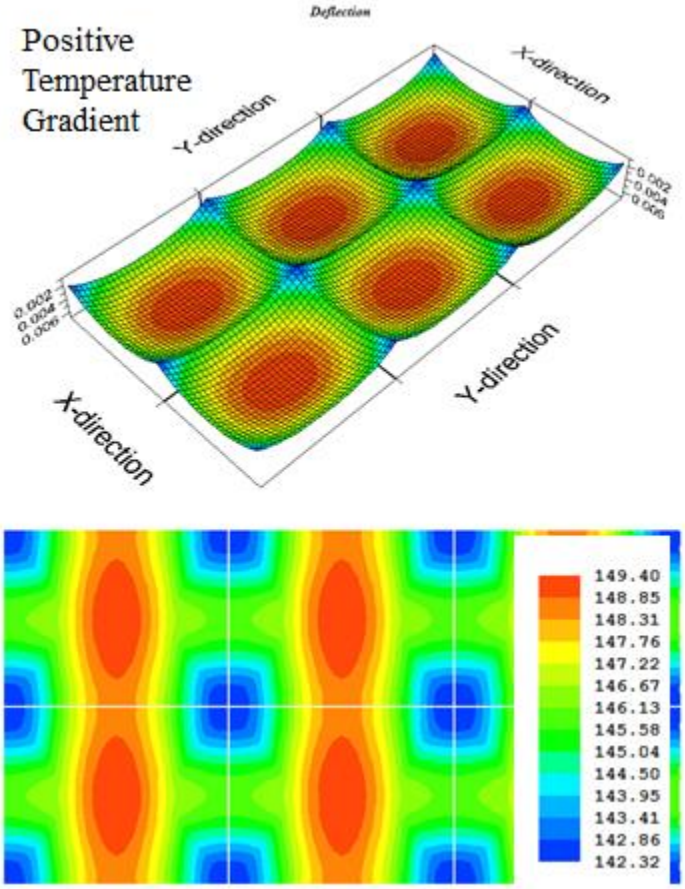

Figure 6.5: Positive Temperature Gradient Producing the Critical Stress at the Interface at Mid-Slab

In Figure 6.5, despite a positive temperature gradient being applied, the slab is curled upward. This curvature, in-spite of the temperature gradient, is due to the influence of the difference in CTE between the pavement layers and the distance of the average slab temperature from the reference temperature. In Figure 6.5, the reference temperature is 100^{o}F and the coefficients of thermal expansion are 5.7x10^{-6}/^{o}F and 5.1x10^{-6}/^{o}F for the top and bottom layers,

respectively. The average pavement temperature is 21°F. Although the top of the pavement is warmer than the bottom, because the average pavement temperature is significantly difference than the reference temperature, the net effect is that the top of the pavement has thermally contracted more than the bottom layer resulting in positive curvature.

Temperature gradients from fall, winter, and spring, when the average pavement temperatures are relatively lower and significantly different than the 100°F reference temperature, contribute the most to the critical stress being at the interface at the corner. Likewise, temperature gradients that develop during the summer, when the average pavement temperature is significantly higher than a 65°F reference temperature, also significantly contribute to the critical stress being at the interface at the corner.

The magnitude of the difference between the average pavement temperature and the reference temperature also plays a significant role in the generation of the critical stress between the layers of the pavement at mid-slab. This can be seen in Table 6.4 because, whether positive or negative, it is always the winter gradient, with the lowest average temperature, that has the most situations for which the critical stress is at the interface at mid-slab.

6.2.2 Critical Stress Location – Temperature and Vehicle Load

The analysis performed in the previous section indicated seven primary locations with respect to the location of the critical stress in composite concrete slabs. Six of these locations were namely at the top of the slab, at the bottom of the slab, and at the composite pavement layer interface for both the outside edge and mid-slab location. The seventh location was at the interface between the layers at the corner of the pavement. The development of distress at any one of these locations however is dependent on that location remaining the critical stress location when traffic

is considered as well. Vehicle loads that comprise the traffic seen by the slab are generally what cause distresses and failure to initiate. The curvature in composite pavement slabs, which in the previous section was shown to not necessarily always be positive for negative temperature gradients and negative for positive temperature gradients, also plays a role in both the location and magnitude of the stress generated by a given vehicle load.

Figure 6.6 shows the distribution of the critical stress location for the homogeneous pavement. The vehicle loads presented in Section 0, and the temperature loads presented in Section 6.1.3 were applied to obtain the data. While a model was created and analyzed for each combination of pavement structural properties, temperature gradient, and each of the two vehicle loads, only the results from the vehicle load that generated the highest critical stress were retained for analysis.

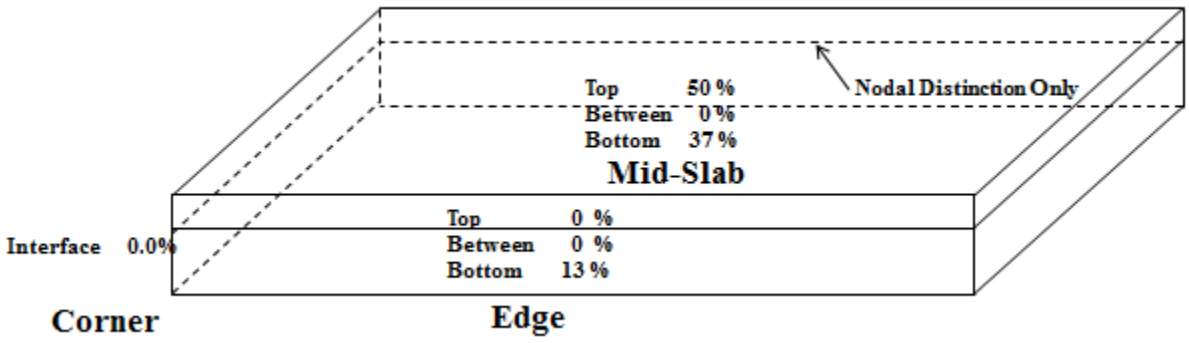

Figure 6.6: Critical Stress Locations for Homogeneous Pavement with Temperature and Traffic Loads

Although the critical stress location is shown to strongly favor the mid-slab location over the edge of the pavement, the actual difference in the stress magnitude between the mid-slab and edge location in each instance is less than ten percent. The mid-slab preference is likely due to

the location selected for the application of the vehicle load. The importance of Figure 6.6 is not the distribution between the edge and mid-slab location but the distribution of the critical stress location between the top and bottom of the pavement. For the homogeneous pavement, these locations correspond with negative and positive applied temperature gradients respectively.

Conditions where the critical stress is at the bottom of the slab are also indicative of the loading condition in which the steering axle of the vehicle is loading the slab at mid-slab, as shown in Figure 6.1.a. Situations where the critical stress is at the top of the slab are due to the steering axle of the vehicle being applied at one end of the slab and the leading axle of the tandem drive axle being applied at the other end of the slab. This loading condition is illustrated in Figure 6.1.b.

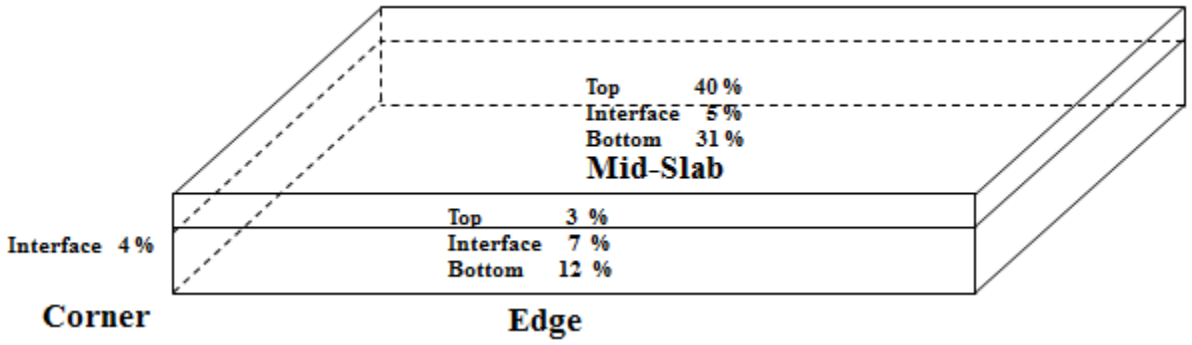

Figure 6.7: Distribution of Critical Stress Location for Composite Pavements with Temperature and Traffic Loads

Figure 6.7 shows that when a vehicle load is also considered for composite pavements, the critical stress is only at the layer interface half as often as it was considering a temperature loading condition alone. Like in the case of the homogeneous pavement, the preference of the critical stress location for the mid-slab relative to the edge is only due to a relatively small

difference in the critical stress magnitude between the two locations. Other than the approximate 15 percent of conditions in which the critical stress occurred at the interface between the pavement layers, a relatively even split between the critical stress occurring at the top and bottom of the slab can be observed.

Figure 6.7, however, is the aggregation of data from the 144 composite pavements examined as part of this sensitivity analysis. A closer examination of the individual constituents of Figure 6.7 reveals an alternative conclusion. Only 21 percent of the composite pavements examined were similar to the homogeneous pavement in the sense that half of the critical stress locations were at the top of the slab and half were on the bottom. The remaining composite pavements had at least one instance of the sixteen temperature and vehicle load conditions where the critical stress was at the interface between the layers along the slab edge. The composite pavements with an even distribution of critical stress locations between the top and the bottom of the slab or those with only one or a few instances where the critical stress location is at the interface will likely only be susceptible to failures similar to that in a homogeneous pavement. This is namely bottom-up or top-down fatigue cracking.

Eight percent of the composite pavement systems analyzed however had half, or more than half, of the temperature and vehicle loading conditions generate the critical stress at the layer interface. By looking at these relatively extreme categories, some important observations regarding composite pavement performance can be made. Table 6.5 presents a comparison of properties between the composite slabs with an even split of critical stresses on the top and bottom of the slab and the composite pavements with half or more of the critical stresses at the interface.

Table 6.5: Comparison of Composite Pavements with Varying Distributions of the Critical Stress Location

Reference Temperature ^{o}F											
65				**100**							
77%		*0%*		23%		*100%*					
Top Layer Thickness											
2-in				**3-in**				**4-in**			
48%		*55%*		29%		*36%*		23%		*9%*	
Top/Bottom Layer Elastic Moduli x10^{6}psi											
4.5/4.8		**4.5/3.6**		**5.4/4.8**		**5.4/3.6**		**6.2/4.8**		**6.2/3.6**	
23%	*27%*	19%	*18%*	16%	*18%*	13%	*9%*	13%	*18%*	13%	*9%*
Top/Bottom Layer Coefficient of Thermal Expansionx10^{-6}											
4.7/5.1			**4.7/5.6**			**5.7/5.1**			**5.7/5.6**		
32%	*0%*		0%	*100%*		10%	*0%*		55%	*0%*	

*Black Text – Composite Pavements with Half Critical Stress Locations on Top of Slab and Half on Bottom

** Red Text – Composite Pavements with More than Half of Critical Stress Locations at Layer Interface*

Several conclusions regarding the specific trends influencing the critical stress location in composite pavements subjected to a relatively significant vehicle load can be made through an examination of Table 6.5. A reference temperature of 100^{o}F leads to the critical stress being at the interface while a reference temperature of 65^{o}F tends to decrease the chance that the critical stress location will be at the interface. With a reference temperature of 100 ^{o}F, the average pavement temperature is far below the reference temperature for the vast majority of the year, and, depending on the specific environment, may always be below the reference temperature. A large difference between the reference temperature and the average pavement temperature, especially for pavements with a high difference in the CTE between the layers, tends to exacerbate the interface stress. This is likely the reason for the high occurrence of composite

pavements with a larger difference in CTE in the category of composite pavements with more than half of the critical stress locations at the layer interface.

A thinner upper layer is influential in both a low and high number of stresses occurring at the layer interface. The thinner upper layer likely results in a relatively low number of instances when the peak stress occurs at the interface because in terms of structural significance, a thinner layer will dictate the overall structural behavior less than a relatively thicker layer. A thinner layer would also be influential in terms of a high instance of the critical stress occurring at the interface because when the upper layer is thinner, it is generally further from the slab's neutral bending axis. The further the interface is from the slab's neutral bending axis, the more significant the contribution of the bending stress due to slab self-weight and vehicle load is to making the critical total stress at the interface.

Relative to some of the other pavement variables considered, the relationship between the differences in the elastic moduli of the layers is relatively weak. The combination with the most structures in either category had both the smallest difference between the layers elastic moduli (0.3×10^6 psi), and was the only combination with a larger upper layer elastic modulus relative to the lower layer.

A relatively large difference in the layer CTE is a predominant factor to control with respect to limiting the occurrence of multiple instances with the critical stress at the layer interface. This observation is due to the fact that the larger the difference in the CTE between the layers, the larger the restrained thermal strain at the interface becomes. This restrained thermal strain results in stresses being generated at the interface. It is therefore expected that the larger differences in CTE, which results in a large degree of restrained thermal strain, is a typical

component of pavements with more than half of the critical stress instances occurring at the interface.

In addition to the factors highlighted in Table 6.5, one third of the composite pavements were found to be curled disproportionately up or down. This is despite the fact that an even number of positive and negative temperature gradients were applied to each pavement. With a preference in the direction of curvature, there is also a preference for the type of distress that initiates.

6.2.3 Composite Pavement Stresses under Extreme Loading Conditions

Pavement slabs can generally fail in two ways. The first way is through fatigue. This type of failure is associated with the application of many loads that are relatively smaller in magnitude. For some types of pavements however, a relatively few load applications that generate stresses with a large enough magnitude may also cause a pavement slab to fail. If failure does not occur, these few loads may at least provide the same amount of fatigue damage as many applications of a much smaller load. Because of the relative significance that extreme loading conditions can have on the performance of a pavement they were examined separately as part of this sensitivity analysis.

In the assessment of fatigue damage and the correlation between fatigue damage and the initiation of a given distress, the magnitude of the stress generated in the slab is compared with the concrete strength. For each ratio of applied stress to material strength, an allowable number of load applications can be applied before failure initiates. Using the pavement layer elastic moduli selected in Section 6.1.2, the compressive strength was estimated using Equation 35. The modulus of rupture was calculated using Equation 36 [9].

$$f_c = \left(\frac{E}{57000}\right)^2 \quad lb/in^2 \qquad \text{Equation 35}$$

$$f_r = 7.5\sqrt{f_c} \quad lb/in^2 \qquad \text{Equation 36}$$

Using Equation 35 and Equation 36, the moduli of rupture for the hypothesized concrete mixes used in this sensitivity analysis are shown in Table 6.6.

Table 6.6: Estimated Modulus of Rupture of Concretes used in Sensitivity Analysis

Elastic Modulus (psi)	Modulus of Rupture (psi)
3.60E+06	470
4.50E+06	590
4.80E+06	630
5.40E+06	710
6.20E+06	810

It was discussed in Section 2.4 that for a given applied stress/strength ratio, there is a corresponding number of cycles that can be applied before failure is observed. While different materials and structures have a different relationship between the stress/strength ratio and the number of cycles until failure occurs, the relationship used in Version 1.1 of the MEPDG for transverse cracking of concrete slabs is of the form shown in Equation 37. This equation is based on datasets from the Long Term Pavement Performance (LTPP) program. Data collected as part of the LTPP program was used to provide a correlation between observed distresses in pavements and measured inputs collected in detail throughout the life of the member pavements.

$$\log(N) = C_1 \cdot \left(\frac{MR}{\sigma_{applied}} \right)^{C_2} + C_3$$ Equation 37

In Equation 37, C_1, C_2, and C_3 are constants of 2.0, 1.22, and 0.4371 respectively. MR represents the modulus of rupture at the location of interest and σ is the stress at the location of interest. Although Equation 36 was not developed specifically for composite pavements, its form provides a reasonable basis for assessment.

Table 6.7 presents the maximum principal stress at the edge of the pavement for the homogeneous pavement. These values are for the extreme temperature loading conditions and the vehicle load that generated the highest principal stress. Considering the homogeneous pavement modulus of rupture from Table 6.6 (630 psi), these conditions resulted in stress/strength ratios for the homogeneous pavement ranging from 0.36 to 0.55. These ratios in Equation 37 correspond with more than 5.3 $x10^8$ and 3.9 $x10^6$ applications until failure is reached, respectively. Additionally, if only these particular temperature gradients were applied evenly until failure was reached, the homogeneous pavement should exhibit bottom-up fatigue cracking. This is due to the larger average stress magnitude from the extreme positive temperature gradients. The homogeneous slab is also always curled upward for the negative temperature gradients and curled downward for the positive temperature gradients.

Table 6.7: Homogeneous Pavement Critical Stress Magnitude with Temperature and Vehicle Load

Critical Stress (psi)							
229	252	230	230	252	225	348	318
Temperature Gradients							
Fall	**Winter**	**Spring**	**Summer**	**Fall**	**Winter**	**Spring**	**Summer**
Extreme Negative Temperature Gradient				**Extreme Positive Temperature Gradient**			

Of the 1,152 conditions analyzed, (8 temperature gradients and the critical vehicle load for each of the 144 composite pavement structures), the magnitude of the critical stress for the extreme temperature loading conditions ranged from 150 to 490 psi and the critical stress/strength ratio ranged from 0.25 to 0.74. The fatigue damage due to all of the extreme temperature gradients was calculated for each pavement. The fatigue damage for the composite pavements was between 28 times less and 17 times more than the fatigue damage for the homogeneous pavements. This also means that the composite pavement with the least fatigue damage had almost 500 times less fatigue damage than the composite pavement with the most fatigue damage. While none of the composite pavements experienced a stress significant enough to cause failure with a single load application, this range represents a significant departure in performance from the homogeneous pavement.

As was illustrated in Section 6.2.1 for composite pavements subjected to a temperature gradient alone, the curvature in the slab due to a positive or negative temperature gradient is not necessarily downward or upward, respectively. This means that although an even number of positive and negative temperature gradients were applied in this analysis, for some composite pavements, the slab is disproportionately curled in one direction. One type of fatigue cracking (bottom-up or top-down) would therefore be highly favored. In the assessment of the critical stress location for temperature loads only, the critical stress was also found to be between the pavement layers a significant percentage of the time. It is therefore important to assess fatigue damage at this location as well.

In order to assess performance, the individual composite pavement structures were gauged against the homogeneous pavement. This was done by taking a count of the number of relatively extreme conditions for each composite pavement subjected to the extreme temperature

loading conditions. Relatively extreme was defined as a temperature gradient in a composite pavement that led to a stress/strength ratio more than 20 percent higher than the stress/strength ratio in the homogeneous pavement when subjected to the same temperature gradient.

In forty-four percent of the composite pavements analyzed, the eight relatively extreme temperature gradients produced none, or only one, instance with a stress strength ratio more than 20 percent higher than the corresponding ratio in the homogeneous pavement. Forty-five percent of composite pavements however had at least four instances in which the critical stress strength ratio was more than 20 percent greater than the stress/strength ratio for the homogeneous pavement. For one composite pavement structures all of the temperature gradients generated a stress in the composite pavement with a resulting stress/strength ratio greater than 20 percent of the corresponding ratio for the homogeneous pavement.

Table 6.8 presents the properties of two groups of composite pavements. The first group has relatively few (0 or 1) situations in which the critical stress/strength ratio is less than 20 percent of critical stress/strength ratio for the homogeneous pavement. In the second group, the composite pavements have four or more situations where the critical stress/strength ratio is more than 20 percent greater than the corresponding value for the homogeneous pavement.

Table 6.8: Composite Pavements with Few and Many Situations with a High Critical/Stress Strength Ratio

Reference Temperature °F											
65				**100**							
48%		46%		52%		54%					
Top Layer Thickness											
2-in				**3-in**				**4-in**			
28%		38%		33%		34%		39%		28%	
Top/Bottom Layer Elastic Moduli x10^{6}psi											
4.5/4.8		**4.5/3.6**		**5.4/4.8**		**5.4/3.6**		**6.2/4.8**		**6.2/3.6**	
28%	3%	0%	34%	33%	2%	2%	32%	36%	2%	2%	28%
Top/Bottom Layer Coefficient of Thermal Expansionx10^{-6}											
4.7/5.1			**4.7/5.6**			**5.7/5.1**			**5.7/5.6**		
28%	26%		28%	28%		17%	18%		27%	28%	

* Black text - Composite pavements with one or no situations in which the critical stress/strength ratio is more than 20 percent of the stress/strength ratio for the homogenous pavement

* Red Text - Composite pavements with four or more situations in which the critical stress/strength ratio is more than 20 percent of the stress/strength ratio for homogeneous pavement

The results presented in Table 6.8 present a stark contrast to the results seen in Section 6.2.2 where the composite pavement structural variables influencing the generation of the critical stress at the layer interface was presented. In Table 6.8, the thermal restraint conditions unique to composite pavements, namely the reference temperature and the difference in the CTE between the pavement layers, seems to not be influential. Instead, having a critical stress/strength ratio more than 20 percent greater than the corresponding condition in the homogeneous pavement seems to be primarily dependent on structural stiffness. In Table 6.8, few pavements with a lower layer elastic modulus of 3.6 x 10^{6} psi exhibit good performance. The general trend is that the higher the flexural stiffness, the better the performance.

The trend with respect to the coefficient of thermal expansion for the composite pavements is that the higher the average CTE, the poorer the observed performance of the composite pavement. No performance correlation between the layers' CTE difference seems to

exist. This can be explained by considering that with a higher average CTE, more total curvature would be observed for a given temperature gradient. Increased slab curvature, would then lead to more stress induced by the vehicle load. A stronger correlation between the critical stress/strength ratio and average CTE rather than the correlation between the critical stress/strength ratio and the difference in the CTE or the reference temperature can be observed. This suggests that fatigue damage from extreme loading conditions in a composite pavement is governed primarily by material strength and by the curvature in the slab. Curvature is primarily a function of the average slab CTE. While the difference in the layer CTE plays a role in the stress/strength ratio, its influence is decidedly less influential than average CTE.

In addition to looking at the number of conditions in which the stress/strength ratio for the composite pavement is unfavorable relative to the homogeneous pavement, a direct comparison of fatigue damage due to all of the extreme temperature loading conditions was made between the composite and homogenous pavements. Ninety-four percent of the composite pavements had the highest fatigue damage at the bottom of the slab, and like the homogeneous pavement, were predicted to have bottom-up fatigue failure initiate first. Of the remaining six percent, less than five percent were predicted to have top-down cracking initiate first. For a single composite pavement subjected to the eight extreme temperature and vehicle loading conditions, the most fatigue damage occurred between the layers. It is surprising that for this composite pavement structure, the relatively large vehicle load did not induce enough bending stress at the slab depth extremes to cause the most fatigue damage there. The properties of this pavement are presented in Table 6.9.

Table 6.9: Pavement with High Interface Fatigue from Extreme Temperature Gradients and Vehicle Load

Upper Layer			Lower Layer			
Thickness (in)	**CTE (ε x10^{-6}/^{o}F)**	**E (x10^{6} psi)**	**Thickness (in)**	**CTE (ε x10^{-6}/^{o}F)**	**E (x10^{6} psi)**	**Reference Temperature (^{o}F)**
2	4.7	6.2	7	5.6	4.8	100

The reasons for the critical stress location being between the layers when this pavement was subjected to only temperature loads was discussed in Section 6.2.1. The critical stress location and location of highest fatigue occurring at the interface persists because the stresses induced by the temperature loading condition are relatively severe. The additional bending stress is also high at this location. The interface is relatively far away from the slab's neutral bending axis. Both factors make the interface the slab location with the most fatigue damage.

A direct comparison of the fatigue damage magnitude for the composite and homogeneous pavements revealed that only seven composite pavements had a lower fatigue damage magnitude from the eight extreme temperature and vehicle loading conditions relative to the homogeneous pavement. The properties of these pavements are presented in Table 6.10.

Table 6.10: Composite Pavements with Lower Fatigue Damage than Homogeneous Pavement for Extreme Temperature Gradients and Vehicle Load

Upper Layer			Lower Layer			
Thickness (in)	**CTE (ε x10^{-6}/^{o}F)**	**E (x10^{6} psi)**	**Thickness (in)**	**CTE (ε x10^{-6}/^{o}F)**	**E (x10^{6} psi)**	**Reference Temperature (^{o}F)**
3	5.7	5.4	6	5.1	4.8	65
4	5.7	5.4	5	5.1	4.8	65
2	5.7	6.2	7	5.1	4.8	65
3	5.7	6.2	6	5.1	4.8	65
4	5.7	6.2	5	5.1	4.8	65
2	4.7	6.2	7	5.1	4.8	100
4	5.7	6.2	5	5.1	4.8	100

From Table 6.10 it can be seen that the average elastic modulus for these pavements is greater than the average elastic modulus of 4.8 x10^6 psi for the homogeneous pavement. These pavements almost all have a reference temperature of 65^{o}F as well. The higher elastic modulus and higher strength of these pavements would be expected to perform better however. It is perhaps surprising that there are not more pavements with a high average stiffness that are included in Table 6.10. Based on discussions in the previous sections regarding the influence of the reference temperature, it is not surprising that the pavement structures in Table 6.10 primarily have the lower of the two reference temperature used in this sensitivity analysis. In one of the two instances in which the reference temperature is higher, the interface is located closer to the slabs neutral bending axis. In this instance, the interface stress would not add significantly to the bending stress induced by the slab weight and vehicle load at the top or bottom of the slab. In the other instance, the slab average CTE is reduced. Lower bending stresses due to the slab's self-weight and the applied vehicle load would be expected due to decreased slab curvature in response to the temperature gradient in the slab.

The lack of the prevalence of either the CTE combination with the lowest average CTE or the combination with the lowest difference in CTE between the layers is surprising. Further investigation revealed that for the pavement structures in Table 6.10, the majority of the fatigue damage at the bottom of the pavement was primarily due to the extreme gradients in the summer. Both the CTE combination with the lowest average CTE and the combination with the lowest difference in the CTE between the layers had higher stresses at the bottom of the pavement for the summer temperature gradients. This could be related to the fact that for the lowest average CTE combination, the top layer CTE is lower than the bottom layer CTE. The opposite condition

is present in the composite pavements in Table 6.10 and could be the influence as to why a superior performance was obtained for these pavements.

In general, the analysis of these results leads to conclusions that are not a significant departure from those that would be made for a homogeneous pavement alone. The performance of both the homogenous and most composite pavements is governed by the same factors under extreme temperature and vehicle loading conditions. These factors are namely the average concrete CTE and average elastic modulus. Through an assessment of fatigue damage for composite and homogeneous pavements, it was found that composite pavements are not beneficial. Superior performance, in terms of fatigue damage, was observed in only a small percentage of composite pavements. This beneficial performance was in part due to the higher strengths used in the composite pavement materials relative to the homogeneous pavement.

6.2.4 Composite Pavement Stresses under Moderate Loading Conditions

The critical stress magnitudes for the homogeneous pavement subjected to the moderate temperature gradients are shown in Table 6.11. These are approximately half of the critical stress magnitude considering an extreme temperature gradient. The critical stress/strength ratios and the number of loads to failure ranges from 0.10 to 0.29 and 1.2×10^{15} and 5.0×10^{9} respectively.

Table 6.11: Homogeneous Pavement Critical Stress Magnitude with Temperature and Vehicle Load Conditions

Critical Stress (psi)							
150	143	173	157	65	107	103	185
Temperature Gradients							
Fall	**Winter**	**Spring**	**Summer**	**Fall**	**Winter**	**Spring**	**Summer**
Moderate Negative Temperature Gradient				**Moderate Positive Temperature Gradient**			

Based on Equation 37, a homogeneous slab could experience multiple orders of magnitude more vehicle load applications with moderate temperature gradients present relative to extreme temperature gradients. For the homogeneous pavement, as well as the composite pavements, the fatigue damage was calculated at the slab edge for the top, bottom, and interface of the slab. Assuming that each of the moderate temperature gradients was applied an even number of times to a homogeneous pavement slab, the homogeneous pavement in this sensitivity analysis would exhibit bottom-up fatigue failure. The fatigue damage for the composite pavements was between 1.2 times less and 1390 times more than the fatigue damage for the homogeneous pavements. This also means that the composite pavement with the least fatigue damage had almost 1680 times less fatigue damage than the composite pavement with the most fatigue damage.

For the composite pavements, the range of the stress/strength ratio when subjected to the moderate temperature gradients ranged from 0.10 to 0.53. As was the case with the homogeneous pavement, the average composite pavement stress strength ratio for the moderate temperature gradients was approximately half of the value for the extreme temperature gradients.

Under moderate temperature gradients and vehicle loading conditions, thirty-four percent of the composite pavements analyzed had two or fewer situations in which the eight moderate temperature gradients produced a stress strength ratio more than 20 percent higher than the corresponding ratio in the homogeneous pavement. Sixty-six percent of composite pavements therefore had three or more instances in which the critical stress/strength ratio was more than 20 percent greater than the stress/strength ratio for the homogeneous pavement.

Table 6.8 presents properties for two groups of composite pavements. The first group has two or fewer situations in which the critical stress/strength ratio is less than 20 percent of critical

stress/strength ratio for the homogeneous pavement. The second group is comprised of composite pavements with three or more situations for which the critical stress/strength ratio is more than 20 percent greater than the corresponding value for the homogeneous pavement.

Table 6.12: Composite Pavements with Few and Many Situations with a High Critical/Stress Strength Ratio

Reference Temperature ^{o}F											
65				**100**							
64%		41%		36%		59%					
Top Layer Thickness											
2-in				**3-in**				**4-in**			
30%		34%		27%		33%		43%		32%	
Top/Bottom Layer Elastic Moduli x10^{6}psi											
4.5/4.8		**4.5/3.6**		**5.4/4.8**		**5.4/3.6**		**6.2/4.8**		**6.2/3.6**	
23%	13%	4%	25%	32%	7%	4%	25%	34%	6%	4%	25%
Top/Bottom Layer Coefficient of Thermal Expansionx10^{-6}											
4.7/5.1			**4.7/5.6**			**5.7/5.1**			**5.7/5.6**		
34%	19%		14%	32%		20%	28%		32%	20%	

* Black text - Composite pavements with two or fewer situations in which the critical stress/strength ratio is more than 20 percent of the stress/strength ratio for the homogenous pavement

* Red Text - Composite pavements with three or more situations in which the critical stress/strength ratio is more than 20 percent of the stress/strength ratio for homogeneous pavement

The results presented in Table 6.8 imply that composite pavements subjected to a vehicle load and moderate temperature gradients have performance tendencies driven by both the composite pavement effects discussed in Section 6.2.1 and overall structural stiffness and strength highlighted in Section 6.2.3. The influence of composite pavement effects can be seen in Table 6.8 by observing that the relatively superior composite pavements tended to have a lower reference temperature. More composite pavements with a low difference in CTE, but high average CTE (top layer CTE of 5.7 x10^{-6} /^{o}F, bottom layer CTE 5.6 x10^{-6} /^{o}F) also belonged to the category of few instances with a high critical stress/strength ratio. This is opposed to a relatively high difference in CTE but lower average CTE (top layer CTE of 4.7 x10^{-6} /^{o}F, bottom layer CTE 5.6 x10^{-6} /^{o}F).

The influence of structural stiffness on composite pavement performance relative to the homogeneous pavement is also evident. The composite pavements exhibiting relatively superior performance all have a higher average stiffness greater than the homogeneous pavement. This higher stiffness and strength of these composite pavements compensates for the higher stresses that may be prevalent in these pavements due to composite pavement effects.

When comparing the eight moderate temperature gradients compared with the eight extreme gradients, fewer composite pavements, only four, had less fatigue damage than the homogeneous pavement. The properties of these two pavements, less than three percent of the total composite pavements considered, are shown in Table 6.13.

Table 6.13: Composite Pavements with Lower Fatigue Damage than Homogeneous Pavement for Moderate Temperature Gradients and Vehicle Load

Upper Layer			Lower Layer			
Thickness (in)	**CTE (ε x10^{-6}/^{o}F)**	**E (x10^{6} psi)**	**Thickness (in)**	**CTE (ε x10^{-6}/^{o}F)**	**E (x10^{6} psi)**	**Reference Temperature (^{o}F)**
4	4.7	5.4	5	5.1	4.8	65
4	4.7	5.4	5	5.6	4.8	65
4	4.7	4.5	5	5.1	4.8	65
4	4.7	4.5	5	5.6	4.8	65

Neither of the four composite pavements shown in Table 6.13 are the same as those that had less fatigue damage for the extreme temperature gradient and vehicle load condition. The fact that these pavements have a 4-in upper layer, higher flexural stiffness, and reference temperature of 65^{o}F is not surprising as these features were discussed in Section 6.2.1 and Section 6.2.3 to be beneficial to composite pavement performance.

Given the propensity in Table 6.9 and Table 6.12 for a large difference in the layer CTE to generate the critical stress at the layer interface and to generally show higher stresses than a lower difference in CTE, the presence of two composite pavements with the largest difference in the layer CTE in Table 6.13 is surprising. As with the extreme temperature gradient case, the fatigue damage at the top of the slab, bottom of the slab, or layer interface was primarily caused by the vehicle load at one or two individual temperature gradients. For pavements in Table 6.13, as well as the homogeneous pavement, the single moderate gradient that caused the highest stress, and subsequently the most fatigue damage, occurred during the summer. This gradient caused the critical stress location to occur at the bottom of the slab at the outside edge. The principal stress at the bottom of the slab edge, for the homogeneous pavement and the four pavements shown in Table 6.13, as well as the difference in the slab deflection between the slab corner and mid-slab are shown in Table 6.14. From Table 6.14, it can be seen that there is less deflection in the composite pavements. The lower deflection results in a larger portion of the slab being supported when the vehicle load applied. This is the primary reason why these particular pavements have a lower overall fatigue damage.

Table 6.14: Comparison of Critical Stress and Deflection for Composite and Homogeneous Pavements

Upper Layer			Lower Layer				Bottom of Slab Critical Stress at Slab Edge (psi)	Deflection Between Slab Corner and Mid-slab (mils)
Thickness (in)	CTE (ε x10^{-6}/^{o}F)	E (x10^{6} psi)	Thickness (in)	CTE (ε x10^{-6}/^{o}F)	E (x10^{6} psi)	Reference Temperature (^{o}F)		
4	4.7	5.4	5	5.1	4.8	65	183	15
4	4.7	5.4	5	5.6	4.8	65	184	7
4	4.7	4.5	5	5.1	4.8	65	184	15
4	4.7	4.5	5	5.6	4.8	65	183	8
9	4.8	4.8	0	NA	NA	NA	185	19

Relative to the assessment of composite pavements subjected to relatively extreme temperature gradients and a vehicle load, a greater percentage of the composite pavements with a moderate temperature gradient and a vehicle load had the most fatigue damage at the interface. Specifically, eighteen pavement structures, or thirteen percent of the total composite pavements, had the highest fatigue damage at the layer interface. The properties of these pavements are shown in Table 6.15.

Table 6.15: Pavement Properties with High Layer Interface Fatigue Damage from Moderate Temperature Gradients and Vehicle Load

Reference Temperature ^{o}F					
65			**100**		
0%			100%		
Top Layer Thickness					
2-in		**3-in**		**4-in**	
33%		33%		33%	
Ratio of Top to Bottom Layer Elastic Moduli x10^{6}psi					
4.5/4.8 = 0.94	**4.5/3.6 = 1.25**	**5.4/4.8 = 1.13**	**5.4/3.6 = 1.5**	**6.2/4.8 = 1.29**	**6.2/3.6 = 1.75**
17%	17%	17%	17%	17%	17%
Ratio of Top to Bottom Layer Coefficient of Thermal Expansion x10^{-6}					
4.7/5.1 = 0.92		**4.7/5.6 = 0.84**	**5.7/5.1 = 1.12**		**5.7/5.6 = 1.02**
0%		100%	0%		0%

Although a larger number of pavements have the highest amount of fatigue damage at the interface when considering the selected moderate temperature gradients relative to the relatively extreme temperature gradients, the same factors influencing composite pavement performance are prevalent. Specifically, only one CTE layer combination, the one with the largest difference in the CTE between the layers, belongs to this group. Additionally, only the reference temperature that is further from the annual average pavement temperature, results in the highest amount of fatigue damage being at the interface.

6.3 SENSITIVITY ANALYSIS CONCLUSIONS AND RECOMMENDATIONS

6.3.1 Conclusions

The composite pavement sensitivity analysis performed using ISLAB determined the stress conditions in composite pavements subjected to sixteen temperature gradients and two vehicle loading scenarios. Three different assessments were made from the results of the executed finite element models. The first assessment evaluated the composite pavement variables controlling the critical stress location and evaluated key influences on differences in the location of the critical stress for composite pavements.

The second assessment focused on a comparison of homogeneous and composite pavements as well as a comparison of composite pavements amongst each other. Specifically, the second assessment focused on the composite pavements when subjected to relatively extreme temperature gradients. While these events are relatively rare occurrences, damage caused by vehicle loads applied during these conditions is extreme. The third assessment that was made evaluated composite pavements subjected to vehicle loads and moderate temperature gradients. These gradients are common in pavements and many load applications are made with moderate temperature gradients present. While the damage caused by vehicle loads applied when moderate temperature gradients are in the slab is significantly less than when an extreme temperature gradient is in the slab, significantly more vehicle loads are applied when moderate gradients are present.

In the first assessment, the influence of so called “composite pavement effects” were evaluated under temperature loading condition alone. Composite pavement effects consist of differences in the nature of composite pavements relative to homogeneous pavements. These

differences include the significance of the reference temperature, different layer thicknesses, different coefficients of thermal expansion between the composite pavement layers, and different layer elastic moduli. Because so many of these composite pavement effects are influenced primarily by environmental loading conditions, the first assessment was used as a baseline assessment of the fundamental differences in composite and homogeneous pavement behavior.

Under temperature loading conditions alone, the magnitude of the stresses generated in a pavement slab are not sufficiently high to cause significant slab damage that could lead to slab failure. Therefore the focus of the first assessment was to look at the critical stress location for composite pavements relative to homogeneous pavements. Observations that were made that could influence composite pavement performance included the observation that for some composite pavements and temperature gradients the critical stress occurs between the composite pavement layers.

The critical stress was found to occur between the pavement layers at both the corner of the slab and at mid-slab. The other observation was that for some pavements, the sign of the temperature gradient did not always produce slab curvature in the traditional direction. A negative temperature gradient in the slab, which in a homogeneous pavement would cause upward slab curvature, was found for some composite pavements to produce downward curvature. The composite pavement effects driving these observations were found to primarily be the selected reference temperature and the difference in the CTE for the two layers.

A higher reference temperature, which is equivalent to the slab's zero stress temperature established during construction, was shown to result in a high number of instances with the critical stress occurring between the composite pavement layers. This happens because for the

majority of the year, the average slab temperature is below the reference temperature, especially if the reference temperature is relatively high as might occur during summer construction.

When the average slab temperature is significantly below the reference temperature, there is a buildup of stress between the pavement layers. This stress is present because each layer has a different CTE and cannot expand or contract as it would if the pavement layers were not bonded together. While there is no stress between the layers when the average slab temperature is equivalent to the reference temperature, an increase in the difference between the average slab temperature and reference temperature results in higher stress at the layer interface. The difference in the layers CTE was also shown to result in many instances of the critical stress occurring between the slab layers. The stress at the layer interface is proportional to both the difference of the average pavement temperature from the reference temperature and the difference in the CTE between the two layers. A larger difference in the layer CTE results in a larger stress increase per degree change in temperature.

The second assessment focused on the composite and homogeneous pavement subjected to relatively extreme temperature gradients and a vehicle load. Based on the results of the first assessment, highlighting the location of the critical stress at the layer interface, fatigue damage was calculated at three locations within the slab. These locations were the top and bottom of the slab at the outside edge of the slab as well as the interface between the layers at this same location. A small percentage of composite pavements were found to have relatively good performance compared to the homogeneous pavement. This was shown by assessing the fatigue damage. Composite pavements were assessed against each other in a similar manner. Since so few composite pavements had beneficial performance relative to the homogeneous pavement, an alternative basis of comparison was desired. The basis that was eventually selected was

composite pavements that had and composite pavements that did not have a low number (1 or 2) of instances for which the critical stress/strength ratio for the composite pavement was less than 120 percent of the critical stress/strength ratio for the homogeneous pavement.

When subjected to extreme temperature gradients and a vehicle load, membership for a given composite pavement structure in either the group that performed well or poorly relative to the homogeneous pavement was found to be predominantly dictated by average CTE or flexural stiffness rather than composite pavement effects such as the influence of the reference temperature, difference in CTE between the layers, or difference in elastic moduli between the layers. In this scenario, the influence of composite pavement effects was decidedly minor.

As part of the second assessment, fatigue damage was calculated at the top of the slab, layer interface, and bottom of the slab. It was found that for the eight extreme temperature gradients with a relatively significant vehicle load applied, a single composite pavement had the most fatigue damage at the layer interface. This suggests that for this pavement, distress could initiate at the layer interface at the slab edge rather than at the top or bottom of the slab. The characteristic of this particular composite pavement is that it had a 2-in top layer thickness, the largest difference in the layer CTE of the composite pavements considered, and a reference temperature of 100^{o}F. Together, these observations from the assessments highlight that this location merits further investigation in a more extensive systematic fatigue analysis for composite pavements. The third assessment focused on the composite pavement subjected to moderate temperature gradients and a vehicle load. Fatigue damage was also calculated for the eight moderate temperature gradients with vehicle loading conditions. Comparing the composite and homogeneous pavements, only two composite pavements had less fatigue damage than the homogeneous pavement. While these pavements had a 4-in top layer thickness, a reference

temperature closer to the average annual air temperature, and high structural stiffness, they also possessed a large difference in the CTE between layers. This observation was anomalous to conclusions drawn throughout the rest of the analysis section.

It was stated however that the majority of the total fatigue damage for these two pavements was coming from one loading scenario. In this loading scenario, the composite pavement slabs with lower fatigue damage than the homogeneous pavement had a relatively low slab curvature. Because of this low slab curvature, the additional stress produced by the vehicle loads was relatively small and is one of the main reasons that these pavements performed superiorly.

In addition to fewer composite pavements performing well relative to the homogeneous pavement under moderate temperature gradients, a higher percentage of the composite pavements, eight percent, had the highest amount of fatigue damage at the layer interface. These pavements included the composite pavement found to have the most fatigue damage at the layer interface when subjected to extreme temperature gradient as well as other similar pavements. The defining characteristics of this group were that they all had the 100 ^{o}F reference temperature and the largest difference in the CTE of layers making up the composite pavements considered. Layer thickness or relative stiffness between the layers did not influence the highest fatigue damage occurring at the interface.

For the moderate temperature gradients, composite pavements were assessed against each other in a similar manner to how they were assessed against each other for the extreme temperature gradients. This was done on the basis of pavements with few compared to many instances in which the stress/strength ratio for the composite pavement was less than 120 percent of the stress/strength ratio for the homogeneous pavement under the same loading condition.

The composite pavement properties that resulted in a given composite pavement belonging to either the group with less or more damage were found to be a combination of the properties that resulted in less or more damage in the first or second assessment. Both composite pavement effects, such as the influence of the reference temperature and the difference in the CTE between the pavement layers, as well as average slab thickness and average slab CTE were found to be influential.

The three assessments made in this chapter provided a spectrum of conditions in which the range of composite pavements considered in this analysis were evaluated. All differences in composite pavement performance relative to homogeneous pavements can be linked to the composite pavement effects of a difference in layer thickness, difference in CTE between the layers, and the significance of the reference temperature. These composite pavement effects are most influential in terms of the fatigue damage created by a given loading scenario when no vehicle load is applied to the slab. These effects are least influential when a vehicle load and extreme temperature gradient are considered. When a vehicle load and only moderate temperature gradients are applied to the slab, the influence of composite pavement effects is between the influence under temperature conditions alone and when a vehicle load is applied with an extreme temperature gradient.

Ultimately, pavement performance is primarily dictated by the loading situations that cause the most fatigue damage. While an analysis of composite pavements under different distributions of loading conditions is beyond the scope of this thesis, it can be stated that for the limited conditions considered in this chapter, the most fatigue damage was caused by the vehicle loads applied under extreme temperature gradient conditions. The fatigue damage caused in these situations was orders of magnitude more than for moderate temperature gradients and a

vehicle load. It is for the extreme temperature gradients and vehicle loading conditions that composite pavements are the most like homogeneous pavements in terms of both the stress magnitude and location of the critical stress and it is most likely this reason that observed performance of composite pavements in the field has been similar to homogeneous pavements.

6.3.2 Recommendations

The analysis performed in this section found that composite pavement performance was only as good as the homogeneous pavement performance in limited situations. These instances were primarily when the composite pavement had a higher strength to offset the higher stresses induced in the pavement by composite pavement effects. Increasing the strength of composite pavement materials relative to homogeneous pavements is therefore a viable option for achieving similar performance between the two types of pavements.

Experience with design was also found to be another barrier to implementation of composite pavements. Based on this work, the overarching theme of a composite pavement design procedure should be the selection of materials aimed at limiting the influence of composite pavement effects. Composite pavement effects can most effectively be mitigated by addressing the fact that thermal incompatibility between composite pavement layers generally results in increased self-equilibrating stresses, increased average curvature, and increased stress due to vehicle loads in pavement slabs. Stresses due to thermal incompatibility can also be exacerbated by the added significance of the reference temperature boundary condition. The greater the difference in the layer CTE, the more significant this boundary condition is.

Based on these two observations, controlling the coefficient of thermal expansion becomes a priority for the successful design of composite concrete pavements. CTE testing

should be required for proposed paving materials and based on results in this analysis, relatively large CTE differences should be scrutinized and thoroughly evaluated due to their propensity for higher total stress as well as for high interface stresses.

While decreasing the difference in CTE between the pavement layers is important, this must not be done at the expense of significantly increasing the average CTE. A significant increase in the average CTE would increase the damage caused by vehicle loads. These objectives could potentially be achieved through careful selection of available aggregate types and aggregate proportioning. The recycling process of old concrete pavements is also one potential source for controlling concrete thermal properties. Understanding and controlling the effects of different crushing and processing procedures on recycled concrete residual mortar content can have a significant impact on the eventual thermal properties of a concrete using recycled aggregate.

For situations in which the design of two concrete mixtures with similar CTEs is not feasible, control of the reference temperature could also reduce the stresses generated in the composite pavement throughout its life. Although the ability to implement such a practice may be schedule or cost prohibitive, especially for projects with an accelerated schedule and high cost associated with project delays, a reference temperature as close as possible to the mean annual average pavement temperature would be the most beneficial reference temperature to achieve. Such an objective could be achieved through specifying the appropriate temperature conditions for paving and acceptable curing methods.

Depending on whether or not two paving mixtures with the same or similar CTEs can be economically achieved, the designer should also consider the relative pavement layer thickness. The larger the discrepancy between the pavement layers' CTEs, the thicker the upper pavement

layer should be. This serves to concentrate the stresses generated at the interface due to thermal incompatibility near the neutral bending axis of the slab and away from the locations at which the critical stress is generated by the slab self-weight during curling and applied vehicle loads. If thermally compatible concrete mixes can be achieved for the upper and lower layers, then the thickness of the upper layer can be driven by economy to the limit of constructability. In European practice, this corresponds to a minimum 2-inch upper layer thickness.

Pavement layer elastic moduli are critical in as much as they are generally proportional to concrete strength. A higher elastic modulus generally corresponds to a higher strength and lower fatigue damage for a given loading condition. The difference in the elastic modulus between the composite pavement layers was found to have a relatively minor influence on composite pavement performance. It is influential in the sense that if one of the layers has a disproportionately lower stiffness, and correspondingly lower strength, then a distress may initiate in this layer prematurely relative to the fatigue life of the other pavement layer.

7.0 CONCLUSIONS AND RECOMMENDATIONS

This research has presented an assessment of temperature, moisture, and strain data from three types of composite pavement structures installed at the MnROAD research facility. Through the analysis of this data, insight into some unique aspects of composite pavement performance was garnered. An assessment of the factors influencing critical tensile stress magnitude and location was performed on composite concrete pavements with diverse material and structural characteristics. The assessment considered stresses due to environmental effects only, as well as the combined influence of environmental effects and vehicle loads. The stress analysis highlights the different ways in which composite and homogenous concrete pavements respond to environmental and vehicle loads and extrapolates these findings to provide an introductory assessment at how these differences might affect pavement life and performance. The following sections summarize the main conclusions obtained from this work as well as recommendations for further work.

7.1 CONCLUSIONS

- Relatively extreme temperature gradients in the underlying PCC component of the HMA/PCC composite pavement were found to occur less frequently than for the PCC/PCC composite pavement. An extension of this assessment to the equivalent linear temperature gradient revealed an even greater disparity in the relative frequency with which extreme

temperature gradients occurred in the HMA/PCC composite pavement relative to the PCC/PCC composite pavement.

- The equivalent linear temperature gradient was shown to differ significantly between two composite pavements in which the same temperature profiles developed.
- It was observed that for the HMA/PCC composite pavement, the HMA initially appeared to exacerbate drying shrinkage. This effect eventually diminished however and the moisture content at the top of the underlying concrete increased.
- The construction of the HMA on the HMA/PCC composite pavement did not seem to influence the curvature of the concrete slab for a given temperature gradient. The indirect effect of the HMA overlay was to reduce the temperature gradients that develop in the underlying concrete slab.
- Positive temperature gradients were observed to occur more frequently in the PCC/PCC cells relative to the HMA/PCC cell.
- The variation in curvature between the two PCC/PCC cells was postulated to be due to both the variation in the relative CTEs of the top and bottom layers within each cell and the differences in the way a change in the pavement weighted average temperature affects each cell.
- In the stress analysis portion of this work, composite pavement effects, including the difference in CTE between the layers, the reference temperature, different layer thicknesses, and different layer elastic moduli were found to be significant with respect to pavement behavior.
- When subjected to certain temperature gradients, in the absence of a vehicle load, the critical stress location for some composite pavements was at the interface between the bonded

pavement layers. The critical stress was found to occur between the pavement layers at both the corner of the slab and at mid-slab.

- A positive temperature gradient did not always produce downward curvature and a negative temperature gradient did not always produce upward curvature in many of the composite pavement structures analyzed. The composite pavement effect driving this type of observation was found to be the selected reference temperature and the difference in the CTE for the two layers.
- The built-in temperature differences between the top and bottom of the slab for the first year after paving ranged from -12.9^{o}F to -24.9^{o}F for Cell 70, -26.7^{o}F to -42.6^{o}F for Cell 71 (excluding questionable data months), and -26.7^{o}F to -38.8^{o}F for Cell 72.
- A higher reference temperature, which is equivalent to the slab's zero stress temperature established during construction, was shown to result in a high number of instances with the critical stress occurring between the composite pavement layers. An increase in the difference between the average slab temperature and reference temperature results in higher stress at the layer interface.
- A higher difference in the CTEs between layers also resulted in many instances for which the critical stress occurred between the slab layers.
- Considering a vehicle load in addition to a temperature gradient, it was found that only a small percentage of composite pavements had lower fatigue damage for the loading conditions considered as compared to the homogeneous pavement.
- Two groups of composite pavements were established as a basis for comparison of composite pavements amongst each other. These groups were defined by their performance, in terms of fatigue damage, when subjected to either eight extreme temperature gradients and vehicle

loading conditions or eight moderate temperature gradient and vehicle loading conditions. The composite pavements subjected to these conditions had either relatively good or relatively poor performance with respect to the baseline homogenous pavement. When subjected to extreme temperature gradients and a vehicle load, membership for a given composite pavement structure in either group was found to be predominantly dictated by average CTE or flexural stiffness rather than composite pavement effects such as the reference temperature, difference in layer CTE, and difference in layer elastic moduli. The influence of composite pavement effects was decidedly minor. Composite pavement effects were only slightly more significant for the moderate temperature gradients and vehicle load scenario.

- Considering the composite pavements subjected to eight relatively extreme temperature gradients and a significant vehicle load, it was found that a single composite pavement had the most fatigue damage at the layer interface. This composite pavement had a 2-in top layer thickness, a relatively large difference in the layer CTE, and a high reference temperature. A slightly higher percentage, eight percent, had the highest amount of fatigue damage at the interface when considering the moderate temperature gradients and vehicle load. These pavements all had a high reference temperature and large difference between the CTEs of the layers. Together, these observations from the assessments highlight that this location merits further investigation in a more extensive systematic fatigue analysis for composite pavements.

7.2 RECOMMENDATIONS

Through a careful analysis of the data collected from the MnROAD cells over the analysis period from May 2010 through March 2011 a greater understanding of the behavior these composite pavements was obtained. Likewise, the assessment of stresses in a wide range of composite concrete pavements using ISLAB has provided insight into potential features controlling the performance of composite pavement structures. This work was not without its limitations however. Implementation of the following recommendations will help in overcoming these limitations and serve to build upon the understanding of composite pavements presented in this thesis.

- There is a need to develop relative humidity sensors that are robust, precise and accurate at high relative humidity levels.
- Only a limited amount of data was available for this analysis. Now that the MnROAD cells have been in-service and data has been continuously collected for a period of 3.5 years, an additional analysis with the most extensive data set should be performed to evaluate the effects of long-term drying shrinkage and creep.
- The prevalence of the critical stress between the composite pavement layers suggests that, despite de-lamination of composite concrete pavements not being cited as an observed failure in European practice, the effect of shear stresses on debonding and fatigue at the layer interface should be assessed.

APPENDIX A

EARLY AGE STRAIN-TEMPERATURE FIGURES USED IN DETERMINING THE ZERO STRESS TEMPERATURE FOR CELL 71

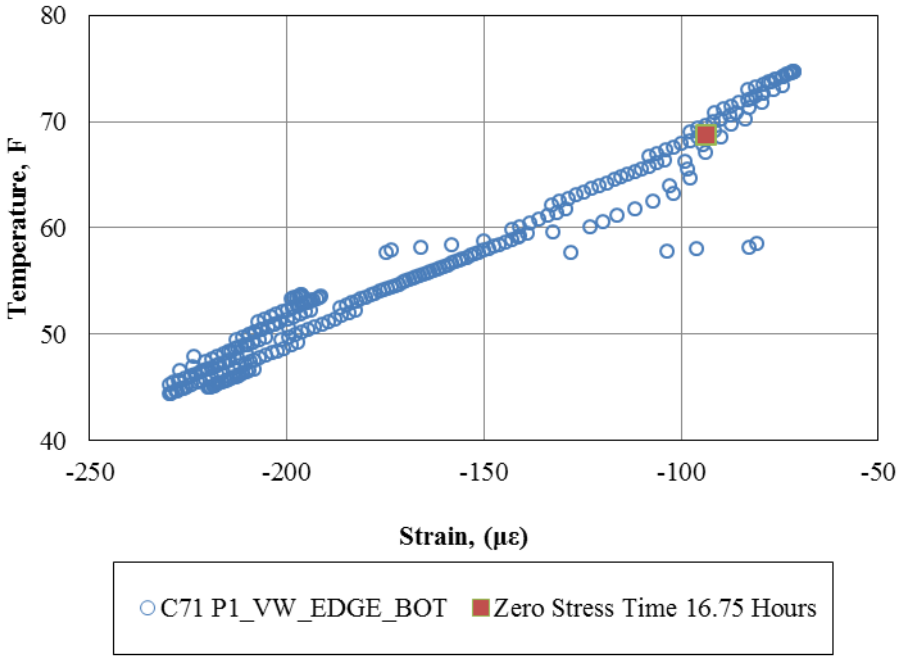

Figure A.1: Panel 1 Bottom Edge Location

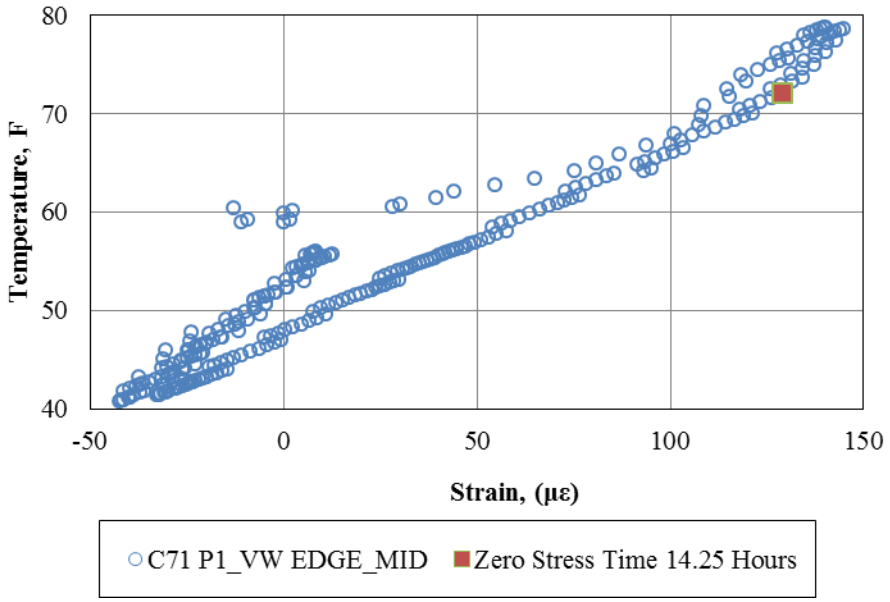

Figure A.2: Panel 1 Edge Mid-Depth Location

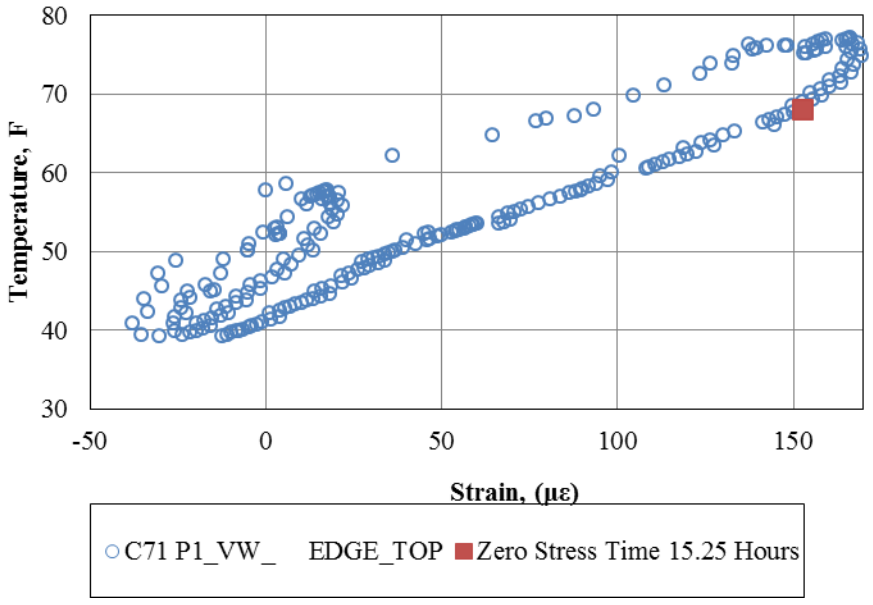

Figure A.3: Panel 1 Edge Top Location

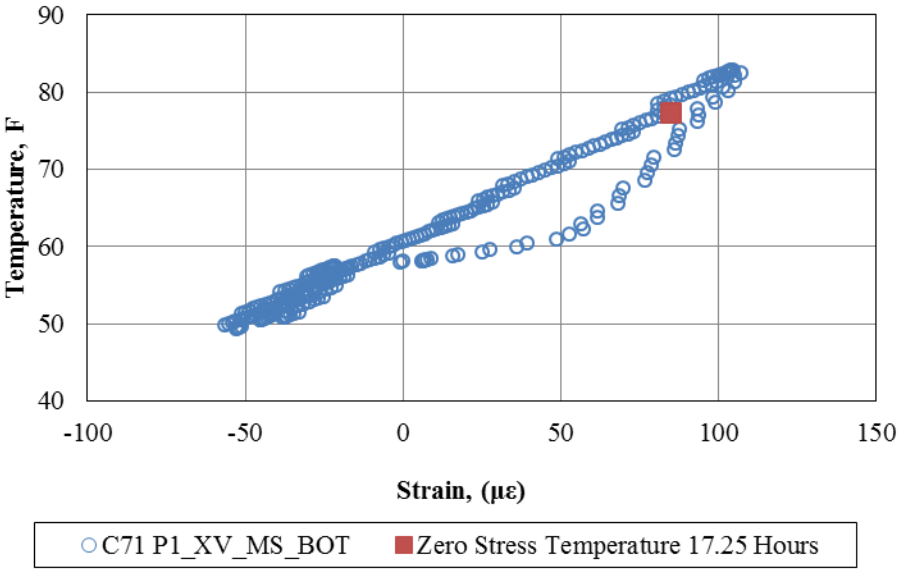

Figure A.4: Panel 1 Mid-Slab Bottom Location

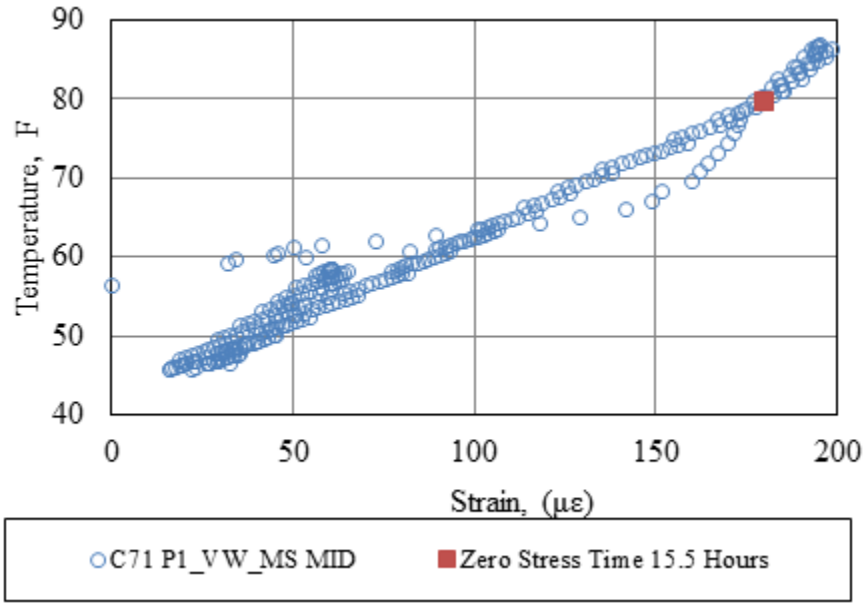

Figure A.5: Panel 1 Mid-Slab Mid-Depth Location

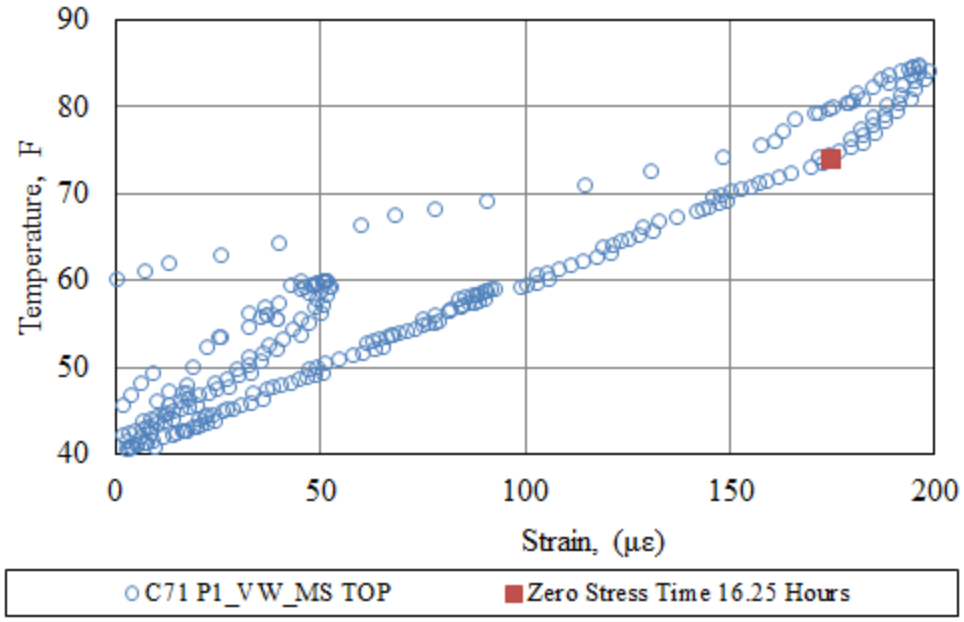

Figure A.6: Panel 1 Mid-Slab Top Location

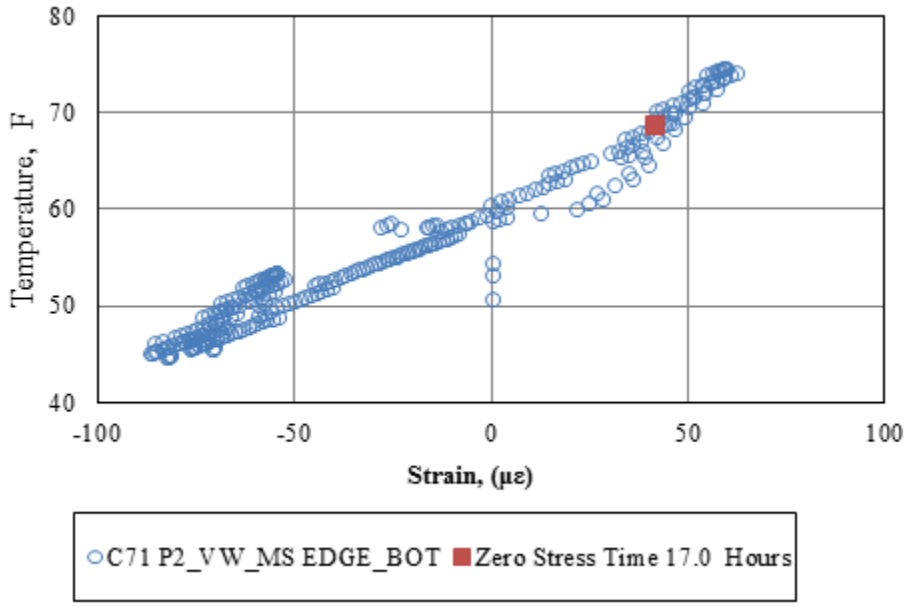

Figure A.7: Panel 2 Edge Bottom Location

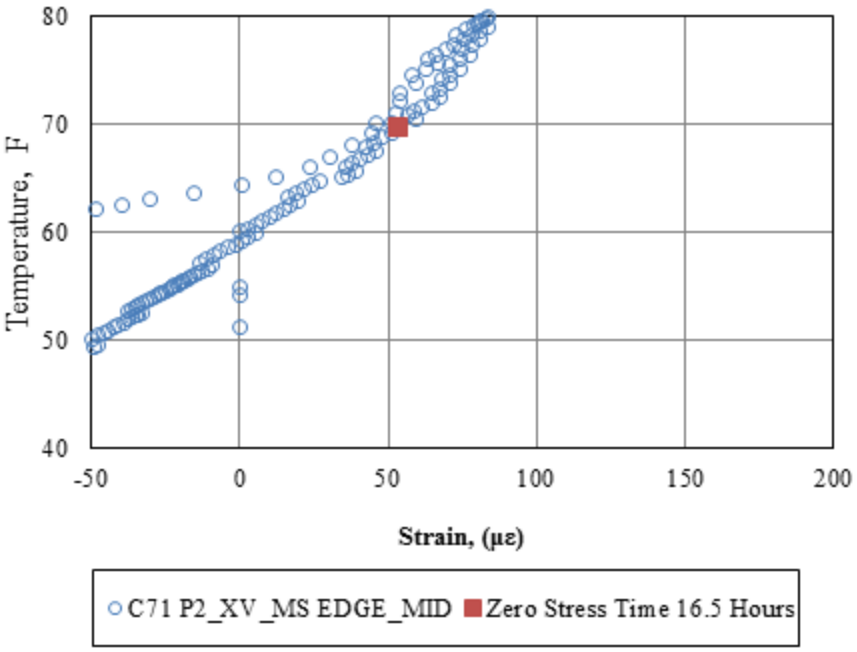

Figure A.8: Panel 2 Edge Mid-Depth Location

APPENDIX B

TRADITIONAL BUILT-IN TEMPERATURE GRADIENT PLOTS

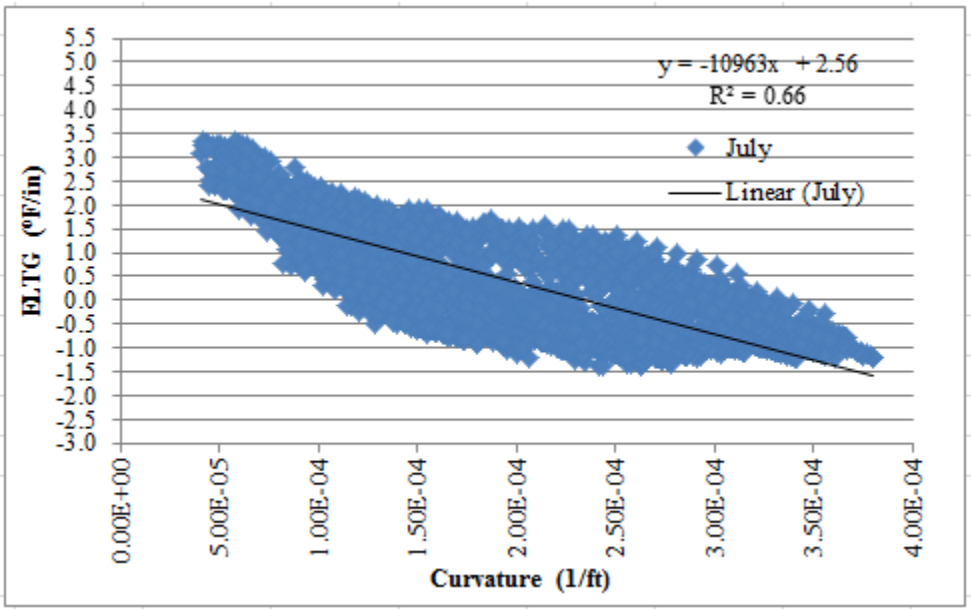

Figure B.1: Built-in Gradient – July – Cell 70

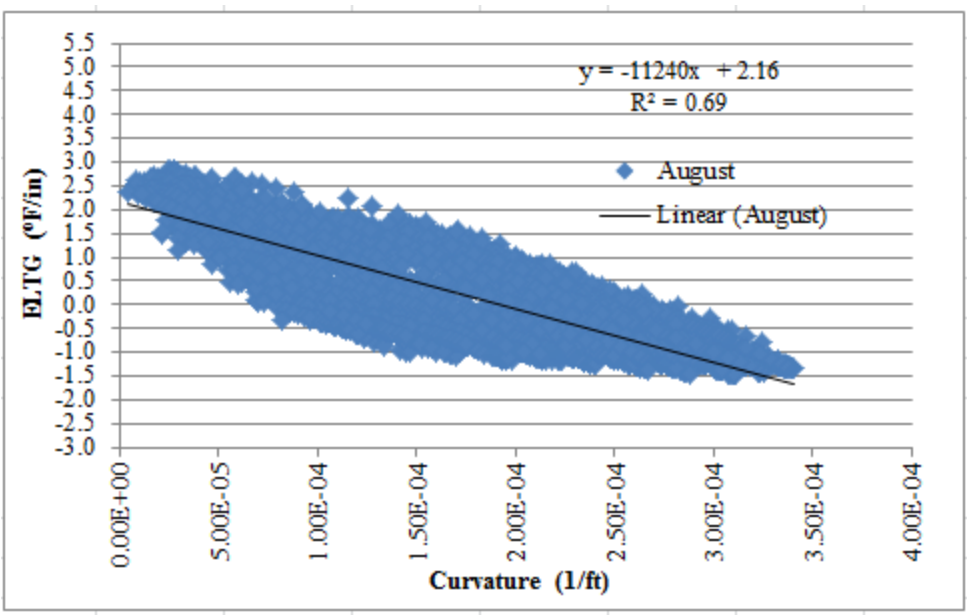

Figure B.2: Built-in Gradient –August – Cell 70

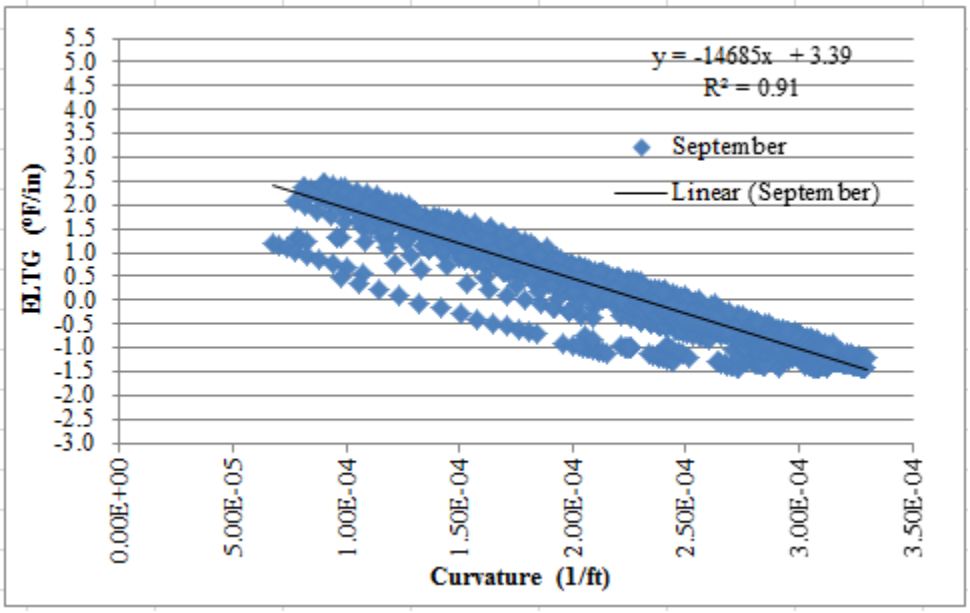

Figure B.3: Built-in Gradient – September – Cell 70

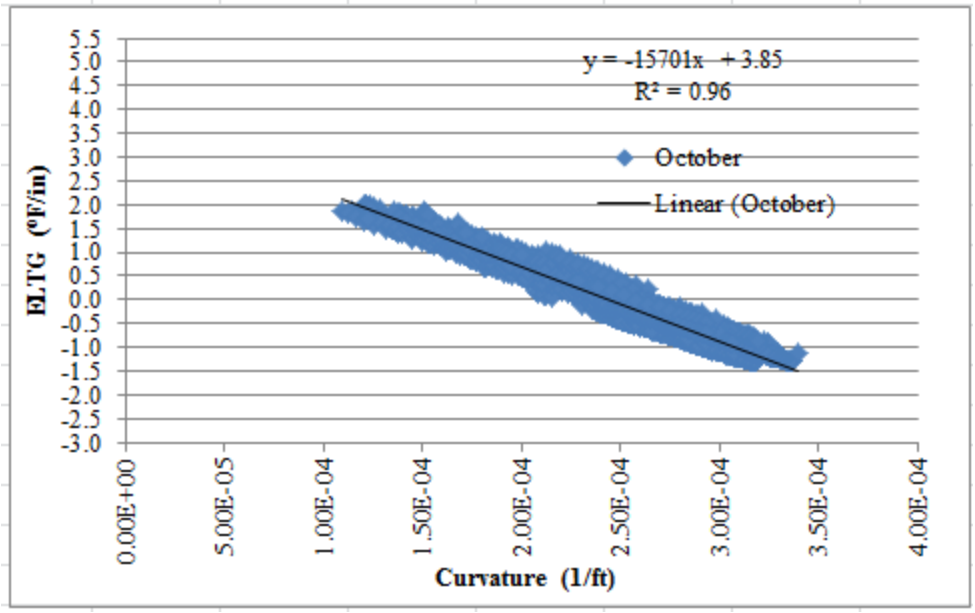

Figure B.4: Built-in Gradient – October – Cell 70

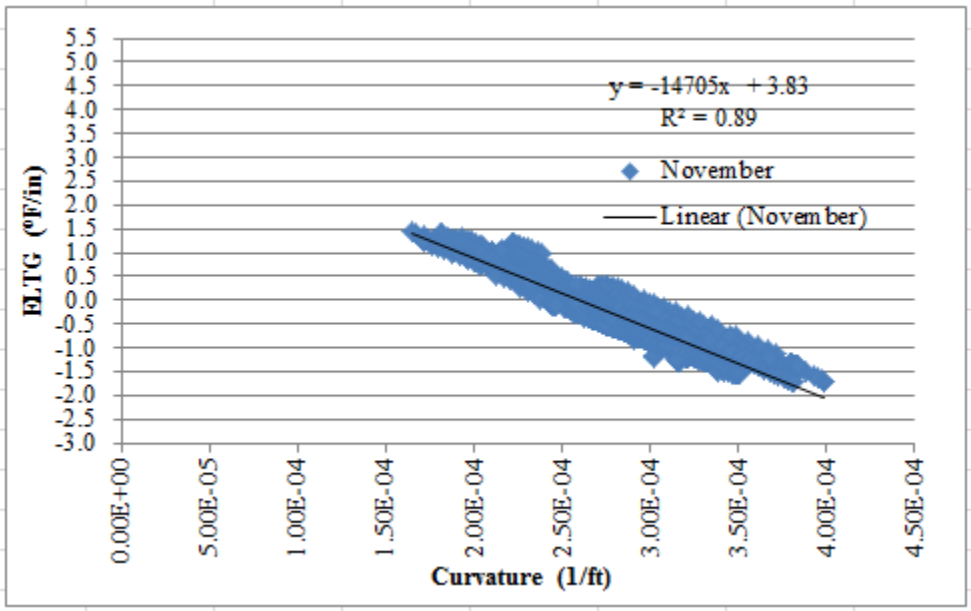

Figure B.5: Built-in Gradient – November – Cell 70

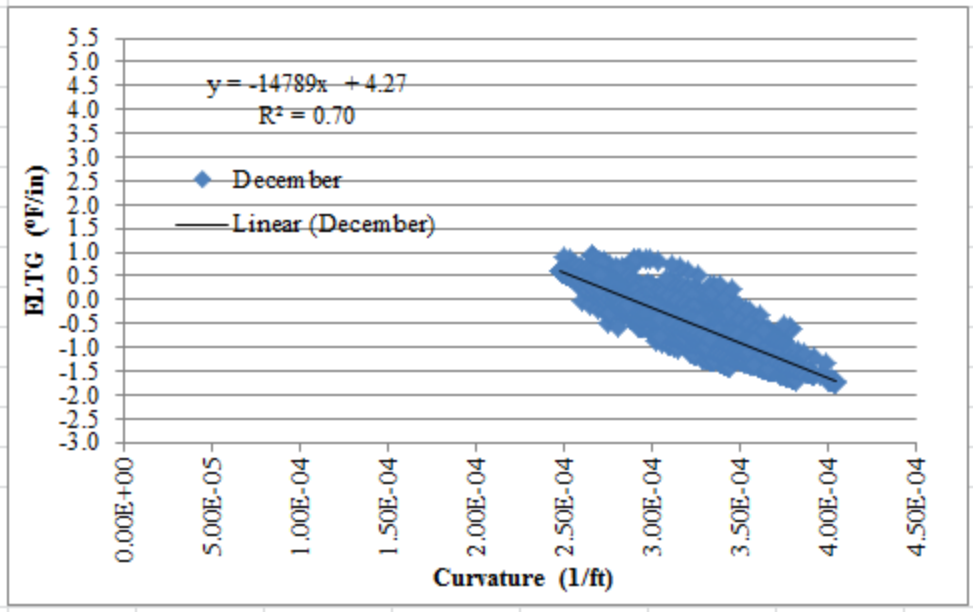

Figure B.6: Built-in Gradient –December– Cell 70

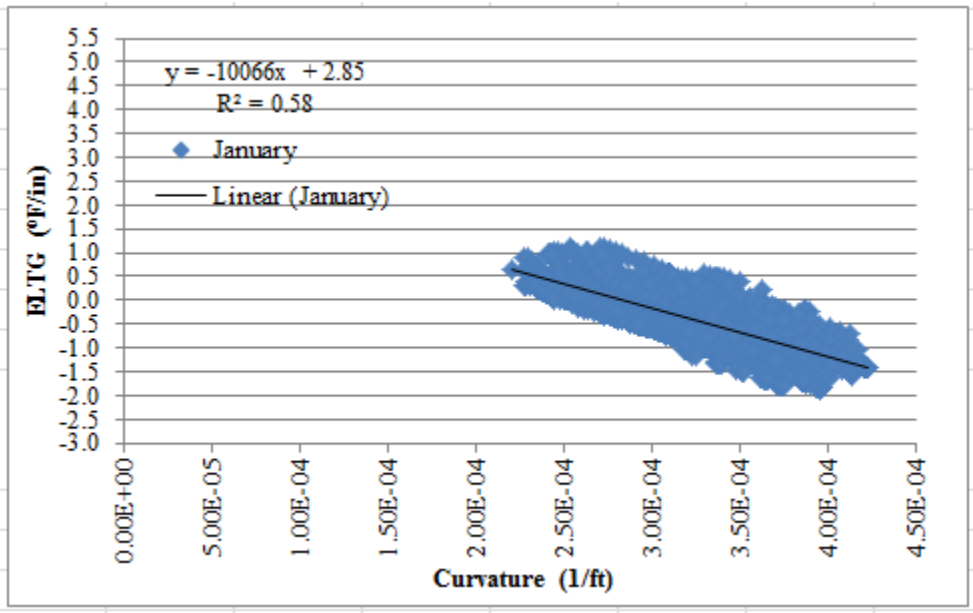

Figure B.7: Built-in Gradient – January – Cell 70

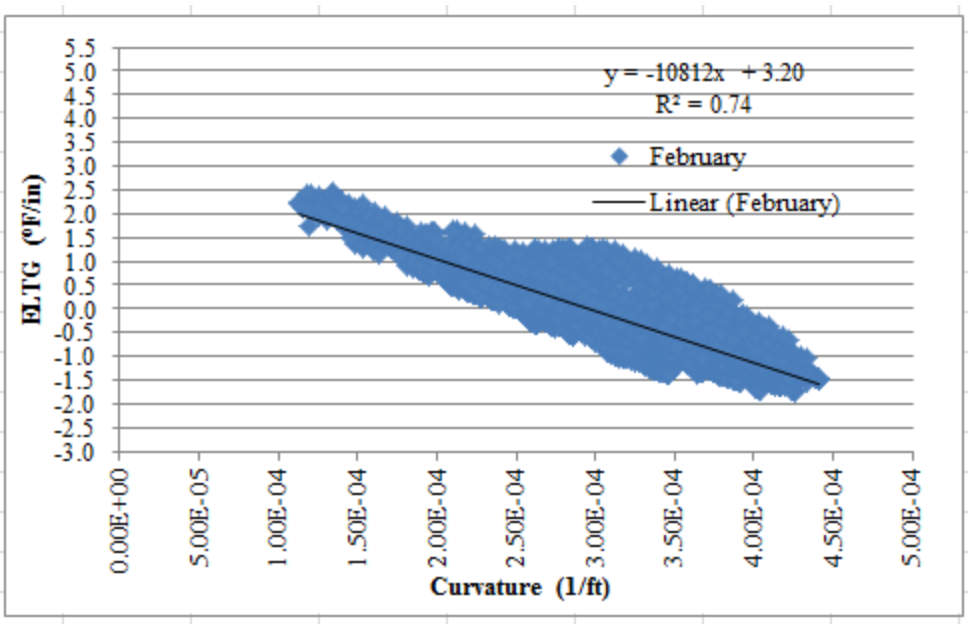

Figure B.8: Built-in Gradient – February – Cell 70

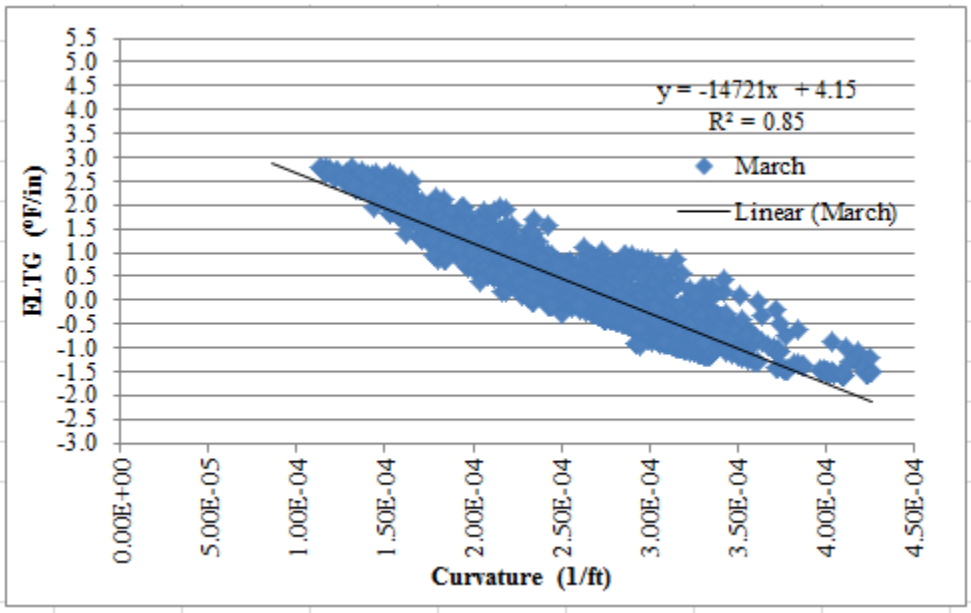

Figure B.9: Built-in Gradient – March – Cell 70

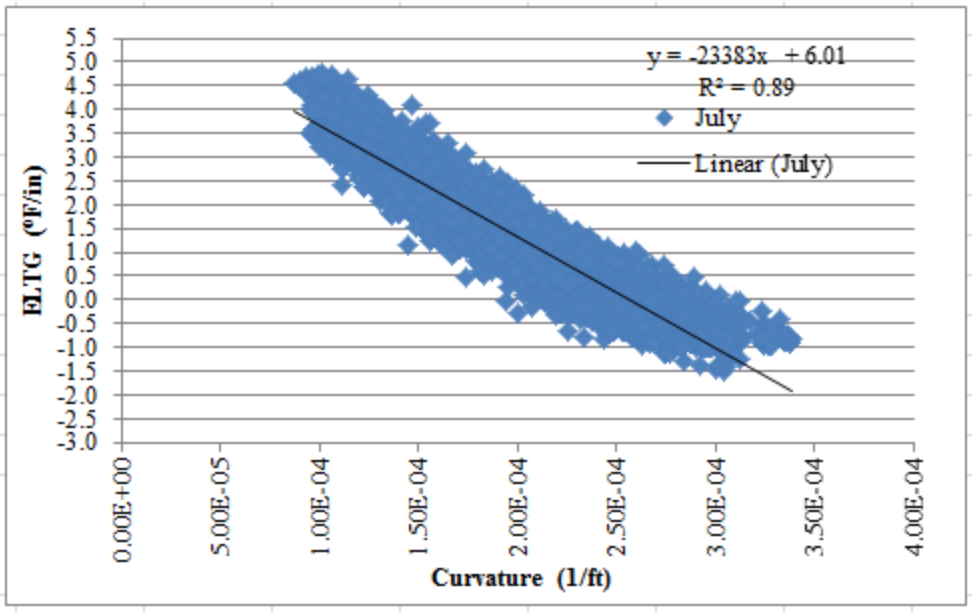

Figure B.10: Built-in Gradient – July – Cell 71

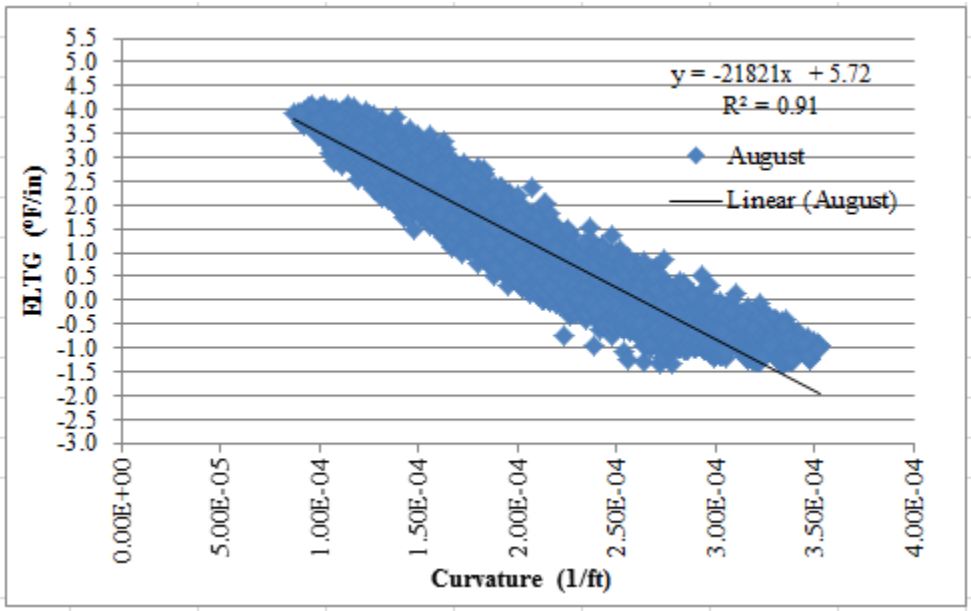

Figure B.11: Built-in Gradient – August – Cell 71

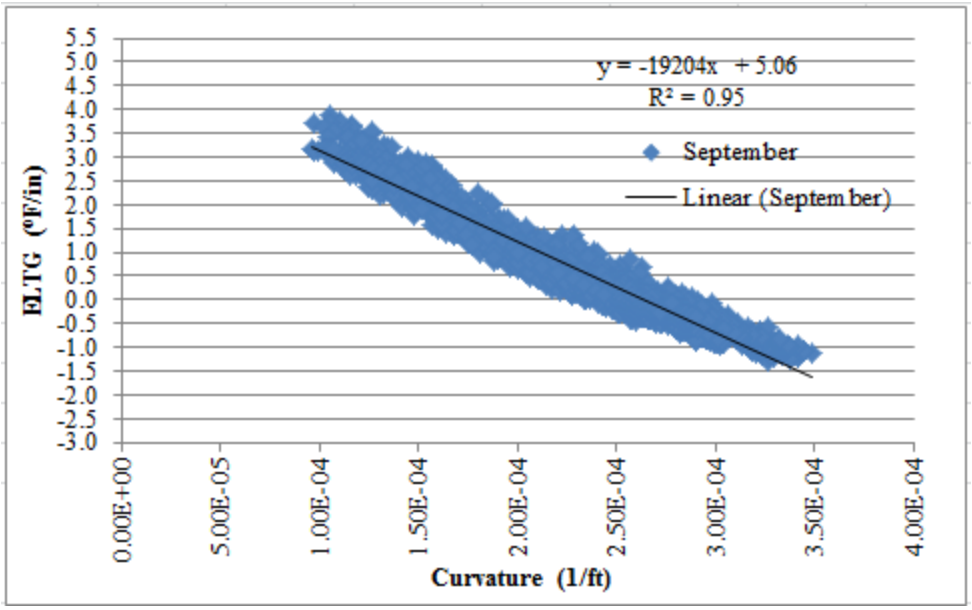

Figure B.12: Built-in Gradient – September – Cell 71

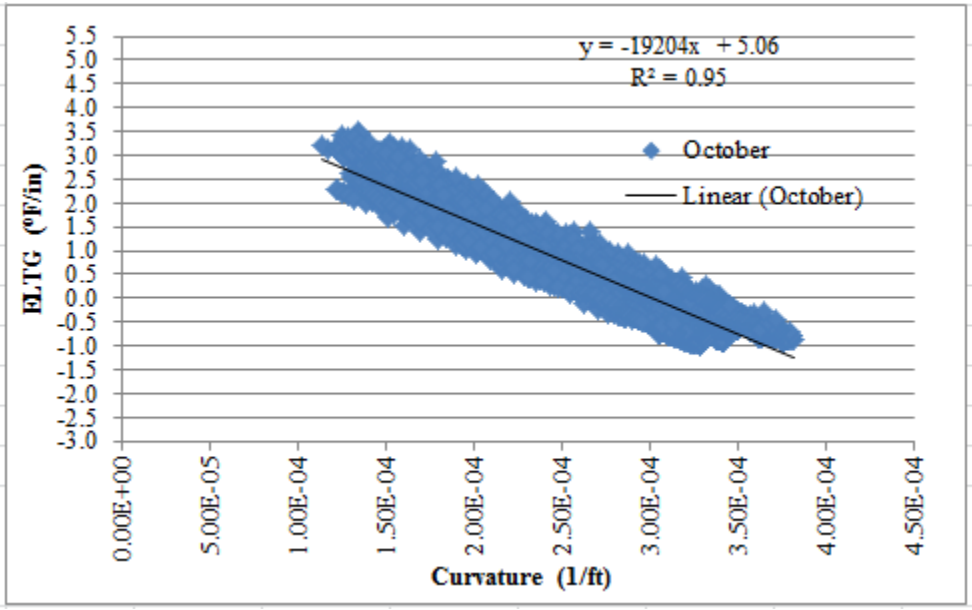

Figure B.13: Built-in Gradient – October – Cell 71

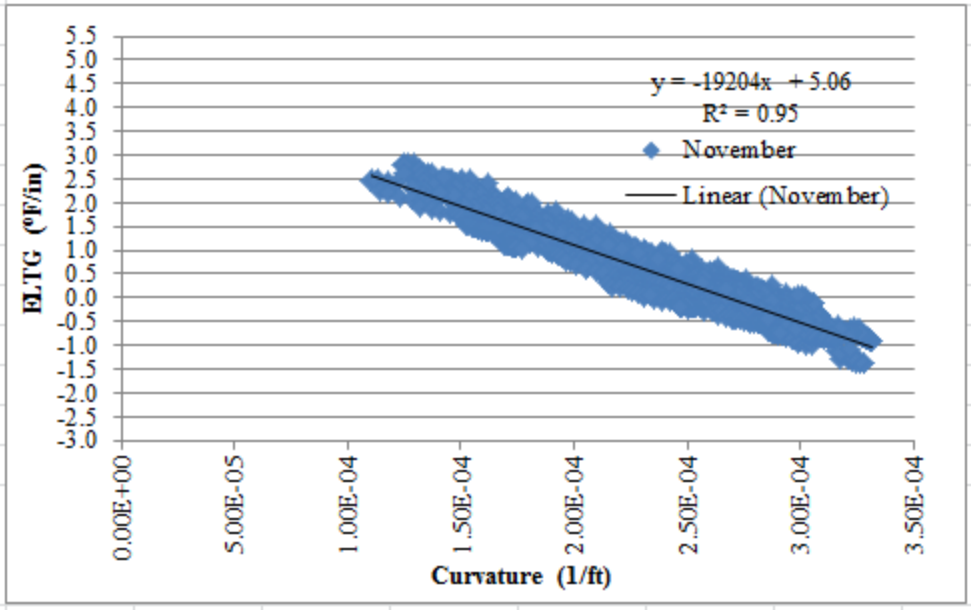

Figure B.14: Built-in Gradient – November – Cell 71

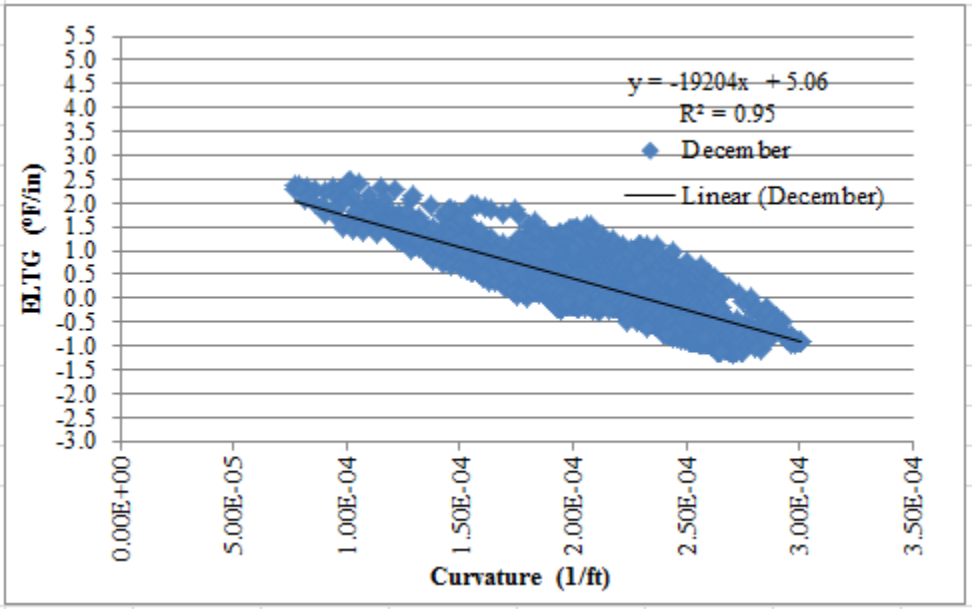

Figure B.15: Built-in Gradient – December – Cell 71

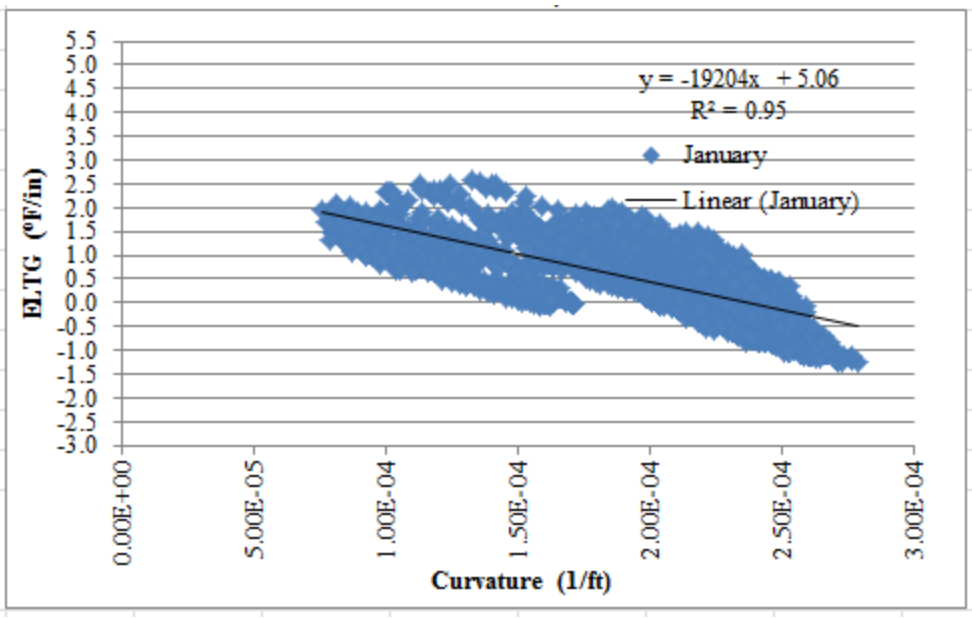

Figure B.16: Built-in Gradient – January – Cell 71

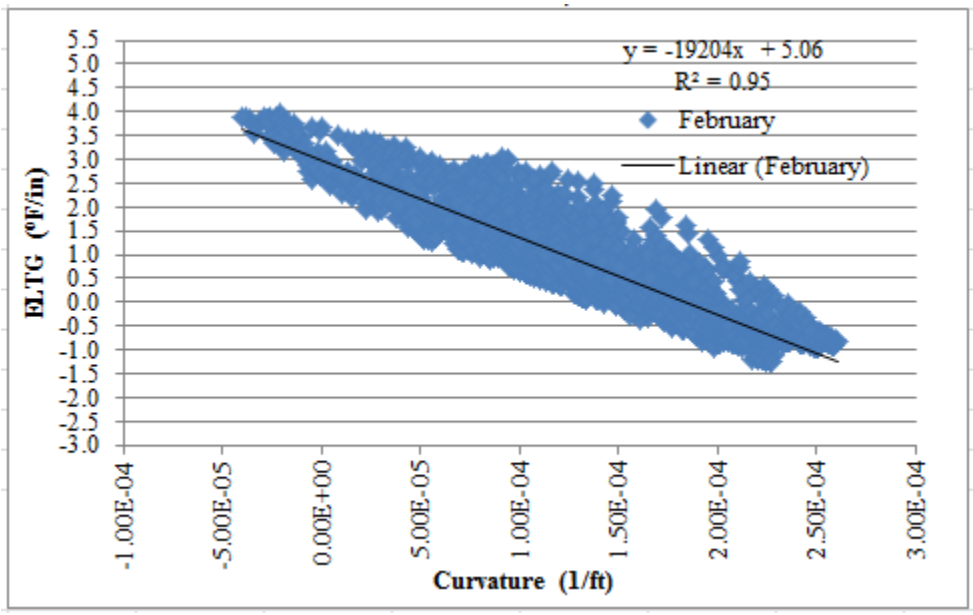

Figure B.17: Built-in Gradient – February – Cell 71

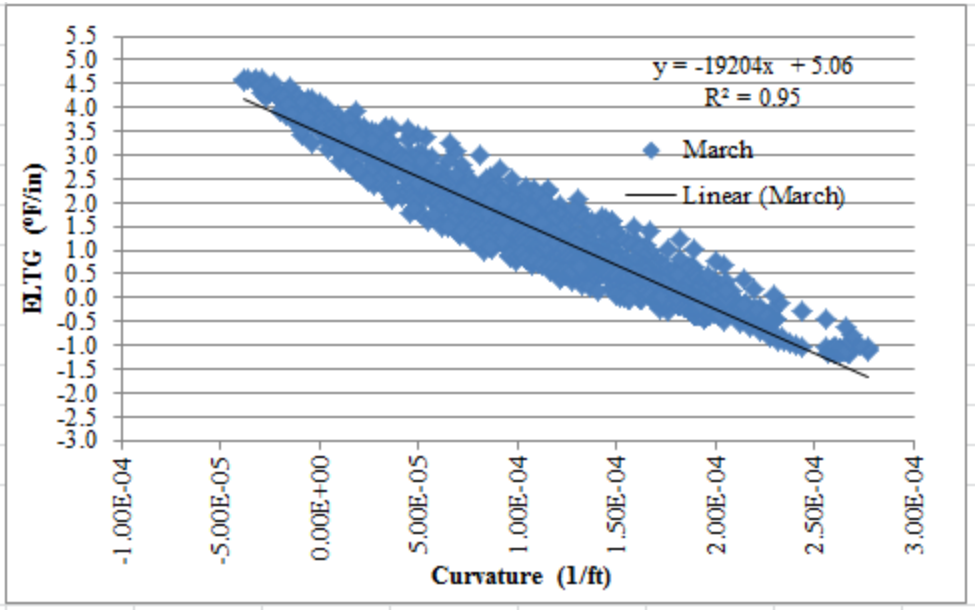

Figure B.18: Built-in Gradient – March – Cell 71

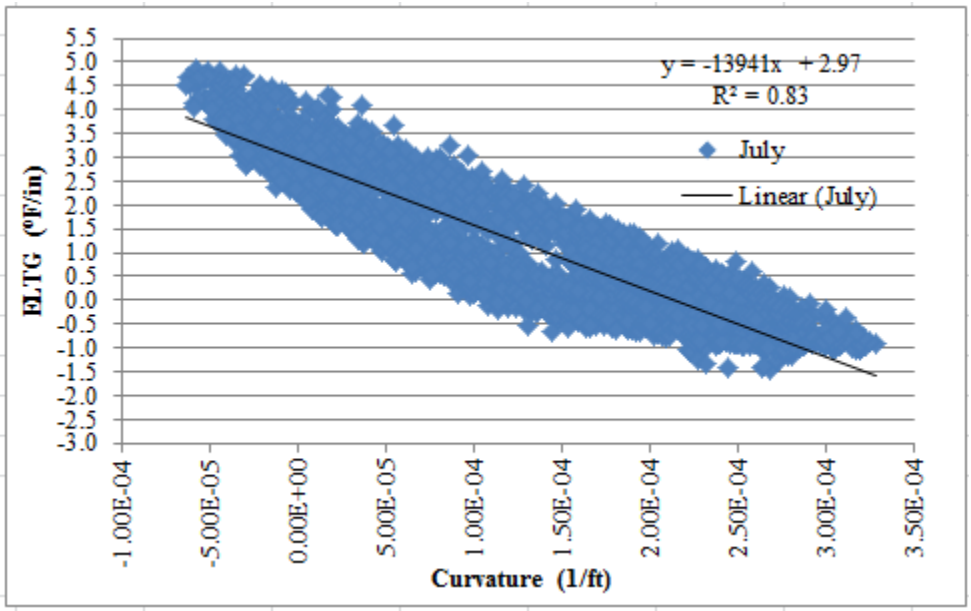

Figure B.19: Built-in Gradient – July – Cell 72

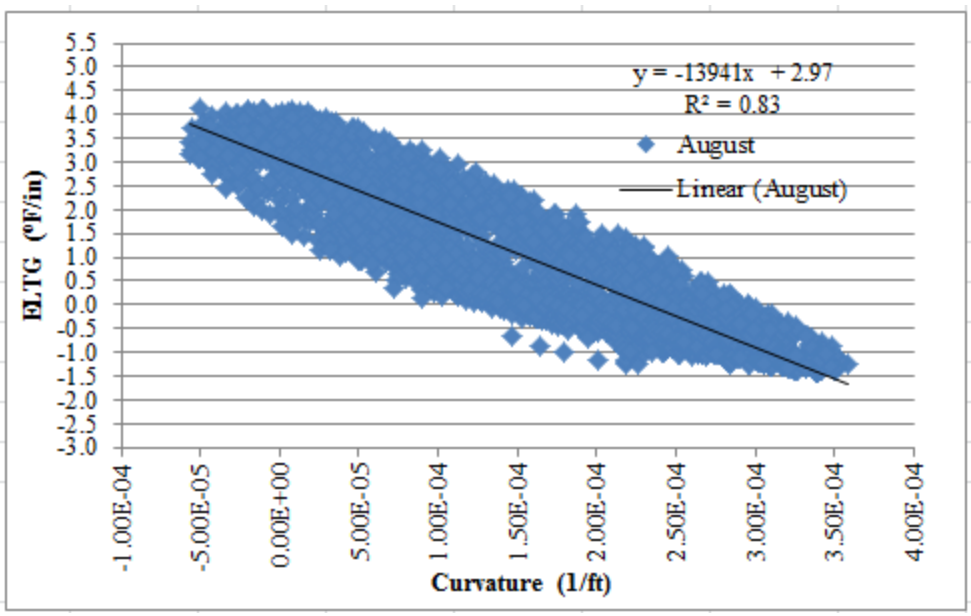

Figure B.20: Built-in Gradient – August – Cell 72

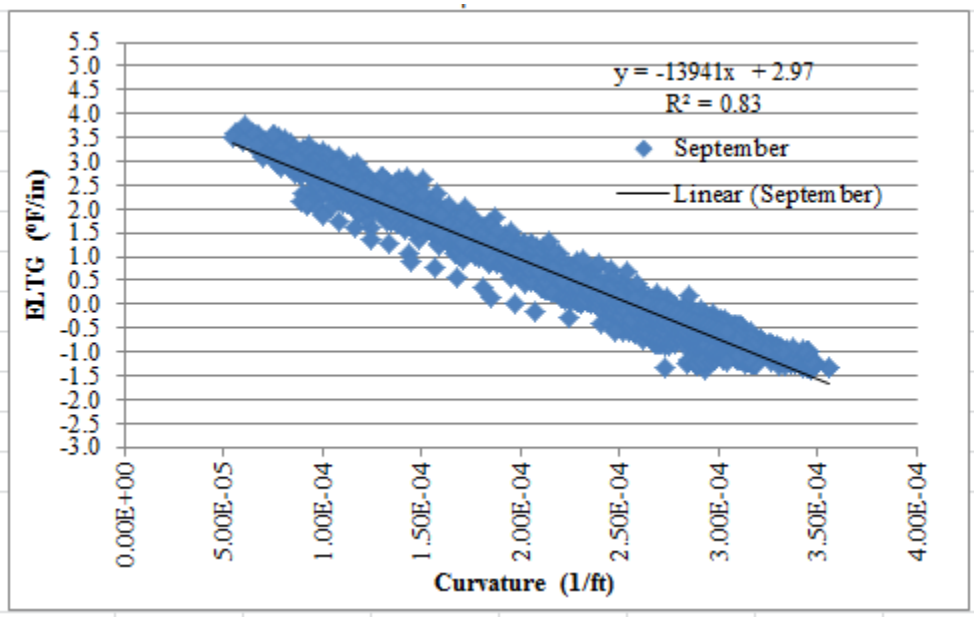

Figure B.21: Built-in Gradient – September – Cell 72

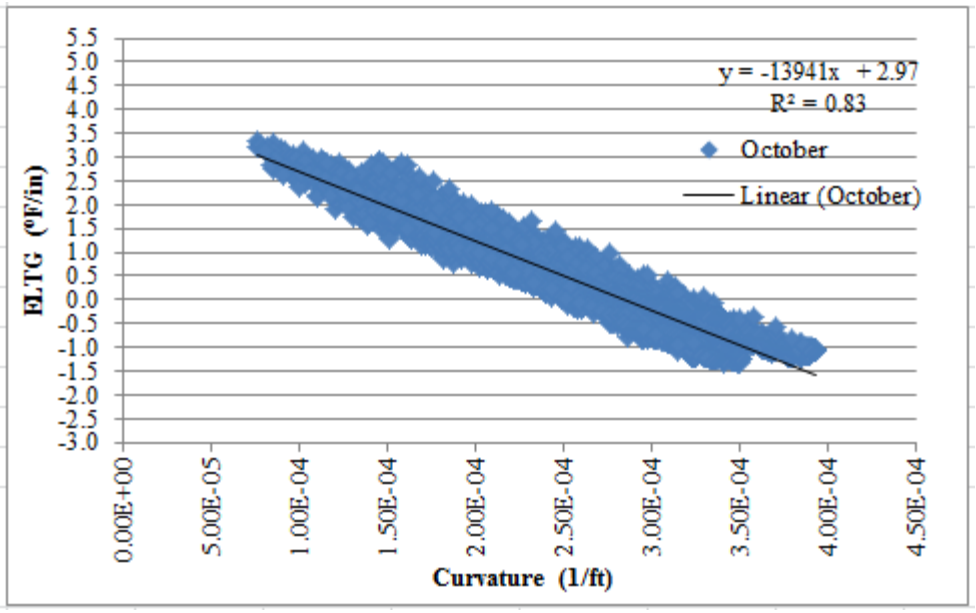

Figure B.22: Built-in Gradient – October – Cell 72

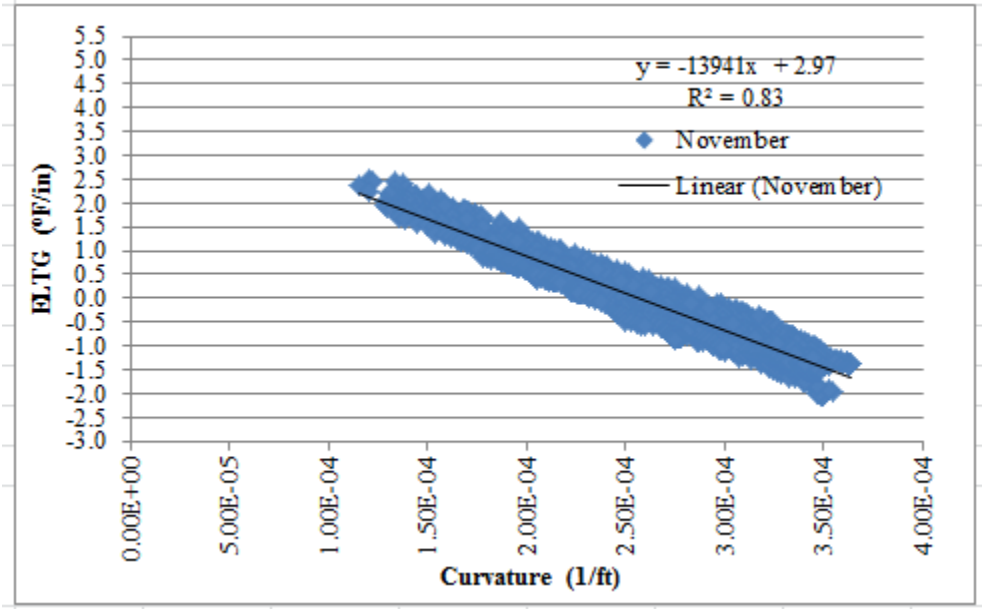

Figure B.23: Built-in Gradient – November – Cell 72

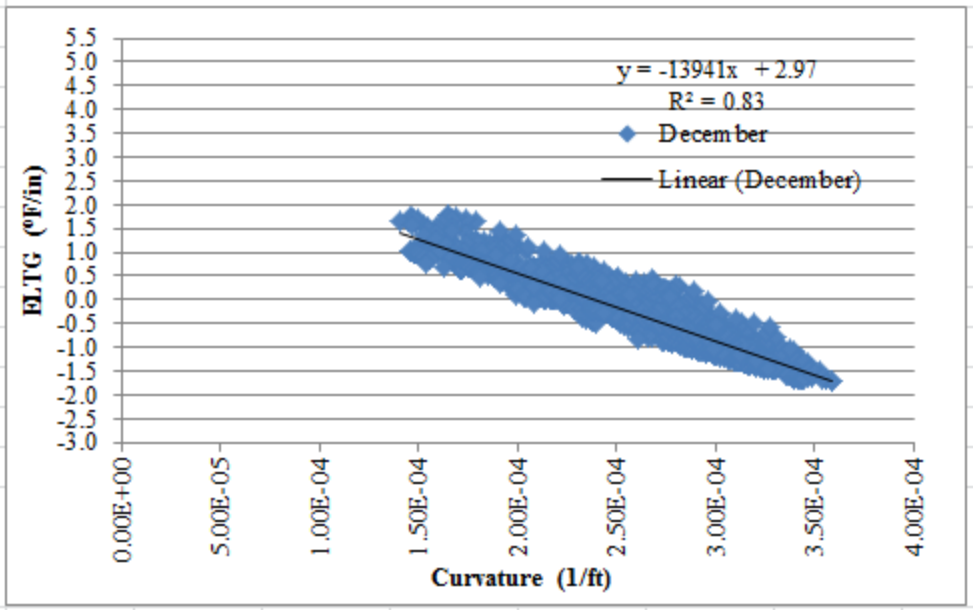

Figure B.24: Built-in Gradient – December – Cell 72

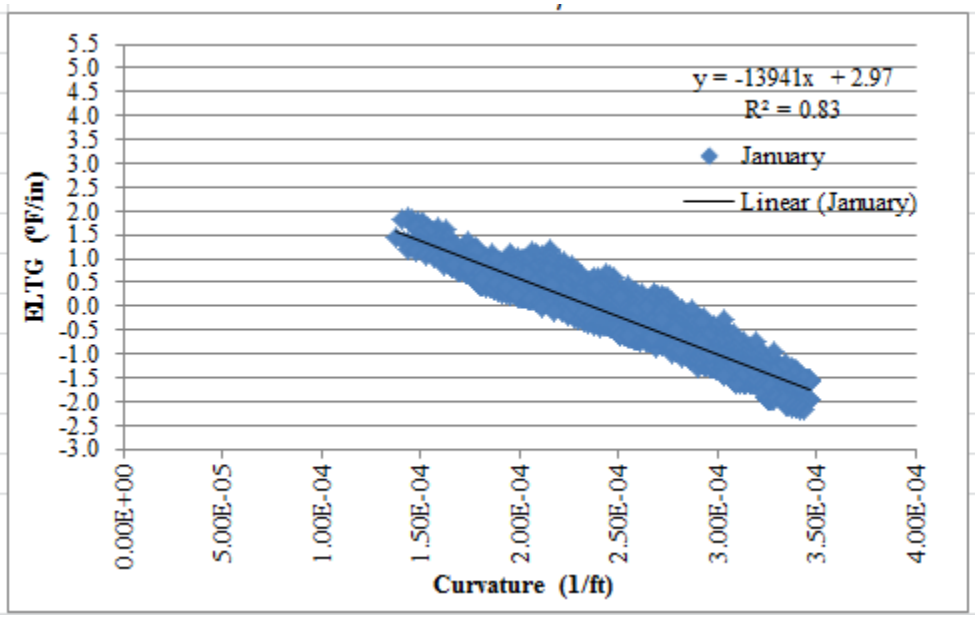

Figure B.25: Built-in Gradient – January – Cell 72

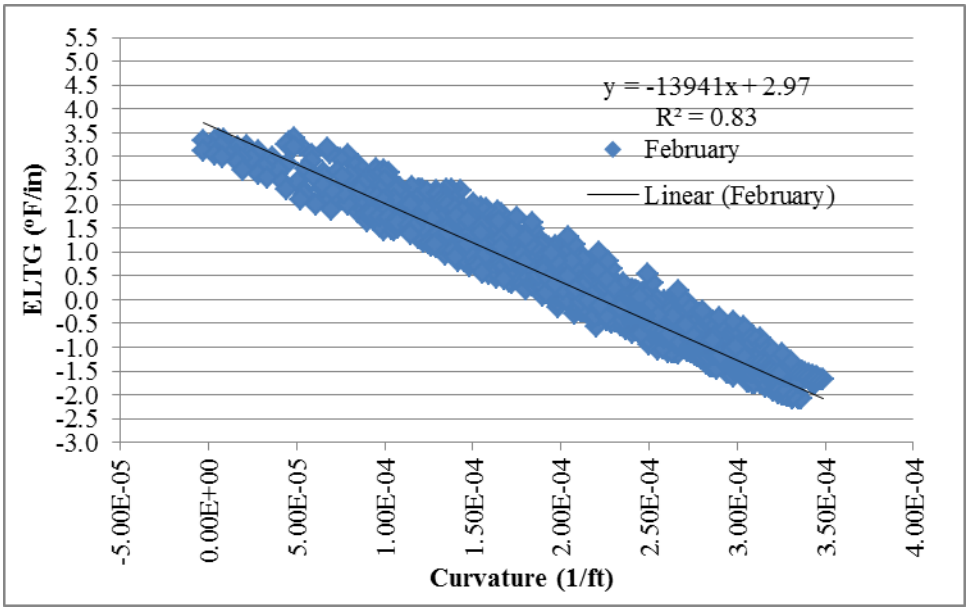

Figure B.26: Built-in Gradient – February – Cell 72

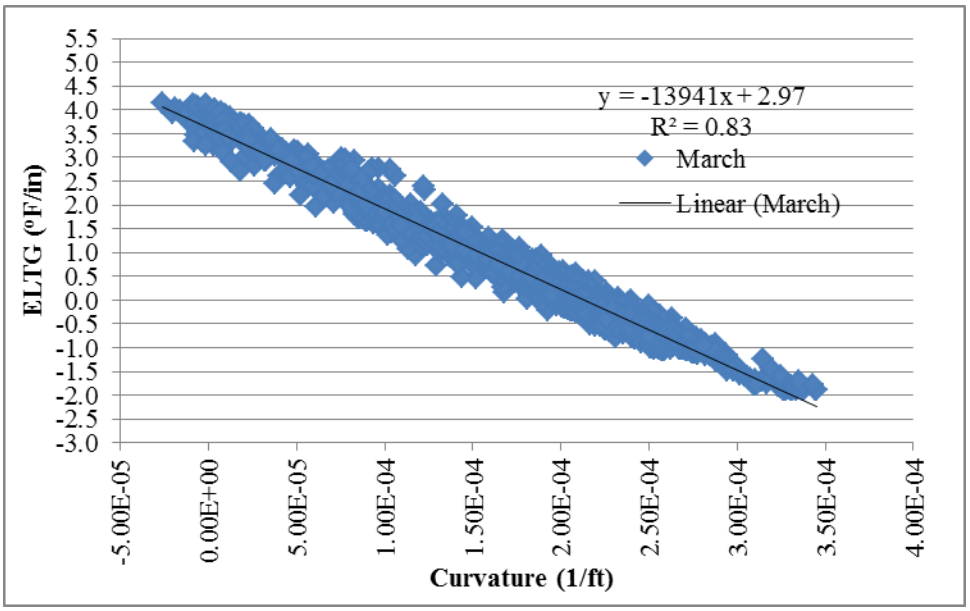

Figure B.27: Built-in Gradient – March – Cell 72

BIBLIOGRAPHY

1. Tompkins, D., L. Khazonovich, and M.I. Darter, *2008 Survey of European Compositve Pavements*, in *Second Strategic Highway Research Program*. 2010, Transportation Research Board: Washington, D.C. p. 61.

2. Cuttel, G.D., et al., *Performance of Rigid Pavements Containing Recycled Concrete Aggregates.* Transportation Research Record, 1997(1574): p. 9.

3. ARA Inc., E.C.D., *Guide for Mechanistic-Empirical Design of New and Rehabilitated Pavement Structures. NCHRP Project 1-37A, Final Report*. 2004, Transportation Research Board of the National Academies: Washington, D.C.

4. Huang, Y.H., *Pavement Analysis and Design*. 2nd ed. 2004, Englewood Cliffs, NJ: Prentice-Hall, Inc. 805.

5. Rao, S. and R.R. Roesler, *Characterizing Effective Built-In Curling From Concrete Pavement Field Measurements.* Journal of Transporation Engineering, 2005. **131**(4): p. 8.

6. Hiller, J.E. and J.R. Roesler, *Simplified Nonlinear Temperature Curling Analysis for Jointed Concrete Pavements.* Journal of Transporation Engineering, 2010. **136**(7): p. 10.

7. Asbahan, R., *Effects of the Built-In Construction Gradient and Environmental Conditions on Jointed Plain Concrete Pavements* in *Civil Engineering*. 2009, University of Pittsburgh: Pittsburgh, PA. p. 586.

8. Mohamed, A.R. and W. Hansen, *Effect of Nonlinear Temperature Gradient on Curling Sress in Concrete Pavements.* Transportation Research Record, 1997. **1568**: p. 7.

9. Mindess, S., J.F. Young, and D. Darwin, *Concrete*. 2003, Pearson Education, Inc.: Upper Saddle River, NJ. p. 644.

10. Kim, K.H., et al., *An Experimental Study on Thermal Conductivity of Concrete.* Cement and Concrete Research, 2003(33): p. 9.

11. Yang, S., *A Temperature Prediction Model in New Concrete Pavement and a New Test Method for Concrete Fracture Parameters*, in *Civil Engineering*. 1996, Texas A&M University. p. 192.

12. Mrawira, D.M. and J. Luca, *Thermal Properties and Transient Temeprature Response of Full-Depth Asphalt Pavements.* Transportation Research Record, 2002. **1809**(1): p. 12.

13. Abraham, H., *Asphalts and Allied Substances*. 4th ed. 1938, Bridgeport CN: Braunworth & Co. Inc.

14. Hu, J., Z. Ge, and K. Wang. *Study of Iowa PCC Thermal Properties for Mechanistic-Empirical Pavement Design*. in *Mid-Continent Transportation Research Symposium*. 2009. Ames, Iowa: Iowa State University.

15. Nishizawa, T., et al., *Temperature Gradient of Concrete Pavement Slab Overlaid with Asphalt Surface Course.* Transportation Research Record, 2007. **1730**: p. 9.

16. Grasley, Z.C., et al., *Relative Humidity in Concrete.* Concrete International, 2006(October 2006): p. 7.

17. Grasley, Z.C., D.A. Lange, and M.D. D'Ambrosia, *Internal Relative Humidity and Drying Stress Gradients in Concrete.* Materials and Structures, 2006. **39**: p. 9.

18. Dhir, M.P., *A Study on the Effect of Temperature Variations on the Bonding of Concrete Overlays.* ACI Journal, 1984. **81**(19): p. 8.

19. Beushausen, H. and M.G. Alexander, *Failure Mechanisms and Tensile Relaxation of Bonded Concrete Overlays Subjected to Differential Shrinkage.* Cement and Concrete Research, 2006. **36**: p. 7.

20. ARA, I., ERES Consultants Division, *Guide for Mechanistic-Empirical Design of New and Rehabilitated Pavement Structures*. 2004: Champaign, IL.

21. Khazanovich, L., *Structural analysis of Multi-Layered Concrete Pavement Systems*, in *Civil Engineering*. 1994, University of Illinois: Urbana-Champaign. p. 334.

22. Ioannides, A.M., L. Khazanovich, and J.L. Becque, *Structural Evaluation of Base Layers in Concrete Pavement Systems.* Transportation Research Record, 1992. **1370**: p. 9.

23. Minnesota_Department_of_Transportation. *Map of Facility*. 2010 [cited 2011 1/19/2011]; Available from: http://www.dot.state.mn.us/mnroad/images/facility.jpg.

24. Tompkins, D., L. Khazonovich, and D.M. Johnson, *BENEFITS OF THE MINNESOTA ROAD RESEARCH PROJECT (MNROAD)*, in *Transportation Research Board 87th Annual Meeting*. 2008: Washington, D.C. p. 17.

25. Federal_Highway_Administration. *Summary of Minnesota Recycled Concrete Aggregate Review.* 2005 [cited 2011 1/20/2011]; Available from: http://www.fhwa.dot.gov/pavement/recycling/rcamn.cfm.

26. Sensiron_Sensor_Company, *Datasheet SHT7x*, in *www.sensiron.com*. 2010.

27. Geokon. *Concrete Embedment Strain Gauges*. 2011 [cited 2011 3/17/2011]; Available from: www.geokon.com/4200-Series.

28. Campbell_Scientific_Company. *Campbell Scientific Website*. 2011 [cited 2011 2/15/11]; Available from: www.campbellsci.com.

29. Ruiz, J.M., et al., *VALIDATION OF HIPERPAV FOR PREDICTION OF EARLY-AGE JOINTED CONCRETE PAVEMENT BEHAVIOR*. Transportation Research Record, 2001. **1778**: p. 9.

30. Janssen, D.J., *Moisture in Portland Cement Concrete*. Transportation Research Record, 1987. **1121**: p. 5.

31. Kim, J.K. and L. C.S. *Moisture Diffusion of concrete Considering Self-Dessication due to Hydration of Cement*. in *15th international Conference on Structural Mechanics in Reactor Technology*. 1999. Seoul, Korea.

32. Shell_Bitumen, *The Shell Bitumen Handbook - Fifth Edition*. 5 ed. 2003: ThomasTelford Publishing.

33. Burnham, T. and A. Koubaa, *A New Approach to Estimate the In-Situ Thermal Coefficient and Drying Shrinkage for Jointed Concrete Pavement*, in *7th International Concrete on Concrete Pavements*. 2001: Orlando, Florida, USA.

34. Ramirez, L.C., et al., *Premature Deterioration of Jointed Plain Concrete Pavements*. 2011, University of Pittsburgh: Pittsburgh, PA. p. 267.

35. Gress, D.L., M.B. Snyder, and J.R. Sturtevant, *Performance of Rigid Pavements Containing Recycled Concrete Aggregate (Update for 2006).* Transportation Research Record, 2006. **2113**: p. 9.